



## Durham E-Theses

---

*Analysis of the astroclimate parameters associated with the tropospheric conditions and their time evolution at Roque de Los Muchachos Observatory*

GUERRA-RAMON, JUAN,CARLOS

### How to cite:

---

GUERRA-RAMON, JUAN,CARLOS (2012) *Analysis of the astroclimate parameters associated with the tropospheric conditions and their time evolution at Roque de Los Muchachos Observatory*, Durham theses, Durham University. Available at Durham E-Theses Online: <http://etheses.dur.ac.uk/3488/>

### Use policy

---

The full-text may be used and/or reproduced, and given to third parties in any format or medium, without prior permission or charge, for personal research or study, educational, or not-for-profit purposes provided that:

- a full bibliographic reference is made to the original source
- a [link](#) is made to the metadata record in Durham E-Theses
- the full-text is not changed in any way

The full-text must not be sold in any format or medium without the formal permission of the copyright holders.

Please consult the [full Durham E-Theses policy](#) for further details.

# Analysis of the astroclimate parameters associated with the tropospheric conditions and their time evolution at Roque de Los Muchachos Observatory

Juan Carlos Guerra Ramon

A Thesis presented for the degree of  
Doctor of Philosophy



Center for Advance Instrumentation  
Department of Physics  
University of Durham  
England

April and 2011

*Dedicated to*

A Zoraida y Carlos por su tiempo y amor en este proyecto.

# **Analysis of the astroclimate parameters associated with the tropospheric conditions and their time evolution at Roque de Los Muchachos Observatory**

**Juan Carlos Guerra Ramon**

Submitted for the degree of Doctor of Philosophy

April 2011

## **Abstract**

The early 1970's saw the start of a new era in astronomy with the first approach to building large telescopes (2 to 5 meters class telescope) and locating them in the right places. The astronomical community started to evaluate these sites using the sky quality "seeing" parameters as one the major constraints to decide where to place the observatory in the world and where is the best location in the observatory. Taking a few words from one of the first site testing works by Merle Walker (Walker,1971) that considered the Islands like as: Canary Islands, Hawaiian islands or Crete, a possible ideal place for Astronomy. *"The best seeing occurs at sites on peaks near sea-coasts having cold ocean currents offshore that reduce the height of the [temperature] inversion layer, and where the laminar air-flow set up over the ocean still persists". (...)* *"Mountain peaks on (small) islands in warm oceans may be good sites, provided that the peaks are sufficiently high to place the observer above the inversion layer".* It is in this new era when many engineers, physicist, meteorologists and astronomers started to search for new places and to develop new instruments to measure the sky quality. Please see the site testing report for La Palma from McInnes (McInnes,1973).

Astronomy is now becoming more sophisticated, with new observatories and new adaptive optics instruments that can compensate the atmosphere to the diffraction limit of the telescopes. The newer Adaptive Optics require more information about the optical parameters that affect image quality and it is also becoming more im-

---

portant to manage the technical and human resources in the observatory for high resolution observations. To obtain the information needed, a new set of instruments have been developed and used, such as: MASS-DIMM, DIMM, SCIDAR, SLODAR, Lusci, etc to mention only a few. They have been the main contributor to analyzing potential new sites for the future extremely large telescopes. They also provide new data for the analysis of the expected performances of the new generation of AO instruments for the TMT or E-ELT.

The purpose of this thesis is to establish the influence of the upper atmosphere, monitored using tropospheric wind speed and temperature, on the local sky conditions, measured by the refractive index parameter  $C_n^2$  and the astroclimate parameters (seeing, isoplanatic angle and coherence time), and their evolution through the years. The meteorological data used come from a launch site located about 150 km away from the observatory and which provides data for meteorological forecasting agencies. It has been determined that the best yearly period for the seeing was the year 2005, which corresponds with the year with lower upper wind speed periods. The use of these meteorological data and the good agreement found with the local sky conditions, provide the first step to constructing a simple parametric optical turbulence model (Trinquet model) of the Observatory Roque de Los Muchachos. This in turn opens the way to performing a nowcast of the astroclimate parameters and the refractive index parameter  $C_n^2$  using the meteorological forecasting data. It can also be used to help design the AO instrumentation capabilities at the ORM (and perhaps by extension elsewhere).

Due to the importance of the knowledge of the vertical  $C_n^2$  distribution and how this affects the Laser Guide Star (LGS) AO observations, an instrument was proposed based on the DIMM technique and using a range-gated CCD detector to measure the backscattered laser light at different altitudes. This can then produce a vertical distribution of the Fried parameter  $r_0$  and the seeing. A simple prototype was built but due to the lack of time and various faults the first experiments could not fulfil the proposed requirements. The preliminary prototype design and the initial on-sky results are provided in appendices of this thesis in order to suggest and support future work.

# Declaration

The work in this thesis is based on research carried out at the The Observatory Roque de Los Muchachos (La Palma) as part-time of my employment in the Telescope Nationale Galileo and Isaac Newton Group Of Telescopes and with the collaboration of the CENTER FOR ADVANCE INSTRUMENTATION "CfAI", England. No part of this thesis has been submitted elsewhere for any other degree or qualification and it allmy own work unless referenced to the contrary in the text.

**Copyright © 2011 by JUAN CARLOS GUERRA RAMON.**

"The copyright of this thesis rests with the author. No quotations from it should be published without the author's prior written consent and information derived from it should be acknowledged".

# Acknowledgements

There are many to give thanks for the support for this work that I couldn't have space to regard to all of them. To my parents, brothers, colleagues and friends for their support and conviction in this work. I want to give thanks to Adriano Ghedina and the AdOpt team (Roberto Ragazzoni, Simone Esposito) to teach me and to give me the first look and the first commissioning and observing nights of the new observational technique called Adaptive Optics. Special thanks to Richard Myers to introduce me in the Adaptive Optics fields, for his support, good talks and share wine during this thesis adventure. Thanks to Richard Wilson for the collaboration in the first stages of the SLODAR projects. To my friends in the CfAi group (Tim, Nigel, Ali...). Thanks to my friends and colleagues in the Telescope Nazionale Galileo, and Isaac Newton Group of Telescopes. Special thanks to my friends in Arcetri (Enrico, Fernando, Armando, Runa, Marcos, Piere, Frank, Rick, Susana, and all the early cafe colleges) to give me the opportunity to contribute to the new adaptive optics systems for the Large Binocular Telescope. Also I want to give thanks to all those friends and colleagues that talking, discussing and enjoying the life have given me the different views to carry on this thesis to the end.

# Contents

<b>Abstract</b>	<b>3</b>
<b>Declaration</b>	<b>5</b>
<b>Acknowledgements</b>	<b>6</b>
<b>1 Introduction.</b>	<b>1</b>
1.1 Solution to the turbulence problem. . . . .	2
1.2 Advantages of observing the diffraction limit in astronomy. . . . .	4
1.3 Main topics of the thesis. . . . .	8
<b>2 The Atmosphere.</b>	<b>11</b>
2.1 Overview. . . . .	11
2.2 The Atmosphere structure. . . . .	11
2.3 The atmospheric Boundary Layer. . . . .	14
2.4 The surface layer. . . . .	17
2.5 The nocturnal boundary layer. . . . .	20
2.5.1 The stable nocturnal layer. . . . .	21
2.5.2 Residual Nocturnal layer. . . . .	22
2.6 Thermodynamics parameters to describe the atmospheric states. . . . .	23
2.6.1 The adiabatic lapse rate ( in unsaturated air). . . . .	24
2.6.2 Potential temperature. . . . .	26
2.6.3 Convective cells. . . . .	28
2.6.4 Indices to determine the atmospheric states. . . . .	29
2.6.5 Jet stream. . . . .	34

---

<b>3</b>	<b>Optical effects of Atmospheric turbulence approximation.</b>	<b>37</b>
3.1	Overview. . . . .	37
3.2	What is the turbulence. . . . .	38
3.3	Tropospheric wind and optical turbulence . . . . .	39
3.4	Temperature and Optical turbulence. . . . .	43
3.4.1	Heffter criteria: a simple model. . . . .	45
3.5	Optical turbulence and the refractive index constant $C_n^2$ . . . . .	47
3.5.1	Obtaining $C_n^2$ from meteorological parameters. . . . .	48
3.5.2	Kolmogorov-Obukhov "two third law". . . . .	50
3.6	Effects of Optical Turbulence. . . . .	51
3.6.1	The optical parameters associated with the turbulence. . . . .	53
3.7	Optical Turbulence Models. . . . .	58
3.7.1	Hufnagel-Valley 5/7. . . . .	59
3.7.2	Dewan Free Atmosphere Model. . . . .	61
3.7.3	Trinquet and Vernin, a parametric model. . . . .	62
<b>4</b>	<b>Sensing the Atmospheric Turbulence</b>	<b>67</b>
4.1	Overview. . . . .	67
4.2	The $C_n^2$ profile. . . . .	68
4.2.1	In situ profiles (rawinsondes). . . . .	68
4.3	Remote soundings (Sodar, RASS and profiler). . . . .	70
4.3.1	Sodar instrument for a vertical profiling of the wind speed. . . . .	71
4.4	Optical remote sensing (DIMM, SCIDAR, SLODAR and MASS-DIMM). . . . .	72
4.4.1	Differential Image Motion Monitor. DIMM. . . . .	73
4.4.2	SCIDAR. . . . .	76
4.4.3	SLODAR. . . . .	79
4.4.4	MASS-DIMM. . . . .	81
<b>5</b>	<b>Correcting the Turbulence</b>	<b>90</b>
5.1	Overview. . . . .	90
5.2	Introduction. . . . .	93
5.3	Wavefront sensing in adaptive optics. . . . .	94

5.3.1	Measurement of curvatures of the wavefront. . . . .	95
5.3.2	Measurement of the local slopes of the wavefront. . . . .	95
5.4	Wavefront Reconstruction. . . . .	98
5.5	Correction systems. . . . .	100
5.5.1	Segmented mirrors. . . . .	101
5.5.2	Continuous Mirrors. . . . .	101
5.5.3	Other devices. . . . .	102
5.6	Control Systems. . . . .	103
5.7	Measurement error. . . . .	104
5.8	Factors influencing the wavefront variance. Error budget. . . . .	106
5.8.1	Tip-Tilt. . . . .	107
5.8.2	WFS error ( $\sigma_{sensor}^2$ ). . . . .	108
5.8.3	Temporal error ( $\sigma_{temp}^2$ ). . . . .	109
5.8.4	Isoplanatic angle ( $\sigma_{ang}^2$ ). . . . .	109
5.8.5	Fitting error $\sigma_{fit}^2$ . . . . .	109
<b>6</b>	<b>Data and Methology.</b>	<b>112</b>
6.1	Overview. . . . .	112
6.2	The Data. . . . .	112
6.2.1	Meteorological data. . . . .	113
6.2.2	Refractive index parameter $C_n^2(h)$ and astroclimatological data on site. . . . .	117
6.3	Methodology. . . . .	120
6.3.1	Seeing from the refractive index values. . . . .	123
6.3.2	Surface layers seeing. . . . .	124
6.3.3	Normalization of the Turbulence energy. . . . .	124
6.3.4	Turbulence profile. . . . .	125
6.3.5	Percentage of energy in each layer. . . . .	125
6.3.6	Fried Parameter ( $r_0$ ). . . . .	125
6.3.7	Total seeing ( $\varepsilon$ ). . . . .	125
6.3.8	Cumulative ascending and descendant seeing. . . . .	126

<b>Contents</b>	<b>10</b>
<hr/>	
<b>7 Data and Analysis</b>	<b>127</b>
7.1 Overview. . . . .	127
7.2 Turbulence measurements. . . . .	128
7.2.1 Astroclimate coherence length "Seeing". Robodimm data. . .	128
7.3 Astroclimate parameters; seeing, isoplanatic angle and coherence time. MASS-DIMM data. . . . .	135
7.3.1 Data-Set. . . . .	136
7.3.2 MASS Channel. . . . .	137
7.3.3 DIMM Channel. . . . .	146
7.3.4 Surface layers seeing. Combine the MASS and DIMM channels.	150
7.3.5 The Refractive Index parameter. The $C_n^2$ profiles. . . . .	150
7.4 Wind and the Refraction Index parameter. . . . .	154
7.4.1 Applying to a daily case. . . . .	169
7.5 Temperature and the optical turbulence. . . . .	180
<b>8 Optical Turbulence Modeling</b>	<b>187</b>
8.1 Overview. . . . .	187
8.2 Introduction. . . . .	189
8.3 Synoptic analysis of models. . . . .	192
8.3.1 Hufnagel-Valley Model. . . . .	192
8.3.2 AXP Model. . . . .	195
8.3.3 Qualitative evaluation of the refraction index profile obtained with the model AXP (thermosode data) and SCIDAR profiles.	203
<b>9 Conclusions and Future Work</b>	<b>207</b>
9.1 Conclusions. . . . .	207
9.2 Future Work . . . . .	210
<b>Appendix</b>	<b>212</b>
APPENDICES.	
<b>A Preliminary results of the Laser Plume DIMM Experiment.</b>	<b>212</b>

---

A.1	Experiment set-up. . . . .	212
A.2	Experiment performances. . . . .	213
A.2.1	First Run. . . . .	214
A.2.2	Second Run. . . . .	218
A.3	Range-Gated operations. . . . .	220
A.3.1	LGS + MASK. . . . .	221
A.4	Conclusions and future work. . . . .	223
A.4.1	Future work. . . . .	224
<b>B</b>	<b>Statistical Analysis of the Seeing.</b>	<b>229</b>
B.1	Overview. . . . .	229
B.2	Data set. Plots. . . . .	229
B.3	Daily Median, Maximum and Minimum. . . . .	233
<b>C</b>	<b>Raw Files</b>	<b>245</b>
C.1	Meteorological Raw. . . . .	245
C.2	MASS-DIMM and Robodimm. . . . .	246
<b>D</b>	<b>MASS-DIMM</b>	<b>254</b>
D.1	Basic Results . . . . .	254
D.2	System description. . . . .	255
D.3	Observations . . . . .	257
D.3.1	Basic Measurements Results. . . . .	257
D.3.2	Comparison between two MASS-DIMM instruments. . . . .	260
D.4	MASS-DIMM. GLAS@WHT Experience. . . . .	267
D.4.1	Observations . . . . .	268
D.4.2	Conclusion of MASS-DIMM and GLAS experience . . . . .	279
<b>E</b>	<b>ZERNIKES POLYNOMIALS AND KARHUENEN-LOEVE FUNC-</b>	
	<b>TIONS. WAVEFRONT DEFORMATIONS</b>	<b>281</b>
E.1	ZERNIKES POLYNOMIALS. . . . .	281
E.2	Karhunen-Love fuctions. . . . .	283
E.3	THE MODAL AND ZONAL RECONSTRUCTORS. . . . .	285

<b>Contents</b>	<b>12</b>
E.3.1 Zonal reconstructor. . . . .	285
E.3.2 Modal reconstructor. . . . .	287
<b>Bibliography</b>	<b>289</b>

# List of Figures

1.1	Near infrared images of Uranus before and after the AO system on Keck was turned on. The image shows at the top its rings and moon Miranda. On the bottom is Uranus and its atmospheric details in the near-infrared. Uranus at K' ( $2.2\mu m$ ) and H ( $1.6\mu m$ ) bands. Credit. Hammel and de Pater. . . . .	5
1.2	Strehl ratios for first-light images of the Keck LGS AO system on Sept.19, 2003. The left panel shows an uncorrected Strehl ratio of four percent. Middle panel: Strehl ratio of 18% for a natural guide star object. Right Panel: Strehl ratio of 36%for the Keck laser guide star. <a href="http://keckobservatory.org/images/gallery/press_images">http://keckobservatory.org/images/gallery/press_images</a> . . . . .	6
1.3	Central region of M92 globular cluster. Image taken by Hubble at $1.6\mu m$ (left) and same region of the globular cluster taken by the Adaptive Optics system mounted in the LBT (right). Credit: Hubble/LBT ( <a href="http://www.lbto.org">http://www.lbto.org</a> ) . . . . .	7
1.4	Temporal evolution of the optical turbulence profiles at the Observatorio del Roque de los Muchachos. The one-day forecast was computed every hour over the course of one month. The color bar represents the prevailing $C_n^2$ values on a logarithmic scale. Trinquet, et al. 2006. . . . .	10
2.1	Scheme of the main atmosphere distribution layers and the vertical temperature variation (yellow line). <a href="http://www.srh.noaa.gov/jet-stream/atmos/layers.html">http://www.srh.noaa.gov/jet-stream/atmos/layers.html</a> . . . . .	13

- 2.2 Conceptual rendered image of the ELT enclosure design proposed by ESO showing a round enclosure. <http://www.eso.org/sci/facilities/eelt/telescope/dome>. . . . . 15
- 2.3 Rendered image of the TMT enclosure both the E-ELT and the TMT dome have chosen a round dome to minimize the turbulence at the surface and ground layer, hence reducing the wind loading. The enclosure is type "Calotte". <http://www.tmt.org/observatory/enclosure-infrastructure>. Credit TMT Consortium. . . . . 17
- 2.4 Example of a wind shear vertical profile for a rough initial input of 0.1. 19
- 2.5 Description of the boundary layer evolution detailing the sub-layer structure that typically develops during the daytime to nighttime transition. Credit Stull, 1988. . . . . 21
- 2.6 Example of 24 hours of the vertical profile of the atmosphere aerosol and cloud vertical structure in continuous measurements, sensed by a LIDAR. Sunrise occurs around 13:00 UTC, and boundary layer (PBL) growth during morning into afternoon is visible in the figure. Aerosol layers in the free troposphere are visible during the previous night, and the planetary boundary layer (PBL) eventually reaches high enough to entrain the boundary layer. The image was taken during the project MPLNET. The gradient colors shows the concentration of aerosol in percentage. <http://www.enc.ncep.noaa.gov>. Credit NASA. . . . . 22
- 2.7 The atmosphere is nearly always stable to dry processes. A parcel displacement upward (downward) in an adiabatic process moves along a dry adiabatic (dotted) line and cools down (warms up) at a rate that is faster than that of the environment,  $\frac{\partial T_E}{\partial z}$ . If the parcel is warmer, it will be less dense and positively buoyant and will rise (accelerate upward). If the parcel is cooler, which is the normal course of events, it will be more dense and will sink (accelerate downward). . . . . 26

- 2.8 Vertical profile of the averaged temperature (dotted) and potential temperature  $\theta$  (solid) as a function of pressure. The data are retrieved from the radiosonde launch in Tenerife. Only the height of interest above the Observatory is plotted. Starting at 700 mb which is about 2500 meters to 15 mb at about 30000 meters. Data from radiosonde 60080. . . . . 29
- 2.9 Idealized Kelvin-Helmholtz billows and the formation of vortices. It shows the time series evolution for a Kelvin-Helmholtz instability that occurs at the interface between two layers stratified when their velocities are different. The development of turbulence occurs with the Richardson index ( $R_i < 0.25$ ). . . . . 31
- 2.10 Creation of the vortex street from the Canary Islands to Madeira. The distance from Madeira to the Canary Islands is about 450 kilometers. A vortex street often occurs when cloud formations over the ocean are disturbed by wind passing over land or another obstacle and the air masses generate a turbulent pattern according to mixing length theory. In this true-color Moderate Resolution Imaging Spectroradiometer (MODIS) image from July 5, 2002, marine stratocumulus clouds have arranged themselves in rows, or streets, which are usually parallel to the direction of wind flow. Credit. Nasa Hubbles gallery. . . . . 32
- 2.11 Profiles of a radiosonde launch in Paranal (Chile) taking the height slab between 6 to 9 km, showing a good correspondence of the variation of the  $C_t^2$  (left) measured with the calculated gradient of the potential temperature  $\theta$  (middle) and Richardson number  $R_i$  (right). The radiosonde gives a high vertical resolution for the temperature and wind speed parameters which can give the same resolution for the  $C_t^2$ ,  $\theta$  and  $R_i$  identifying the turbulent layers. Credit. Vernin and Avila, 1998. . . . . 33

- 2.12 Typical Jet stream picture of the jet stream circulation during two periods (winter and summer). The grey zones show the strength of the jet stream and how typically are located during the winter and summer periods. <http://squall.sfsu.edu/crws/jetstream.html> . . . 35
- 3.1 Scheme of the turbulent process generated by the energy cascades. The turbulent cells move from the outer scale ( $L_0$ ) to an inner scale ( $l_0$ ). Lewis F. Richardson has defined this energy transfer process as; *"big whirls have little whirls that feed on their velocity; Little whirls have lesser whirls and so on to viscosity."* Credit. Adapted from Andrews and Philips, 2005. . . . . 39
- 3.2 A year-long distribution of the wind speed measured in knots for the year 2008. Those measurements are from the database of the radiosonde data collected from station 60018 (launch site in Tenerife) every day at 00 UT, the strength of the wind changes shows a seasonal component with a calm period from June to September. (The gradient bar shows the velocities from black minimum (0 knots) to maximum white (150 knots) . . . . . 41
- 3.3 Tropospheric wind rose for different sites in the Northern Hemisphere; San Pedro Martir (SPM), Manua Kea, Observatorio Roque de los Muchachos (ORM) and Southern Hemisphere; Paranal and La Silla. Credit. Garcia-Lorenzo, et al. 2005. . . . . 42
- 3.4 Linear coefficient of Pearson correlation obtained from the daily measurements at different sites (La Palma, Manua Kea, San Pedro Martir, Paranal and La Silla) of the wind speed at different height levels with the wind speed at 200mb. Credit Garcia-Lorenzo, et al. 2005. . . . . 44
- 3.5 Daily vertical distribution of the temperature for the year 2006, the crosses show the minimum temperature where the tropospheric inversion layer occurs at the height of the jet stream. . . . . 45

- 3.6 Plot of the daily radiosonde data which fulfill of the Heffter conditions. Data taken from the radiosonde database for the year 2008. The white pixel indicates fulfill of the Heffter criterion and the black pixels indicates that dont fulfill the Heffter criterion showed in the equations 3.3. The vertical axis gives the altitude, which starts at 3 km. The Observatory Roque de los Muchachos is about 2.4 km above sea level. 47
- 3.7 The Kolmogorov and Von Karman spectral model for the refractive index fluctuations. The inner scale of the turbulence is 1cm and the outer scale is 10m. The Kolmogorov is represented by the  $-11/3$  power law and the Von Karman roll-off in the border of the limits of the inertial range. Credit. Adapted from Andrews and Phillips, 2005. 52
- 3.8 Depiction of the beam, propagating wave front, windspeed vector and the Fried coherence length  $r_0$ . . . . . 54
- 3.9 Isoplanatic angle ( $\theta_0$ ), angle in which the coherence length doesn't vary and two objects can be compensated with the same wavefront. . 56
- 3.10 A vertical Huffnagel-Valley HV5/7 profile is represented with the wind speed data obtained from the Tenerife radiosonde and the median wind speed in the first 15 kilometers. . . . . 61
- 3.11 Diagram showing the forecasting scheme, with the optical turbulence monitor (seeing or  $C_n^2(h)$  profiler) passing information from the local weather stations (pressure, temperature, humidity and wind speed) to the forecasting layer where the results go to the decision center where the observational program can be adjusted depending on "forecasted" sky quality. Credit: Adapted from Trinquet, 2008. . . . . 63
- 4.1 Example of a  $C_n^2(h)$  profile measured by a MASS-DIMM instrument at Roque de los Muchachos Observatory during the night of the 6<sup>th</sup> on May 2009. The white stripe corresponds to wrong data acquisition. It shows strong turbulence at the higher layer of the atmosphere above 4km during the whole night. . . . . 69
- 4.2 Photograph of a thermosonde and the boom. The boom is located about 10 meters below to avoid disturbances from the balloon. . . . 70

- 4.3 Sodar instrument and the output image of the vertical profile of the wind speed strength. Credit NOAA. . . . . 71
- 4.4 RASS instrument on the left and a vertical plot of the wind speed and the temperature measured in Aztec station. Credit. NOAA. [<http://profiler.noaa.gov/npn/profiler.jsp>] . . . . . 72
- 4.5 Schema of a profiler instrument operations. Credit. NOAA. . . . . 73
- 4.6 DIMM monitor at the ORM. The instrument is installed in a platform at 5 meters above the ground and located in Northerly direction from the WHT. . . . . 74
- 4.7 Schematic diagram of the DIMM instrument. Simple instrument based on a telescope with a mask in the entrance pupil with two holes with one prism and a detector where the star is splitted in two spots. Credit. Image adapted from Sarazin and Roddier, 1990 . . . . 75
- 4.8 Scheme of the SCIDAR technique layout. From the observation of binary stars, it obtains a stack of consecutive images of scintillation. The average auto-correlation function of them gives information about the  $C_n^2(h)$  profiles, and average cross-correlation functions give the wind speed of the layers. Credit: Fuensalida et al, 2004 . . . . . 77
- 4.9 Figure of SCIDAR measurements acquire. (a) Cross-correlation of scintillation images for the detected triplets, the retrieved height above the telescope and the winds speeds are indicated. The uncertainty in the height of the single layers is around 25 meters. (b) Graphical display of the real time profile determined from the auto-correlation using a wide binary of separation 35 arcsec the maximum attainable height above the telescope is limited to around 2 km, and the vertical resolution is around 200 meters. Credit. LBT-SCIDAR Egner, et al,2007. . . . . 78
- 4.10 Average and median turbulence profile  $C_n^2$  of a set of 68 observations during the year 2004 at the ORM. Credit. Fuensalida et al. 2004. . . 79

- 4.11 Statistical  $C_n^2(h)$  profiles for a set of observations with G-SCIDAR at the ORM. (Blue line average, dashed blue line median). The number of nights is indicated in the plot. Right image observations during July. Left image observations during March. Credit. Fuensalida et al, 2004. . . . . 79
- 4.12 Portable SLODAR mounted at Paranal Observatory beside of the VLT. Credit. ESO . . . . . 80
- 4.13 A simple schematic illustration of SLODAR resolution.  $\theta$  is the angular separation of the double star with a telescope pupil of diameter  $D$  and  $w$  is the single size of the subaperture array. The bottom image shows the Shack-Hartmann spot patterns for a binary star, and real-time plots of the turbulence-altitude profile and the integrated turbulence strength versus time. Credit. Wilson,2002 . . . . . 81
- 4.14 Simple scheme of MASS operation. Credit. <http://www.ctio.noao.edu/%Eatokovin/profiler/> . . . . . 83
- 4.15 MASS weighting function representation. Credit: <http://www.eso.org/gen-fac/pubs/astclim/espas/workshops/AO-ATMO-2003/Tokovinin.pdf> . 84
- 4.16 Schematic representation of the atmosphere coverage of the DIMM and the MASS turbulence sensing monitors. The recombined profile is also shown. . . . . 88
- 5.1 Principle scheme of an adaptive optics system: The phase errors of the incoming wavefront are measured by a wavefront sensor unit and processed in real time. The real-time computer drives the correction units such as; tip-tilt and deformable mirror to correct the wavefront in an inversely shaped way to the measured distortions providing a corrected wavefront (high resolution images) for the science instrument. Credit. Bryan Christie. . . . . 93
- 5.2 Compilation of the all refereed LGS AO science papers. The large peak in 2007 comes with the use of the Keck II AO systems. Credit. Liu, 2008 . . . . . 97

- 5.3 Schematic diagram of a Shack-Hartmann wavefront sensor. Wavefronts from astronomical objects are distorted by the atmosphere and reach the pupil of the telescope. At a conjugate of the pupil a microlens array is placed. Each microlens forms an image on its focal plane. The average slope of the wavefront in the area of the microlens is obtained from the position of the center of gravity of the image. Adapted from Boston micromachines.<http://www.boston-micromachines.com> . . . . . 98
- 5.4 Pyramid wave front sensor scheme. The light is focused on the vertex of the pyramid and four images are formed on the detector; a relay lens helps to collimate the four beams. The analysis of the intensities in the four pupils is used to retrieved the slopes variation due to the wavefront errors. Adapted from Ragazzoni 2002. . . . . 98
- 5.5 Flow diagram of the phase reconstructor for a Shack-Hartmann wavefront sensor. . . . . 99
- 5.6 Segmented deformable mirror for NAOMI, with 76 elements. . . . . 101
- 5.7 Example of a secondary adaptive mirror, that consists in a continuous deformable mirror of 910mm formed by 672 voice-coil actuator. Credit LBT. . . . . 102
- 5.8 Two images of the bimorph deformable mirror. (a) shows the rear view of the bimorph DM of the CFHT. The (b) shows the front of the bimorph DM. This type of deformable mirror is used in Adaptive Optics instruments in Subaru or VLT. . . . . 103
- 5.9 Diagram representing anisoplanatism. It can be clearly seen that the path taken by the analyzed light and that of the correction is different. A part of the turbulence is not seen and so cannot be corrected. (Right) The image of the galactic center taken with NAOS on the VLT. In this image we see the effect of anisoplanatism, causing deterioration in the image away from the center, where the AO loop has been closed. Credit. E. Marchetti, ESO. . . . . 107

- 
- 6.1 Location of La Palma and Tenerife, Radiosonde launch site (A) at Tenerife and the La Palma Observatory site at 120 km from the launch site and an altitude of 2400 meters above sea level. Credit. Adapted from Google Earth. . . . . 115
- 6.2 Access webpage of the Wyoming Meteorological department. The nearest station is situated in Tenerife ( station number 60018) at 120 kilometer east from the Roque de Los Muchachos Observatory (La Palma Island). Credit *http : //weather.uwyo.edu/upperair–/sounding.html* . . . . . 116
- 6.3 Using the ARL web interface to retrieve meteorological data. The case of La Palma has longitude and latitude coordinates: latitude: 28.45 degrees, longitude W 17.48 degrees. . . . . 118
- 6.4 MASS-DIMM set up in the tower side by side to the Robodimm. . . . 119
- 6.5 Schematic diagram showing the methodology to manipulate the data. 122
- 7.1 2D distribution of the evolution of the seeing through the years 2002 to 2008. The gradient colors show the intensity of the distribution of the measurements. . . . . 132
- 7.2 Monthly seeing distribution retrieved from the Rododimm data from September 2002 to December 2008 showing the standard deviation in vertical bars. . . . . 133
- 7.3 Representation of the monthly seeing distribution for 2002 to 2008. The blue line represent the median values and the shadows are the 95% confident intervals. . . . . 134
- 7.4 Cumulative distribution of the seeing parameter for a daily average of the whole data set. The red line: summer time. The red dash line: winter time. . . . . 136
- 7.5 Boxplot representation of the whole dataset of the seeing values from 2002 to 2008 with a monthly distribution for all the years. The best months are August and September with the lowest median values, but July show a less variability. . . . . 137

- 7.6 Boxplot of the free seeing for the whole year 2008 showing the monthly distribution. The orange dots represent the median and the blue bars are the standard deviation. The x-axis represents the months by numbers (1 to 12; January to December), the y-axis represents the free seeing in arcsecs retrieved from  $C_n^2$  profiles obtained with the MASS-DIMM instrument. There is no data for the month 3 (March). 141
- 7.7 Statistical analysis of the isoplanatic angle for the year 2008. Data retrieved from the MASS-DIMM instrument. The x-axis represents the months ( 1- January to 12- December) and y-axis represents the isoplanatic angle measured in arcseconds. There is no data for March (3). . . . . 142
- 7.8 Statistical analysis of the coherence time for the year 2008. Data retrieved from the MASS-DIMM instrument. The x-axis represents the months ( 1- January to 12- December) and y-axis represents the coherence time in seconds. There is no data for March (3). . . . . 143
- 7.9 Temporal evolution of the total seeing measured with the DIMM channel. . . . . 147
- 7.10 Cumulative distribution calculated from the seeing measured with the DIMM channel. A 10 minutes median value per day is calculated (red line) and the daily median value is plotted (blue line). . . . . 148
- 7.11 Histogram of the seeing distribution per month during the year 2008. This shows the histograms of the total seeing per month. . . . . 149
- 7.12 Monthly median seeing for the surface,free and total seeing. The data considered are filtered with a minimum integration of 4 hours of measurements. . . . . 151
- 7.13 Statistics of the refractive index parameter  $C_n^2$  during the year 2008. The  $C_n^2$  vales are in logarithm. The logarithm of the refractive index  $C_n^2$  shows a weak turbulence for values -20 and strong turbulence for values -14. . . . . 152

- 7.14 Percentage of the ground layer and the free (boundary and boundary+Free) contribution to total  $C_n^2(h)$  retrieved from the total seeing (DIMM measurements) and the free seeing (MASS measurements). The free is measured with the MASS channel in 6 height slabs (0.5, 1,2,4,8 and 16 km) and the boundary is taking the first three slabs (0.5,1 and 2 km). . . . . 153
- 7.15 Example of turbulence profile restored from the MASS profiles. The Figure shows one frame of the whole sequence of the atmospheric profile obtained in real time during the acquisition process. The right plot shows the median value of the  $C_n^2$  for the measured height slab and the left plot shows the positive and negative cumulative sum of the  $C_n^2$  indicating that the predominant strength occurs about 2 km. The plot reports all the parameters calculated from the recombination of the free and the total atmosphere. . . . . 155
- 7.16 Retrieved the profiles of the wind speed from the radiosonde data station 60018 (Tenerife) for the year 2008. The balloons are launched at midnight (00 UT) every day and the plot represents a 2D profile of the vertical wind speed through the year. The height goes from 3 to 30 km. . . . . 156
- 7.17 2D image of the daily distribution of wind speed measurements starting in the years 2002 to 2008, the daily distribution is represented in a gradient colors. With the strong wind speed is representing in white. Day without data are represented has black columns. Data taken from radiosonde database. . . . . 160
- 7.18 Monthly distribution of the wind speed at a height between 9 to 12 km for the years from 2004 to 2008. The height analyzed is just in the region of the jet stream. . . . . 162

- 7.19 Wind speed distribution of the tropospheric wind in a height slab between 9 to 12 km. The blue line is the fitting of the local regression polynomial to the data and the grey zone is the 95% confidence interval region. Data obtained from the radiosonde launched at 120 km from the Roque de los Muchachos Observatory. . . . . 163
- 7.20 Monthly median wind speed distribution for the year 2008. The plot data are retrieved from the table 7.13. The wind speed has been taken from median value in the altitude slab between 9 to 12 km where the jet stream is located; the monthly distribution show a more stable conditions during the summer period extended to the autumn (October and November). The bars represents the standard deviation 165
- 7.21 Plot of the median wind speed, the whole seeing measured by a DIMM and free atmosphere seeing (above 0.5km) measured by the MASS. Statistics is referred to the year 2008. To scale the whole set of data for representation purpose, the wind speed is in logarithm scale. The total seeing and free seeing are in normal scale. Seeing measured in arcseconds and wind speed in  $ms^{-1}$ . . . . . 167
- 7.22 Seasonal effect of the isoplanatic angle in relationship with the seasonal effects of the wind speed at the tropospheric height (200mb). Data for the year 2008. March doesn't have MASS-DIMM measurements. The blue line represents the isoplanatic angle with the y-axis on the left and the red lines represents the wind speed with the y-axis on the rights. . . . . 169
- 7.23 Four months figures set for the median daily; total seeing, free seeing and wind speed at the troposphere altitude (9 to 12 km) for measurements collected in January, May, August and November of the year 2008. The wind speed is shows in a logarithmic scale for visual purpose. 174
- 7.24 Reconstructed  $C_n^2$  profile from the MASS measurements. It shows an explosion in the middle altitude below the 4 km that propagates down to the lower layers. Also it can seen at 16 km. This event occurs the 1<sup>st</sup> on February 2008 . . . . . 175

- 
- 7.25 Daily median seeing values for the total seeing and free seeing with the calculated surface seeing for measurements taken during August of the year 2008. . . . . 179
- 7.26 Daily median values for the seeing (total, free and surface) and the tropospheric wind speed, showing events where increase of the wind speed in the upper layers affects the seeing evolution with increase of the free seeing contribution to the total. The peak of this event took about 3 days to disappear with and increase of the free seeing values . The wind speed has logarithmic scale for visual comparison with the seeing values. . . . . 180
- 7.27 Figure set of the temperature profiles for the data collected from the radiosonde database and it shown in a gradient color profile that goes from blue to white, the crosses indicate where the troposphere inversion layer is produced. . . . . 183
- 7.28 Frequency of occurrences of calm and active turbulence states at four height slabs. The data represent the monthly median of the data taken for the year 2008. . . . . 184
- 7.29 Percentage of the monthly distribution of the turbulence strength for the year 2008. Different colors to express the height slabs measured with the MASS instrument (0.5,1,2,4,8 and 16 km). No data available for March. . . . . 186
- 8.1 Richardsons artistic vision of how should be the forecast "factory". Credit. Franc Schuiten. . . . . 188

- 8.2 Schema of the information from the model of  $C_n^2$  and how many parameters can be added to the whole system to retrieve a performance of the system measuring the PSF of the source through the turbulent medium. The values are identified as; "r<sub>0</sub>" coherence length (Fried parameter), "iso" isoplanatic angle, "λ" wavelength, " $C_n^2(h)$ " refractive index coefficients. "Nlayer" number of turbulent layers determined, "Hlayer" height of the turbulent layers, "Vlayers" velocity of the layers, "Nwfs" number of wavefront sensors used, "Nactuators" number of actuator, "Npix" number of pixels of the detector. . . . . 191
- 8.3 Representation in gradient color image of the vertical  $C_n^2(h)$  profile from the modified H-V model, applying the monthly median wind speed between the heights 5 to 15 km. The scales goes from -21 to -16 that represents: -21 a stable (weak) atmosphere and -16 a turbulent state. The  $C_n^2(h)$  is measured ( $m^{-2/3}$ ). The x-axis is represented by the months (January to December) and y-axis is the height (Km). . . 194
- 8.4 Statistical median monthly  $C_n^2(h)$  profiles retrieved from the MASS measurements located at Observatorio Roque de los Muchachos (La Palma) with a distance of 120 km away from the radiosonde launch (Tenerife). The MASS gives 6 heights slabs; 0.5,1,2,4,8 and16 km where are represented in the y-axis by; 3,3.5,4.5,6.5,10.5 and 18.5 Km.respectively. The x-axis gives the month with an empty 3 (March) due to the fact that the MASS instrument was out of operation. . . . 195
- 8.5 Set of figures representing the temporal variation of the  $C_n^2(h)$  profiles obtained from the AXP model for 4 years of meteorological data retrieved from the database (Chapter 6). The figure represents a 2D gradient of the logarithm of the  $C_n^2(h)$  values with the x-axis for the days and the y-axis for the altitude. (a) the year 2005, (b) year 2006, (c) year 2007 and (d) year 2008. . . . . 198

- 8.6 Monthly statistics plots of the  $C_n^2(h)$  retrieved from two models; the Hufnagel-Valley and the AXP. The solid blue line is the median value for the AXP model and the dashed lines are the 1<sup>st</sup> and 3<sup>rd</sup> quartiles. The solid black line is the median for the H-V model and the dashed red lines are the deviation formed by 1<sup>st</sup> and 3<sup>rd</sup> quartiles. . . . . 199
- 8.7 Scatter plot for reconstructed  $C_n^2(h)$  profiles obtained from the AXP and HV model. The x and y -axis shows the logarithm of the  $C_n^2(h)$  vales ( $m^{-1/3}$ ). The red dash line shows the linear fitting and the solid red line is the smooth series. The figure includes two boxplots with the distribution of the series and with the median value displacement. 200
- 8.8 Comparison of the median distribution of the  $C_n^2(h)$  profiles from the MASS measurements and the  $C_n^2(h)$  profiles retrieved from the AXP model. x-axis ( $\log C_n^2(h)$ ), y-axis is the heights (Km). The data shows the data compiled for June 2008. . . . . 202
- 8.9 Boxplot representation of the monthly distribution of the  $r_0$  parameter obtained with the AXP model for the year 2008. . . . . 203
- 8.10 Comparison between the MASS and AXP free seeing. The AXP model free seeing is represented in the left and the MASS free seeing is represented in the right side of the figure. The x-axis represents the months by 1 to 12 which corresponds ; January to December). . . 204
- 8.11 Comparison plots of  $C_n^2(h)$  profiles measured with the SCIDAR instrument set at Roque de Los Muchachos and the  $C_n^2(h)$  profiles calculated from the AXP model using the radiosonde data from the database. The x-axis shows the altitude (Km) and the y-axis shows the  $C_n^2(h)$  ( $m^{1/3}$  ). The two set of plots represent the median values for the  $C_n^2(h)$  profiles from SCIDAR and AXP for 6 nights on March 2004. For the AXP data it has been taken from the meteorological data for the first 6 days of March. . . . . 205

8.12	Comparison plots of $C_n^2(h)$ profiles measured with the SCIDAR instrument settled at Roque de Los Muchachos and the $C_n^2(h)$ profiles calculated from the AXP model using the radiosonde data from the database. The x-axis shows the altitude (Km) and the y-axis shows the $C_n^2(h)$ ( $m^{1/3}$ ) The two set of plots represent the median values for the $C_n^2(h)$ from SCIDAR and AXP for 7 nights on July 2004. For the AXP data it has been taken from the meteorological data for the first 7 days of July. . . . .	206
9.1	Monthly median seeing for all the data set available from the September 2002 to December 2008. . . . .	210
9.2	Monthly median wind speed at tropospheric heights (9 to 12 km). . . . .	210
A.1	The system setup at the fork of the WHT. . . . .	213
A.2	Polaris star, and a zoomed image. . . . .	215
A.3	Polaris star, and a zoomed image. . . . .	215
A.4	Shedir star, and a zoomed image. . . . .	215
A.5	Shedir FWHM for x and y. . . . .	216
A.6	Polaris image through the mask and reading the range-gated ccd at 75Hz, Not gating. . . . .	216
A.7	Polaris star, and a zoomed image. . . . .	217
A.8	Surface plot of the Polaris image through the mask and reading the range-gated ccd at 75Hz, Not gating. . . . .	217
A.9	Polaris image through the mask and reading the range-gated ccd at 100Hz, Not gating. . . . .	217
A.10	Surface plot of the Polaris image through the mask and reading the range-gated ccd at 100Hz, Not gating. . . . .	218
A.11	Polaris ar 10Hz . . . . .	219
A.12	Image . . . . .	219
A.13	Polaris ar 10Hz . . . . .	220
A.14	Optional caption for list of figures . . . . .	221
A.15	Polaris image in range gated mode . . . . .	221

A.16	Polaris Range gated . . . . .	222
A.17	Surface profile of the image number 9 in the upper part of the CCD. . . . .	223
A.18	Surface profile of the image number 10 in the lower part of the CCD. . . . .	223
A.19	Set of images of the Rayleigh laser spot . . . . .	226
A.20	Oscilloscope screenshot at 100Hz and 10Km gated=500m . . . . .	227
A.21	Oscilloscope screenshot at 50Hz and 8km gated=700m . . . . .	227
A.22	Oscilloscope screenshot at 20Hz, 8km gated=500m . . . . .	228
B.1	Boxplot representation of the yearly seeing. . . . .	230
B.2	Boxplot of the monthly seeing . . . . .	231
B.3	Histogram of the total seeing distribution during the year 2002 during the month September to December. . . . .	235
B.4	Monthly seeing distribution retrieved from the Rododimm data from September 2002 to December 2008 showing the standard deviation in vertical bars. . . . .	236
B.5	Calendar of the mean seeing calculated per very day since 2002 to 2008. The year 2002 starts to get data on September. The white cells indicate not data available and it has to be noted that the year 2002 starts on September and March 2008 the robodimm was stopped by technical problems. . . . .	237
B.6	Boxplot statistics for the maximum and minimum seeing calculated from 2003 to 2008. The x-axis represents the months (1 to 12 means January to December) . . . . .	238
B.7	Daily variation of the maximum seeing calculated for every hour during August for the years from 2002 to 2008 . . . . .	239
B.8	Daily variation of the minimum seeing calculated for every hour during August for the years from 2002 to 2008 . . . . .	240
B.9	Daily variation of the median seeing calculated for every hour during August for the years from 2002 to 2008 . . . . .	241
B.10	Daily variation of the maximum seeing calculated for every hour during September for the years from 2002 to 2008 . . . . .	242

- B.11 Daily variation of the minimum seeing calculated for every hour during September for the years from 2002 to 2008 . . . . . 243
- B.12 Daily variation of the median seeing calculated for every hour during September for the years from 2002 to 2008 . . . . . 244
- C.1 Meteorological parameters from the station 60018 sited in Guimar, Tenerife Island. This is 150 km away from the La Palma. . . . . 247
- C.2 Extracted file from the radiosonde database with all the meteorological parameters used in the Wind speed and potential temperature analysis and the columns are the input for different  $C_n^2$  models (Hufnagel-Valley and AXP). . . . . 248
- C.3 AWK script used to filter the MASS raw files . . . . . 249
- C.4 Raw file of the the MASS channel, with many parameters saved. . . . 250
- C.5 Extracted output file from the MASS channel with the  $C_n^2$  values per each layer and the isoplanatic angle and the coherence time (Tau) . . 251
- C.6 Extract of a output file from DIMM channel. The value of seeing used in the analysis of the thesis is the values in the column 7. Each column has an identification that is; **1.** UT-Date, **2.** UT-Time (from PC unless 'time 1' is set in telescope.ini), **3.** HR star number (from name field in the object list), **4.** Star name (from the comment field in the object list), **5.** Airmass, **6.** Total number of exposures (short+long), **7.** Seeing [arcsec],  $(x+y)/2$ , corrected for zenith distance and exposure time, **8.** x-seeing, corrected for zenith distance and exposure time, **9.** y-seeing, corrected for zenith distance and exposure time, **10.** Total flux (short exposure), **11.** dx, star-separation [pixels] in 'X' (focus), **12.** dy, star separation (pixels) in 'Y' (alignment). . . . . 252
- C.7 Extract of a output file from RoboDimm channel. The Robodimm gives 4 measurements of the seeing, two longitudinal and two transversal, that the median of those give the seeing. . . . . 253
- D.1 View of the robodimm and MASS-DIMM . . . . . 258
- D.2 MASS-DIMM instrument with the MASS device and the CCD attached. 258

- D.3 Real time display for the MASS channel. . . . . 258
- D.4 Real time display of the DIMM channel. . . . . 258
- D.5 Block diagram of the instruments set up. . . . . 258
- D.6 Mainly description of the MASS-DIMM systems. With the hardware and also the realtime displays are shown. Turbina realtime screenshot showing the strength of the turbulence at different altitudes, the free atmosphere seeing, the scintillation index and the isoplanatic angle images of the photocounts are sampled at 1ms during 1 minute. The real time GUI interface for the DIMM channel (CDIMM package) which measure the seeing in drift mode with an integration time of 4msec and control the telescope and the detector. The system Turbina and DIMM and synchronized during the measurements procedure. which control the telescope and the CCD. . . . . 258
- D.7 Sahara dust plume. Image captured by the MODIS. Credit NASA. . . 259
- D.8 Laser Guide Star scatter due to an event of dust. Credit. Juan Carlos Guerra . . . . . 259
- D.9 Turbina screenshot during the observing night on august 24th of 2008. It is showed a strong turbulence between the 1 and 8 kilometers starting at midnight 24:00 and finishing at 3:30. The astroclimate parameters; the isoplanatic angle, the free seeing and the coherence time are also plotted. The x-axis corresponds with the time where midnight corresponds with 24 and 1 a.m. is 25. The y-axis is the altitude (Km). 260

- D.10 Screenshot of the turbina package working during one observations night (September 4th 2009) showing a strong turbulence below 4 kilometers after the 24:00. This night shows a variability profile of the isoplanatic angle and the free seeing after the long turbulent burst of about one hour (1pm to 2 pm) after this burst the atmosphere shows a turbulent residual where it doesn't reach a dissipation of the turbulent energy and reach a more stable conditions. The x-axis is the time (0 UT is 24) the y axis is the altitude (kilometers) and the  $C_n^2$  is represented by the gradient colour bars with the minimum 0 (non-turbulent) with a  $C_n^2$  about  $10^{-21}$  to a turbulent with a  $C_n^2$  about  $10^{-14}$ . . . . . 261
- D.11 Location of the two sites for the mass-dimm instruments. The IAC sets up the unit in the DHV location [1] and the ING sets up the unit close to the WHT [2]. Robodimm tower. . . . . 262
- D.12 Vertical profiles of the  $C_n^2$  for the two MASS-DIMM. The vertical bars at each altitude represents the magnitude of the refractive index structure constant integrated over that layer. The figure shows the discrepancy for the lower layers when it was observed Gamma Draconis with the MASS-DIMM@ING. The IAC device is located at south east from the ING. Data taken on 4<sup>th</sup> on July . . . . . 263
- D.13 Vertical profiles of the two MASS-DIMM. The vertical bars at Each altitude represents the magnitude of the refractive index structure constant Integrated over that layer. The figure shows the discrepancy in the lower layer, where the MASS@ING has detected a burst between 1:30 to 2:15 am that the MASS@IAC has not detected. . . . 264
- D.14 Free seeing measurements for the MASS@las Moradas and the MASS@ING. There are a few differences, but in general view the two plots are quite similar. Data taken the night 4th on July 2008 . . . . . 265
- D.15 Comparison plot of the free seeing measurements for the MASS@las moradas and the MASS@ING. The measurements were taken the night on the 12th on June, 2008. . . . . 266

- D.16 Cumulative distribution of the free seeing measurements for two nights (the 12th on June and 4th on July, 2008) taking by the MASS@IAC and MASS@ING. . . . . 267
- D.17 The isoplanatic angle measured by the MASS@IAC and MASS@ING during one night 12th on June. The analysis in the plot shows the 10 minutes median values for the measurements. . . . . 268
- D.18 Post-processing profile from  $C_n^2$  data. The temporal evolution of the strength of the during the four days is very well identified, passing from very stable night 22<sup>nd</sup> to a very turbulent night 24<sup>th</sup> and 25<sup>th</sup>, the 23<sup>rd</sup> is identified that the ground layer is starting to be turbulent. The vertical bars at each altitude represents the magnitude of the refractive index structure constant integrated over that layer. . . . . 270
- D.19 Post-processing profile from  $C_n^2$  data. The temporal evolution of the strength of the during the four days is very well identified, passing from very stable night 22<sup>nd</sup> to a very turbulent night 24<sup>th</sup> and 25<sup>th</sup>, the 23<sup>rd</sup> is identified that the ground layer is starting to be turbulent. The vertical bars at each altitude represents the magnitude of the refractive index structure constant integrated over that layer. . . . . 271
- D.20 Statistical 10 minutes median seeing and free seeing during the GLAS observing nights. The x-axis shows the time the data are available from 21-04-08 at 2:47:48. showing different evolution patterns Blue lines shows the total seeing measured with the DIMM channel and the red lines shows the Free seeing computed from the  $C_n^2$  profiles with the altitude from 0.5 km to 16 km. . . . . 273
- D.21 Statistical of 10 minutes median values per the isoplanatic angle and coherence time ( $\tau$ ) evolution during the GLAS run. . . . . 274
- D.22 Shows a 10th magnitude star observed with NAOMI+GLAS+INGRID, the seeing measured by the Robodimm was 0.8 arcsec and the corrections brings this down to 0.2 arcsec. Pixel scale: 0.04 arcsec/pixel. 275
- D.23 Percentage of the vertical distribution of the  $C_n^2$ . . . . . 275

---

D.24	Statistical variation of the free atmosphere seeing and the total seeing. Every point represents a 10 minutes median value. Blue line is the total seeing and red line is the free atmosphere seeing (from 0.5 to 16km). . . . .	278
D.25	Statistical values per 10 minutes median for the isoplanatic angle and time coherence parameters during the NAOMI+GLAS run (22nd on April 2008). . . . .	279
E.1	Summary of the first 15th Zernikes polynomious in polar coordinates. The radial component $\rho$ varies between 0 and 1. . . . .	282
E.2	Spatial representation of the Zernikes polynomial. . . . .	283
E.3	Relationship of the normalized residual error ( $D = r_0$ ) for the Zernikes polynomial and K-L functions. Credit. (Dai, 1996) . . . . .	287

# List of Tables

1.1	Median seeing for various astronomical sites worldwide. Values are obtained after site characterization campaigns. . . . .	2
2.1	Typical surfaces roughness lengths relationship. . . . .	18
2.2	Relationship between the lapse rate and the gradient of the temperature.	25
2.3	Traditional or local lapse rate names and definitions commonly used to determine static stability. Table compiled from Stull,1988). . . . .	28
2.4	Values of the gradient Richardson number for different types of flow. Compile from the work (Vernin and Avila 1998). . . . .	32
3.1	Potential temperature gradient and its relationship to the atmosphere states. . . . .	44
3.2	Portion of the output file from a radiosonde data set (4 <sup>th</sup> on July 2008) and choosing the temperature, pressure and height to retrieve for calculating the potential temperature and the gradients and the differential vertical values. Looking for each height where the Heffter criterion is fulfilled a new column is built indicating that a critical inversion is developing (shown as symbol ***). . . . .	64
3.3	This shows how the magnitudes for the Fried coherence length, wind speed and coherence time and the Greenwood frequency. . . . .	65
3.4	Coefficients used in the AXP model. The altitude is measured in kilometers and the vertical resolution is one kilometer. Where $P(h)$ and $A(h)$ are coefficients, $C_t^2(h)$ is the temperature coefficient index. . . . .	66
4.1	MASS weighting function extremes measured in meters. . . . .	85

4.2	Comparison of site conditions taken the seeing ( $\epsilon$ ) measured in arcseconds, isoplanatic angle( $\theta$ ) measured in arcseconds and coherence time ( $\tau$ ) measured in msec. Wavelength used $550\mu$ m . . . . .	89
5.1	Summary of some running AO instruments in different observatories. The Strehl Ratio is measured in K-Band. . . . .	92
6.1	Summary of the data available to perform post-processing statistical analysis . . . . .	113
6.2	Example of the output of sounding profile cut from 700 to 570 mb of the data from the station 60018 (Tenerife, Canary Islands ) on 21 <sup>st</sup> July 2008 showing the vertical profile for pressure (hPa), temperature (C), wind speed (knots), wind direction (degrees) in significant levels (meters). The data are available for two synoptic time at 12 and 00 UT. The values in the table are; Pres-Pressure, Hgth- Height, Temp-Temperature, Dwpt-Dew point, Relh-Relative humidity, Mix, Drct-wind direction, wsp-wind speed, THAT-Potential temperature (K). Convert knots to $ms^{-1}$ (1 knots = $0.514ms^{-1}$ ). . . . .	116
6.3	Output file of sounding profile showing the data vertical distribution using the GFS Sounding for location: 28.45 North 17.48 West, the data are vertical distributed with the temperature, relative humidity, wind speed and wind direction per each vertical value. The data are available for two synoptic times at 12 and 00 UT. . . . .	117
6.4	Seeing measured with the Robodimm after filtering and extracting the median value of the longitudinal and transversal seeing. . . . .	120
6.5	Seeing measured from the DIMM channel (MASS-DIMM instrument) This is an extracted portion of the time series for the day 22 <sup>nd</sup> April 2008. . . . .	120

- 6.6 Output file from the MASS measurements taken on 1st on april 2008, after filtering the file and selecting the interested variables for the post-process analysis. The vertical distribution of the  $C_n^2(h)$  for the 6 six height slabs are represented with  $C_{n_1}$  corresponds to the height 0.5km and so on. The height slab are; 0.5, 1, 2, 4, 8 and 16 km. . . . 121
- 6.7 Free seeing, isoplanatic angle ( $\theta$ ) and the coherence time ( $\tau$ ) extracted from MASS-DIMM data on 19<sup>th</sup> February 2008. The output file is filtered and saved to the new output file for the MASS channel. . . . 121
- 6.8 Modelling scenarios for the data. . . . . 121
- 7.1 Monthly distribution of the seeing (arcseconds) through the years 2002 to 2008. The months with no data available are due to the Robodimm either not running or a performing only a few sporadic data acquisitions per night. . . . . 129
- 7.2 Statistical values for the median (50%), first (25%) and third quartiles (75%) of the total daily average seeing (arcseconds) parameter above Roque de Los Muchachos Observatorio. The two periods summer and winter represents the months; Summer (June to September ) and winter (November to March). . . . . 135
- 7.3 Number of suitable nights observed during the year 2008 with the total of 148 nights. . . . . 138
- 7.4 Statistics of the astroclimate parameters (free seeing, isoplanatic angle and coherence time) obtained with the MASS channel for the 1<sup>st</sup> (25%), 2<sup>nd</sup> (median) and 3<sup>rd</sup> (75%) quartiles. Statistics are applied to the whole year and two different periods. Summer(June, July, August and September) and winter (November, December, January, February and March). The free seeing and isoplanatic angle are measured in arcseconds and the coherence time in milliseconds. . . . . 139

7.5	Statistics of the astroclimate parameters (free seeing, isoplanatic angle and coherence time) obtained with the MASS channel for the 1 <sup>st</sup> (25%), 2 <sup>nd</sup> (median) and 3 <sup>rd</sup> (75%) quartiles. Statistics are applied to the whole year and two different periods. Summer(June, July, August and September) and winter (November, December, January, February and March). The free seeing and isoplanatic angle are measured in arcseconds and the coherence time in milliseconds. . . . .	140
7.6	Summary of the monthly statistics of the isoplanatic angle for a time series evolution of the parameter through 2008. . . . .	144
7.7	Summary of the monthly statistics of the coherence time for a time series evolution of the parameter through 2008. . . . .	144
7.8	Statistical analysis of the free seeing through 2008 with the contribution of the boundary seeing and free seeing. The 1 <sup>st</sup> Q. and 3 <sup>rd</sup> Q. represent the first and third quartiles. The free seeing is measured in arcseconds. . . . .	145
7.9	Statistics summary of the seeing measured with the DIMM channel for measurements in the year 2008. Measure in arcseconds . . . . .	146
7.10	Seeing variance of the measurements in the year 2008 over time scale from 10 minutes to 1 hour. Variance ( <i>arcseconds</i> ) <sup>2</sup> . . . . .	147
7.11	The monthly median value for the $C_n^2$ parameter and the free seeing. The atmosphere turbulence is considered turbulent for $C_n^2$ values of $10^{-14}$ and weak for values about $10^{-20}$ . . . . .	152
7.12	Summary of the tropospheric wind speed (knots) with the median and standard deviation. . . . .	164
7.13	Monthly statistics of the tropospheric wind speed at an altitude between 9 and 12 km. . . . .	166
7.14	Monthly statistics for the median isoplanatic angle and wind speed at 200mb during the year 2008. . . . .	168
7.15	Pearson correlation values for the tropospheric wind speed respect the free seeing (arcsec) and the total seeing (arcsec ). . . . .	170

7.16	January data for the statistical median; total seeing (arcsec), free seeing (arcsec) and tropospheric wind speed ( $ms^{-1}$ ).	170
7.17	May data for the statistical median; total seeing (arcsec), free seeing (arcsec) and tropospheric wind speed ( $ms^{-1}$ ).	171
7.18	August data for the statistical median; total seeing (arcsec), free seeing (arcsec) and tropospheric wind speed ( $ms^{-1}$ ).	172
7.19	Table set of the daily median values of the seeing; total seeing (arcsec) and free seeing (arcsec) and the wind speed at the altitude between 9 to 12 km. Measurements for the months January, May, August and November of the year 2008.	173
7.20	Daily median seeing for the total (arcsec), free (arcsec) and computed surface seeing (arcsec). Data taken on January 2008.	176
7.21	Daily median seeing for the total (arcsec), free (arcsec) and computed surface seeing (arcsec). Data taken on May 2008.	177
7.22	Daily median seeing for the total (arcsec), free (arcsec) and computed surface seeing (arcsec). Data taken on August 2008.	178
7.23	Daily median seeing for the total (arcsec), free (arcsec) and computed surface seeing (arcsec). Data taken on November 2008.	179
8.1	Summaries of the statistics of the wind speed taking the height slab between 5 to 15 km. The wind data are retrieved from the radiosonde database. The launch site is 120km away from the observatory. The 1 <sup>st</sup> Q and the 3 <sup>rd</sup> Q are the first and the third quartiles.	193
8.2	Pearson correlation values for the $C_n^2(h)$ profiles obtained using the H-V and AXP model with the same meteorological parameter.	197
8.3	Summary of the number of observing nights used to perform the correlation of the MASS measurements with the $C_n^2(h)$ profiles retrieved from the AXP model using the data for the year 2008.	200
8.4	Summary of the monthly Pearson correlation for the AXP and MASS $C_n^2(h)$ values.	201
A.1	Tested stars.	214

A.2	X and Y profile for the polaris image . . . . .	215
A.3	Shedir FWHM x and y axis. . . . .	216
A.4	FWHM in X and Y for the images A.13(a) and A.13(b) . . . . .	220
B.1	Statistical values for the median (50%), first (25%) and third quartiles (75%) of the total daily average seeing parameter above Roque de Los Muchachos Observatorio. The two periods summer and winter represents the months; Summer (June to September ) and winter (November to March). . . . .	230
B.2	Statistics of the seeing for the year 2003. . . . .	232
B.3	Statistics of the seeing for the year 2004. . . . .	232
B.4	Statistics of the seeing for the year 2005. . . . .	232
B.5	Statistics of the seeing for the year 2006. . . . .	232
B.6	Statistics of the seeing for the year 2007. . . . .	233
B.7	Statistics of the seeing for the year 2008. . . . .	233
D.1	Statistics summary for the free seeing, isoplanatic angle and the coherence time of the MASS measurements during the GLAS nights of 22nd, 23rd and 24th on June 2008. . . . .	272
D.2	Resume of the observations logs getting the seeing measured with the instrument INGRID at open and close loop. . . . .	274
D.3	Statistics of the percentage distribution of the boundary and free turbulence over the total turbulence measured by the MASS-DIMM instrument. The time series is averaged every 10 minutes. . . . .	277
E.1	Residual variance of a wavefront after the corrections of the j first Zernikes polynomials for the atmosphere case. . . . .	284
E.2	Variance of the $\sigma_j^2 - \sigma_{j-1}^2$ for the modes j-esimo. The fist mode piston is not considered. . . . .	284
E.3	K-L coefficients for the first 21 first radial modes. . . . .	286

# Chapter 1

## Introduction.

Astronomical observation of an object consists, at any time, in detecting the wavefront. Initially the wavefront is flat before crossing the atmosphere. During the crossing, the wavefront passes through layers with different temperatures and thus different refractive indices. Wind currents produce turbulent mixing of the layers, creating inhomogeneities in temperature and therefore, the index of refraction. Those inhomogeneities in temperature are governed by the law of Kolmogorov-Obukhov turbulence (Fried, 1965). As a result, the wavefront of an astronomical object is no longer flat when it reaches the observer on Earth.

This disturbance in the wavefront leads to a blurring and scintillation of images of celestial objects. The magnitude of distortion of an image due to atmospheric turbulence is commonly known as the *seeing*. Quantitatively, the seeing is defined as the Full Width at Half Maximum (FWHM) of the point spread function of the brightness of a star. This quantity is usually expressed in arcseconds.

The term optical resolution refers to the ability of an instrument to separate two objects in an image. Specifically, in astronomy, the resolving power of a telescope determines what minimum angular separation it is able to resolve.

Due to the wave nature of light when it passes through a circular aperture it is diffracted causing an interference pattern. The resulting interference pattern is a circular patch surrounded by a series of concentric rings. The central spot is known as the *Airy disk* and its size depends on the size of the optics and the wavelength. The optical resolution limit due to diffraction of a telescope can be calculated using

the Rayleigh criterion by the expression:

$$\sin \theta = 1.22 \frac{\lambda}{D} \quad (1.1)$$

where  $\theta$  is the angular resolution,  $\lambda$  is the wavelength and  $D$  is the circular diameter. The factor  $1.22$  comes from the position of the first Airy ring. This factor is used as an approximation of the eye's ability to distinguish two point source where the Airy disk are overlapped.

As an immediate consequence of atmospheric turbulence, the spatial resolution of ground-based telescopes are not limited by the size of the Airy disk. Even in the best ground-based observatories, it is not possible to achieve spatial resolutions in the optical or infrared better than atmospheric seeing. For most observatories this value is around 1 arcsecond (Table 1.1), which is well above the theoretical resolving power of any research-class telescope. For example, a 10 meters telescope operating at wavelengths centered in the visible, can in principle resolve structures separated by an angle of only 10 milli-arcseconds, a factor 100 times better than typical astronomical seeing.

Observatory	seeing(arcsec)	References
Roque de los Muchachos	0.76	Munoz-Tunon et al, 1997
Paranal	1.0	Sarazin et al 2008
Mt Graham	0.97	Taylor et al,2004
Manua Kea	0.50	Racine,1989
La Silla	0.79	<a href="http://www.ls.eso.org/lasilla/seeing">www.ls.eso.org/lasilla/seeing</a>

Table 1.1: Median seeing for various astronomical sites worldwide. Values are obtained after site characterization campaigns.

## 1.1 Solution to the turbulence problem.

Until recently, the only option to avoid such a drastic limit imposed by the atmosphere on the resolving power of the telescope was to place it in orbit, as, for example, the Hubble Space Telescope. This type of telescope always works at the diffraction

limit in principle and does not suffer from background radiation in the atmosphere. Furthermore, the atmosphere imposes restrictions on the wavelengths where the atmospheric transmission is low or zero. But the cost is so high of putting a telescope in orbit and then maintaining it, that it led to the seeking of other options, which also solve the problem of ground-based telescopes. Speckle interferometry allows diffraction limited images from the ground and has proved to be a formidable tool for the detection of binary stars very close together. However, in terms of sensitivity, speckle interferometry is even worse than that obtained in conventional images limited by seeing (Roddier et al. 1982). On the other hand, lucky imaging applications, enabled by the emergence of increasingly rapid detection with very low noise (e.g., Law, 2006) is leading to the diffraction limit and a reasonable Strehl ratio. Lucky imaging has the disadvantage that for seeing through 1 arc second, it ignores almost 90% of the data depending of the telescope size and the wavelength. The probability to get diffraction limited images is represented by the equation;

$$P \approx 5.6e^{\left(-0.1557\left(\frac{D}{r_0}\right)^2\right)} \quad (1.2)$$

where  $D$  is the telescope diameter and  $r_0$  is the Fried parameter, that is related to the wavelength with the following  $\lambda^{6/5}$  (Fried, 1967).

An alternative to these techniques is *Adaptive Optics*. Adaptive optics is a technique that improves the quality of an optical system in real time by reducing the perturbations introduced by the atmosphere into the wavefront. This type of system measures the wavefront distortions very rapidly and then corrects them by using a deformable mirror. Although the theory has existed since the 1950s (Babcock,1953), the major advances came in the 1990s with the increase in computing power and the improvements in the deformable mirrors. The current implementation cost is much lower than to put a telescope in orbit.

Therefore, adaptive optics has become a fundamental and essential tool that should be implemented in any research-class telescope where the aim is to reach the diffraction limit and to obtain the maximum limit of detectability.

There are three main technical disadvantages present today:

- We need a bright point source reference. Due to rapid temporal variation of the

wavefront when going through different turbulent layers in the atmosphere, it is necessary to sample the point source at a high frequency. If it is not bright enough, there will not be a signal to noise ratio to sample the wavefront. Typically the R magnitude limit used as a reference star is  $\approx 12$  (Hippler et al. 2000). To improve this aspect the laser guide star has started to show its potential (Davies et al. 2000).

- The point source must be close to the scientific object which it is intended to observe, because the field of vision corrected by these systems is limited. This is due to differences between the wavefronts from different directions reaching the primary mirror, e.g. let us take the K band ( $2.2\mu m$ ), where the isoplanatic angle (the solid angle in which the correction is acceptable) (see Chapter 3) is in an order of 40 arcseconds in diameter. MultiConjugate Adaptive Optics (MCAO) aims to solve this limitation (Fusco et al. 2006).
- Cost. Although low compared to the budget required to install and maintain an orbiting telescope, adaptive optics systems for astronomical use are still expensive, both in money and personnel, and only a few observatories with high annual budgets are running instruments with AO technology.

## **1.2 Advantages of observing the diffraction limit in astronomy.**

The advantages of being able to carry out astronomical observations at the diffraction limit can be grouped into two categories:

- Increased spatial resolution. The diffraction limit of a telescope grows in proportion to its diameter. In the case limited by the seeing, the final resolution of the telescope does not depend on diameter. The spatial resolution is of vital importance in astronomy; for example, the progressive understanding of complex morphologies, such as the study of a planet's atmospheric evolution, disk galaxies, jets in active galaxies, star clusters, and, of course, direct detection

of extrasolar planets. In short, any problem that requires the separation of structures, which are the majority in astronomy.

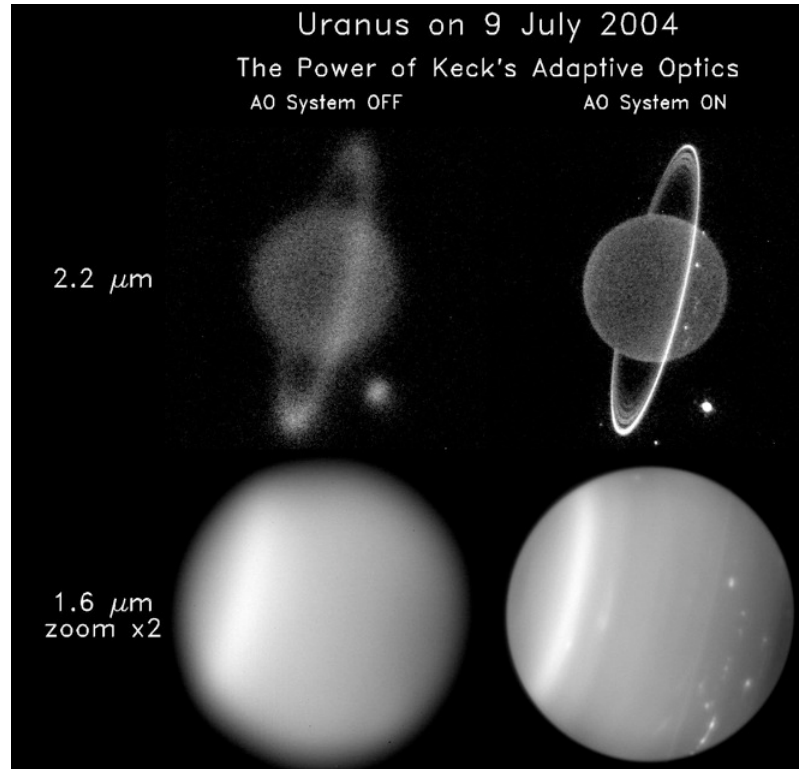


Figure 1.1: Near infrared images of Uranus before and after the AO system on Keck was turned on. The image shows at the top its rings and moon Miranda. On the bottom is Uranus and its atmospheric details in the near-infrared. Uranus at K' ( $2.2\mu\text{m}$ ) and H ( $1.6\mu\text{m}$ ) bands. Credit. Hammel and de Pater.

- Sensitivity. The detectability of astronomical objects, defined as the observation time needed to achieve a certain signal to noise ratio, raises with the fourth power of the diameter of the telescope, while the seeing limited case raises only with the second power.

Numerically, we can say that a 10 meters diameter telescope operating at the diffraction limit at wavelengths in the visible has a detectability of 80000 times that of a 3.5m telescope limited by a seeing of 1 arcsecond. Once again, it demonstrates the vital importance of this technique for the case of weak signals, such as the de-

tectability of supernova at high redshift, measurements of cosmological parameters, or new searches for extrasolar planets (Figure 1.2).

Currently, the images obtained by adaptive optics systems rival and even exceed in terms of image quality those obtained by the Hubble Space Telescope (Figure 1.3).

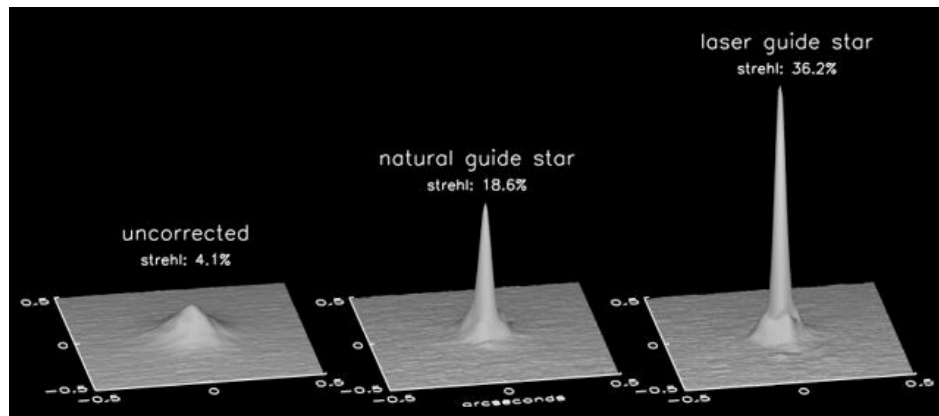


Figure 1.2: Strehl ratios for first-light images of the Keck LGS AO system on Sept.19, 2003. The left panel shows an uncorrected Strehl ratio of four percent. Middle panel: Strehl ratio of 18% for a natural guide star object. Right Panel: Strehl ratio of 36% for the Keck laser guide star. [http://keckobservatory.org/images/gallery/press\\_images](http://keckobservatory.org/images/gallery/press_images).

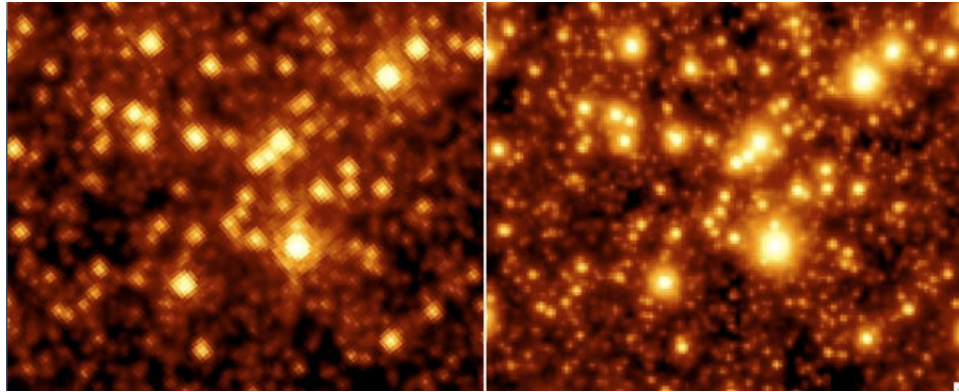


Figure 1.3: Central region of M92 globular cluster. Image taken by Hubble at  $1.6\mu m$  (left) and same region of the globular cluster taken by the Adaptive Optics system mounted in the LBT (right). Credit: Hubble/LBT (<http://www.lbto.org>)

## 1.3 Main topics of the thesis.

Adaptive Optics engineering is becoming an important tool in the future of Astronomy and especially in the developing of new instruments for large aperture telescopes such as the E-ELT<sup>1</sup> or TMT<sup>2</sup>. New techniques in Adaptive Optics include developments such as Multi-Object Adaptive Optics (MOAO) (Morris, et al. 2010), which corrects the wavefront in a large field of view (FOV) using a tomographic reconstruction of the optical turbulence for the science field using natural guide stars (NGS) or laser guide stars (LGS) distributed in the field of view. Several other such new techniques have been studied and they are commonly known as: Ground Layer AO (GLAO), Laser Tomography AO (LTAO) and Multi-Conjugate AO (MCAO). They all require a good understanding of where, when and how the optical turbulence is formed.

Traditionally optical turbulence has been measured using radiosonde balloons, which can measure with a high vertical resolution, but this technique has the disadvantage of high cost and therefore is not suitable to use as a common instrument in astronomical observatories. Other instruments have been developed to measure optical turbulence as determined by the refraction index  $C_n^2$  (see Chapter 4) and they are becoming more reliable. These include SCIDAR, SLODAR and MASS, which can all give real time measurements with less cost.

In order to understand the optical turbulence in the Observatorio Roque de los Muchachos, and how this knowledge can be used to help in AO observations and developments, several issues have been addressed:

- The use of meteorological data to inform a simple model that could characterize the optical turbulence in the upper atmosphere.
- Taking long term seeing data and comparing it with long term meteorological data (wind speed at 200mb) in order to determine the seasonal variations and their relationship.

---

<sup>1</sup>E-ELT: European-Extreme Large Telescope

<sup>2</sup>TMT: Thirty Meter Telescope

- Development of novel techniques to measure the optical turbulence during Laser Guide Star+AO observations. A particularly interesting goal would be taking the optical turbulence information from the LGS.
- Establish the base for a developing a novel statistical approach to forecast the seeing.

The field of meteorological models applied to the determination of the optical turbulence started with a first proposed idea by Coulman (Coulman, et al. 1986). This field has been growing in importance due to the fact that the models can be excellent tools for long term site testing, and can also be used to forecast the optical turbulence, which is an important input to flexible scheduling, which in turn improves the telescope time efficiency. The atmospheric turbulence is a complicated process which takes many state equations to be computed, as e.g., in the estimation of the turbulent fluctuation of the refractive index and the seeing over the Mauna Kea Observatory (Businger, et al. 2003) using the information from the turbulent kinetic energy provided by the Pennsylvania State University-NCAR Mesoscale Model. Another method, which computed the optical turbulence from meteorological measurements is the mesoscale model Meso-NH which has been used to simulate the optical turbulence at Cerro Paranal observatory (Masciadri, et al. 1999a,b).

Considering the above argument that the model of the refractive index can be an important tool, and if this model can be performed in a "light" manner, with a simple algorithm and low computing load, then such a model would be the "grail". This principle of simplicity is adopted by the Trinquet and Vernin model (AXP) (Chapter 8), where the refraction index distribution above the observatory can be reconstructed using meteorological data measured off site. Figure 1.4 shows the predicted optical turbulence temporal evolution above the Observatorio Roque de Los Muchachos (Trinquet, et al. 2006).

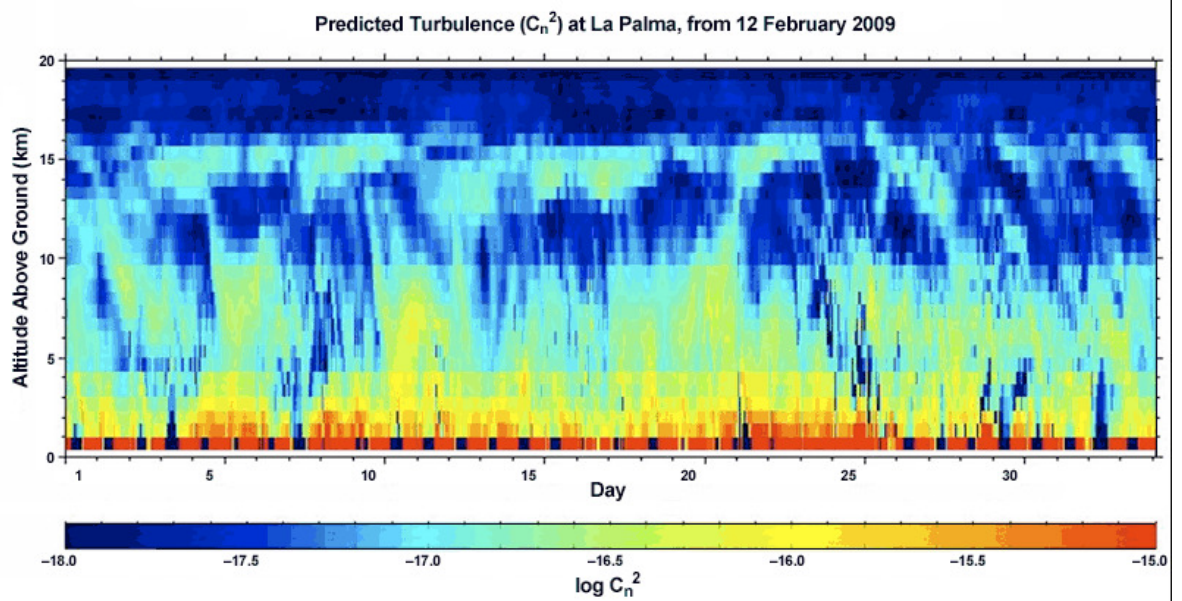


Figure 1.4: Temporal evolution of the optical turbulence profiles at the Observatorio del Roque de los Muchachos. The one-day forecast was computed every hour over the course of one month. The color bar represents the prevailing  $C_n^2$  values on a logarithmic scale. Trinquet, et al. 2006.

# Chapter 2

## The Atmosphere.

*”There was a time in the universe where there were no stars and so the Extreme Large Telescope has the ability of going from today to back to the first stars ..Thats incredibly exciting.”*

*Raymond Carlberg.*

---

### 2.1 Overview.

The atmosphere is the most influential factor in ground-based astronomical observations. The influence on Astronomy ranges from the determination of the better sites to place ground based observatories to the influence of the local conditions that can degrade the images from scientific targets. This chapter provides a description of the atmosphere layering distribution and the different physics that has influence on the optical propagation.

### 2.2 The Atmosphere structure.

The vertical structure of the atmosphere can be classified in a variety of ways depending on which physical property is used. The proportions of atmospheric constituents, in the absence of sources or sinks, is determined by either molecular diffusion or mixing due to fluid dynamics. Molecular diffusion will attempt to order the atmosphere

in such a way that the lightest gases are presents at the top of the atmosphere while the heaviest molecules occupy the bottom. Mixing due to the motion of the molecules is independent of molecular gases. If this is the dominant process, the atmosphere's composition will be independent of height. At lower heights the mean free path between molecular collisions is so small that the time necessary for molecular diffusion is many orders of magnitude greater than that required for turbulent motion to homogenise them. However, at higher heights the mean free path increases to such an extent that molecular diffusion is the dominant mechanism. The region below this height is known as the homosphere while the region above is called the heterosphere. The level of transfer of dominance from the turbulent mixing to the molecular diffusing is called the turbopause. The increase in mean free path of particles with height combined with the transition to more stable species of ions, results in an increase in the number of electrons. These electrons and the positive ions are produced by the ionization of molecular oxygen, nitrogen and nitrogen monoxide by the Sun's radiation and have longer lifetimes than electrons produced at lower levels. This region where the number of free electrons is significant begins around 60 km and is known as the ionosphere. The most common classification of the Earth's atmosphere is based upon the temperature profile. As indicated in figure 2.1, the vertical profile can be divided into four different regions: the troposphere, stratosphere, mesosphere and thermosphere. The transition areas between these layers contain local extrema and are labelled tropopause, stratopause and mesopause respectively. The behaviour of the temperature profile shown in figure 2.8 can be understood by considering the dominant processes occurring at specific heights.

The Earth's surface is heated by incoming solar radiation, and re-radiates the absorbed energy as a black body spectrum. The heating of the atmosphere by the ground causes active convection and a decrease in temperature due to the volume expansion. Molecules and gases, like water vapour, absorb some of the re-radiated energy, thus heating the atmosphere. In the stratosphere the temperature gradient is reversed due to the absorption of the ultraviolet solar radiation by ozone. The local temperature minimum between the troposphere and stratosphere is labelled as tropopause. The dissociation of ozone molecules heats the atmosphere creating an

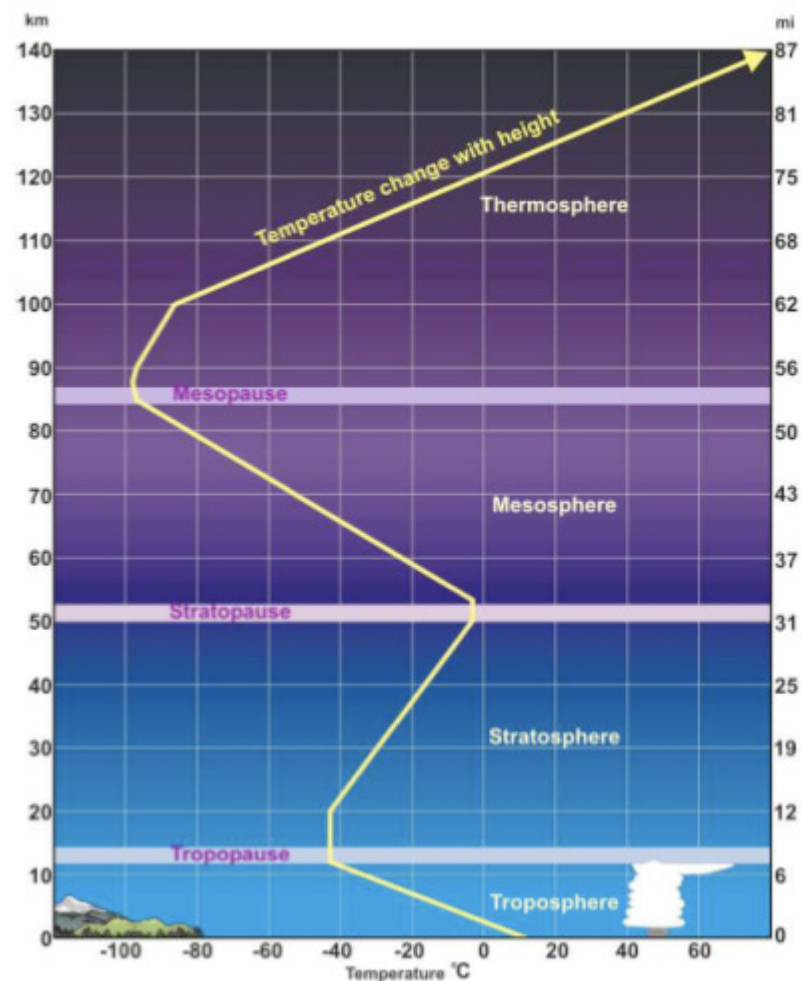


Figure 2.1: Scheme of the main atmosphere distribution layers and the vertical temperature variation (yellow line). <http://www.srh.noaa.gov/jet-stream/atmos/layers.html>.

increase in temperature. The local region where the temperature is a maximum is labelled the stratopause. Above the stratopause, the ozone concentration decreases, along with the subsequent decrease in temperature. This decrease continues up to the mesopause at  $\approx 100\text{km}$ , where a reversal in the temperature gradient is observed due to the absorption of the solar ultraviolet radiation by atomic and molecular oxygen. The region above the mesopause is known as the thermosphere.

## 2.3 The atmospheric Boundary Layer.

The lower part of the atmosphere, which is directly influenced by the surface of the Earth, is known as the boundary layer. It has a depth varying from 100 meters up to one or two kilometers. This is the most important region from the point of view of astronomical imaging and corrector systems, as it is the region containing the most of the energy driving the atmosphere from the surface, which is heated by the Sun. The nature of the boundary layer is somewhat different from the free atmosphere in that the dynamics of the layer is dominated by turbulence. And simply the turbulence can be defined as a random eddying motion of the air with two primary physical processes:

- Radiative cooling and heating of the surface is stronger than at the higher levels in the atmosphere. The principal source and sink of heat is the surface. Strong solar heating leads to turbulent convection and mixing of boundary layers, whereas strong cooling typically at night tends to stabilize the boundary layers.
- The wind flowing over the surface becomes turbulent as it flows over the obstacles. Effectively this means that the wind becomes gusty and this has an important impact on the transport of the heat from the surface higher into the atmosphere changing the refractive index in different atmosphere layers.

The boundary layer dynamics are determined by the presence or absence of the turbulence where turbulence involves "random" motions of the air, which are manifested by the gustiness and these random motions are accompanied by fluctuations in temperature and humidity on similar timescales. The importance of turbulence is that it acts to cause rapid diffusion or mixing of the heat of the air and effectively turbulence stirs the air close to the ground. The fact that the turbulence also mixes wind velocity means that it transfers the friction of the air flowing over the ground to the upper air.

Turbulence is one of the great unsolved problems in modern science and how it is affected by the wind shear near surface obstacles as telescopes domes can be a

very important matter for astronomical observations. This could certainly be the case for the *E-ELT* or *TMT* enclosure shown in figure 2.2 and 2.3 where the E-ELT dome will be of similar size to that of a football stadium with a diameter at its base of order 100 m and a height of order 80 m. Also, this kind of enclosure can affect the convection arising as a result of an unstable atmosphere with different temperature gradients and local conditions. To minimize the enclosure contribution to the convection and to the local turbulence, which could affect the quality and performance of astronomical observations, such structures are generally designed with a round dome. There are exceptions where the enclosure geometry has changed, in those exceptions can be included the Very Large Telescopes (VLT), Telescope Nazionale Galileo (TNG), the New Technology Telescope (NTT) or the Large Binocular Telescope (LBT). It is said that infrastructures like TMT or E-ELT will challenge the current engineering limits which could project the ground-based astronomy to the edge. How John Dewey<sup>1</sup> said; *"Every great advance in science has issued from a new audacity of the imagination"*.

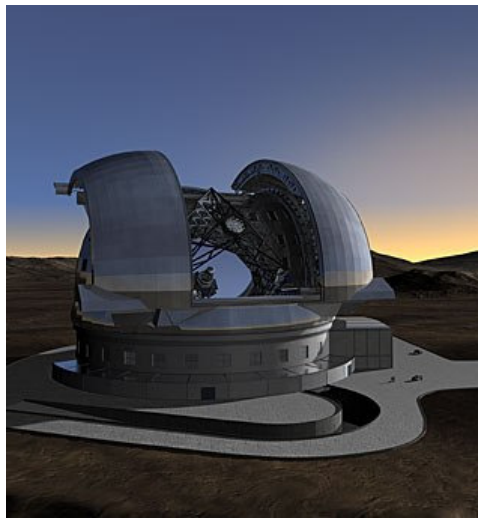


Figure 2.2: Conceptual rendered image of the ELT enclosure design proposed by ESO showing a round enclosure. [http : //www.eso.org/sci/facilities/eelt/telescope/dome](http://www.eso.org/sci/facilities/eelt/telescope/dome).

---

<sup>1</sup>John Dewey, (1859-1952) American philosopher and one of the fathers of the philosophy of pragmatism. His ideas have been an influence in education and social reforms.

In conditions of low wind, the radiative transfer at the surface of the Earth dominates the production or suppression of turbulence. The heating of the lower meters of the atmosphere depends on the heating of the surface, and the transfer of heat from the surface into the air. These processes can be quantified by looking at the surface energy balance. The surface energy balance is determined by the different fluxes of heat energy at the ground. The system is forced by the radiative balance between net incoming short wave radiation from the Sun and upwards long wave cooling. The response in terms of heat flowing from the surface into the atmosphere has two components:

- The sensible heat flux. This is the heat flux as energy flows into the air by conduction and convection. It depends on the temperature difference between the surface and the air, as well as the air speed and the strength of the turbulence (stronger turbulence increases the heat flow). When warm air flows over a cold surface can be negative, as sensible heat flows from the air into the ground (for example, a telescope surrounding painted in white reduces the ground absorption so that during the night this heat is not exchanged with the surrounding surface layer making a more stable atmosphere without many changes in the temperature gradients).
- The latent heat flux is the flux of heat from the Earth's surface to the atmosphere that is associated with evaporation or transpiration of water at the surface and subsequent condensation of water vapor in the troposphere. It is an important component of Earth's surface energy budget<sup>2</sup>.

There is also a significant heat flux through exchange with layers below the surface, known as the ground heat flux.

---

<sup>2</sup>The amount of energy given out by the Sun, and the energy received by the Earth. Within that is the energy reflected and the energy given off from the Earth.



Figure 2.3: Rendered image of the TMT enclosure both the E-ELT and the TMT dome have chosen a round dome to minimize the turbulence at the surface and ground layer, hence reducing the wind loading. The enclosure is type "Calotte". <http://www.tmt.org/observatory/enclosure-infrastructure>. Credit TMT Consortium.

## 2.4 The surface layer.

Apart from the effect of surface heating on production and suppression of turbulence, there is also a significant process of wind shear generation of turbulence. The surface of the Earth is rough on all scales from the roughness associated with grains to trees, buildings or mountains protruding into the air. As the wind flows over any of these obstacles, it produces turbulence on a similar horizontal scale to the obstacle. Looking at the coming Extreme Large Telescope (TMT or E-ELT) the dome structures is an important issue in the design and how these enclosures can minimize the wind load and the turbulence over the telescope aperture. A standard result (Parlange and Brutsaert,1988) is that in neutral conditions, the average wind profile in the surface layer up to 30 meters has a logarithmic form,

$$U(z) = \frac{u_*}{k} \ln \left( \frac{z}{z_0} \right) \quad (2.1)$$

where  $u_*$  is the friction velocity and is a measure of the strength of the turbulent variations in wind speed ("gust") and  $z$  is the height above the surface. This parameter is a measure of the efficiency of the turbulence in mixing atmospheric constituents. The *von Karman constant* is defined as  $k$ , which has a value approximately of 0.40, and  $z_0$  is the roughness length, and is related to the shape and distribution of the obstacles over which the wind is blowing.

The von Karman constant has been subject to periodic scrutiny over the years. Reviews (Foken, 2006; Hogstrom, 1988; Hogstrom, 1996) report values of  $k$  between 0.35 and 0.42. The overall conclusion of over 18 studies is that  $k$  is constant, close to 0.40, and invariant to the friction Reynolds number between 0.1 and  $10^5$ . The roughness length  $z_0$  has been summarized for different terrains as shown in Table 2.1.

Type of terrain	Roughness length $z_0$ (m)
Cities, forest	0.7
Suburbs, wooded countryside	0.3
Village, countryside with trees and hedges	0.1
Open farmland, few trees and buildings	0.03
Flat grassy plains	0.01
Flat desert, rough sea	0.001

Table 2.1: Typical surfaces roughness lengths relationship.

The figure 2.4 shows an example of the wind profile assuming the knowledge of the wind at different heights and using the equation 2.1 to get wind speed vertical contributions. Let us assume that the wind is blowing at  $7.7ms^{-1}$  measured at 20 m height and we wish to know the wind speed at 60 m height. If the roughness length is considered as 0.1m, then;

$$v_{ref} = 7.7ms^{-1} \quad z_{ref} = 20m \quad z=60m \quad \text{and} \quad z_0 = 0.1m$$

Hence,

$$v = 7.7 \frac{\ln\left(\frac{60}{0.1}\right)}{\ln\left(\frac{20}{0.1}\right)} = 9.29 \text{ ms}^{-1}$$

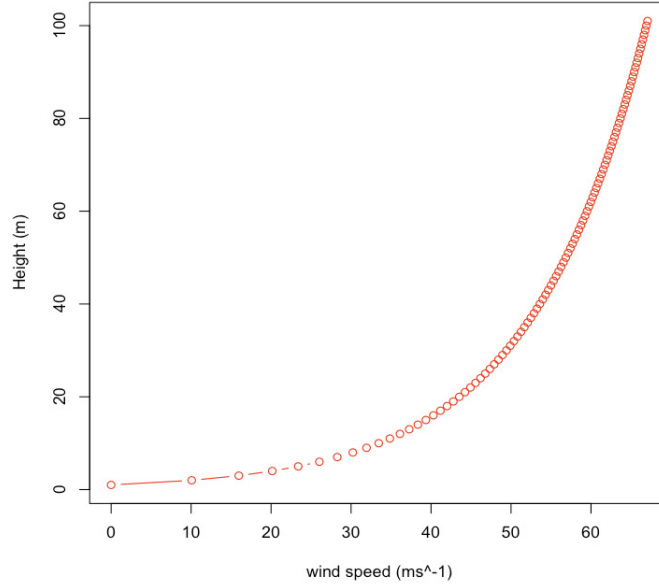


Figure 2.4: Example of a wind shear vertical profile for a rough initial input of 0.1.

Note that this logarithmic form fails to apply close to the ground (where the functions becomes infinite). In practice it is used down to around the roughness length  $z = z_0$ . The turbulence eddies in the boundary layers also carry heat away from or toward the surface (when the ground is cooled by radiation into air or during a clear night). Under these circumstances there is temperature gradient in the surface layers closely related to the wind profiles. A standard result is that when heating or cooling is not too strong, then the average temperature profile in the surface layer also has a logarithmic form.

$$T(z) = T_s \frac{T_*}{k} \ln\left(\frac{z}{z_0}\right) \quad (2.2)$$

where  $T_s$  is the temperature of the surface,  $T_*$  is the fraction temperature,  $z$  is the height above the surface and  $z_0$  has the same value of the roughness length.

The atmosphere from the astronomical point of view has a more interesting form during the night where the atmosphere is in a more stable condition. The nocturnal

atmosphere in the following sections is described by the boundary layer and the surface layer.

## 2.5 The nocturnal boundary layer.

The nocturnal boundary layer is ill behaved and difficult to quantify. Typically it is associated with low wind speeds near the surface as the air layer above has a thermal profile that is stably stratified. This effect, however, causes elevated wind gusts (low level jets) and sporadic turbulence and momentum from above must ultimately be absorbed by the surface (Mahrt, 1999). Attributes of the stable boundary layer that must be quantified include radiative heat loss on clear nights, drainage of air with undulating terrain, shear instabilities and intermittent turbulence, generation of gravity waves, and the formation of fog and or dew. Stull (Stull,1988) defines the atmospheric boundary layer as; *the part of the troposphere that is directly influenced by the presence of the Earth's surface, and responds to surface forcings with a time scale of about an hour or less.* Figure 2.5 illustrates how the work done by Stull defines the atmosphere distribution and it shows the typical scheme of the boundary layer. The solar heating causes thermal plumes to rise, transporting moisture, heat and aerosols. The plumes rise and expand adiabatically until a thermodynamic equilibrium is reached at the top of the atmospheric boundary layer. The moisture transferred by the thermal plumes forms convective clouds.

At night the atmospheric environment near the ground is no longer the same for desert and mountains, particularly if the mountain acts more like a peak than a plateau. This is because during the night, radiative cooling of the mountain surface occurs like that of a desert, but the cool dense air tends to flow down the mountain away from the peak, preventing the formation of thick layers on top of the mountain. Consequently, the decrease in the turbulence defined by refraction index parameter  $C_n^2$  (Chapter 3) with altitude at nighttime does not generally follow the power law  $h^{-4/3}$  altitude dependence; instead, similarity theory predicts the power-law relation  $h^{-2/3}$  representing more stable conditions.

The boundary layer from the periods from sunset to sunrise is called the noc-

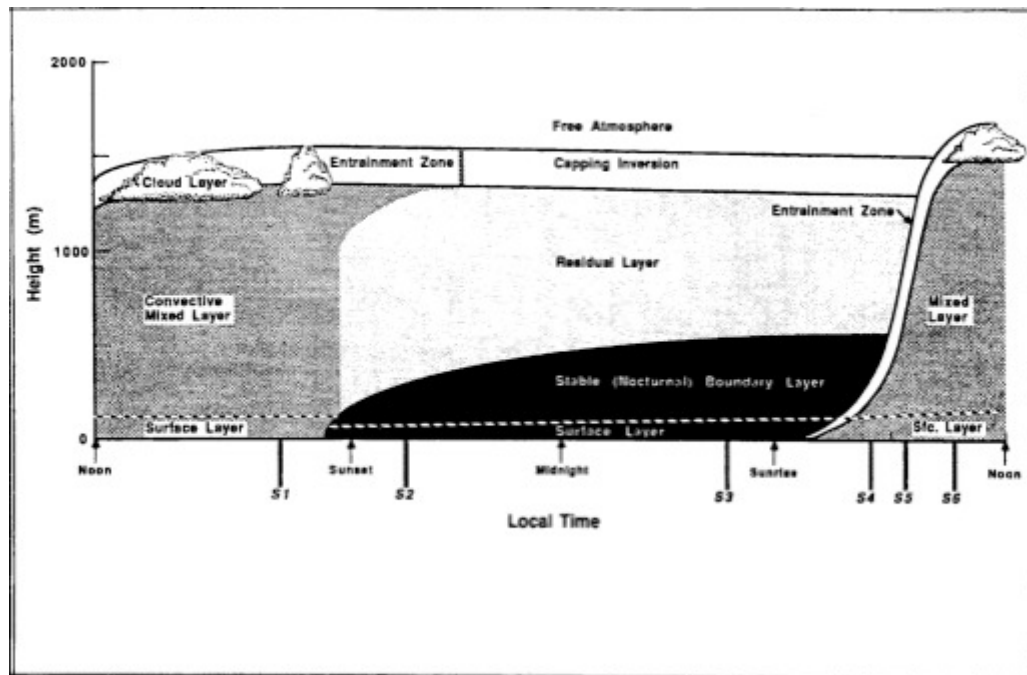


Figure 2.5: Description of the boundary layer evolution detailing the sub-layer structure that typically develops during the daytime to nighttime transition. Credit Stull, 1988.

turnal boundary layer. It is often characterized by a stable layer, which forms when the solar heating ends and the radiative cooling and surface friction stabilize the lowest part of the atmospheric boundary layer (ABL). Above that, the remnants of the daytime convective boundary layer (CBL) form a residual layer. The nocturnal boundary layer may also be convective when cold air advects over a warm surface. Figure 2.6 shows a measurements of the atmosphere layers using new LIDAR techniques which gives a distribution of the boundary layer evolution during the day in a similar manner how it has been proposed by Stull ( see figure 2.6 above).

### 2.5.1 The stable nocturnal layer.

(Andrews, et al. 2009 ) reported that at stable surface conditions like it is during the night, the Earth's surface cools by radiation and becomes colder than the air, producing more stable conditions. This surface cooling produces a strong temperature inversion that can reach tens or hundreds of meters or more. Within the temperature

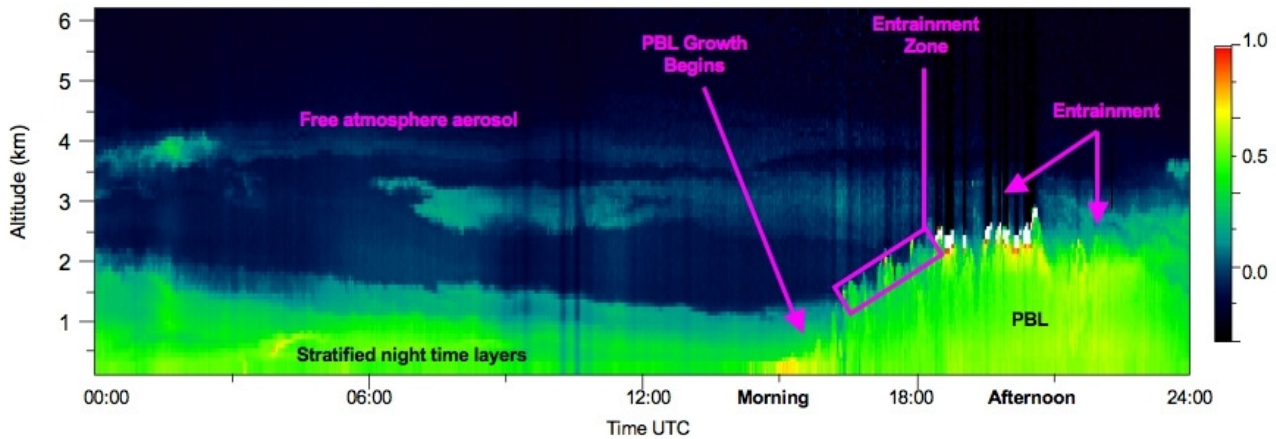


Figure 2.6: Example of 24 hours of the vertical profile of the atmosphere aerosol and cloud vertical structure in continuous measurements, sensed by a LIDAR. Sunrise occurs around 13:00 UTC, and boundary layer (PBL) growth during morning into afternoon is visible in the figure. Aerosol layers in the free troposphere are visible during the previous night, and the planetary boundary layer (PBL) eventually reaches high enough to entrain the boundary layer. The image was taken during the project MPLNET. The gradient colors shows the concentration of aerosol in percentage. <http://www.enc.ncep.noaa.gov>. Credit NASA.

inversion, the refraction index  $C_n^2$  will typically increase with increasing wind speed up to around  $4\text{ms}^{-1}$ , and then decrease with stronger wind speeds exceeding  $4\text{ms}^{-1}$  (Andrews et al, 2009). The temperature gradient which represents the Nocturnal Boundary layers is characterized by a subadiabatic temperature profile.

### 2.5.2 Residual Nocturnal layer.

After sunset the formation of cells of different refractive index (blooming) tends to disappear reducing the turbulence in the Mixed Layers. The residual layer is called the Residual Nocturnal Layer. This layer presents a neutral stratification

## 2.6. Thermodynamics parameters to describe the atmospheric states. 23

with isotropic turbulence<sup>3</sup>. The Residual Layer is isolated from the ground by the surface boundary layer and it is not affected by the surface effects. Stull has included the residual layers inside of the atmospheric boundary layer.

## 2.6 Thermodynamics parameters to describe the atmospheric states.

The atmosphere is a compressible fluid in which the density of the atmosphere is a function of pressure and temperature,  $\rho = \rho(p, T)$ . It's vertical distribution can give a knowledge of the atmosphere status which can be stable or unstable.

Let us consider convection in a compressible fluid such as the atmosphere, which obeys the perfect gas law,

$$\rho = \frac{P}{R \cdot T} \quad (2.3)$$

where  $\rho$  is the density of an air cell (parcel) in an environment with atmospheric pressure  $P$  and temperature  $T$ .  $R$  is defined as the constant of proportionality, is known as the universal gas constant ( $= 287JKg^{-1}K^{-1}$ ) Let us consider the temperature and density at two heights  $z$  and  $z_1$ , then  $P_1 = P(z_1)$ ,  $T_1 = T(z_1)$ , and  $\rho_1 = \frac{P_1}{R \cdot T_1}$ . We consider the adiabatic displacement of the parcel to be  $z_2$ . The parcel will adjust to this pressure, in doing so it will expand, do work on its surroundings and thus cool. So the parcel temperature is not conserved during displacement even if that displacement occurs adiabatically. In fact there is a second and very important process that changes the temperature of rising parcels. It is common experience that such parcels may become saturated with water vapor and the water vapor may condense to form clouds, thereby releasing the latent heat into the parcel.

---

<sup>3</sup>Field of irregular motions of a fluid such that all time-averaged functions describing the statistics of the field are unaffected by rotation or reflection of the axes of reference. In the atmosphere, isotropy is approached well away from the Earth's surface.

## 2.6. Thermodynamics parameters to describe the atmospheric states. 24

### 2.6.1 The adiabatic lapse rate ( in unsaturated air).

The most common vertical derivative in meteorology is the lapse rate. The lapse rate is defined as the rate at which temperature decreases with height. Since  $\frac{dT}{dz}$  would be the rate at which temperature increase with height, the lapse rate is actually  $-\frac{dT}{dz}$ . The most common form of the lapse rate is the *dry adiabatic lapse rate*.

Consider a parcel of ideal gas of unit mass with a volume  $V$ , so that  $\rho \cdot V = 1$ . If an amount of heat  $\Delta Q$  is exchanged by the parcel with the surroundings then applying the first law of thermodynamics (dry air, no latent heat release) given us:

$$\Delta Q = C_v dT + PdV \quad (2.4)$$

where  $C_v dT$  is the change in internal energy due to a change in parcel temperature of  $dT$  and  $PdV$  is the work done by the parcel on its surroundings by expanding an amount  $dV$ . Here  $C_v$  is the specific heat at constant volume.

Looking at equation 2.4, the rhs can be arranged to express it in terms of  $dT$  and  $d\rho$  and deducing  $dT$  depends on  $d\rho$ . Taking that  $\rho \cdot V = 1$  and  $V = 1/\rho$ , then

$$dV = d(1/\rho) = -\frac{1}{\rho^2}d\rho \quad (2.5)$$

Thus;

$$PdV = -\frac{P}{\rho^2}d\rho = -\frac{RT}{\rho d\rho} \quad (2.6)$$

where in the last step the ideal gas law  $P = \rho \cdot R \cdot T$  has been used. But on differentiation yields;

$$dP = RTd\rho + \rho R dT$$

Hence;

$$PdV = -RTd\rho/\rho = -d\rho/\rho + RdT$$

the first law equation 2.4 can be written as;

$$\Delta Q = (R + C_v)dT - d\rho/\rho = C_p dT - d\rho/\rho \quad (2.7)$$

since  $C_p = R + C_v$ , where  $C_p$  is the specific heat at constant pressure.

For adiabatic motions,  $dQ=0$ , whence

## 2.6. Thermodynamics parameters to describe the atmospheric states. 25

$$C_p dT = dP/\rho \quad (2.8)$$

Now if the motions are in hydrostatic balance then  $dP = -g \cdot \rho \cdot dz$ , where  $\rho$  is the density of the environment (since the parcel and the environmental pressure must be locally equal and the environmental pressure must be in hydrostatic balance with the environment density). Before being perturbed the parcel's density was equal to that of the environment. If the displacement of the parcel is sufficiently small, its density is still almost equal to that of the environment  $\rho \approx \rho_E$ , and so, under adiabatic displacement the parcels temperature will change according to;

$$dT/dz = -g/C_p = -T_d \quad (2.9)$$

where  $T_d$  is the dry adiabatic lapse rate. This is the rate at which the parcel temperature decreases with height under adiabatic displacements.

Putting in the value of  $C_p = 1005 JKg^{-1}K^{-1}$ , we find that  $T_d \approx 10 Kkm^{-1}$ . Thus, typically a parcel of dry air displaced vertically cools by  $10^\circ Ckm^{-1}$ .

The lapse rate index is the parameter used to determine the atmosphere states. The stability or instability of an air mass depends on whether the isolated rising parcel (thermal), which cools at a fixed rate determined by the dry adiabatic lapse rate to condensation level, and by the saturated lapse rate thereafter, finds itself at any moment to be warmer or cooler than the surrounding air. If warmer, the parcel is less dense and buoyancy forces will force it to rise further. The air is said to be *unstable*. If cooler, it will be more dense and will sink. The air is said to be *stable*. When air is stable, there is no convection: air which is displaced up or down by mountains, for example, will return to its previous altitude. The unstable state is associated with convection.

Unstable	$dT/dz < lapse\ rate$
Neutral	$dT/dz = lapse\ rate$
Stable	$dT/dz > lapse\ rate$

Table 2.2: Relationship between the lapse rate and the gradient of the temperature.

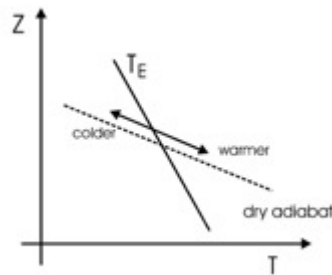


Figure 2.7: The atmosphere is nearly always stable to dry processes. A parcel displacement upward (downward) in an adiabatic process moves along a dry adiabatic (dotted) line and cools down (warms up) at a rate that is faster than that of the environment,  $\frac{\partial T_E}{\partial z}$ . If the parcel is warmer, it will be less dense and positively buoyant and will rise (accelerate upward). If the parcel is cooler, which is the normal course of events, it will be more dense and will sink (accelerate downward).

Therefore, a compressible atmosphere is unstable if temperature decreases with the height faster than the adiabatic lapse rate. This is no longer a simple "top-heavy" criterion (atmosphere density must decrease with the height under all conceivable circumstances) nor even a "bottom-warm/top-cool" criterion. Because of the influence of adiabatic expansion, the temperature must decrease with height at greater than the finite rate for instability to occur.

As an example of an air parcel ascending from 800 mb stays parallel to the dry adiabats since its temperature doesn't change as long as its stays cloud-free the new temperature would be about  $-17.5^{\circ}\text{C}$ . This is much colder than the air already at that level ( $-9^{\circ}\text{C}$ ) so the air parcel would sink back down.

The atmosphere is almost always stable in dry conditions. Before proceeding it is important to introduce the *potential temperature*, a temperature-like variable that is conserved in adiabatic motions.

### 2.6.2 Potential temperature.

The non conservation of temperature (T) under adiabatic displacement makes the temperature a less-than-ideal measure of atmospheric thermodynamics. However,

## 2.6. Thermodynamics parameters to describe the atmospheric states. 27

we can identify a quantity called potential temperature which is conserved under adiabatic<sup>4</sup> displacement.

Using the perfect gas law,  $P = \rho RT$ , the adiabatic statement in equation 2.8 can be arranged as;

$$C_p dT = R \cdot T dP$$

$$dT/T = R/C_p dP/P = k dP/P$$

where  $k = R/C_p$  for a perfect diatomic gas like the atmosphere. Thus,

$$d \cdot \ln(T) - k \cdot d \ln P = 0$$

and we can define the temperature  $\theta$ , given by

$$\theta = T \left( \frac{P_0}{P} \right)^k \quad (2.10)$$

which unlike  $T$  is conserved in adiabatic motion  $d\theta = 0$ . Here by convection we take  $P_0$  to be the constant reference pressure of 1000hPa. The figure 2.8 shows the vertical profile of the potential temperature. From its definition equation 2.10 we see that the potential temperature  $\theta$  is the temperature a parcel of air would have if it were expanded or compressed adiabatically from its existing  $P$  and  $T$  to a standard pressure  $P_0$ . It allows one, for example, to directly determine how the temperature of an air parcel will change as it is moved around adiabatically; if we know  $\theta$ , all we need to know at any instant is the pressure, and then equation 2.10 allows us to determine its temperature at that instant.

As an example to describe it; let us consider the temperature of an air parcel at 300 mb is  $T=229K(-44^\circ C)$ , then if it is brought down to the ground adiabatically, its temperature will be  $T=323K(50^\circ C)$ . Thus its potential temperature is  $\theta = 323K$ .

The stability of the column to a dry adiabatic process can be expressed in terms of  $\theta$ .

Returning to the displacement of the air parcel at the undisturbed position  $z_1$ , it has environmental temperature and pressure and therefore also environmental potential temperature  $\theta_1 = \theta(z_1)$ , where  $\theta(z)$  is the environmental potential tem-

---

<sup>4</sup>Adiabatic process in which a material undergoes a change in its physical states (eg. volume, pressure or temperature) without any heat added to or released from it.

## 2.6. Thermodynamics parameters to describe the atmospheric states. 28

perature profile. Since the parcel preserves the potential temperature ( $\theta$ ), it still has  $\theta = \theta_1$  when displaced to  $z_2$ . Since its parcel pressure is the same as that of its environment, it is warmer or cooler than its environment according to whether  $\theta_1$  is greater or lesser than  $\theta(z_2)$ . Since  $\theta(z_2) \cong \theta(z_1) + \left(\frac{d\theta}{dz}\right) \Delta z = \theta_1 + \left(\frac{d\theta}{dz}\right) \Delta z$ , then the parcel can have the following atmosphere states;

Unstable	$(d\theta/dz) < 0$
Neutral	$(d\theta/dz) = 0$
Stable	$(d\theta/dz) > 0$

Table 2.3: Traditional or local lapse rate names and definitions commonly used to determine static stability. Table compiled from Stull,1988).

### 2.6.3 Convective cells.

The heat exchanged between the surface of the Earth, the air and the wind shear determine the structure of the boundary layer, the first 1-2km above the surface. At night, radiation into space is caused by the negative heat flux that creates cool dense air next to the surface. This stable air interacts with the wind to create a series of stratified horizontal layers<sup>5</sup> Much research has been done to understand the size and velocity of the convective cell or "blobs", and recently Gilbert ( Gilbert et al, 2006) has detected the small temperature variation in the convections determining the relationship between the temperature and the heat flow. The vertical thickness of the boundary layer and the lateral size of the convective cells in the atmosphere are related by a functional relationship that is not yet known. A measurement of the lateral separation between convective cells is a useful quantity, because it determines the horizontal scale of the optical turbulence degradation over ground based telescopes. The horizontal scale of degradation is called the outer scale.

---

<sup>5</sup>During daytime a positive flux creates convective cells that rise into the atmosphere with velocities of about  $5m.s^{-1}$ , where this value depends of the surface terrain.

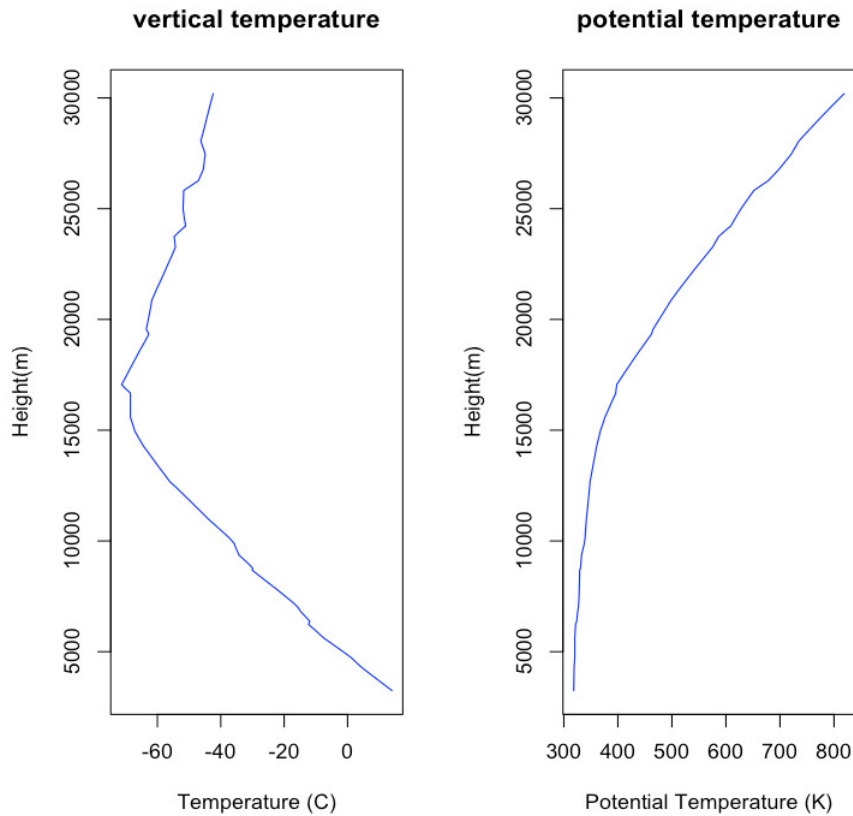


Figure 2.8: Vertical profile of the averaged temperature (dotted) and potential temperature  $\theta$  (solid) as a function of pressure. The data are retrieved from the radiosonde launch in Tenerife. Only the height of interest above the Observatory is plotted. Starting at 700 mb which is about 2500 meters to 15 mb at about 30000 meters. Data from radiosonde 60080.

#### 2.6.4 Indices to determine the atmospheric states.

The factors that govern the movements of the air parcels in the atmosphere are related to the dynamic condition. The physical equations that govern the dynamic of the atmosphere in laminar to turbulent conditions have been introduced by Richard-

## 2.6. Thermodynamics parameters to describe the atmospheric states. 30

son<sup>6</sup> (Richardson 1922) which give the index for changing from one state to another ( from laminar to turbulent flows).

### **Richardson Number.**

Static instability in the atmosphere leads to spontaneous vertical mixing (convection) in the form of thermals and possibly cumulus clouds. Vertical mixing may occur in a stable environment, in particular in the form of breaking waves. These breaking waves are a major cause of turbulence at the higher altitude, especially just above the planetary boundary layer or near the jet stream, where they often produce clear-air turbulence (CAT). The evolution of these breaking waves has been described mathematically by Kelvin and Helmholtz, hence the term Kelvin-Helmholtz billows, the evolution of which is shown in Figure 2.9. The likelihood of Kelvin-Helmholtz instability can be evaluated by means of the Richardson's number  $R_i$ , the ratio of the static stability  $N^2$  to the square of the wind shear  $dU/dz$ :

$$R_i = \frac{N^2}{(dU/dz)^2} \quad (2.11)$$

where  $N$  is the Brunt-Vaisala stability parameter,  $U$  is the wind shear and  $z$  is the height (meters). The Brunt-Vaisala stability parameter is defined as;

$N^2 = \frac{g}{\theta} \frac{d\theta}{dz}$ , Where  $g$  the gravitational acceleration (about  $9.8ms^{-2}$ ),  $T$  the temperature (Kelvin),  $\theta$  the potential temperature (Kelvin), and  $z$  the height (meters).

For higher  $N$ , the more stable the flow. Both stability and wind shear are calculated locally, and  $R_i$  may vary rapidly across a sheared boundary, such as on top of the stable nocturnal boundary layer. Even under these statically stable conditions, instability is possible, when the wind shear is strong enough to break up the stable layer and produce breaking waves. This occurs when  $R_i < 0.25$ . This is called the *Richardson critical value*. Kelvin-Helmholtz waves will grow and overturn to

---

<sup>6</sup>Lewis Fry Richardson (1881-1953). Pioneering work in numerical analysis, meteorology, and numerical weather prediction. His later work on mathematical modeling of psychology, causes of conflict, and the statistics of wars is outlined in terms understandable to fluid dynamicists. "*Big whorls have little whorls that feed on their velocity, and little whorls have smaller whorls and so on to viscosity.*"

## 2.6. Thermodynamics parameters to describe the atmospheric states. 31

produce patches of turbulent mixing (Turner, 1973). Figure 2.9 represents this type of instabilities and is obvious in the appearance of billows (whirlwinds) of different sizes in the air.

In addition the Kelvin-Helmholtz instability can be observed in the nature of the atmosphere when it generates cloud vortices and those vortex evolution can be seen in the figure 2.10 which shows the formation of Kelvin-Helmholtz billows in the Canary Islands regions .

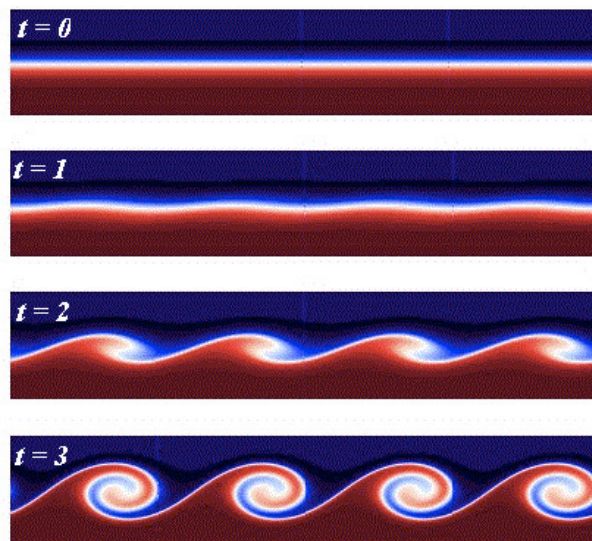


Figure 2.9: Idealized Kelvin-Helmholtz billows and the formation of vortices. It shows the time series evolution for a Kelvin-Helmholtz instability that occurs at the interface between two layers stratified when their velocities are different. The development of turbulence occurs with the Richardson index ( $R_i < 0.25$ ).

When buoyancy forces displace the atmosphere flow vertically they form hydrodynamical unstable zones, leading to turbulence (Vernin-Avila, 1998). Thus the gradient of the Richardson number gives an indication of where the turbulence motions will occur. Table 2.4 below shows the relationship between the gradient of the Richardson number and the determination of the flow of turbulence. These parameters have been collected from the work done by Vernin and Avila (Vernin and Avila, 1998) taking high resolution data from several radiosonde launches in the Roque de los Muchachos Observatorio (ORM) sited at La Palma (Canary Islands) during site testing campaigns.

## 2.6. Thermodynamics parameters to describe the atmospheric states. 32

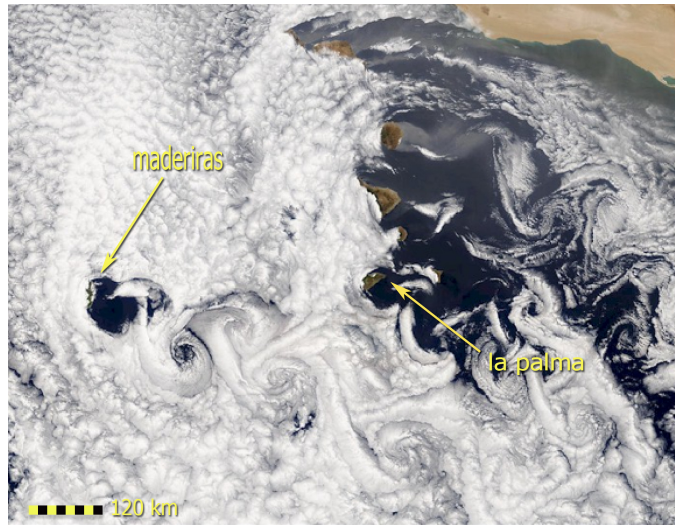


Figure 2.10: Creation of the vortex street from the Canary Islands to Madeira. The distance from Madeira to the Canary Islands is about 450 kilometers. A vortex street often occurs when cloud formations over the ocean are disturbed by wind passing over land or another obstacle and the air masses generate a turbulent pattern according to mixing length theory. In this true-color Moderate Resolution Imaging Spectroradiometer (MODIS) image from July 5, 2002, marine stratocumulus clouds have arranged themselves in rows, or streets, which are usually parallel to the direction of wind flow. Credit. Nasa Hubbles gallery.

Pot. temp gradient $\frac{\partial\theta}{\partial z}$	Static stability	$R_i$	Flow
$> 0$	Stable	$> 0.25$	Laminar.
$> 0$	Stable	$0 < Ri < 0.25$	Turbulent.
$= 0$	Neutral	0	Turbulent.
$< 0$	Unstable	$< 0$	Convective (turbulent).

Table 2.4: Values of the gradient Richardson number for different types of flow. Compile from the work (Vernin and Avila 1998).

A comparison of the data from the micro-thermal measurements of the temperature structure parameter  $C_t^2$  to the potential temperature  $\theta$  and the gradient Richardson number  $R_i$  is shown in the Figure 2.11. The vertical profiles go from

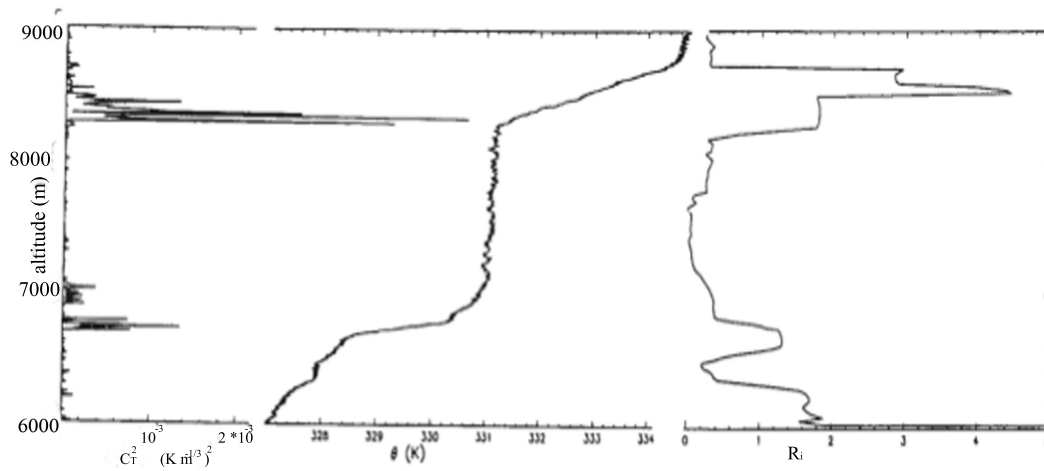


Figure 2.11: Profiles of a radiosonde launch in Paranal (Chile) taking the height slab between 6 to 9 km, showing a good correspondence of the variation of the  $C_t^2$  (left) measured with the calculated gradient of the potential temperature  $\theta$  (middle) and Richardson number  $R_i$  (right). The radiosonde gives a high vertical resolution for the temperature and wind speed parameters which can give the same resolution for the  $C_t^2$ ,  $\theta$  and  $R_i$  identifying the turbulent layers. Credit. Vernin and Avila, 1998.

6000 to 9000 meters above sea level and it shows a strong layers that appear at 6800 and 8400 meters, which are located in the lower and upper boundaries of the turbulent mixed region which is the zone having nearly zero potential temperature with height (between 7000 and 8200 meters). It is in this region where the potential temperature gradient  $\theta$  is near zero with a small Richardson number, which requires forceful, turbulent mixing to create and maintain.

### Reynolds number.

The Reynolds number  $R_e$  determines when the change of a fluid from a laminar state to a turbulent state occurs. The free atmosphere is considered to be most of the time turbulent with  $R_e$  values of about  $10^6$  to  $10^{10}$ . There are two types of fluid flow; laminar flow is smooth and steady, and turbulent flow is unstable and random. Turbulence is a characteristic of the latter and is defined as irregular or random motions in a fluid. The transition between these two flows is defined by a

## **2.6. Thermodynamics parameters to describe the atmospheric states. 34**

dimensionless quantity called the Reynolds number;

$$R_e = \left( \frac{v \cdot L}{\mu/\rho} \right) \quad (2.12)$$

where  $v$  is the flow velocity ( $ms^{-1}$ ),  $L$  is characteristic length (m),  $\mu$  is the viscosity ( $ms^{-1}$ ), and  $\rho$  is the fluid density. When the Reynolds number is below 2000, the flow is considered to be laminar, but when the flow is greater than 3000, the flow is turbulent. Turbulence is produced from a multitude of sources such as convection from hot surfaces, wind shear, or weather systems. This turbulent mixing generates local changes in temperature, humidity, and atmospheric composition, which can lead to changes in the index of refraction (Fiorino, 2005).

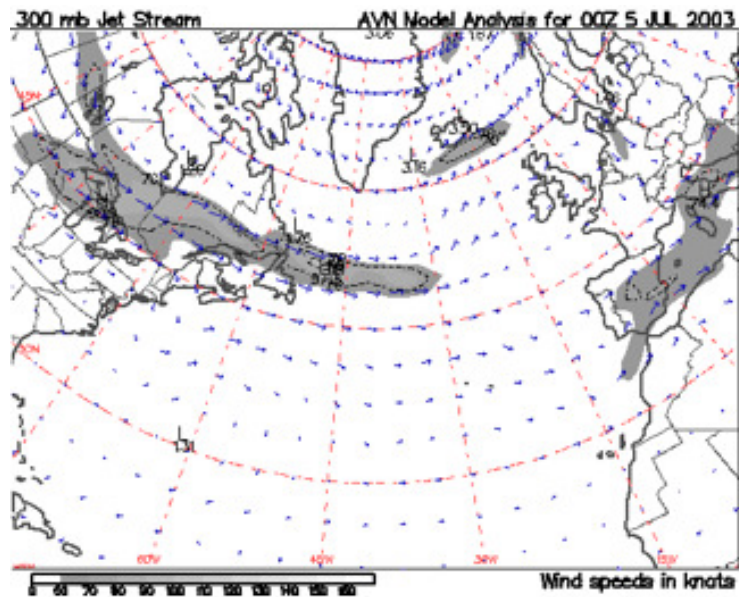
### **2.6.5 Jet stream.**

In the discussion of the upper layer, it is important to mention the influence of the Jet Stream on the total turbulence above the ground and how it interacts with the lower layers making them more turbulent.

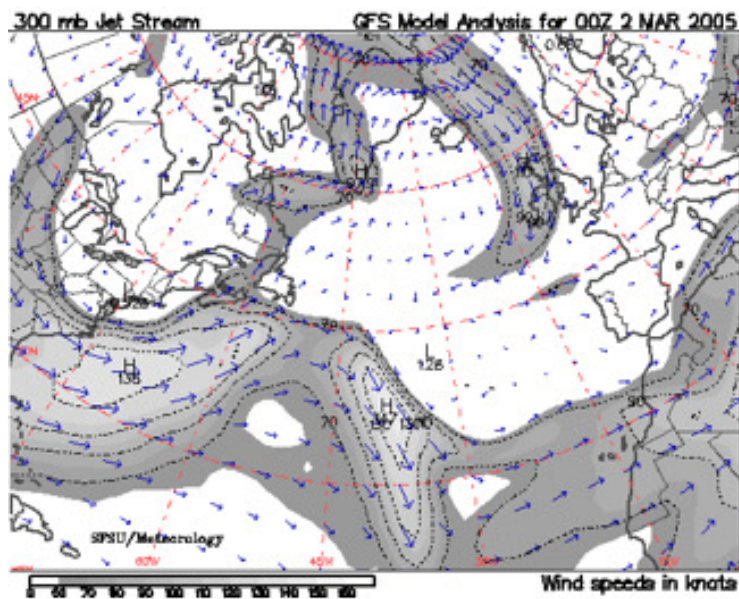
The Jet Stream is a narrow band of exceedingly high speed winds, which is known to exist in the higher levels of the atmosphere at altitudes ranging from 7000 to 12000 meters above the ground or even higher.

The jet stream appears to be closely associated with the tropopause and with the polar front. It typically forms in the break between the polar and the tropical tropopause where the temperature gradients are intensified. The mean position of the jet stream shears south in the winter and north during the summer. Because the tropopause is thicker in summer than in winter, the tropopause and the jet stream will normally move to higher altitudes in summer.

The jet stream flows from west to east and may encircle the entire hemisphere. More often, because they are stronger in some places than in others, they break into segments some 2000 to 6000 kilometres long. They are usually about 500 kilometres wide and may be 1 to 2 kilometres thick. These jet stream segments move in an easterly direction following the movements of the pressure ridges and troughs in the upper atmosphere.



(a) Summer where the jet stream (grey zones) is displaced to the north and its strength is reduced in the Canary Islands.



(b) Winter where the jet stream (grey zones) is displaced to the mid-latitudes with an increase of its strength in the Canary Islands region.

Figure 2.12: Typical Jet stream picture of the jet stream circulation during two periods (winter and summer). The grey zones show the strength of the jet stream and how typically are located during the winter and summer periods.

<http://squall.sfsu.edu/crws/jetstream.html>

## **2.6. Thermodynamics parameters to describe the atmospheric states. 36**

The winds in the central core of the jet stream are the strongest and may reach speeds as great as  $128ms^{-1}$ , although they are generally between  $51ms^{-1}$  and  $77ms^{-1}$ . Wind speed decreases toward the outer edges of the jet stream and may be blowing at only  $13ms^{-1}$  there. The rate of decrease of the wind speed is considerably greater on the north edge than the southern edge. Wind speeds in the jet stream are on average stronger in winter than in summer.

For the Atlantic region and especially in the Canary Islands the jet stream distribution shows a seasonal regime with a displacement to the north of the Atlantic Ocean during the summer time and a displacement to the tropic during the winter time, hence increasing the influence over the Canary Islands. The Figure 2.12 an example of the displacements of the jet stream in the North Atlantic regions in two periods of the year (July and March).

# Chapter 3

## Optical effects of Atmospheric turbulence approximation.

*"In the customary description of turbulence, there are always more unknowns than equations .. "*

*Tennekes and Lumley, 1972*

---

### 3.1 Overview.

Turbulence in the Earth's atmosphere is caused by random variations in temperature and pressure that alter the refractive index of air, both spatially and temporally. As optical waves propagate through the atmosphere, the waves are distorted by these refractive-index fluctuations. Such distortions can adversely affect many types of optical systems, such as those used for optical communications and imaging, as well as astronomy observations. During the last 100 years, modeling the effects of turbulence on optical propagation has received much attention and a focus on statistical modeling has produced several useful theories. Statistical analyses are necessary because it is impossible to exactly describe the refractive index for all positions in space and for all time, there are too many random behaviors and variables to account for in a closed-form solution. The most widely accepted theory, due to its consistent agreement with observation, was first put forward by A.N. Kolmogorov

1941. His theory is the basis for all contemporary theories of turbulence.

This Chapter covers the formation of optical turbulence and the use of different models to retrieve the refractive index structure parameter  $C_n^2$ .

## 3.2 What is the turbulence.

It was Lewis F. Richardson (1922) who first proposed a qualitative description of turbulence by imagining it as a process of decay which proceeds through an energy cascade, in which eddies subdivide into ever smaller eddies until they disappear by means of heat dissipation through molecular viscosity. This cascade begins at the outer scale wavenumber, with an eddy size equal to the outer scale length,  $L_0$ , and continues on until the eddies are equal to the inner scale length,  $l_0$ . The main energy losses occur in the energy dissipation region, which is separated from the energy input region by the inertial range. The Figure 3.1 shows the scheme representation of the energy transfer during turbulent process proposed by Richardson.

All the energy is thus transmitted without any significant losses through the inertial range to the viscous dissipation region. The energy transfer through the spectrum from small to large wavenumbers, or from large scale eddies to small-scale ones, can be seen as a process of eddy division. If the Reynolds number (Chapter 2, section 2.6), the dimensionless ratio of the inertial to the viscous forces, of the initial flow is high, it becomes unstable and the size of the resulting eddies is of the order of the initial scale of the flow  $L_0$ . The Reynolds number characterizing the motion of these eddies is smaller than that of the initial flow, but still sufficiently high to make these eddies unstable and cause further division into smaller eddies.

During this process the energy of a large decaying eddy is transferred to smaller eddies, i.e., a flow of energy is established from small to large wavenumbers. Each division reduces the Reynolds number of the product eddies. This continues on until the Reynolds number becomes sub-critical. At that point the eddies are stable and have no tendency to decay any further. It is clear that the larger the Reynolds number of the initial flow, the greater the number of successive divisions. Thus the inner scale length reduces with increasing Reynolds number corresponding to the

outer scale length.

A finite inertial range is observed when the viscous range is separated from the energy range. This occurs when  $Re \gg Re_{critical}$ . In practice an inertial range is observed for  $Re > 106 - 107$ , Tatarskii (1971), and can be described by a universal theory based on dimensional analysis as advanced by Kolmogorov. (Kolmogorov, 1941).

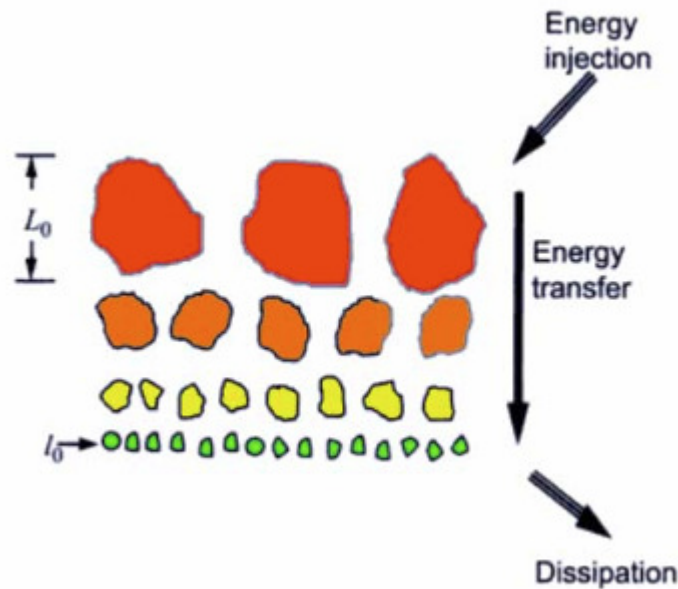


Figure 3.1: Scheme of the turbulent process generated by the energy cascades. The turbulent cells move from the outer scale ( $L_0$ ) to an inner scale ( $l_0$ ). Lewis F. Richardson has defined this energy transfer process as; *"big whirls have little whirls that feed on their velocity; Little whirls have lesser whirls and so on to viscosity."* Credit. Adapted from Andrews and Philips, 2005.

### 3.3 Tropospheric wind and optical turbulence

The wind controls the intensity and the temporal frequency of wavefront fluctuations when it is traveling through the atmosphere. In theoretical models this effect is introduced through the average turbulence wind speed and by considering the Taylor hypothesis. The Taylor hypothesis is an approximation that allows for es-

timating spatial turbulence statistics using measurements from air moving past a single point. For low intensity turbulence in a uniform mean flow the turbulence pattern is assumed to be "frozen". This hypothesis is valid under most conditions, but becomes questionable when free convection velocity fluctuations are of the same order or larger than the mean velocity, or when the frequency of the turbulent eddies is not significantly higher than the magnitudes of the mean wind shear (Arya, 2001).

(Sarazin and Tokovinin, 2001) have studied the correlation for Cerro Paranal and Cerro Pachon between the wind speed at the troposphere and the ground wind speed using in-situ wind speed measurements done by radiosonde balloons and a local mast. He found a clear relationship between ground wind velocity ( $V_0$ ) and the wind velocity at 200 mb ( $V_{200mb}$ ) pressure level after studying these two sites. The accuracy of this correlation is estimated to be about 20%. Sarazin has proposed a general formula to relate both wind speed levels as;

$$V_0 = 0.4 \cdot V_{200mb} \quad (3.1)$$

where  $V_0$  is the ground wind speed and the  $V_{200mb}$  is the wind speed at the jet stream height. It is in this region (about 200mb) where the jet stream is located and its evolution can generate states of strong or low turbulence events which contribute to the total optical turbulence ( measured with the seeing or the isoplanatic angle ). This information is an important input for Adaptative Optics instrumentation particularly in Multi-Conjugated Adaptative Optics (MCAO) or only Ground Layer Adaptative Optics (GLAO), or even tomographic techniques using multiple natural or laser guide stars in the field (MOAO).

The long-term data available in climatological databases constitutes a very useful source to study the behavior of meteorological parameters, such as wind speed at a height of 200 mb, and their use in building models and forecasting methods. We have used the NCEP (National Center for Environmental Prediction) and Wyoming University database [[www.weather.uwyo.edu/upperair/sounding.html](http://www.weather.uwyo.edu/upperair/sounding.html)] to collect a set of meteorological parameters ( temperature and wind speed mainly ) in a vertical distribution from the data obtained by radiosonde launched in Tenerife (described in Chapter 6).

The vertical profiles of the wind speed can be analysed and compared with other meteorological parameters or they can be statistically compared with the astroclimate parameters obtained with turbulence monitors such as, DIMM, MASS-DIMM or SCIDAR. An example of the wind speed profile and its yearly distribution can be seen in the Figure 3.2 where the behavior through the year 2008 is shown.

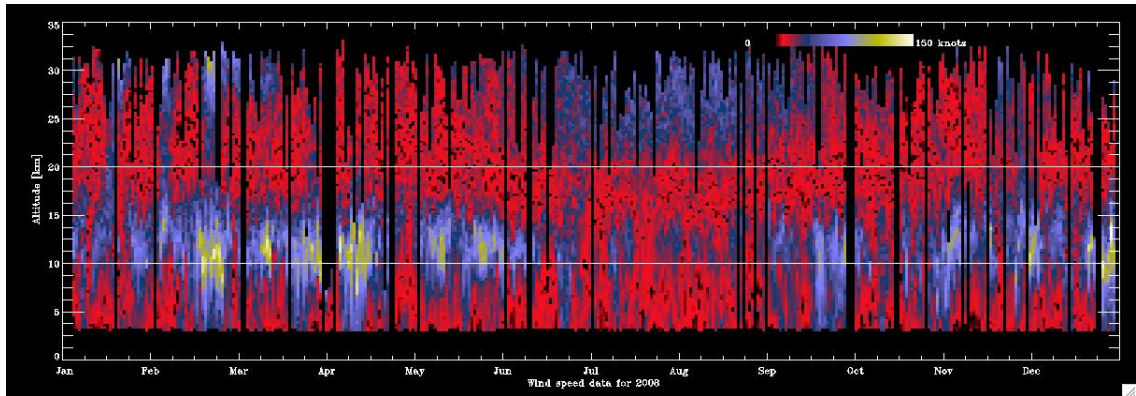


Figure 3.2: A year-long distribution of the wind speed measured in knots for the year 2008. Those measurements are from the database of the radiosonde data collected from station 60018 (launch site in Tenerife) every day at 00 UT, the strength of the wind changes shows a seasonal component with a calm period from June to September. (The gradient bar shows the velocities from black minimum (0 knots) to maximum white (150 knots))

To get a better understanding of the tropospheric wind at the other sites a relative frequency plot of the wind direction is represented by a wind rose in figure 3.3. The data are taken from the NCEP/NCAR 14-Re-analysis database (Garcia Lorenzo, et al. 2005). It is clearly shown that the dominant trade wind at 200mb is coming from WNW for all the sites with a difference in the 700 mb data at Manua Kea, where there is a big component of the wind coming from the E-ENE direction.

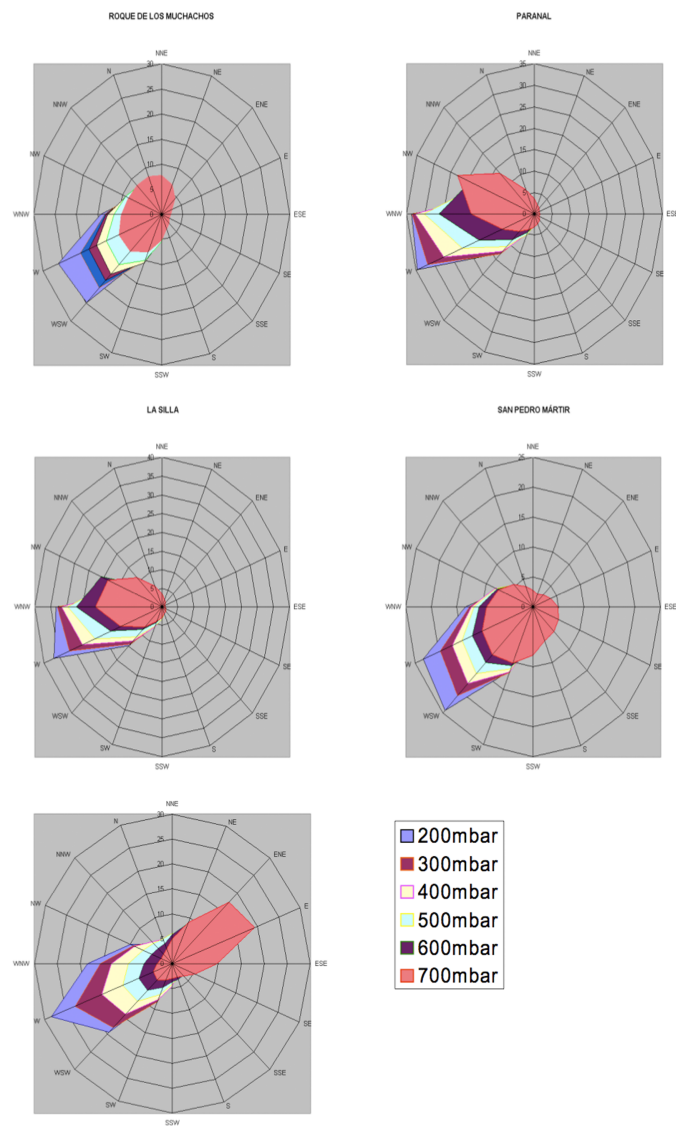


Figure 3.3: Tropospheric wind rose for different sites in the Northern Hemisphere; San Pedro Martir (SPM), Manua Kea, Observatorio Roque de los Muchachos (ORM) and Southern Hemisphere; Paranal and La Silla. Credit. Garcia-Lorenzo, et al. 2005.

The tropospheric wind can be related to the winds at different height levels as a first approximation to a linear correlation between the  $V_0$  and  $V_{200mb}$ , comparing individual daily measurements at each pressure levels with the measurements at 200 millibars. The resulting Pearson coefficients is showed in the figure 3.4, where there is a high correlation between the winds at different levels and the  $V_{200mb}$ . The low correlation shown at low levels (figure 3.4) could be due to the local orography of each observing site shown in the figure 3.4 which shows the observing sites analysed; La Palma, Manua-Kea, Paranal, La Silla and San Pedro Martir, that indicate a good correlation of the all sites at  $V_{200mb}$ . This result presented by Garcia Lorenzo is similar to those found by Sarazin (Sarazin and Tokovinin, 2002).

This good correlation between the wind speeds makes this a useful parameter that can be used to build simple models to retrieve the atmospheric turbulence coefficient parameter  $C_n^2$  and even to use in site evaluation and characterization.

### 3.4 Temperature and Optical turbulence.

The turbulent motion of the air parcel is an adiabatic process, where the temperature changes, which means that there are fluctuations of the air refractive index. This is a typical effect that we can observe in our everyday life when looking to the horizon on a road during a hot day and the vision of distant objects is disturbed by the convective air movements from the ground and are also perturbed by the wind. A similar effect can be seen looking at the sky during the night (twinkling stars). The effects of turbulent air and fluctuations are caused by changes in heating and cooling of the atmosphere and Earth surface caused mostly by the sunlight and the diurnal cycle. The temperature and its potential temperature (Section 2.6.2) are parameters used to calculate and to determine the different states of the atmosphere. Defining the potential temperature as the temperature that a parcel of air will have if raised or lowered to the 1000 millibars level by;

$$\theta(z) = T(z) \left( \frac{1000}{P(z)} \right)^{-0.286} \quad (3.2)$$

And assuming adiabatic conditions, the potential temperature is the same for a

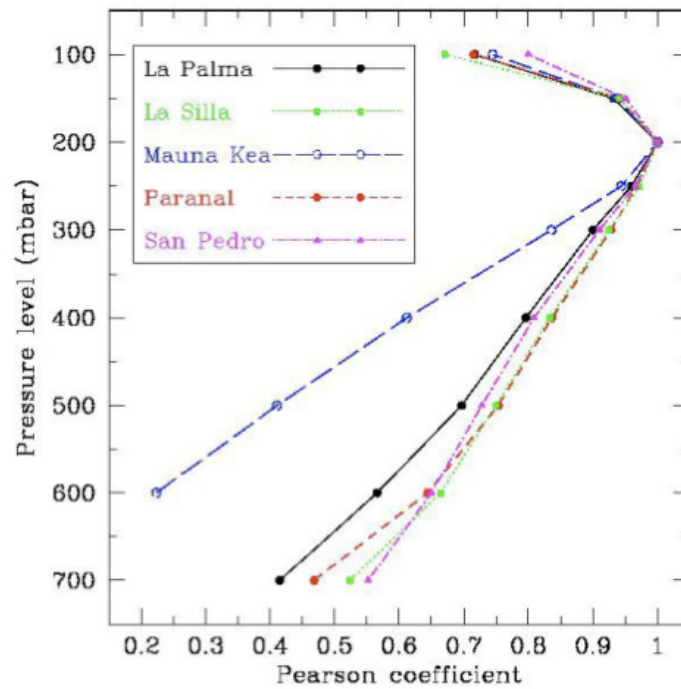


Figure 3.4: Linear coefficient of Pearson correlation obtained from the daily measurements at different sites (La Palma, Manua Kea, San Pedro Martir, Paranal and La Silla) of the wind speed at different height levels with the wind speed at 200mb. Credit Garcia-Lorenzo, et al. 2005.

parcel of air, as it rises or sinks and it can determine the state of the atmosphere; stable, unstable or neutral depending on which those conditions prevails. The Table 3.1 shows the stability criteria applied to the gradient of the potential temperature.

$\frac{\partial\theta}{\partial z} > 0$	Stable
$\frac{\partial\theta}{\partial z} = 0$	Neutral
$\frac{\partial\theta}{\partial z} < 0$	Unstable

Table 3.1: Potential temperature gradient and its relationship to the atmosphere states.

In the Figure 2.8 an example is shown of the potential temperature vertical distribution obtained from the temperature values collected from radiosonde data.

The optical turbulence implies two phenomena: the dynamical turbulence and

the changes in the refractive index of the air where there is mixing of air parcels at different temperature, pressure or chemical composition. The potential temperature gives a straightforward relationship between the atmospheric states (see table 3.1) and it can be used as an index of when the atmosphere becomes turbulent. Figure 3.5 shows a seasonal distribution of the vertical temperature and the height where the inversion layers occur. A seasonal relationship is shown in the figure, where the inversion heights has a large dispersion for the months October to May and shows a stable low dispersion during the summer time (June to September), which corresponds to stability of the upper atmosphere.

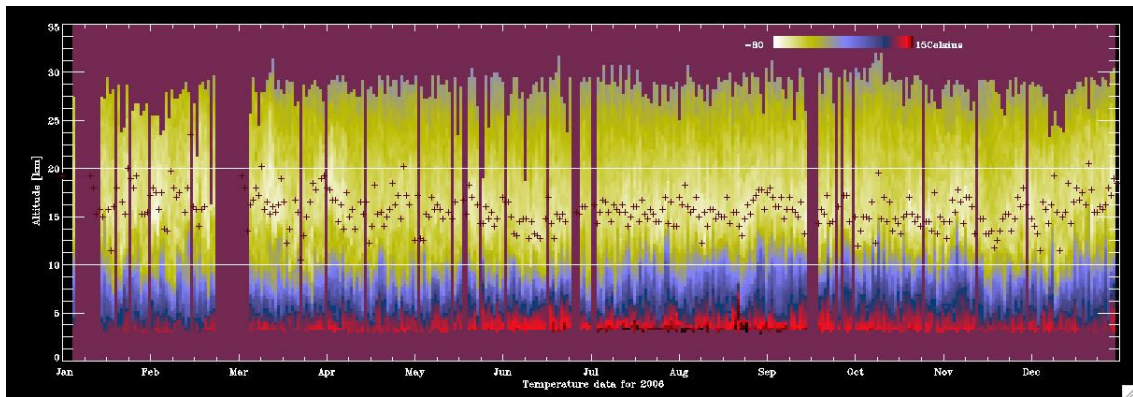


Figure 3.5: Daily vertical distribution of the temperature for the year 2006, the crosses show the minimum temperature where the tropospheric inversion layer occurs at the height of the jet stream.

### 3.4.1 Heffter criteria: a simple model.

The potential temperature discussed earlier (table 3.1) and its gradient are related to many stability definitions in the study of the atmosphere. This simple approach can be used as an index of atmospheric stability as has been defined in table 3.1. Heffter (1980) used a single method to identify the "critical inversion" layers which can set the top of the atmosphere boundary layer (ABL). The inversion layers are identified at the height  $z$  where the potential temperature (lapse rate) and the temperature differences between the inversion base (bottom) and top meet the following relationship.

$$\begin{aligned}\frac{\Delta\theta}{\Delta z} &> 0.005Km^{-1} \\ \theta_t - \theta_b &> 2K\end{aligned}\tag{3.3}$$

where  $\theta$  is the potential temperature,  $\Delta\theta/\Delta z$  is the potential lapse rate in the inversion layer  $\theta_t$  and  $\theta_b$  are the potential temperature at the top and the bottom of the inversion layer.

Applying the Heffter geometrical analysis to radiosonde measurements, e.g. taking one set of data, 4<sup>th</sup> on August 2008, (see Table 3.2) and building a table with the meteorological parameters and the Heffter equations (equations 3.3) it is possible to perform a visual identification of where the Heffter criteria are fulfilled. This first look at the vertical profiles can easily identify where the active layers are developing turbulence.

The Heffter criteria can be used to identify the critical inversion layer and can be correlated with turbulent layers identified by local turbulence monitors such as the MASS-DIMM instrument. The Heffter criteria can be built from a whole set of data from a meteorological radiosonde, identifying the time evolution of the distribution of the critical inversion layers. Figure 3.6 shows the Heffter criterion applied to the whole data set of the year 2008 and indicates the Heffter criterion by ones and zeros which are true or false (white and black respectively) in a 2D plot.

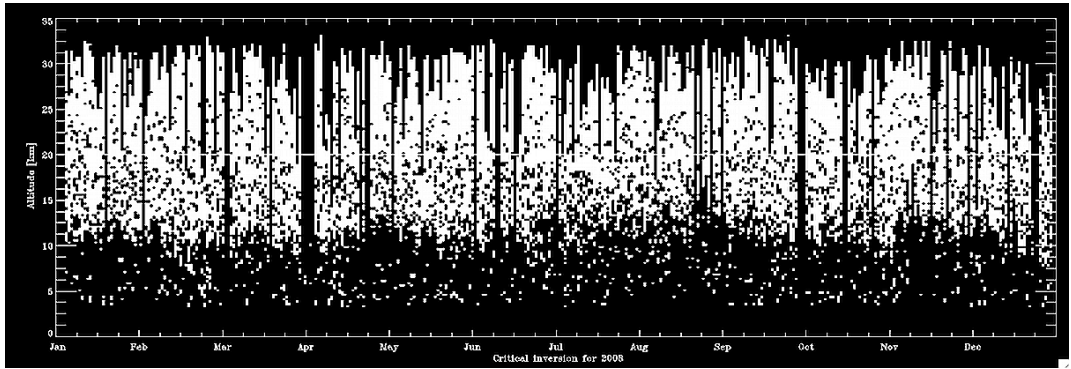


Figure 3.6: Plot of the daily radiosonde data which fulfill of the Heffter conditions. Data taken from the radiosonde database for the year 2008. The white pixel indicates fulfill of the Heffter criterion and the black pixels indicates that dont fulfill the Heffter criterion showed in the equations 3.3. The vertical axis gives the altitude, which starts at 3 km. The Observatory Roque de los Muchachos is about 2.4 km above sea level.

### 3.5 Optical turbulence and the refractive index constant $C_n^2$ .

As described in the previous sections, atmospheric turbulence induces random irregularities in the index of refraction, and wavefronts propagating through this turbulence become distorted, which causes the image of a light source to wander and spread. Statistics are used to quantify these characteristics because the changes in the atmospheres index of refraction are random.

Optical turbulence occurs when turbulent winds in the Earth's atmosphere mix the vertical moisture and the temperature gradients caused by solar heating of the Earth's surface. This mixing creates irregularities in the refraction index of the atmosphere in the forms of eddies or cells (Section **2.6.3**). In 1941 Kolmogorov-Obukhov applied a dimensional analysis to an isotropic velocity field and derived the inertial sub-ranges predictions from the forms of the velocity spectra and velocity structure functions. They found that a subclass of optical turbulence within subranges defined as the range of the optical turbulence bounded by the turbulent outer scales  $L_0$  and below by the inner scale  $l_0$  share a degree of consistency.

Briefly this can be seen as stochastic field changing in the refractive index  $n(\vec{r})$  at a vector  $\vec{r}$  in the turbulent atmosphere which can be characterized by the structure function with  $n(r_1)$  and  $n(r_2)$  as the values of the refractive index at the positions  $r_1$  and  $r_2$  respectively. The fluctuation of the refractive index  $n(r)$  using the refractive index structure function  $D_n$  is defined as;

$$D(r_1, r_2) = \langle |n(r_1) - n(r_2)|^2 \rangle \quad (3.4)$$

For isotropic and homogenous turbulence, the refractive index structure functions depends only on the modulus of the separation vector  $r = r_1 - r_2$ , then  $D_n(r_1, r_2) = D_n(r)$ .

### 3.5.1 Obtaining $C_n^2$ from meteorological parameters.

The optical turbulence has a strong relationship with the meteorological parameters (temperature, humidity and wind speed) and it can be the result of small changes (fluctuations) in the temperature. The refractive index can be expressed by;

$$n = \frac{77.6 \cdot P}{T} \left( 1 + \frac{0.00753}{\lambda^2} - 7733 \frac{q}{T} \right) \cdot 10^{-6} \quad (3.5)$$

where  $P$  is the pressure (millibars),  $T$  is the temperature (Kelvin),  $\lambda$  is the wavelength (micrometer), and  $q$  is the specific humidity ( $gm^{-3}$ ). This relationship makes it obvious that important macroscale atmospheric parameters affecting the refractive index are the temperature and humidity, whose variations are large compared

to pressure changes. These should be part of any macroscale model for predictions of optical turbulence strength. The refractive index structure parameter  $C_n^2$  is related to the meteorological conditions by the equation defined below; (Buffton et al, 1972).

$$C_n^2 = \left( 7.9 \cdot 10^{-6} \frac{P^2}{T^2} \right) (C_T^2 + 0.113C_{TQ} + 3.2 \cdot 10^{-3}C_Q^2) \quad (3.6)$$

where  $C_t^2$  is the temperature structure parameter,  $C_Q^2$  is the water vapor structure parameter and  $C_{TQ}$  is the temperature water vapor structure coefficient or covariance. Neglecting the influence of the humidity in the light through the atmosphere from the equation 3.5 remains, the  $C_t^2$  as the most important parameter to be determined. To determine it, it is essential to know the temperature gradient all along the image line of sight.

This coefficient can be measured using radiosonde data (more details in Chapter 7) which can measure the random fluctuations of the refractive index due to the different vertical temperature gradients. Using the equation 3.5 applied to the change of the temperature in two points, this structure function can be defined as;

$$D(r_1, r_2) = \langle |T(r_1) - T(r_2)|^2 \rangle \quad (3.7)$$

where  $T(r_1)$  and  $T(r_2)$  are the temperatures at position  $r_1$  and  $r_2$  respectively. Assuming isotropic and homogeneous turbulence,  $D_n$  and  $D_T$  follow the 2/3 Kolmogorov-Obukov law (see next section equation 3.10 ) and can be formulated as;

$$\begin{aligned} D_n &= C_n^2 r^{2/3} \\ D_T &= C_T^2 r^{2/3} \end{aligned} \quad (3.8)$$

With  $r$  is the vector position for  $r_1$  and  $r_2$ . The value of the refractive index structure coefficient  $C_n^2$  is mainly dependent on the thermal irregularities, and it can be expressed as;

$$C_n^2 = \left[ \frac{80 \cdot P(z)}{T^2(z)} \cdot 10^{-6} \right]^2 C_T^2 \quad (3.9)$$

where  $P(z)$  is the pressure (mb) and  $T(z)$  is the temperature at height  $z$ .  $C_n^2$  is generally regarded as a measure of the strength of the refraction index fluctuation

and is therefore the parameter needed to analyse the atmosphere turbulence and to parameterize the image degradation due to turbulence.

### 3.5.2 Kolmogorov-Obukhov "two third law".

Flows in the Earth's atmosphere with length scales of several meters to kilometers, and wind speeds of a few meters per second are almost always turbulent. The turbulent energy is generated by eddies on a large scale. The characteristic size  $L_0$  of this outer scale is still discussed and may be a few tens to hundreds of meters in most cases. The large-scale cells spawn a hierarchy of smaller cells (see Figure 3.1). While the dissipation of kinetic energy plays no role for large scale eddies, it becomes important in small scale eddies of a characteristic size  $l_0$ . This inner scale is of the order of a few millimeters. Kolmogorov and Obukhov developed a simple law ("2/3 law") on the assumption of isotropic and homogenous turbulence and this can be defined as;

$$D_n(r) = C_n^2 r^{2/3} \quad \text{for } l_0 \ll r \ll L_0 \quad (3.10)$$

where  $r$  is the distance between two points to determine the temperature structure constant  $C_T^2$ .  $C_n^2$  is the structure constant of the refractive index. The refractive index can be characterized by the spatial power density  $\Omega(k)$ , where  $k$  is a three dimensional wave vector. From the above two thirds law, it can be deduced that the associated power spectral density for the refractive index can be expressed by the Kolmogorov spectrum equation;

$$\Phi(k) = 0.0033 C_n^2(z) |k|^{-11/3} \quad \text{for } k_0 \ll k \ll k_l \quad (3.11)$$

where  $k$  is the wavenumber that is defined as  $2\pi/l$ , and  $l$  is the size of the turbulent eddies (eg. Small turbulent eddies corresponds to large spectrum wavenumber and large turbulent eddies corresponds with small spectrum wavenumbers). To perform a calculation of the Kolmogorov model it has to be assumed that the outer scale  $L_0$  is infinity and the inner scale  $l_0$  is negligible (range of millimeters). In the case of  $k > k_0$ , Tartaski suggested using a Gaussian function to truncate the

Kolmogorov spectrum and the power spectral density can be rewritten as;

$$\Phi_n(k) = 0.0033C_n^2(z)k^{-11/3}e^{-k^2/k_m^2} \text{ for } k_0 < k < \infty \quad (3.12)$$

where  $k_m = 5.92/l_0$ , the cutoff at high wavenumbers. In the von Karman spectrum, the inner scale effects can be neglected and the power spectrum equation can be expressed as;

$$\begin{aligned} \Phi_n(k) &= 0.0033C_n^2(z) (|k|^2 + |k_0|^2)^{-11/6} & 0 < k \ll 1/l_0 \\ \Phi_n(k) &= 0.0033C_n^2(z) (|k|^2 + |k_0|^2)^{-11/6} e^{(-k^2/k_m^2)} & 0 \leq k \leq \infty \quad k_m = 5.92/l_0 \end{aligned}$$

The wavenumber  $k_0$  has been defined by many authors with a discrepancy in the results, as for example Ishimaru (1978), Ellerbroek (1997) and Young, et al. (1998) define  $k_0$  as  $l < L_0$ , where  $L_0$  is the outerscale. But Kopeika (1998) and Clifford (1978) defined  $k_0$  as  $2\pi/L_0$ . When one is interested primarily in the phase of a wavefront that has propagated through turbulence (the usual situation in adaptive optics), then the outer scale  $L_0$  is usually of much greater significance than the inner scale  $l_0$ , in particular with respect to issues such as wavefront tilt. Figure 3.7 shows the Kolmogorov and the Von Karman spectrums with the inner and outer scale modifications.

The outerscale  $L_0$  for ORM has been studied by Abahamid (Abahamid et al.,2004) using the GSM instrument and they have determined a median outerscale of  $20m$ .

## 3.6 Effects of Optical Turbulence.

The previous sections have discussed the theoretical development of optical turbulence: where it comes from, and how it is measured. From the astronomical point of view the effects of optical turbulence on the light propagating from a star or on laser beam propagation are important to consider. A diffraction-limited optical system observing at wavelength  $\lambda$  has an angular resolution  $\theta_{res}$  corresponding to;

$$\theta_{res} = 1.22 \frac{\lambda}{D_T} \quad (3.13)$$

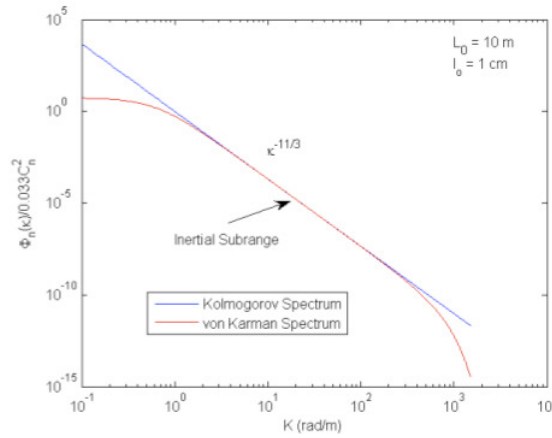


Figure 3.7: The Kolmogorov and Von Karman spectral model for the refractive index fluctuations. The inner scale of the turbulence is 1cm and the outer scale is 10m. The Kolmogorov is represented by the  $-11/3$  power law and the Von Karman roll-off in the border of the limits of the inertial range. Credit. Adapted from Andrews and Phillips, 2005.

where  $D_T$  is the telescope diameter and  $\lambda$  is the wavelength. In the real world the telescope aperture is in the presence of atmospheric turbulence and with a large aperture the image is turbulent-limited (also called "seeing-limited"), such that the angular resolution can be expressed as;

$$\theta_{res} = 0.98 \frac{\lambda}{r_0} \quad (3.14)$$

Where  $r_0$  is the turbulence coherence length (Fried parameter).

In the next section will be described parameters that can be measured and they are associated with the effects of the optical turbulence on light that is traveling through the atmosphere.

The passage of light through the atmosphere produces many effects that affect the image quality; these effects can include blurring or distortion of images produced by the deviation from a perfect spherical wave shape by errors in the incoming wavefront. The effects can be seeing during short or long exposures of the source, where using the proper optical elements to focus the image on a detector (CCD) the images at short exposure times will change in shape and form, and using long

exposures the images are blurred. Another important concept is the **Strehl ratio**. This ratio is a traditional criterion to measure the quality of the image given by the ratio of peak diffraction intensities of an aberrated vs. perfect wavefront (Airy disk). The ratio indicates the level of image quality in the presence of wavefront aberrations. It has a maximum value of 1 for an undistorted wavefront. The Strehl ratio is connected to a good approximation with the mean square phase error by the Marechal approximation (Born and Wolf,1970).

$$SR \approx e^{-(\sigma_\varphi^2)} \quad (3.15)$$

Where the mean square phase error is the variance of the wavefront by which the detected phase differs from an undistorted (plane) phase. Assuming that a plane phase would be 0, we calculate the mean square phase error by  $\langle \varphi^2 \rangle$ .

The Marechal criterion states that a system is regarded as well corrected if the Strehl ratio is greater than or equal to 0.8, which corresponds to a rms wavefront error  $\lambda/14$ .

Also the Strehl ratio can be defined by the optical transfer function (OTF) as;

$$SR = \frac{\int OTF_{distorted}(f_x, f_y)df_xdf_y}{\int OTF_{undistorted}(f_x, f_y)df_xdf_y} \quad (3.16)$$

where  $OTF(f_x, f_y)$  is the Fourier transform of the point spread function (PSF) of the image.

Applying the Strehl ratio to an Adaptive optics system, the Strehl ratio increases with the number of actuators following the relations; (Rodier et al,1991)

$$SR \approx e^{-\left(\frac{N_0}{N}\right)^{5/6}} \quad (3.17)$$

where  $N_0$  is the number of actuator that is needed to get a Strehl ratio of 1/e.

### 3.6.1 The optical parameters associated with the turbulence.

The effects of the atmospheric turbulence on a stellar wavefront traveling through the atmosphere have multiple parameters that are important to know and to char-

acterize like; the Fried parameter  $r_0(\lambda)$ , the spatial coherence outer scale  $L_0$ , the isoplanatic angle  $\theta_0(\lambda)$ , and the coherence time which determine the response time of the deformable mirror. The knowledge of these parameters are important to the optimization of high resolution imaging such as Adaptive Optics observing techniques (GLAO, MCAO, SCAO, ExAO, LTAO or MOAO)<sup>1</sup>

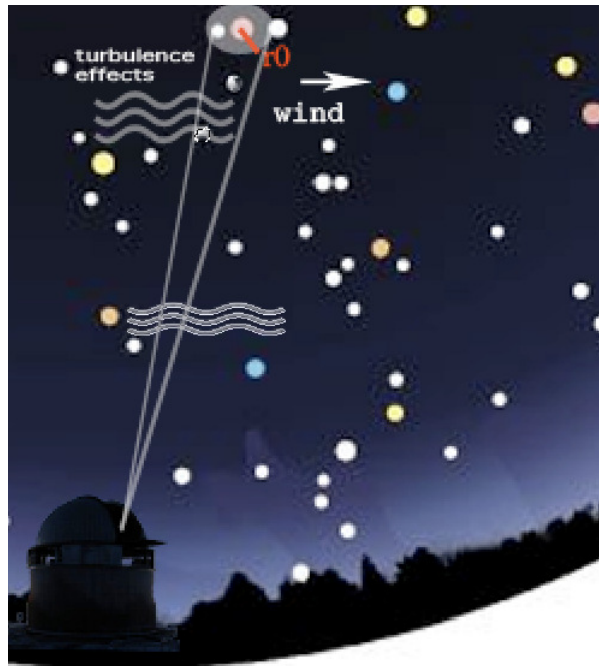


Figure 3.8: Depiction of the beam, propagating wave front, windspeed vector and the Fried coherence length  $r_0$ .

### Coherence length, $r_0$ .

Originally introduced by D. L. Fried (Fried, 1965),  $r_0$  can be defined as the diameter of the surface wavefront over which the deviation of phase fluctuations is equal to 1

---

<sup>1</sup>GLAO: Ground Layer Adaptive Optics.  
MCAO: Multi-Conjugated Adaptive Optics.  
SCAO: Single Conjugated Adaptive Optics.  
ExAO: Extreme Adaptive Optics.  
LTAO: Laser Tomography Adaptive Optics.  
MOAO: Multi Object Adaptive Optics.

radian. The parameter  $r_0$  is expressed in terms of the optical energy of turbulence characterized by the structure constant  $C_n^2(h)$  fluctuations of the refractive index of the air by the following equation (Roddiier, 1981):

$$r_0 = \left[ 0.423 \left( \frac{2\pi}{\lambda} \right)^2 \sec(\zeta) \int C_n^2(h) dh \right]^{-3/5} \quad (3.18)$$

where  $\zeta$  is the zenith angle of observation and  $\lambda$  the wavelength. In astronomy this parameter is associated with the "sky quality" value called *seeing* and determines the full width half maxima (FWHM) of the spot-image with the following mathematic expression,

$$\varepsilon = 0.98 \frac{\lambda}{r_0} \quad (3.19)$$

where  $\lambda$  is the wavelength ( $\mu m$ ) and  $r_0$  is the coherence Fried parameter. The parameter  $r_0$  is chromatic and varies as  $\lambda^{6/5}$ . This dependency leads to pupils that become entirely consistent in the infrared, even in the presence of turbulence:  $r_0 = 10cm$  at  $\lambda = 0.5\mu m$  leads to  $r_0 = 8.4m$  at  $\lambda = 20\mu m$ . It therefore follows that for a given diameter, a telescope will provide images closer to the diffraction limit in the infrared than in visible light. Also the equation of the coherence length equations 3.18 can be modified for the case of the laser propagation in the atmosphere where a weighting factor included to take into account the spherical traveling waves. Then the equation for  $r_0$  can be rewritten as; (Pike et al. 2011)

$$r_0 = \left[ \frac{2.905}{6.88} \left( \frac{2\pi}{\lambda} \right)^2 \int_R C_n^2(h) \left( \frac{R-h}{R} \right)^{5/3} dh \right]^{-3/5} \quad (3.20)$$

where  $C_n^2(h)$  is the index of refraction structure constant as a function of altitude ( $m^{-2/3}$ ),  $h$  is altitude (m) and  $R$  is the laser height (m).

The coherence length has a time evolution that can varies from seconds with rapid changes of the atmospheric turbulence to hours stable sky condition with weak atmospheric turbulence. There are some works by Racine and others which determine the time variation. (Racine 1996, Ziad et al 1999 and Vernin et al 1998).

**Isoplanatic angle,  $\theta_0$ .**

The Isoplanatic angle ( $\theta_0$ ) is defined as the maximum angle over which the phase difference between two stars is small and it is essentially identical (Klueckers et al., 1998) and it has been defined as: (Parenti and Sasiela, 1994)

$$\theta_0 = \left[ 2.9k^2 \sec^8/3(\zeta) \int C_n^2(h)h^{5/3}dh \right]^{-3/5} \quad (3.21)$$

where  $\zeta$  is the angle from the zenith,  $h$  is the height and  $k$  is defined as  $2\pi/\lambda$ . At the zenith equation 3.21 can be rewriting as; (Fried,1982)

$$\theta_0 = 2.91 \left( \frac{2\pi}{\lambda} \right)^2 \int_0^{H_{max}} C_n^2(h)h^{5/3}dh \quad (3.22)$$

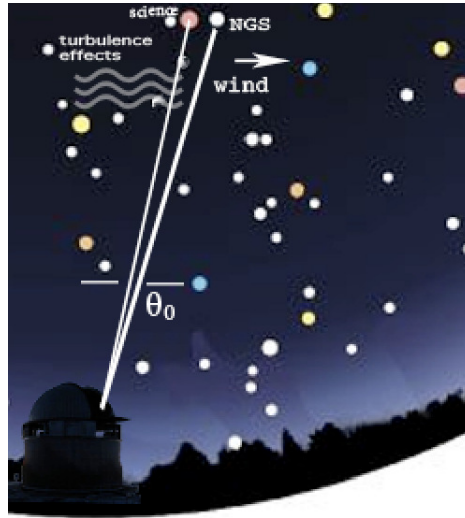


Figure 3.9: Isoplanatic angle ( $\theta_0$ ), angle in which the coherence length doesn't vary and two objects can be compensated with the same wavefront.

The isoplanatic angle ( $\theta_0$ ) is dependent on the altitude  $h^{5/3}$ , so a small isoplanatic angles indicates strong turbulence at high altitude and large values correspond to weaker turbulence at high altitude.

**Coherence time,  $\tau_0$** 

The coherence time  $\tau_0$  characterizes the time evolution of the wavefront deformation, that is the time over which the wavefront can be considered to be coherent. If we

are considering that the atmosphere has one turbulent layer that is moving with a speed  $V$ , the wavefront coherence time is the time it takes for the turbulent layer to move a distance  $r_0$ . But the atmosphere is more complicated and is formed from many turbulent layers moving at different speeds and directions, so the coherence time evolution depends on the distribution of atmospheric turbulence and especially on the wind (direction, speed). For an atmosphere with multiple layers, the average of the wind speed can be expressed as; (Roddier 1981).

$$\vec{V}_0 = \left[ \frac{C_n^2(h) |\vec{V}^{5/3}(h)| dh}{\int C_n^2(h) d(h)} \right]^{3/5} \quad (3.23)$$

where speed  $\vec{V}(h)$  is weighted by the energy in the turbulent layers  $C_n^2(h)$

Then, the coherence time can be expressed as a function of the vertical distribution and the refractive index parameter as;

$$\tau_0 = 0.057\lambda^{6/5} \left( \int_0^\infty V^{5/3}(h) C_n^2(h) dh \right)^{-3/5} \quad (3.24)$$

Also it can be represented in a simple equivalent expression as;

$$\tau_0 = 0.31 \frac{r_0}{V_0} \quad (3.25)$$

The implication of this parameter to an adaptive optics systems is that shorter  $\tau_0$  implies that the Adaptive optics systems has to work faster giving less time to analyse the wavefront and to send the commands to the deformable mirror (DM) with a resulting of a bad performance of the AO system.

### Greenwood frequency, $f_G$ .

The Greenwood frequency is a characteristic frequency for atmospheric temporal behavior experienced by the AO system. It can be regarded as a recommendation for the bandwidth that limits residual wavefront error to 1 rad. It does not mean that all the atmospheric turbulence moves at this frequency. The atmospheric turbulence is in a constant state of motion where big cells of air move slowly and little cells are moving fast. But this parameter can give a measure of how fast the adaptive optics

system must respond to correct the changing turbulence. The Greenwood frequency ( $f_G$ ) can be calculated with the following equation; (Tyson and Frazier, 2004)

$$f_G = 2.31\lambda^{-6/5} \left[ \sec\zeta \int C_n^2(h) V^{5/3}(h) dh \right]^{3/5} \quad (3.26)$$

where  $\zeta$  is the zenith angle,  $V(h)$  is the wind speed ( $ms^{-1}$ ), and  $h$  is the height (m). Also the Greenwood frequency can be written as;

$$f_G = 0.43 \frac{V_0}{r_0} \quad (3.27)$$

To understand the magnitude of each of the previously defined parameters the Table 3.3 summarizes the values for various ranges.

### 3.7 Optical Turbulence Models.

There are many varieties of optical turbulence models that have been utilized to model the refractive index ( $C_n^2(h)$ ) profiles from meteorological parameters. The models to predict  $C_n^2(h)$  from meteorological forecast values have become an issue of great interest in observatory time management. Sarazin (Sarazin,1997) discussed and proposed a queue observing mode for the VLT, where in good seeing conditions all the observing programs requiring high resolution using AO or interferometry can be triggered by it. Most recently, Businger (Businger, 2002) has proposed similar observing modes for the Manua Kea Observatory. So a model of predicted optical turbulence is playing a real role during observation preparation, and it also plays an important role in the site characterization of remote areas such as Antartica (Dome C) where Meso-scale models have been applied. (Lascaux, et al. 2009). Each model has its own unique set of input parameters and equations used to calculate  $C_n^2(h)$  parameters. Some models are very basic with minimal inputs and simple equations, while others are more involved and use complex mathematical calculations or utilize large databases of meteorological data to derive  $C_n^2(h)$  profiles (Fiorino, 2005b). Standard models are relatively simple ones that calculate optical turbulence using an analytical equation or set of equations. These models consist of one equation or a system of equations that are derived by fits to thermosonde or stellar scintillometer

data. There are only a few input parameters for these calculations, which include values such as altitude, pressure level, or sometimes wind speed. Instead of capturing all of the vertical fluctuations of  $C_n^2(h)$  within a given profile, standard models provide a smooth and generalized trendline. An example of this type of model, which is often used in atmosphere turbulence modeling is the Hufnagel-Valley 5/7 (next Section).

Alternatively, statistical models are purely mathematical representations of optical turbulence profiles. Within the bounds of observations and climatology, they produce physically realistic turbulence spectra using random number generation, Monte-Carlo, or other mathematical techniques. Realistically, optical turbulence profiles are not smooth functions with altitude, such as the standard models produce, but highly variable. Statistical models attempt to capture the fluctuations (Fiorino, 2005b).

Numerical models are similar to, but more complicated, than the standard model because they use additional meteorological inputs, such as temperature, time-of-day, and humidity to produce optical turbulence profiles. They are called numerical models because they obtain their necessary inputs from the output of physically-based numerical weather prediction models or from physically collected data.

### 3.7.1 Hufnagel-Valley 5/7.

In 1974 Hufnagel developed a model on the basis of stellar scintillations and thermometer measurements. He attempted to correlate the scintillation spectrum with meteorological wind parameters such as the peak wind speed at the tropopause, the speed at significant inversions layers and the speed at low Richardson's number. Like all models, it had several limitations. It has been only valid at mid-latitude locations from 3km to 24km above the surface. Due to the complexity of the computations involved and uncertainty in the input parameters, only a mean value of  $C_n^2(h)$  could be calculated. Later P. B. Ulrich in 1988, following the suggestions of G. C. Valley, extended the model from 3 km down to the surface. The most popular version of this model is called the *Hufnagel-Valley 5/7 (HV 5/7)* model because the input parameters yield  $C_n^2(h)$  profiles such that the coherence length is 5 cm and

the isoplanatic angle is  $7\mu rad$  for an Earth to space path (Good et al. 1988). Since the profile varies from site to site and from time to time this model can only give a rough idea of the layer structure. The structure constant can be modeled using the following formula:

$$C_n^2(h) = 2.2 \cdot 10^{-23} h^{10} e^{-h} + 10^{-16} e^{-h/1.5} + 1.7 \cdot 10^{-14} e^{-h/0.1} \quad (3.28)$$

and using the weighted wind component to improve the model accuracy the Hufnagel-Valley equation can be expressed as;

$$C_n^2(h) = \left[ 5.94 \cdot 10^{-53} h^{10} \left( \frac{W}{27} \right)^2 e^{-h/1000} + 2.7 \cdot 10^{-16} e^{-h/1500} + A e^{-h/100} \right] \quad (3.29)$$

where  $A$  is the surface  $C_n^2(h)$  value with a default value of  $1.7e^{-14}$  ( $m^{-2/3}$ ),  $h$  is the altitude in meters, and  $W$  is the root mean square wind speed ( $ms^{-1}$ ). In recent studies of the Hufnagel-Valley model applied to the Canary Islands (Chueca et al, 2004) has used a "modified" Hufnagel-Valley equation to model the  $C_n^2(h)$  profiles above the Canarian observatories (Teide and Roque de Los Muchachos Observatorio). This work has included a correlation of the  $C_n^2(h)$  measurements obtained by the SCIDAR instrument. The "modified" H-V model has the following expression;

$$C_n^2(h) = B \left[ 3.11 \cdot 10^{-56} h^{10} w^2 e^{-h/1000} + 10^{-16} e^{-h/1500} \right] + A e^{-h/100} \quad (3.30)$$

where  $w^2$  is the pseudo wind-speed,  $B$  is the models of the fine structure of the turbulence and  $A$  is the scale factor for surface turbulence. At a high-altitude observing site, such as the Canarian observatories (2400 meters asl), it is found that turbulence is weak. Then, a good approximation is taking  $B=1$ . The pseudo wind-speed  $w^2$  is the high-level turbulence speed which is evaluated by;

$$w^2 = \frac{1}{15} \int_5^{25} v^2(h) dh \quad (3.31)$$

where  $v(h)$  is the wind speed at elevation  $h$ . The factor  $1/15$  is in kilometers. The integral is measured from 5 km to 25 km.

The Figure 3.10 shows an example of the H-V 5/7 model applied to the data obtained from the Tenerife radiosonde. Two peaks are visible: one at the ground and another one about 10km; the atmosphere is stable above 15 km. The model shows two clear maxima which can vary depending of periods of the year (summer or winter) and also can change from one to year to another year.

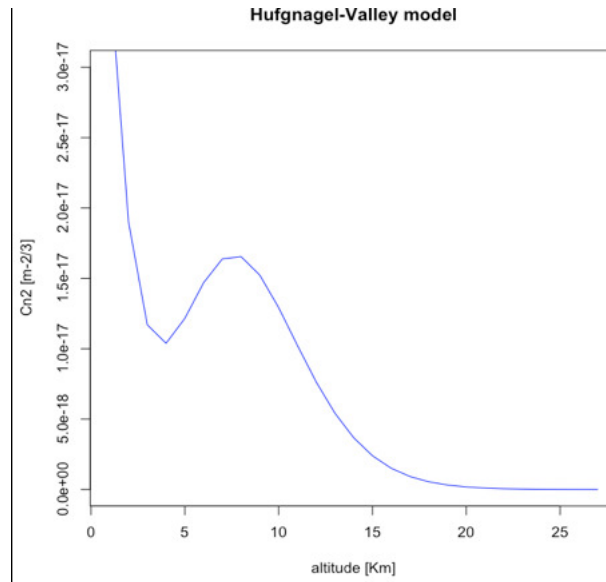


Figure 3.10: A vertical Huffnagel-Valley HV5/7 profile is represented with the wind speed data obtained from the Tenerife radiosonde and the median wind speed in the first 15 kilometers.

### 3.7.2 Dewan Free Atmosphere Model.

The Dewan Optical turbulence model (Dewan et al, 1993) was developed with the main purpose of using standard radiosonde data to derive the  $C_n^2(h)$  profiles. This synoptic model is based on the Tatarski (Tatarski,1961) free atmosphere turbulence model, which can be applied to the optical turbulence defined as the refractive turbulence index  $C_n^2(h)$

$$C_n^2(h) = 2.8 \left[ \frac{80 \cdot 10^{-6} P}{T^2} \right] L_0^{4/3} \left( \frac{\partial T}{\partial z} + \gamma \right)^2 \quad (3.32)$$

where  $P$  is the pressure (mb),  $T$  is the temperature (Kelvin),  $\gamma$  is the adiabatic lapse rate equal to  $9.810^{-3} \text{ Km}^{-1}$  and  $z$  is the height in meters. All these vari-

ables are easily obtained from the radiosonde data or by forecasting models such as GFS.<sup>2</sup> The variable  $L_0$  is referred to by Tatarski (1961) as the outer scale length. Dewan used the Tatarski relationship for  $C_n^2(h)$  using statistical relationships for  $L_0$  developed as a function of wind shear using the studies in smoke trails profiles. The relationship obtained for  $L_0$  is specific to the troposphere and the stratosphere (Dewan et al.,1994).

$$\begin{aligned} L_0^{4/3} &= 0.1^{4/3} \cdot 10^{(1.64+42 \cdot S)} && \text{troposphere} \\ L_0^{4/3} &= 0.1^{4/3} \cdot 10^{(0.56+50 \cdot S)} && \text{stratosphere} \end{aligned}$$

Where  $L_0$  is measured in meters and  $S$  is the wind shear modulus which is defined as;

$$S = \left[ \left( \frac{\partial u}{\partial z} \right)^2 + \left( \frac{\partial v}{\partial z} \right)^2 \right]^{1/2} \quad (3.33)$$

where  $u$  is the wind speed at direction North to South and  $v$  is the wind speed at direction East to West.

### 3.7.3 Trinquet and Vernin, a parametric model.

Trinquet (Trinquet and Vernin, 2006) and collaborators have developed a simple model based on mesoscale meteorological data with the main contribution from the gradient of the potential temperature ( $\theta$ ) and a set of fixed parameters obtained from the statistical analysis of radiosonde profiles obtained from different locations on the Earth.

The model is built from the correlation between the  $C_n^2(h)$  and macroscopic mean profiles of the horizontal wind-speed component and temperature with a vertical resolution of 100m to 1km. The parametric model (AXP) is initialized using global data provided by meteorological agencies complemented by local measurements.

---

<sup>2</sup>GFS: General Forecast System which is a numerical weather prediction model developed by NOAA. This can give 7 days forecast with a low spatial resolution and temporal resolution

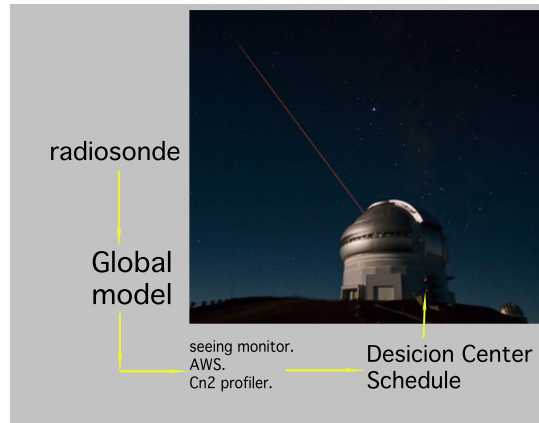


Figure 3.11: Diagram showing the forecasting scheme, with the optical turbulence monitor (seeing or  $C_n^2(h)$  profiler) passing information from the local weather stations (pressure, temperature, humidity and wind speed) to the forecasting layer where the results go to the decision center where the observational program can be adjusted depending on "forecasted" sky quality. Credit: Adapted from Trinquet, 2008.

The structure function of the temperature fluctuation  $C_t^2(h)$  is assumed to follow a median value corrected by the gradient of the mean potential temperature ( $\theta$ ). Then the  $C_t^2(h)$  can be expressed as;

$$C_T^2(h) = \langle C_T^2(h) \rangle \left[ A(h) \frac{d\bar{\theta}}{dh} \right]^{p(h)} \quad (3.34)$$

Where the parameters  $A$  and  $p$  are functions of the altitude  $h$  and they are retrieved from the statistical analysis of radiosonde observations. Table 3.4 shows the coefficients for the parameters  $A(h)$ ,  $p(h)$  and  $C_t^2(h)$  with a spacing of 1km up to 30 km. The refractive index structure constant  $C_n^2(h)$  is determined from equation 3.9 and the vertical profiles can be reconstructed for any region worldwide where the vertical profiles for the potential temperature, pressure and temperature are known.

This model Trinquet and Vernin has showed an accuracy of the 58% with an error  $\pm 30\%$  from observations. This gives the capability to use forecast meteorological data to build local optical turbulence profiles providing predictions for the seeing, altitude, and intensity of the main optical turbulence (OT) producing layers profiles.

heightPres [hPa]	Height [m]	Temp [C]	Pot.temp $\theta$ [K]	$\Delta\theta/\Delta z$	$\theta_2 - \theta_1$ [K]	Critical Inversion
700	3246	14.0	318.38	0.001	0.579	
631	4106	6.1	318.95	0.001	0.168	
615	4319	4.2	319.12	0.003	1.180	
break	....	.....	.....	.....	.....	.....
200	12420	-54.1	347.65	0.003	0.876	
192	12681	-56.1	348.53	0.009	0.563	
190	12746	-56.4	349.09	0.008	4.112	***
174	13294	-59.3	353.20	0.008	4.016	***
160	13818	-62.0	357.22	0.008	1.877	
154	14056	-63.2	359.09	0.007	1.165	
150	14220	-64.1	360.26	0.009	1.947	
145	14427	-65.0	362.21	0.010	5.321	***
133	14953	-67.1	367.53	0.013	1.238	
131	15045	-67.3	368.76	0.014	1.911	
128	15185	-67.6	370.68	0.014	1.312	
126	15280	-67.8	371.99	0.013	3.943	***
120	15574	-68.5	375.93	0.018	4.604	***
115	15830	-68.5	380.53	0.018	11.101	***
104	16434	-68.5	391.64	0.019	4.418	***
100	16670	-68.5	396.05	0.005	1.133	
96	16913	-70.3	397.19	0.006	0.796	
93.7	17057	-71.3	397.98	0.027	1.249	
93	17103	-71.1	399.23	0.027	7.049	***
89	17367	-70.1	406.28	0.027	7.402	***
85	17643	-69.1	413.68	0.028	16.442	***
77	18237	-66.9	430.12	0.029	9.149	***

Table 3.2: Portion of the output file from a radiosonde data set (4<sup>th</sup> on July 2008) and choosing the temperature, pressure and height to retrieve for calculating the potential temperature and the gradients and the differential vertical values. Looking for each height where the Heffter criterion is fulfilled a new column is built indicating that a critical inversion is developing (shown as symbol \*\*\*).

$\lambda$	Fried $r_0$	Wind speed	Coherence time	Greenwood freq.
$0.5 \mu m$	10 cm	$20 \text{ m s}^{-1}$	5 msec	40 Hz
$2 \mu m$	53 cm	$20 \text{ m s}^{-1}$	265 msec	16 Hz
$10 \mu m$	36 m	$20 \text{ m s}^{-1}$	1.8 sec	0.2Hz

Table 3.3: This shows how the magnitudes for the Fried coherence length, wind speed and coherence time and the Greenwood frequency.

Altitude(Km)	P(h)	A(h)	$\langle C_t^2(h) \rangle$
Boundary	0.5	1.6E+2	NA
1 to 2	0.3	1.8E+2	5.2E-5
2 to 3	1.3	5.6E+2	4.2E-5
3 to 4	1.7	4.6E+2	2.8E-5
4 to 5	1.7	3.8E+2	2.5E-5
5 to 6	2.6	2.6E+2	1.8E-5
6 to 7	1.1	4.6E+2	1.5E-5
7 to 9	0.8	6.8E+2	1.6E-5
8 to 9	0.6	1.0E+3	1.6E-5
9 to 10	0.3	2.2E+3	1.9E-5
10 to 11	0.5	6.8E+2	2.6E-5
11 to 12	0.7	3.2E+2	3.4E-5
12 to 13	0.6	2.2E+2	4.4E-5
13 to 14	0.1	8.3E+3	4.8E-5
14 to 15	0.2	1.0E+3	5.5E-5
15 to 16	-0.4	3.2E+1	6.5E-5
16 to 17	-0.3	1.5E+1	8.3E-5
17 to 18	2.5	5.6E+1	1.1E-4
18 to 19	-0.9	2.6E+1	1.1E-4
19 to 20	3.3	3.8E+1	9.5E-5
20 to 21	-1	2.6E+1	8.2E-5
21 to 22	1.5	4.6E+1	7.4E-5
22 to 23	-1.9	3.2E+1	7.5E-5
23 to 24	1.3	4.6E+1	8.7E-5
24 to 25	1.1	4.6E+1	1.1E-4
25 to 26	1.5	3.8E+1	1.3E-4
26 to 27	1.1	3.8E+1	1.7E-4
27 to 28	2.2	3.2E+1	2.4E-4
28 to 29	1.8	3.2E+1	3.0E-4
29 to 30	0.2	1.2E+1	5.1E-4

Table 3.4: Coefficients used in the AXP model. The altitude is measured in kilometers and the vertical resolution is one kilometer. Where  $P(h)$  and  $A(h)$  are coefficients,  $C_t^2(h)$  is the temperature coefficient index.

# Chapter 4

## Sensing the Atmospheric Turbulence

*"The difference is as great between the optics seeing  
as the object seen."*

*Alexander Pope.*

---

### 4.1 Overview.

Optical Turbulence (OT) acts to distort light in the atmosphere, degrading images from large astronomical telescopes and reducing the data quality of astronomical images and in laser communication links. Some of the degradation due to turbulence can be corrected by adaptive optics. However, the severity of optical turbulence, and thus the amount of correction required is largely dependent upon the location of the observatory. Therefore, it is vital to understand the climatology of optical turbulence at such locations. In many cases, it is impractical and expensive to setup instrumentation to characterize the climatology of optical turbulence, so a less expensive system would be a convenient alternative.

The importance of understanding the atmospheric turbulence behavior and the necessities of real time measurements have meant that remote sensing techniques have emerged as a new research area that has been a useful tool to characterize the optical turbulence. These remote sensing techniques range from the launch of

radiosonde balloons, the use of radar or acoustics instruments, or the use of optical systems like the LIDAR, SCIDAR, SLODAR or even the MASS-DIMM.

Such remote sensing techniques have been used to characterize the local atmosphere turbulence for future observatory sites such as the E-ELT or TMT. And it is an important tool in the design of the future Adaptive optics instrument.

This Chapter provides an introduction to the different instruments (from radiosonde to MASS-DIMM) used to profile the atmosphere turbulence and to retrieve the refractive index constant  $C_n^2(h)$  and the astroclimate parameters (seeing, isoplanatic angle and coherence time).

## 4.2 The $C_n^2$ profile.

A thorough description of the astronomical seeing at an observatory is given by producing a profile of the turbulence strength as a function of the altitude called the refraction constant index of turbulence  $C_n^2(h)$  (Section 3.5). Coulman (Coulman, et al., 1995) have shown by in situ measurements that the energy of optical turbulence in the interaction between different layers in a dynamic turbulent process can be from thin layers (ten meters) to large eddies (hundreds of meters). An example of a profile is shown in Figure 4.1, which corresponds to an observation at the Roque de Los Muchachos Observatory (La Palma). Some of the most common methods to get vertical profiles of  $C_n^2(h)$  using an optical approach are; MASS, SLODAR or SCIDAR among other instruments.

### 4.2.1 In situ profiles (rawinsondes).

Despite the advance in technology toward developing remote sensing devices for probing the atmosphere, the rawinsonde is still the standard and most widely distributed tool to determine the atmospheric boundary layer (ABL) structure (Seibert et al, 2000). Rawinsondes in the Canary Islands are launched in Guimar (30 m ASL, WMO 60018) at two specified synoptic times (00:00 and 12:00 UTC). The ascent rate of the sonde is  $5 \text{ m s}^{-1}$ ; accordingly the transmitted signal received from the sonde represents a 50 m layer as averaged over a period of 10 seconds. The accuracy

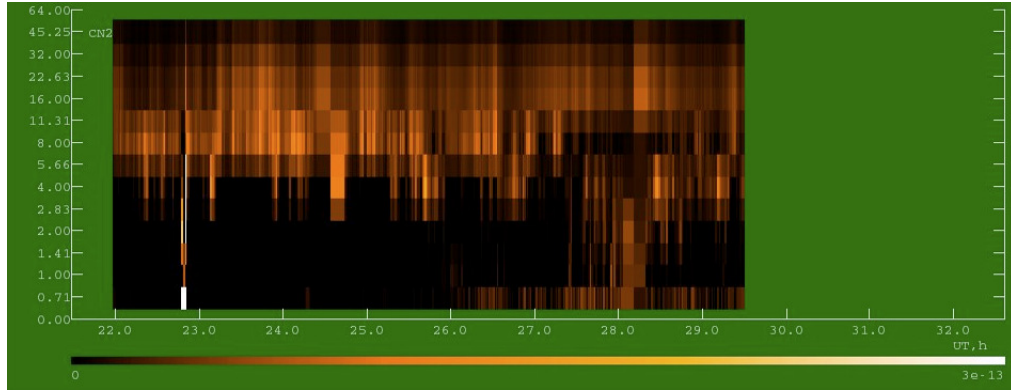


Figure 4.1: Example of a  $C_n^2(h)$  profile measured by a MASS-DIMM instrument at Roque de los Muchachos Observatory during the night of the 6<sup>th</sup> on May 2009. The white stripe corresponds to wrong data acquisition. It shows strong turbulence at the higher layer of the atmosphere above 4km during the whole night.

of the dry temperature measurement is 0.5 K. The shortcoming of this routine is the slanted atmospheric profile obtained while ascending, especially during strong winds, which however is not the case for summer conditions in the Canary Islands. Thermosondes are balloon-borne instrument packages that measure in-situ the temperature structure constant  $C_t^2(h)$ . An image of a thermosonde is shown in Figure 4.2. This instrumentation consists of probes at the ends of a 1m long styrofoam boom. The changing resistance of a thin wire between them is used to calculate the root mean square temperature fluctuations using (Roadcap and Murphy 1999), the temperature structure constant can be expressed as;

$$C_t^2(h) = \left[ \frac{(T(r_1) - T(r_2))^2}{r^{2/3}} \right] \quad (4.1)$$

where  $r$  is the distance between the two thermal sensors  $|r_2 - r_1|$ (meters),  $T(r_1)$  and  $T(r_2)$  are the temperatures at  $r_1$  and  $r_2$  measured in (C) respectively. The temperature structure constant is vertically measured every seven to eight meters, beginning from the surface to an altitude of 30 km above sea level. The thermosonde relays the temperature information to a ground station, which then calculates  $C_n^2(h)$  as a function of altitude using the equation (Section 3.7),

$$C_n^2 = C_t^2 \left[ 79 \cdot 10^{-6} \frac{P}{T^2} \right]^2 \quad (4.2)$$



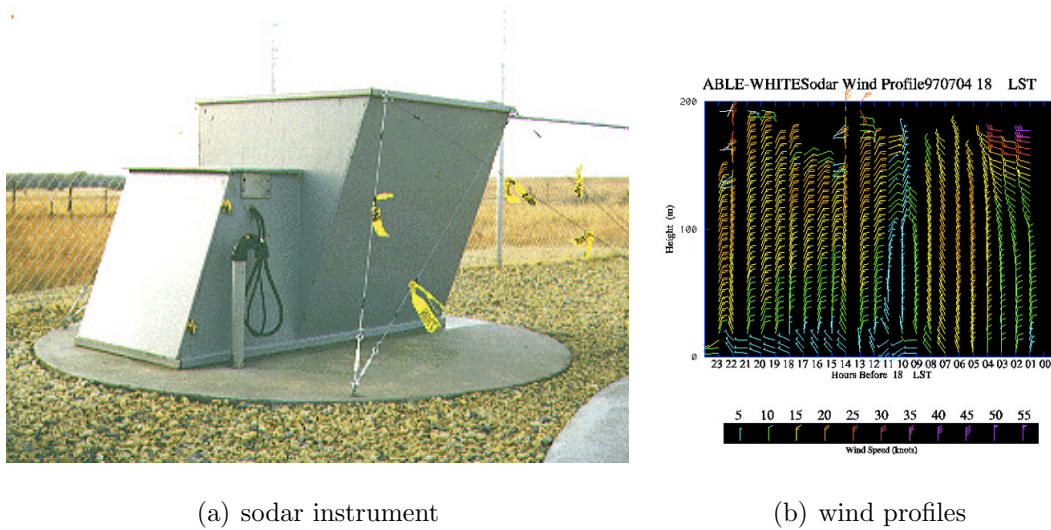
Figure 4.2: Photograph of a thermosonde and the boom. The boom is located about 10 meters below to avoid disturbances from the balloon.

### 4.3 Remote soundings (Sodar, RASS and profiler).

Among the remote sensing empirical methods for measuring the atmosphere boundary layer (ABL) parameters and especially mixing-layer height (MLH), the acoustic sounder (SODAR) is the most widespread instrument (Beyrich, 1997), it works in a similar manner to the Profiler/RASS system<sup>1</sup>. They send out acoustic waves and measure it's Doppler shifted frequency to determine the three dimensional wind field in the lower atmosphere (up to 300 meters). This is an interesting instrument to measure the surface layers with a high vertical resolution. The Figure 4.3 shows a SODAR instrument and an example of the wind velocity data.

---

<sup>1</sup>Radio Acoustic Sound System; is a system for measuring the atmospheric lapse rate using backscattering of radio waves from an acoustic wave front to measure the speed of sound at various heights above the ground.



(a) sodar instrument

(b) wind profiles

Figure 4.3: Sodar instrument and the output image of the vertical profile of the wind speed strength. Credit NOAA.

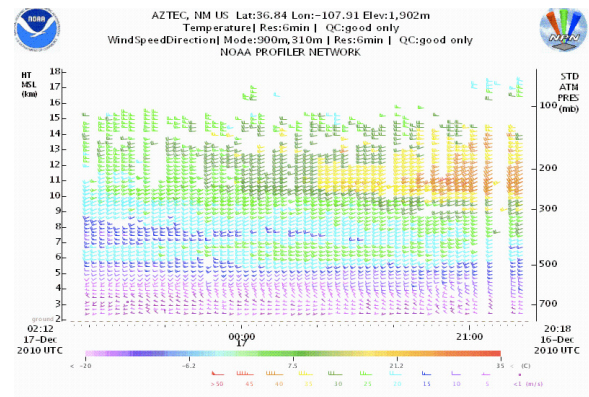
### 4.3.1 Sodar instrument for a vertical profiling of the wind speed.

The RASS (Radio Acoustic Sounding System) are usually collocated with a profiler and are used in conjunction with the profiler to provide virtual temperature profiles ( $T_v$ ) generally from 0.1-2.5 km above the surface. The RASS unit sends out an acoustic (sound) wave in the vertical direction and the propagation speed of the acoustic wave depends on the temperature and moisture composition of the atmosphere. The speed of the acoustic wave is related to the virtual temperature by the relationship;  $C_a = 20.47(T_v)^{1/2}$ . The profiler then sends out its own pulse which backscatters off of the RASS acoustic wave. It measures the Doppler shifted frequency of the acoustic wave, thus one can obtain  $C_a$  from the Doppler shifted frequency. The RASS measurements of the vertical profile of  $T_v$  are generally reported every hour, though it only takes a few minutes to obtain the measurements. An example of a RASS is showed in the figure 4.4.

The profiler determines wind speed and direction by measuring the distance to a target from one pulse and the change in that distance from successive pulses. Actually, what is really measured is a change in the phase of the returned signal (i.e., fraction of a wavelength) between pulses (Weber, et al. 1993). The profiler detects



(a) sodar instrument



(b) wind profiles

Figure 4.4: RASS instrument on the left and a vertical plot of the wind speed and the temperature measured in Aztec station. Credit. NOAA. [[http : //profiler.noaa.gov/npn/profiler.jsp](http://profiler.noaa.gov/npn/profiler.jsp)]

these changes and translates them into wind velocity data. To measure the three dimensional winds, the antenna is electronically switched from the northward, vertical and eastward pointing beams. Each beam requires 2 minutes for data collection, one minute for each mode. Thus, a total of 6 minutes is required to complete data collection for one vertical profile of the horizontal and vertical winds. Horizontal winds are derived from the data collected in each of the three beams in a manner similar to the dual-Doppler technique. Figure 4.5 shows a schema of the profiler instrument.

## 4.4 Optical remote sensing (DIMM, SCIDAR, SLODAR and MASS-DIMM).

Optical instruments to measure the optical turbulence during the night allow one to obtain measurements of the temporal behavior of the optical turbulence and wind speed and its vertical distribution within a reasonably short time (about 5 minutes per profile). The four instruments described briefly below have been used in many site characterization campaigns and most recently they have been used for support of AO observations (e.g. GLAS@WHT during the AO nights). This thesis does

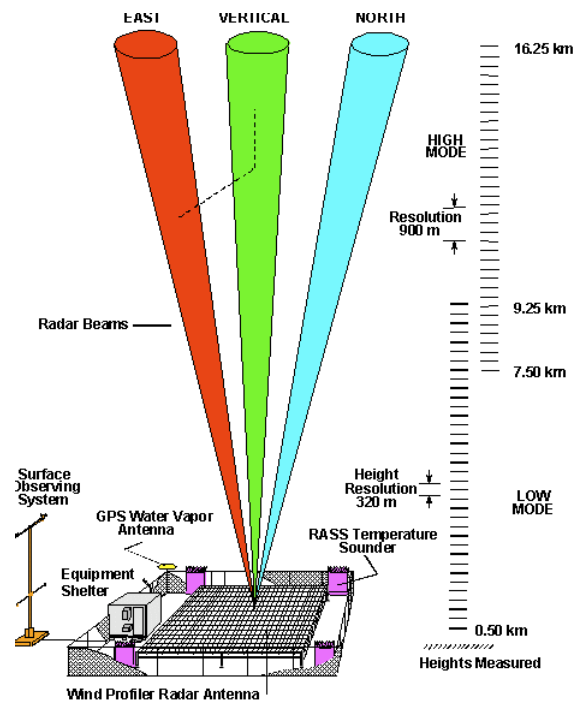


Figure 4.5: Schema of a profiler instrument operations. Credit. NOAA.

not involve the development of these techniques, but it will profit from the data collected from one of these techniques: the MASS-DIMM sited at La Palma. A general description of the four popular turbulence monitors follows.

#### 4.4.1 Differential Image Motion Monitor. DIMM.

The Differential Image Motion Monitor has been extensively used to characterize the atmosphere turbulence, and it has been extended to many astronomical observatories worldwide as an instrument to support observations and to quantify quality of the night observations with the common words "good seeing night", or a "bad seeing night". For a good observatory like Observatorio Roque de Los Muchachos, with a median seeing around 0.8 arcseconds, every observation below this parameter will be considered a good seeing night. Figure 4.6 shows the DIMM monitor operated by the ING actually running in the Roque los Muchachos. A description of the DIMM and its algorithm is provided in the following subsections.



(a) dimm instrument



(b) tower

Figure 4.6: DIMM monitor at the ORM. The instrument is installed in a platform at 5 meters above the ground and located in Northerly direction from the WHT.

#### **Instrument description and algorithm.**

Schematically, the instrument is composed of a small telescope (typically between 35 and 40 cm) observing a single bright star. At the entrance pupil, the starlight passes through a mask having two holes of diameter  $D$  separated at distance  $d$  (Hartmann apertures), which are symmetric with respect to the center of the pupil, in order to obtain dual star images (spots) whose relative motion in the image plane represents local wavefront tilts. The re-imaging of the entrance pupil is obtained by a collimator and a prism in the image plane introducing a symmetrical tilt in the direction parallel to the separation of the holes (Sarazin and Roddier 1990). A schematic example is shown in Figure 4.7.

The light from a single star illuminates each sub-aperture with a different column of air in front of which the turbulence induces phase fluctuations. These phase fluctuations, in turn, produce random motion for each sub-image. While the telescope vibrations affect each image in the same manner, the existing turbulence induces random differential motions in the sub-images. Thus, variations in the image separations can be used for obtaining a quantitative estimate of the turbulence. In the Kolmogorov turbulence scenario at the near field approximation, the longitudinal and transversal (in the direction of the prism tilt) values for the seeing (FWHM) are calculated from the longitudinal and transversal covariance of the spot separation

measured in the image plane. The total seeing estimation is the average of the longitudinal and transversal seeing. Since the method is differential, it is not affected by vibrations of the telescope, shaking due to wind, or tracking errors.

The calculated seeing represents the total turbulence energy ( $C_n^2(h)$ ) in the column of atmosphere observed by the DIMM corrected to airmass 1.

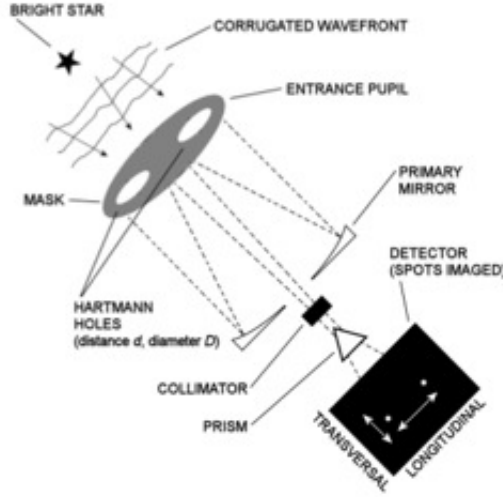


Figure 4.7: Schematic diagram of the DIMM instrument. Simple instrument based on a telescope with a mask in the entrance pupil with two holes with one prism and a detector where the star is splitted in two spots. Credit. Image adapted from Sarazin and Roddier, 1990

Following the Tatarski spectrum of wavefront phase fluctuations, where the variance of the differential image motion in the direction longitudinal and transversal across 2 sub-apertures can be defined as;

$$\sigma_t^2 = 2\lambda r_0^{-5/3} (0.179d^{-1/3} - 0.145r^{-1/3}) \quad (4.3)$$

$$\sigma_l^2 = 2\lambda r_0^{-5/3} (0.179d^{-1/3} - 0.0968r^{-1/3}) \quad (4.4)$$

where  $\sigma_l^2$  and  $\sigma_t^2$  are respectively the longitudinal and transverse variance of the distance between the two images centroids. The  $d$  is the sub-aperture diameter,  $r_0$  is the Fried parameter and  $r$  is the subaperture separation.

#### 4.4.2 SCIDAR.

The SCIDAR (Scintillation Detection and Ranging) technique allows one to measure the strength of the optical turbulence ( $C_n^2(h)$ ), as well as the velocity of the turbulent layers as a function of the height and time. This technique is based on the variance of the scintillation produced by turbulent layers on the light from a binary system. Since the technique was first proposed (Azouit and Vernin 1980, Vernin and Azouit 1983) it has been improved thanks to the work led by Jean Vernin and related teams. The SCIDAR technique studies the scintillation patterns produced by atmospheric turbulence in the light from the two stars of a binary system on the pupil of the telescope, to determine the vertical structure of turbulence and velocity of the turbulent layers as function of the height.

The methodology of this technique is to obtain a high number of instantaneous scintillation patterns (1 to 3 milliseconds) with a telescope with an aperture greater than 1.5 meters. The atmospheric turbulence profiles are derived from the average autocorrelation functions of scintillation patterns, while the velocities of the turbulent layers are related to the correlations obtained from a series of patterns. Considering a simple case of a turbulent layer located at a height  $H$  and observing a binary system separated an angle  $\theta$  in the sky, the result is to have two identical but phase-shifted scintillation patterns on the detector. Calculating the autocorrelation of those scintillation patterns the result is a triple point with one central peak and two separated smaller lateral peaks. The amplitude of the lateral peaks is proportional to the strength of the turbulence, and the distance between the central peak and the lateral is used to calculate the height of the turbulent layer. This simple situation can be generalized to the case where we have several turbulent layers where a number of triplets are associated with a particular height (see Figure 4.9). This technique requires an 1.5 meter telescope to monitor the atmosphere turbulence up to 20 km, otherwise the scintillation pattern from the higher layers will go off the telescope pupil depending on the binary star separation.

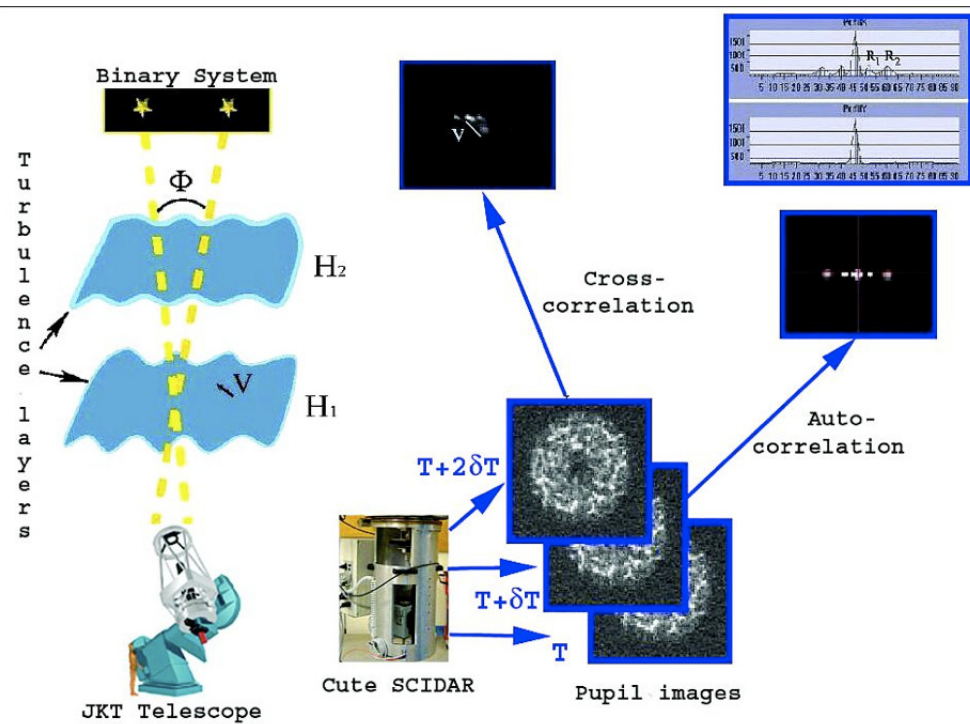
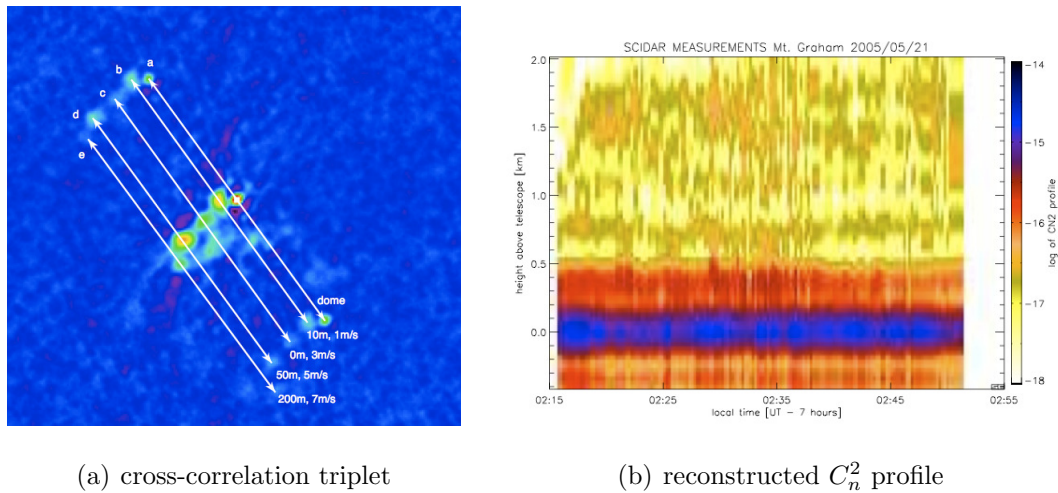


Figure 4.8: Scheme of the SCIDAR technique layout. From the observation of binary stars, it obtains a stack of consecutive images of scintillation. The average auto-correlation function of them gives information about the  $C_n^2(h)$  profiles, and average cross-correlation functions give the wind speed of the layers. Credit: Fuensalida et al, 2004

The classical SCIDAR technique has been running over many years, but this technique has been carry a problem that it cannot measure the turbulence in the lower layers near the telescope. To resolve this problem Generalized SCIDAR (G-SCIDAR) was proposed (Fuch et al, 1998) where the detector plane is conjugated below the ground allowing to resolve ground layer turbulence and even the telescope dome contribution

The Instituto de Astrofísica de Canarias (IAC) (Fuensalida et al, 2004b) has developed SCIDAR instrument which has been running permanently in the Jakobus Kapteyn Telescope (JKT) at the ORM since 2004. Figure 4.8 shows the scheme of the SCIDAR mounted at the JKT. The figure 4.10 and 4.11 shows the statistics (average and median) of a set of observations during the year 2004. In the statistical



(a) cross-correlation triplet

(b) reconstructed  $C_n^2$  profile

Figure 4.9: Figure of SCIDAR measurements acquire. (a) Cross-correlation of scintillation images for the detected triplets, the retrieved height above the telescope and the winds speeds are indicated. The uncertainty in the height of the single layers is around 25 meters. (b) Graphical display of the real time profile determined from the autocorrelation using a wide binary of separation 35 arcsec the maximum attainable height above the telescope is limited to around 2 km, and the vertical resolution is around 200 meters. Credit. LBT-SCIDAR Egner, et al,2007.

profiles shown in this figures it is easy to identify that the turbulence is concentrated in a layer near the ground level while only a few traces of other layers are located at 2.5 and 10.6 km above the observatory. The IAC group has been led to the conclusion that the temporal evolution of the monthly profiles at the ORM generally found that more than half of the turbulence is concentrated in layers closest to the ground, especially during the winter months. The figure (figure 4.11left) shows the profiles for March. In summer the well-stratified turbulence appears in two or three levels, ground level 2, 5 and 12.6km as shown in figure 4.11right, in which is presented the average profile for the month of July (year 2004). This layer distribution is favorable to the use of Ground Layer correcting systems, such as GLAO. This technique is important to establish the development of future AO instruments to be installed at the ORM.

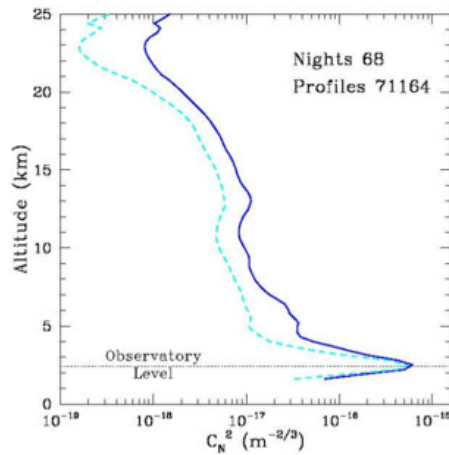


Figure 4.10: Average and median turbulence profile  $C_n^2$  of a set of 68 observations during the year 2004 at the ORM. Credit. Fuensalida et al. 2004.

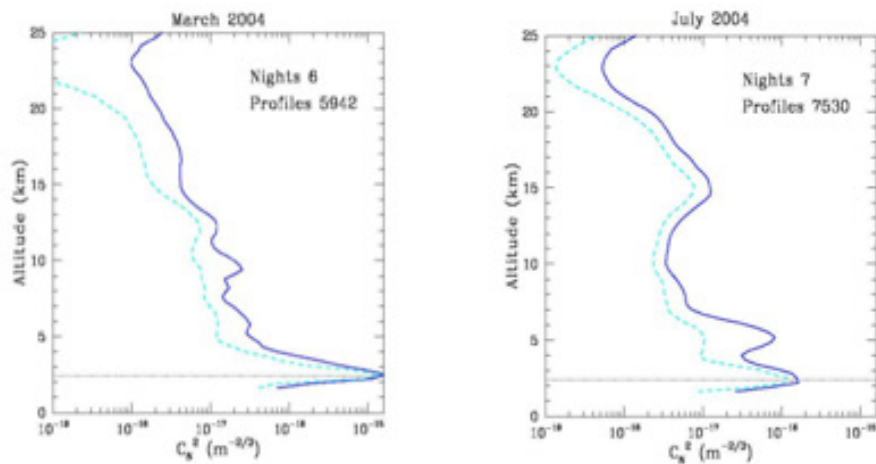


Figure 4.11: Statistical  $C_n^2(h)$  profiles for a set of observations with G-SCIDAR at the ORM. (Blue line average, dashed blue line median). The number of nights is indicated in the plot. Right image observations during July. Left image observations during March. Credit. Fuensalida et al, 2004.

#### 4.4.3 SLODAR.

Slope Ranging Detection and Ranging (Wilson, 2002) is a method for measurement of the strength, altitude and motion of the atmospheric turbulence that results in astronomical seeing. The main applications of the technique are in astronomical

site characterization and for real-time optimization of observations with adaptive optical image correction. The technique was developed by the Center of Advanced Instrumentation (CfAI) in Durham and first tested at the William Herschel telescope at the ORM, La Palma. The system has been advanced to a dedicated SLODAR seeing and turbulence monitor based on small telescopes (aperture 45 cm) and the new EMCCD (with zero read noise) and its portability has been a good characteristic to place the slodar systems in many observatories such as the European Southern Observatory at the Cerro Paranal observatory in Chile, in Manua Kea Observatory Hawaii and at the SALT Observatory in South Africa.

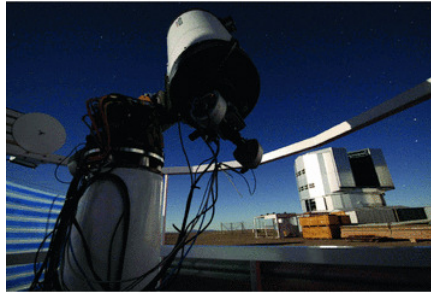


Figure 4.12: Portable SLODAR mounted at Paranal Observatory beside of the VLT. Credit. ESO

SLODAR works similar to SCIDAR measuring the local gradients of the phase aberration using a Shack-Hartmann as wavefront sensor. A double star is observed with a separation  $\theta$  (arcsec). Then the two images travel through the lenslet and focused to the detector creating an array of spots of each sub-aperture. The binary star system have to be large enough that they can be resolved in each sub-aperture. The size of each subaperture has to be equal or less than the  $r_0$  and bigger enough to get flux to allow to measure the centroids of the spots.(Butterley, 2006). The typical exposure time is about 4 ms. A simple equation can give us the relationship of each aperture to the height of the turbulence.

$$\delta h = \frac{D/n_{subap}}{\theta} \quad (4.5)$$

where  $D$  is the diameter of the telescope,  $n_{subap}$  is the number of subapertures and  $\theta$  is the stars separation (arcseconds)

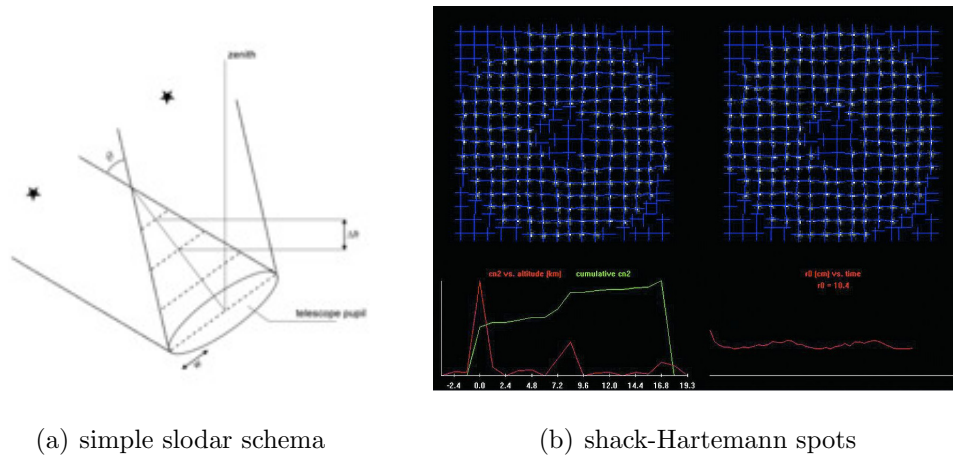


Figure 4.13: A simple schematic illustration of SLODAR resolution.  $\theta$  is the angular separation of the double star with a telescope pupil of diameter  $D$  and  $w$  is the single size of the subaperture array. The bottom image shows the Shack-Hartmann spot patterns for a binary star, and real-time plots of the turbulence-altitude profile and the integrated turbulence strength versus time. Credit. Wilson,2002

The number of layers sensed by a SLODAR instrument depends on the number of the sub-apertures of the SH wavefront sensor. In the case of the SLODAR used at Paranal, the SH is a  $8 \times 8$  lenslet array, therefore 8 different layers in the ground layer are sensed by the instrument, with a vertical resolution depending on the separation ( $\theta$ ) of the binary star.

#### 4.4.4 MASS-DIMM.

The MASS-DIMM is a portable instrument to measure the optical turbulence with a low vertical resolution, which can be adapted to many Observatories with a low human and technical capacity. The simplicity of the instrument has led to it being used during long atmospheric turbulence characterization campaigns, such as TMT (Cerro Armazones) or in many potential E-ELT sites: Argentina, Atlas (Morrocco), or La Palma (Spain). Its uses have been extended and it has been even used in Antarctica (Dome C) it has been used to characterize the optical turbulence.

### Instrument Description

The MASS concept was developed at the Cerro Tololo Inter American Observatory (CTIO),(Kornilov, 2002) in collaboration with the Sternberg Astronomical Institute of Moscow University, as a relatively inexpensive technique for the determination of atmospheric turbulence profiles through single star scintillation.

The MASS has several advantages over other techniques for atmospheric turbulence monitoring. With MASS, turbulence profiles can be generated (unlike a DIMM, which measures integrated properties), only a small aperture telescope is required (unlike SCIDAR), continuous observation is possible (unlike microthermal balloon probes), and high altitude turbulence can be determined (unlike SODAR). In addition, the MASS does not require good image quality or precise tracking and can be mounted behind a window of only modest optical quality. Finally, because it is insensitive to turbulence close to the ground, no requirement exists to place it on a tower or away from sources of heat. Disadvantages of the MASS are that only relatively low resolution profiles can be obtained, and it is not sensitive to the surface layer (below about 500 m). For determination of astroclimate parameters important for an astronomical observatory (total atmospheric seeing, isoplanatic angle, coherence time), the MASS must therefore be combined with another instrument type such as DIMM or SCIDAR.

Including a second channel where a DIMM device can be attached, makes the instrument more complete and able to work more efficiently characterizing the atmosphere turbulence. The MASS-DIMM instrument (Multi Aperture Scintillation Sensor-Differential Image Monitor Motion) detects fast variations of light in 4 concentric apertures using photomultipliers. The 1 ms photon counts accumulated during 1 min. are converted to 4 normal scintillation indices and to 6 differential indices for each pair of apertures. This set of 10 numbers is fitted by a model of 6 thin turbulent layers at pre-defined altitudes of 0.5, 1, 2, 4, 8, and 16 km above the site (Tokovinin et al, 2003). Another model of 3 layers at "floating" altitudes is fitted as well. Turbulence integrals in these 6 (or 3) layers represent the optical turbulence profile (OTP) measured by MASS. Turbulence near the ground does not produce any scintillation: MASS is "blind" to it (layers below 500 meters) and

can only measure the seeing in the free atmosphere. The DIMM may compensate for this limitation, and indeed the combination of a DIMM and a MASS gives the possibility of measuring both seeing and low-resolution turbulence profiles from the ground. MASS has been cross-compared with the Generalised-SCIDAR during a campaign performed at Mauna Kea. (Tokovinin et al., 2005).

The method derives the turbulence profiles from the scintillation patterns and the spatial fluctuations in intensities are dependent on the altitudes of the turbulent layers. The light from the star is collected on four concentric ring mirror apertures acting as a spatial filter (a simple schematic diagram is shown in Figure 4.14). The dependence between the layer distance and scintillation is used to separate the contributions from different layers. The distribution of the turbulence in altitude is calculated from the statistical processing of the series of photon counts within each sub-aperture ring with 1 ms sampling (Tokovinin and Kornilov, 2003).

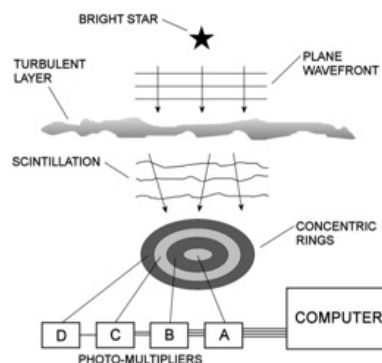


Figure 4.14: Simple scheme of MASS operation. Credit. [http://www.ctio.noao.edu/% Eatokovin/profiler/](http://www.ctio.noao.edu/%E2%80%A2Eatokovin/profiler/)

Each ring mirror aperture, called A, B, C and D in Figure 4.14, converges light to four photon counters. In the method both the scintillation index (SI) and the differential scintillation index are retrieved. The scintillation index in each aperture is computed as the variance of intensity normalized by the average intensity squared (thus, SI is not dependent on the star brightness, but only on the strength of the scintillation). The differential scintillation index for two apertures (i.e. A and B) is defined as the variance of the ratio of intensities in A and B normalized by the

square of the average intensity ratio A/B (Tokovinin and Kornilov, 2003).

Both indices are calculated as the product of the turbulence energy in a given layer and the corresponding instrumental weighting function relative to that layer. Thus, the  $C_n^2(h)$  of each layer is calculated inversely. The MASS-DIMM has been in operation in many Observatories as part of the study of the turbulence above the observatory, and, for example, it has been operating at Paranal since 2003 and gives the  $\langle C_n^2(h) \rangle$  corrected at airmass 1 for 6 layers placed at 0.5, 1, 2, 4, 8 and 16 km above the telescope pupil.

**MASS weighting functions.**

The MASS weighting functions can be assumed as triangles having the peak in correspondence to the layer specific altitude  $h_i$  (Figure 4.15). Alternatively, one may say that the peak corresponds to the altitude in which the MASS has the maximum sensitivity to the signal. The altitudes and the bases of each weighting function are fixed on a 2n logarithmic grid. The six altitudes are expressed by the formula  $h_i = 2h_{i-1}$ , where  $i = 1, 2, \dots, 6$  and  $h_1 = 500m$ . The width of the base of each triangle, assumed as the thickness ( $\Delta h_i$ ) of the sensed layer is defined by the formula  $\Delta h_i = 2h_i - \frac{h_1}{2} = \frac{3}{2}h_1$ , where  $2h_i = max_i$  and  $h_i/2 = min_i$  correspond respectively to the two extremes of the base.

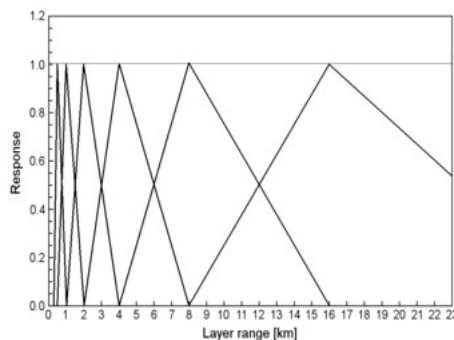


Figure 4.15: MASS weighting function representation. Credit:

<http://www.eso.org/gen-fac/pubs/astclim/espas/workshops/AO-ATMO-2003/Tokovinin.pdf>

Table 4.1 reports the altitude, the base width and the base extremes for each

layer sensed by the MASS operating at Roque de Los Muchachos. As one can argue from the table, the resolution of the profile decreases as  $1/\Delta h_i$ , but the relative resolution  $\Delta h_i/h_i$  is constant for each layer.

Layer	h	$\delta h$	Min	Max
1	500	750	250	1000
2	1000	1500	500	2000
3	2000	3000	1000	4000
4	4000	6000	2000	8000
5	8000	12000	4000	16000
6	16000	24000	8000	32000

Table 4.1: MASS weighting function extremes measured in meters.

### Algorithms.

The DIMM instrument measures the summed Free+Boundary seeing. The data is stored in a file on the local DIMM computer. A new file is generated every night. The MASS instrument estimates the seeing at different height slabs; 0.5,1,2,4,8 and 16 km above the ground level. The turbulence in the lower 0.5 km of the atmosphere, the so called boundary layer is not detected by the MASS instrument.

Both MASS and DIMM data are measured and recorded approximately every 60 seconds. The turbulence moment has been defined by Hardy (Hardy, 1998) and its mathematical expression is;

$$\mu_m = \int_0^{\infty} C_n^2(z) z^m dz \quad (4.6)$$

For the seven layer turbulence profiles generated by the DIMM and MASS, a discrete version of this equation is appropriate:

$$\mu_m = \sum_{i=0}^6 C_n^2(i) z^m(i) \quad (4.7)$$

where  $z(i)$  is the vector (0.5, 1, 2, 4, 8 and 16 km) for each of the six layers.

The MASS instrument measures  $C_n^2(i)$  for every height slab but it doesn't detect the surface layer turbulence at height equal to zero. The coherence length  $r_0$  can be represented as;

$$r_0^{5/3} = 0.423k_0^2\mu_0 \quad (4.8)$$

where  $k_0$  is the wavenumber  $k_0 = 2\pi/\lambda$ . The value of  $\mu_0$  is retrieved from the DIMM seeing data and thus the boundary layer can be calculated;

$$C_n^2(0) = \mu_0 - \sum_{i=1}^6 C_n^2(i)z^0(i) = \mu_0 - \sum_{i=1}^6 C_n^2(i) \quad (4.9)$$

The Fried parameter  $r_0$  shown in equation 4.8, is the measure of the lateral coherence scale of the wavefront phase and it can be calculated directly from equation 4.7.

The isoplanatic angle  $\theta_0$  is a measure of the angular correlation of the wavefront phase. It has been seen in Chapter 3 that the isoplanatic angle can be calculated using:

$$\theta_0^{-5/3} = 2.91k_0^2\mu_0 = 2.91k_0^2 \sum_{i=0}^6 C_n^2(i)z^{5/3}(i) \quad (4.10)$$

considering  $z(0) = 0km$ , then the isoplanatic angle calculated from the MASS data is;

$$\theta_0^{-5/3} = 2.91k_0^2\mu_0 = 2.91k_0^2 \sum_{i=1}^6 C_n^2(i)z^{5/3}(i) \quad (4.11)$$

An important consideration in the new AO systems is the use of the LGS to correct the wavefront phase of one or multiple science objects, In this scenario, the backscattered light from the laser is used to correct the wavefront, but the LGS has a finite height and the corrections can differ from the starlight (science object), and the focal anisoplanatic effect takes account of this due to an angular displacement which gives a phase variance that can be expressed as;

$$\sigma_\phi^2 = \left(\frac{D}{d_0}\right)^{\frac{5}{3}} \quad (4.12)$$

where  $d_0$  is a parameter depending in the turbulence profile and the range  $L$  to the LGS.  $D$  is the telescope diameter and  $d_0$  has been proposed by Sasiela (Sasiela,1994) as;  $d_0 = 2.877L\theta_0$  where the lateral coherence scale parameter  $d_0$  is a measure of the differential wavefront phase between the laser and the star and  $\theta_0$  is the isoplanatic angle of the LGS up to the height  $L$ . The tilt is an uncertainty in the LGS scenario then the focal anisoplanatism can be retrieved from the tilt and piston remove phase variance. This effects will be very strong when telescope diameter is bigger that the  $d_0$ .

$$d_0^{5/3} = k_0^2 \left( 0.5 \frac{\mu_{5/3}}{H^{5/3}} - 0.452 \frac{\mu_2}{H^2} \right) \quad (4.13)$$

where  $H$  is the laser height and  $\mu_{5/3} = \int C_n^2 d(z) z^{5/3}$ .

#### Ground-layer Seeing from the Difference between DIMM and MASS instrument.

The DIMM system is equally sensitive to all optical turbulence in the atmosphere above the altitude of the telescope regardless of height. All turbulent layers combine and contribute to the overall image motion used to derive the DIMM seeing. When determining the integrated MASS seeing, the MASS instrument in combination with the analysis algorithm has a sensitivity profile along the optical path with zero sensitivity to turbulence between the telescope entrance and approximately 250 m, with linearly rising sensitivity up to an altitude of 500 m and then almost constant sensitivity beyond (Tokovinin et al. 2003). The integrated seeing as measured by the MASS thus omits most of the contribution from the lowest 500 m. Thus the difference between the DIMM and MASS seeing measurements gives a measure of the strength of the seeing in the lowest few hundred meters, which we call the ground-layer seeing. It is calculated using the following equation;

$$\varepsilon_{ground} = \left( \varepsilon_{total}^{5/3} - \varepsilon_{free}^{5/3} \right)^{3/5} \quad (4.14)$$

The Figure 4.16 shows an schematic representation of the atmosphere coverage by the DIMM and by the MASS.

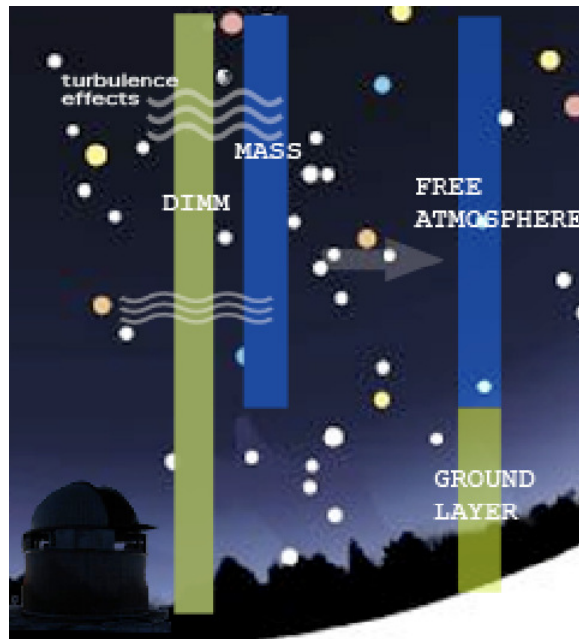


Figure 4.16: Schematic representation of the atmosphere coverage of the DIMM and the MASS turbulence sensing monitors. The recombined profile is also shown.

The stronger ground-layer turbulence experienced at the northern hemisphere sites is a result of the interaction of the wind flow with the local terrain, causing more low-altitude turbulence and increasing the thickness of the highly turbulent ground layer. The ORM site located at 24 degrees north is located on a sloping area with a deep slope and the Caldera Taburiente<sup>2</sup> behind the site. The Mauna Kea site located at 13 degrees North is located on a relatively flat, sloping lava field, about 150 m below the Mauna Kea summit ridge. Paranal Observatory is sited at 23 degrees South in the Atacama altiplano. Thus we can attribute the stronger ground-layer seeing at the San Pedro Martir, Roque de Los Muchachos and Mauna Kea sites to the local topography. There are many works related to site evaluation for all observatories and a comparison of the different sites is shown in the work done by Lawrence (Lawrence et al, 2003) and the results are shown in Table 4.2 where it is summarised the seeing, isoplanatic angle and the coherence time for different

<sup>2</sup>Caldera de Taburiente is an enormous crater of 10 kilometers cross and 2000 meters high, with the highest peak at 2400 meters and the ORM is settle at the top

sites, both north and south. It should be noted that these results come from old data and they wouldn't represent the actual sky conditions. But they can give an indicator of the differences between the sites.

Site	$\epsilon$	$\theta$	$\tau$
DomeC	0.27	5.7	7.9ms
South Pole	1.8	3.2	1.6ms
San Pedro Martir	0.59	1.6	5.5ms
Cerro Paranal	0.8	2.6	3.3ms
Manua Kea	0.5-0.7	1.9	2.7ms

Table 4.2: Comparison of site conditions taken the seeing ( $\epsilon$ ) measured in arcseconds, isoplanatic angle( $\theta$ ) measured in arcseconds and coherence time ( $\tau$ ) measured in msec. Wavelength used  $550\mu$  m

The southern hemisphere subtropical jet stream passes over the region where the three Chilean sites are located (Wallace and Hobbs, 2006), resulting in stronger levels of high-altitude turbulence and integrated MASS seeing. The La Palma and Manua Kea sites (Northern sites) are generally not under the jet stream winds, and when the northern subtropical jet stream wanders to lower latitudes over the northern hemisphere sites, the wind speed is low. Additionally, (Els et al. 2008) show that the increase in high-altitude turbulence with high-altitude wind speed is not as significant for the northern test sites as it is for the Chilean sites; thus the MASS seeing of the northern sites is somewhat lower than that of the southern sites.

# Chapter 5

## Correcting the Turbulence

*"..Observe the motion of the surface of the water, which resembles that of hair, which has two motions, of which one is caused by the weight of the hair, the other by the direction of the curls; thus the water has eddying motions, one part of which is due to the principal current, the other to random and reverse motion."*

*Leonardo Da Vinci, Turbulenza, 1500*

---

### 5.1 Overview.

Adaptive optics is a technology that was developed to correct the fluctuations of the wavefront in real time and to retrieve spatial frequencies filtered by the atmosphere. A measure of the disturbance phase on the pupil can, upon analysis, be used to order an optomechanical correction of optical defects and obtain long exposure images with a resolution close to the diffraction limit of the telescope, hence exploiting its capability to obtain high resolution images.

The method was initially proposed by Babcock<sup>1</sup> in 1953 (Babcock, 1953), and involved the correction of the wavefront of a disturbed wave using a deformable mirror. With the increasing necessity of obtaining better astronomical images this technique started to receive a large degree of interest in the astronomy engineering field. However, due to the low computational power available in the earlier years it has been necessary to wait 20 years until the first adaptive optics system was built (Hardy et al. 1977).

The first operational adaptive optics system used for astronomical observation in ESO<sup>2</sup> was called COME-ON (Rousset et al, 1990) and provided images corrected for the atmosphere turbulence in the infrared band using a telescope of 1.52 meters. The instrument used a deformable mirror of 19 piezo-electric actuators and a Shack-Hartmann wavefront sensor. This initial instrument was improved over many years and its concept was changed to the final configuration that was called ADONIS (Le Mingnant, et al 1999) which was the first astronomical AO instrument that has produced science data. From the other side of the Atlantic Ocean, the National Observatory Astronomy Optics (NOAO) in the USA developed a new technique for sensing the atmosphere called curvature sensing<sup>3</sup> (Roddier, 1988). This new technique was tested in an experimental instrument with 19 actuators installed in the Canada-France-Hawaii Telescope (CFHT) on Manua Kea; this instrument was called PUEO (Rigaut et a, 1997, Rigaut et al, 1998). Actually almost all telescopes of 8-10m class are equipped with adaptive optics instruments and current research focuses on improving the performance of these systems. Table 5.1 shows some of the currently running AO instruments.

---

<sup>1</sup>Horace Welcome Babcock, (1912-2003) was the first astrophysics to propose the Adaptive optics as a method to compensate in real time the wavefront from a star when it is perturbed by the atmosphere.

<sup>2</sup>ESO, European Southern Observatory sited at Paranal and La Silla Observatories in Chile, that is formed with four 8 meters class telescopes (VLTs) and other series of minor telescopes like VISTA or NTT.

<sup>3</sup>Curvature sensing; system based on the measures of the intensity  $I_1$  in an intrafocal plane and the intensity  $I_2$  in an extrafocal plane and compares these intensities to determine the curvature of the wavefront. The normalised difference  $(I_1 - I_2)/(I_1 + I_2)$  is used to reconstruct the wavefront.

Facility	Name	Strelh Ratio	Magnitude	Instrument
Keck-II	Keck-II	0.8	<i>NGS</i> $\approx$ 13.0	NIRC2,NIRSPECT
	Hokupa		<i>LGS</i> $\approx$ 18.0	
Gemini-N	ALTAIR	0.65	<i>NGS</i> $\approx$ 13.0	NIRI,GNIRS
			<i>LCG</i> $\approx$ 18.0	
Subaru	37 elements CS	0.3	<i>NGS</i> $\approx$ 16.0	CIAO,IRCS
MMT	Secondary Adaptive	0.7	<i>NGS</i> $\approx$ 13.0	
			<i>LGS</i> $\approx$ 17.0	
VLT	NAOS	0.7	<i>NGS</i> $\approx$ 13.0	CONICA
	MCAO	0.3	<i>NGS</i> $\approx$ 16.0	SINFONI
Herschel	NAOMI	0.6	<i>NGS</i> $\approx$ 12.0	Omega
LBT	Secondary Adaptive 672 actuators	0.84	<i>NGS</i> $\approx$ 13.0	IRTC

Table 5.1: Summary of some running AO instruments in different observatories. The Strelh Ratio is measured in K-Band.

Many astronomical discoveries were made possible thanks to the option of the adaptive systems such as the discovery of a black hole at the center of our galaxy (Genzel et al. 2003) or the first direct detection of an exo-planet (Chauvin et al. 2004) using the system VLTI<sup>4</sup> / NAOS (Rousset et al. 2003). There are many AO systems, and they are more or less complex eg; Adaptive Optics system in the LBT with a secondary Adaptive mirrors. But for all the systems the common scheme is illustrated in the Figure 5.1.

This Chapter describes briefly the concepts of the Adaptive Optics techniques considering its conceptual hardware and physics.

---

<sup>4</sup>VLTI. Very Large Telescope Interferometry, An observational capability based on the combination of the four VLT Unit Telescopes and of the four moveable 1.8m Auxiliary Telescopes.

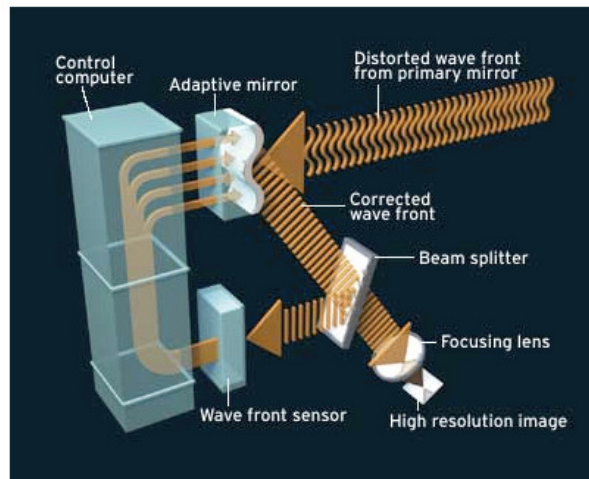


Figure 5.1: Principle scheme of an adaptive optics system: The phase errors of the incoming wavefront are measured by a wavefront sensor unit and processed in real time. The real-time computer drives the correction units such as; tip-tilt and deformable mirror to correct the wavefront in an inversely shaped way to the measured distortions providing a corrected wavefront (high resolution images) for the science instrument. Credit. Bryan Christie.

## 5.2 Introduction.

The AO system contains three main components: the deformable mirror (DM), the wavefront sensor and the wavefront reconstructor. The DM is usually a thin flexible mirror with a large number of pistons or actuators behind it. When commanded correctly, the actuator motions should provide the desired wavefront changes via the mirror. The DM stroke required is typically of the order of several microns with an accuracy of roughly 10 nm. The wavefront sensor measures turbulence induced distortion in the wavefront coming from a reference source. The reconstructor is a computational algorithm and hardware that rapidly computes an approximate wavefront error that matches the measured wavefront slopes and can be used to command the deformable mirror (DM).

A simple scheme of an AO system is shown in Figure 5.1. The wavefront from a star or a reference source (LGS) is entering the telescope equipped with an AO system. The aberrated wavefront enters the system and using optical elements (off-

axis parabolae, tip/tilt mirror, relay optics, etc) relays the re-imaged pupil onto the deformable mirror (DM) used to correct the wavefront distortion by means of an actuator system. A beam splitter divides the light into two paths; the wavefront sensing path and the science path. In the wavefront sensor the re-image telescope pupil is projected onto a lenslet array (Shack-Hartmann lenslet array), which focuses the light from the reference source onto a CCD detector at each sub-aperture. A wavefront distortion causes the image formed by a given lenslet to move on the detector. The wavefront reconstructor integrates the measured shifts (slope errors) and reconstructs the deformation of the wavefront. This deformation is then imposed on the DM by a controller to correct the atmosphere-induced distortion of the wavefront in the beam relayed to the science detector.

Wavefront correction is done with the deformable mirror (DM), which usually has a continuous reflective surface with a mechanical deformation system to match the desired wavefront. The types most commonly used in AO systems are thin plate mirrors with stacked piezoelectric actuators (PZT) (Myers et al, 2003) or bimorph mirrors (Adelman, 1977; Kokorowski, 1979; Steinhaus and Lipson, 1979), but a new technology using MEMs<sup>5</sup> is emerging.

### 5.3 Wavefront sensing in adaptive optics.

The wavefront sensor is the device responsible for measuring the atmospheric distortion that occurs in the wavefront. Although the atmosphere disturbs the amplitude and phase of the wave, the phase variations are the largest contributor to the degradation of the image. For this reason the current adaptive optics systems do not measure or correct for variations in the amplitude (scintillation).

When the systems reach a phase correction so high that the amplitude variations are important, it may be necessary to correct them. In fact, applications have been proposed such as the detection of planets in stars other than the Sun which require the correction of amplitude variations (Angel, 1994). In any case, current systems

---

<sup>5</sup>MEMS, Micro Electro Mechanical Systems. This system is base on very small mechanical devices driven by electricity and can be used in deformables mirrors.

only measure the phase aberrations. There are many works describing many types of wavefront sensors and in this work there follows a brief description of the different types of wavefront sensors and how the wavefront can be reconstructed from the data measured with the wave front sensor.

### **5.3.1 Measurement of curvatures of the wavefront.**

Roddier in a compilation of work has developed the theory to find out the curvature of the wavefront from out of focus images (Roddier, 1988, 1990, 1991). It has been applied in combination with an adaptive variable curvature mirror (Forbes 1989, Forbes and Roddier 1991) in the adaptive optics system developed by the University of Hawaii (Graves et al. 1991, Roddier and Roddier 1988 , Roddier et al. 1987, 1991a, b). The advantage of this system is that sensor information can be sent directly to the actuators in the deformable mirror.

### **5.3.2 Measurement of the local slopes of the wavefront.**

The following describes various types of sensors based on measurement of local slopes of the wavefront, special attention is payed to the most commonly used of the wavefront sensors for AO, the Shack-Hartmann.

#### **Edge Sensor.**

This involves placing a very thin segment ( knife edge) at an intermediate image. The intensity distribution in the following image of the pupil plane corresponds approximately to gradients in the direction perpendicular to the segment. This technique, already proposed by Babcock (1953) in his seminal article on adaptive optics, is rarely used despite having been improved by Goad (1986).

#### **Lateral displacement interferometric sensors.**

This involves moving the wavefront laterally and mixing it with itself. In this interference pattern the phase difference between the two patterns become different intensities which can be measured with a CCD. With this method the planar ref-

erence wavefront can be eliminated. Measuring the intensities of the patterns and knowing the lateral displacement the slopes of the wavefront ("tilt") in the direction of travel of the wavefront can be determined. (Hardy 1978, 1982, Hardy and McGovern 1987, Hardy et al. 1977, Koliopoulos, 1980).

#### Shack-Hartmann sensor.

This sensor is commonly used in adaptive optics systems which range from astronomical applications to medical analysis (e.g, study of the eye layers). Figure 5.3 shows an outline of the light path through the Shack-Hartmann microlenses in three different cases: planar, tilted and aberrated wavefront. The images from the microlenses are focused on the detector. At a conjugate plane of the pupil a microlens array is placed. The average slope of the wavefront in the area of the microlens is obtained from the position of the center of gravity of this image  $x_G$  (Allen et al. 1987, Gaffard and Boyer 1989, Rousset et al. 1987, Schaud et al. 1991):

$$x_G = \frac{\lambda f}{2\pi} \frac{1}{S} \int_S \frac{\partial \theta(\vec{r})}{\partial x} d\vec{r} \quad (5.1)$$

where  $\lambda$  is the wavelength,  $f$  the focal length of the microlens and  $S$  the surface of the pupil of a microlens. The local slope is the average of the first derivative of the phase. Importantly, the position of the center of gravity of the image depends on the wavefront slopes, which in the first approximation is independent of wavelength. So, this sensor is an achromatic instrument. This property is essential as it is possible to use light more efficiently than in other sensors. Even so, the signal strength is a fundamental limit to the performance of the adaptive optics system. If the diameter of the microlenses is of the order of  $r_0$  and exposure times of milliseconds, most of the objects in the sky are too faint to obtain acceptable noise levels on the sensor (Beckers, 1993).

The percentage of sky visible (i.e., the regions where there is a source of sufficient brightness within the isoplanatic field) increases by using longer wavelengths; from visible ( $0.55\mu m$ ) is about  $2.6e^{-4}\%$  to  $1.32\%$  in the infrared ( $2.2\mu m$ )(Beckers, 1993). To improve the sky coverage that an AO system can be applied in areas where there is no suitable natural guide star (NGS), the use of artificial reference star (LGS)

created with laser has become a solution to the sky coverage limits (Fugate et al. 1991, Gardner et al. 1990).

The laser beam is focused in the center of the field of vision and high above the telescope. Some light is scattered in the direction of the telescope and used in the sensor to measure wavefront aberrations. This technique is coming into regular use with an important science impact. A review of the science impact and the contribution of the Keck is showed in the figure 5.2. (Liu, 2008)

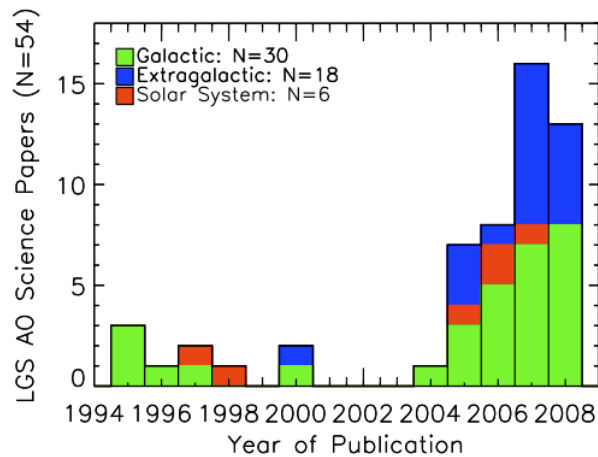


Figure 5.2: Compilation of the all refereed LGS AO science papers. The large peak in 2007 comes with the use of the Keck II AO systems. Credit. Liu, 2008

### Pyramid sensor.

The Pyramid sensor was proposed by Ragazzoni (Ragazzoni, 1996) for a new adaptive optics system based on a modification of the Foucault test. The simple scheme of this sensor is shown in figure 5.4. It consists of one pyramids with a top angle of 90 degrees. The incoming beam is focused on the top of the first pyramid which divides the beam into four. The focal plane of the pyramid prism and the relay lens create four pupil images. From these images, with specially developed algorithms, the wavefront errors are computed (Ragazzoni, 2002).

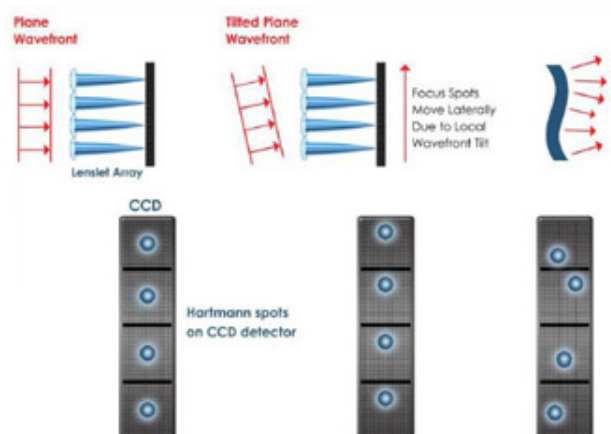


Figure 5.3: Schematic diagram of a Shack-Hartmann wavefront sensor. Wavefronts from astronomical objects are distorted by the atmosphere and reach the pupil of the telescope. At a conjugate of the pupil a microlens array is placed. Each microlens forms an image on its focal plane. The average slope of the wavefront in the area of the microlens is obtained from the position of the center of gravity of the image. Adapted from Boston micromachines. <http://www.boston-micromachines.com>

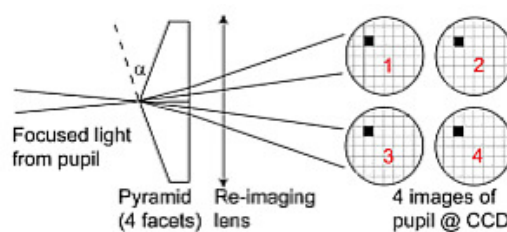


Figure 5.4: Pyramid wave front sensor scheme. The light is focused on the vertex of the pyramid and four images are formed on the detector; a relay lens helps to collimate the four beams. The analysis of the intensities in the four pupils is used to retrieved the slopes variation due to the wavefront errors. Adapted from Ragazzoni 2002.

## 5.4 Wavefront Reconstruction.

The wavefront sensors do not provide a direct measure of the wavefront phase, which is the required physical quantity. It is therefore necessary to reconstruct

the phase from data from the sensor. This section studies the case of the Shack-Hartmann sensor. The sensor provides information that is the local average slope of the wavefront in the area of each of the microlenses. Figure 5.5 shows a flow diagram that summarises the reconstructor process of the phase.



Figure 5.5: Flow diagram of the phase reconstructor for a Shack-Hartmann wavefront sensor.

To reconstruct the phase it is fairly common to decompose the wavefront on a functional basis. The basis set often chosen is the *Zernike polynomials* (Noll, 1976), which are orthonormal on a circular pupil:

$$\phi(\vec{r}) = \sum_{i=2}^{i_{max}} a_i Z_i(\vec{r}) \quad (5.2)$$

The Appendix **E** describes this decomposition in more detail. The coefficient is not measured for the first of the polynomials (piston). This term corresponds to a constant factor that adds to the whole wavefront and can not be determined from the first derivatives. The phase is retrieved by determining the coefficient  $a_i$ . Considering  $\vec{p}$  as the vector of the local slopes provided by the sensor and  $\vec{a}$  the vector of coefficients of the wavefront.  $\vec{p}$  and  $\vec{a}$  can be expressed as;

$$\vec{p} = D\vec{a} \quad (5.3)$$

where  $D$  is the matrix that characterizes the wavefront analyzer. Its  $i$ th column is the slope obtained when the wavefront is equal to  $Z_i$ . It is necessary to invert this equation to find the coefficients of the wavefront from the measurements. It is evident that the number of coefficients that can be estimated must be less than the number of local measurements to ensure that the problem is well defined. It may be interesting in this case to include the statistics of phase and the noise in the

measurement (Sasiela,1985). If one does not know the statistics of the coefficients and uncorrelated Gaussian noise is assumed we obtain the classical solution of least squares (Herrmann, 1980):

$$\vec{a}_{estim} = [D^T D]^{-1} D^T \vec{p} \quad (5.4)$$

Another possibility is to define a procedure that minimizes the average variance of the phase on the surface of the pupil between the real and the reconstructed phase (Wallner, 1983). It is important not to confuse this theoretical process of reconstruction of phase with the corrective control. This imposes new constraints, and it is clear that the reconstructed phase surface cannot be represented perfectly. In a real system one has to find an optimal basis taking into account the statistics of turbulence (Cho and Petersen 1989 )and (Gendron, 1993), the features of the corrective element (Gaffard and Ledanois, 1991) and the geometry of the sensor (Marais et al. 1991).

## 5.5 Correction systems.

Once they are known, the wavefront correction element compensates for the aberrations. The correction elements are usually mirrors. The design must allow for varying the shape of the mirror surface so that it can adjust to the instantaneous distortion of the wavefront. This is generally accomplished using piezoelectric or electrostrictive materials that deform the surface by applying a voltage. Deformable mirrors are characterized by their size, the number of actuators and time taken to apply the shapes. As the dominant aberration is the tilt (average slope of the wavefront) correctors are usually divided into two subsystems: a mirror that covers the entire aperture and controls the average slope of the wavefront (Tip/Tilt), and an adaptive mirror that corrects higher-order and lower-order distortions. It should be noted that the mirrors are usually placed before the beam splitter that distributes part of the power to the wavefront sensor and the rest to the scientific instrument. Examples of correction systems can be the segmented deformable mirror as it is NAOMI (Myers, 2003) or the new secondary adaptive system at the LBT with a

continuous deformable secondary mirror of 672 actuators (Riccardi, 2004).

### 5.5.1 Segmented mirrors.

The Shack- Hartmann sensors measures the local slope of the wavefront and the segmented mirrors consist of an array of mirrors equivalent to the wavefront sensor, thereby simplifying the control of actuators, which adjust the segment inclination directly in proportion to the local slope in the corresponding microlens (Dunn 1987, 1989, 1990, Smithson 1987, Smithson et al. 1984, 1988). The problem arises of adjusting the piston of each of the mirrors and ensuring continuity of the wavefront. Another drawback is the gaps between the different mirrors which causes a loss of signal and diffraction of light, and also an increase in Infrared emissivity. An example of a segmented mirror is shown in the figure 5.6 which is formed by 76 elements.

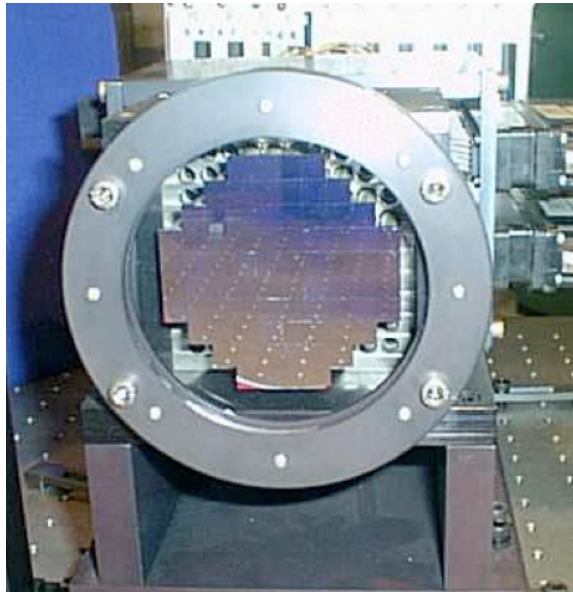


Figure 5.6: Segmented deformable mirror for NAOMI, with 76 elements.

### 5.5.2 Continuous Mirrors.

These mirrors automatically maintain the continuity of the wavefront. However, the local inclination of the mirrors has to be calculated, not directly using the

information from the wavefront sensor as in the case of segmented mirrors. It is important to optimize the response functions of the actuators to match the selected wavefront sensor. In one type of continuous mirror the actuators produce local curvature rather than gradients in the wavefront (Roddier et al. 1991a, b). This is achieved by techniques using oppositely polarized bimorph piezoelectric materials (Forbes 1989, Jagourel et al. 1990a, b, Kokorovski 1979, Steinhaus and Lipson 1979). These systems combine the advantages of both types of mirrors: keeping the continuity of the wavefront automatically and allowing sensor measurements to feed the actuators directly providing a smooth fit of the wavefront which is an advantage to correct the low-order of aberrations. Figure 5.7 shows an example of a continuous mirror of 672 actuators used in LBT secondary AO system. Figure 5.8 shows the bimorph deformable mirror used in the Canadian-France-Hawaii Telescope.

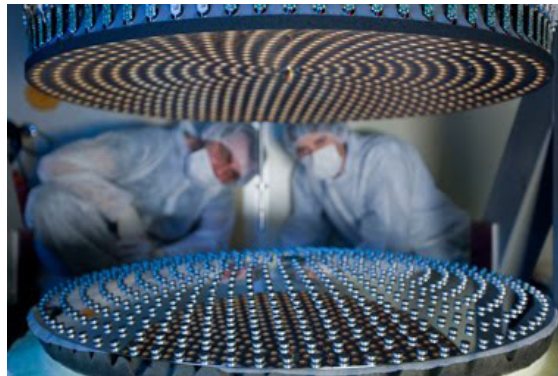


Figure 5.7: Example of a secondary adaptive mirror, that consists in a continuous deformable mirror of 910mm formed by 672 voice-coil actuator. Credit LBT.

### 5.5.3 Other devices.

There are many other ways to vary the optical path. Babcock (1953, 1958) proposed using an oil film as a deformable element. Membrane mirrors take advantage of the deformation of a thin membrane by applying electrostatic forces (Clampin et al. 1991, Durrance and Clampin 1989, Grosso and Yellin 1977, Merkle et al. 1981). These are fragile and can be used to correct low orders. It has also been proposed to use liquid crystal devices (Bonaccini et al. 1990, 1991).

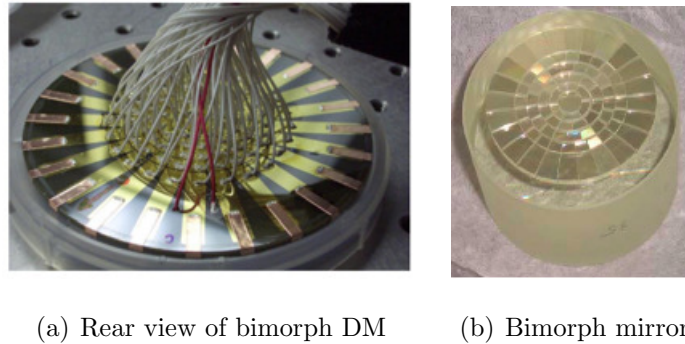


Figure 5.8: Two images of the bimorph deformable mirror. (a) shows the rear view of the bimorph DM of the CFHT. The (b) shows the front of the bimorph DM. This type of deformable mirror is used in Adaptive Optics instruments in Subaru or VLT.

## 5.6 Control Systems.

The systems that drive the actuators of the adaptive mirrors using the wavefront information are very complex (Boyer 1991, 1990 a). But the most simple ones only correct low order aberrations, where a large number of potentially very noisy signals can be processed to reduce the influence of noise on the wavefront correction. These processes must be carried out faster than the characteristic time of the atmospheric turbulence (coherence time), which is typically of the order of milliseconds, and which explains the complexity of control systems.

Most systems work with modal control. The wavefront signals are combined to express the wavefront as a linear combination of a number of modes, usually Zernike polynomials (description in Appendix E). Other bases are also used such as the Karhunen-Love polynomials (Wang and Markey 1978) or the eigenvectors of a given system. The actuator system is calibrated so that they can adjust these modes and linear combinations of them. The time constants can be adjusted to match slow low-order aberrations and the rapid control of higher order aberrations.

Analog systems are sometimes used to achieve the high speed processing required, whilst in others digital controllers are used to implement algorithms that are robust under changes in the flow conditions, the noise, the Fried parameter or the characteristic time of the atmosphere.

The control is simplified when there is a correspondence between each signal of

a microlens on the sensor and each actuator (control zone), as in the case of segmented mirrors with Shack-Hartmann sensors and curvature sensors with bimorphs. However, this requires control signals with good signal to noise ratio. In most astronomical observations that condition is not satisfied and there is a need to spatially filter the signals. The spatial frequency content of the wavefront aberrations cause aliasing effects. This aliasing will cause the increase of the residual error and increasing the background light of the point spread function (PSF). A spatial filtering technique can reduce this phenomenon by using a field stop at the focal plane before the wavefront sensor. This stop acts as a low-pass filter on the phase, significantly reducing the high-spatial-frequency content phase seen by the wave-front sensor at moderate to high Strehl ratios (Poyneer and Macintosh, 2004).

## 5.7 Measurement error.

This section summarizes the influence of various factors which limit the AO system performance and it can be a metric of how the WFS is measuring the wavefront to be corrected. This knowledge of the measurement error can be applied to the error budget analysis and it can be used to optimize the AO system performance before building the system; e.g., the development of an AO system to correct high-orders. This need a large number of sub-apertures to reduce the error in the high-order modes and the aliasing but by increasing the number of sub-apertures we are reducing the number of photons per sub-aperture, which means, that the error on measurement can be increased.

### Finite spatial resolution.

The finite spatial resolution on the wavefront sensor and adaptive mirror for a zonal control system produces a residual variance in the wave front equal to:

$$\Delta_{spacial} \approx 0.34 \left( \frac{r_E}{r_0} \right)^{5/3} \quad (5.5)$$

where  $r_E$  is the size of the microlenses of the wavefront sensor and  $r_0$  is the separation of the actuators in the the deformable mirror. The value 0.34 depends

on the system used.

### Finite time resolution.

This error is often called the time delay error. It is due to the changes occurring in the wavefront during the time between detection and compensation. The effect on the wavefront residual variance can be expressed as:

$$\Delta_{temporal} \approx \left( \frac{f_G}{f_S} \right)^{5/3} \quad (5.6)$$

where  $f_S$  represents the bandwidth of the correction cycle and is about  $0.3/\tau_d$ , where  $\tau_d$  being the time difference between wavefront measurement and correction and  $f_G$  is the Greenwood frequency (Section 3.6.1).

### Photon noise.

In general, the signal reaching the wavefront sensor is very weak and has low signal to noise ratio (SNR). This causes a residual wavefront variance.

$$\Delta_{photon} = 4 \cdot SNR^{-2} rad^2 \approx \frac{4}{N_p} rad^2 \quad (5.7)$$

where  $N_p$  is the number of detected photons. When the number of photons is very low ( $\ll 100$ ), the photon noise starts to severely limit the performance of the system, which can only correct the lower order modes and the system is working in partial correction which limits the final compensation of the wavefront ( decreases the Strehl ratio).

### Polychromatic approximation.

Atmospheric refractive index varies with wavelength, but this variation is generally ignored in adaptive optics. It could be compensated because the refraction index profile as a function of wavelength is known with great accuracy. However, the effect is only important if one uses long wavelengths to measure the wavefront and the compensation is done at shorter (Hogge and Butts, 1982), which is not a usual case in astronomy. On the contrary, it is common to measure in the visible and correct

in the infrared. In this case the residual variance is about  $0.005 \text{ rad}^2$ , which can be ignored in all real applications.

#### **Anisoplanatism path.**

This is the angle between the guide star (GS) and the science object in which the Adaptive optics system can correct the wavefront considering the phase constant (Fried,1982, Roddier,1999). In fact, the quality of the corrections degrades when we are moving outside of this angle. The figure 5.9 shows a schematic representation of the aniplanatism phenomenon with a science object and a reference star off axis. This reference star can be a laser guide star (LGS).

#### **Amplitude variations.**

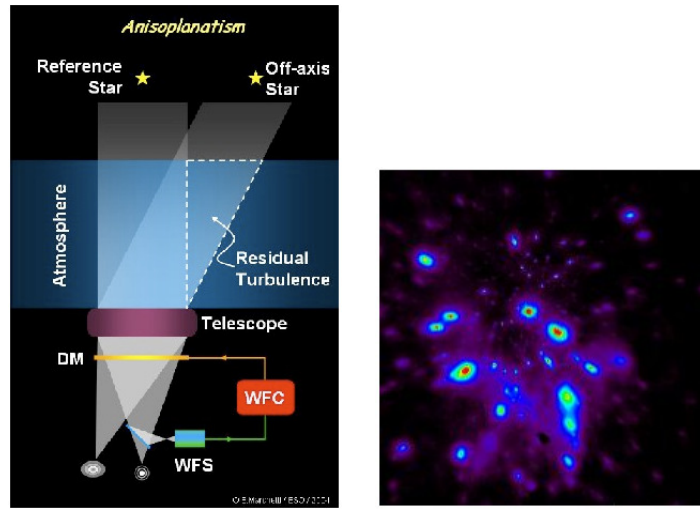
Variations in the phase of the wave passing through the atmosphere contribute to a much greater extent than the amplitude degradation of the image. For this reason the current adaptive optics systems in general ignore the amplitude variations. In systems operating in total correction this can lead to a reduction in Strehl Ratio of 10 to 15% in the visible. However, in partial correction systems, its effect is negligible.

## **5.8 Factors influencing the wavefront variance. Error budget.**

In order to achieve a certain telescope image quality it is necessary to construct an error budget taking into account the telescope characteristics and the astroclimate parameters. And it can be summarised as the sum of the different errors:

$$\sigma_{tot}^2 = \sigma_{tt}^2 + \sigma_{sensor}^2 + \sigma_{fit}^2 + \sigma_{ang}^2 + \sigma_{temp}^2 \quad (5.8)$$

The main effects that influence the variance of the wavefront phase corrected with an adaptive optics system are:



(a) Schema of anisoplanatism effect

(b) Image taken of the galaxy center using NAOS

Figure 5.9: Diagram representing anisoplanatism. It can be clearly seen that the path taken by the analyzed light and that of the correction is different. A part of the turbulence is not seen and so cannot be corrected. (Right) The image of the galactic center taken with NAOS on the VLT. In this image we see the effect of anisoplanatism, causing deterioration in the image away from the center, where the AO loop has been closed. Credit. E. Marchetti, ESO.

### 5.8.1 Tip-Tilt.

According to Fried (1965) and Noll (1976), for an image without compensating with adaptive optical, the phase variance in a circular area of diameter is;

$$\sigma_{uncomp}^2 = 1.02 (d/r_0)^{5/3} \quad (5.9)$$

then, following this equation for a circular surface of diameter  $d = r_0$ , the quadratic variance of the phase is equal to 1 radian. Once, the average Tip-Tilt of the phase is corrected, the above expression changes according to Noll (Noll 1976):

$$\sigma_{tt}^2 = 0.134 (d/r_0)^{5/3} \quad (5.10)$$

Then, compensating only the Tip-Tilt the improvement in the wavefront variance

of image corrected is a factor of 10. The Tip-Tilt aberration of the image is the greater factor that contribute to the distortion of the wavefront.

### 5.8.2 WFS error ( $\sigma_{sensor}^2$ )

The WFS error depends on the type and design of the WFS. The measurements of a wavefront sensor are affected by noise-induced by the sensor itself, which causes errors in estimating the wavefront phase. This noise can be photonic noise due to the signal and the background noise from the sky. The noise includes the sky background signal and electronic noise causing by the dark current and the detector read noise. The general form of the noise variance due to the photonic component is (Roddiier, 1999):

$$\sigma_{phot}^2 \approx \frac{1}{n_{phot}} \left( \frac{\theta_b d}{\lambda} \right)^2 rad^2 \quad (5.11)$$

where  $n_{phot}$  is the number of photon per sub-aperture and exposure time,  $\theta_b$  is the angular size of the source image, and  $d$  is the sub-aperture diameter. Since the signal to noise ratio (SNR) in each sub-aperture is  $n_{phot}^{1/2}$ , the photon noise variance is inversely proportional to SNR in each sub-aperture. The value of  $\theta_b$  determines the observing conditions of the wavefront sensor, being equal to  $\lambda d$  for the case of diffraction limit, and  $\lambda r_0$  for the case limited seeing conditions. The measurement of photonic noise is given by (Rousset et al,1987);

$$\sigma_s^2 = \frac{\pi}{2} \frac{1}{n_{phot}} \left( \frac{N_T}{N_D} \right)^2 rad^2 \quad (5.12)$$

Where  $N_T$  is the FWHM of the one sub-aperture and  $N_D$  is the diffraction pattern of one sub-aperture in pixels. In the case Shack-Hartmann WFS the electronic noise and its variance of the centroids is given by (Rousset et al,1987);

$$\sigma_s^2 = \frac{\pi^2}{3} \frac{\sigma_e^2}{n_{phot}^2} \left( \frac{N_S^2}{N_D} \right)^2 rad^2 \quad (5.13)$$

where  $N_S^2$  is the total number of pixels used to calculate the centroids,  $\sigma_e^2$  is the RMS of the number per electrons per pixels per image and the  $n_{phot}/\sigma_e N_S$  is the SNR. Now, considering the sky background and the total number of photons of

background ( $n_{bg}$ ) distributed in  $N_S^2$  pixels, then  $n_{bg} = \sigma_e^2 N_S^2$ . So, the equation 5.13 can be rewritten as;

$$\sigma_s^2 = \frac{\pi^2}{3} \frac{n_{bg}}{n_{phot}^2} \left( \frac{N_S^2}{N_D} \right)^2 \text{ rad}^2 \quad (5.14)$$

and;

$$SNR = \frac{n_{phot}}{\sqrt{n_{bg}}} \quad (5.15)$$

### 5.8.3 Temporal error ( $\sigma_{temp}^2$ ).

Even when an Adaptive optics system is correcting properly the atmosphere, there are always delays between the time that the turbulence distorts the wavefront ( $\tau_0$ ) and the time when is performing the corrections ( $\tau$ ). The phase variance due to these delays  $\tau$  with respect to  $\tau_0$  is equal to  $f_G^{-1}$  (Hardy, 1998):

$$\sigma_{temp}^2 = 28.4 \left( \frac{\tau}{\tau_0} \right)^{5/3} \quad (5.16)$$

### 5.8.4 Isoplanatic angle ( $\sigma_{ang}^2$ ).

The variance of wavefront phase due to angle of separation  $\theta$  between the reference star (measuring the wavefront) and the science target is given by the ratio between the angle  $\theta$  and the isoplanatic angle  $\theta_0$  (Hardy, 1998).

$$\sigma_{ang}^2 = \left( \frac{\theta}{\theta_0} \right)^{5/3} \quad (5.17)$$

### 5.8.5 Fitting error $\sigma_{fit}^2$ .

All deformable mirrors has a finite number of degrees of freedom and this produce error in the shape of the mirror trying to compensate the coming wavefront. The precision with which a deformable mirror with a separation between actuator of  $r_s$  can correct the aberrations is giving by the expression (Hudgin, 1977).

$$\sigma_{fit}^2 = A \cdot \left( \frac{r_s}{r_0} \right)^{5/3} \quad (5.18)$$

where  $A$  is a constant that comes from the design of the deformable mirror. This value can be includes the response to the of the turbulence spectra generated by a modal base reproduced by the deformable mirror using its influence function. The influence function is the response of the deformable mirror surface to the action of a single actuator while the rest remainat a fixed voltage. Any deformation of the mirror can be represented theoretically by a linear combination of all influence functions of the mirror. Then the prior knowledge of these influence functions provides the basic tool control the deformable mirror (Clafin and Bareket, 1986, Tyson 1991). The values change in a range of 0.349 for a Gaussian influence functions to 0.28 with a pyramidal influence function (Hudgin, 1977). Therefore, the analysis of the number of actuator that a deformable mirror must have to produce a desired Strehl ratio is determined using the previous equations and assuming the separation of the actuator defined as;

$$r_S^2 = \frac{\pi D^2}{4N_{act}} \quad (5.19)$$

where  $D$  is the telescope diameter and  $N_{act}$  is the number of actuators. Combining the equations 5.18 and 5.19 we have;

$$\ln\left(\frac{1}{S}\right) = A \left[ \sqrt{\frac{\pi}{4N_{act}}} \frac{D}{r_0} \right]^{5/3} \quad (5.20)$$

Then, the number of actuators must have a deformable mirror to compensate the atmospheric turbulence characterized by a coherence length  $r_0$  and the system has to achieve a defined Strelh Ratio (S). This expression is;

$$N_{act} = 0.785 \left[ \frac{\ln\left(\frac{1}{S}\right)}{A} \right]^{-1.2} \left( \frac{D}{r_0} \right)^2 \quad (5.21)$$

As example; considering a telescope of diameter 2m, that works in J band and the  $r_0 = 28cm$ , and the system has to achieve a Strelh of 50%, than the number of actuators that it will be necessary are 30.

Noll (Noll, 1975) proposed another approximation to the fitting error using the residual variance of the wavefront after the correction. This fitting error applied to the Zernikes polynomials is;

$$\sigma_{fit}^2 \approx 0.944 N_m^{-\sqrt{3/2}} \left( \frac{D}{r_0} \right)^{5/3} \quad (5.22)$$

where  $N_m$  is the number of corrected modes. Then taking equation 5.18 and last the fitting variance can be expressed as;

$$\sigma_{fit}^2 \approx 0.360 N_m^{-\sqrt{3/2}} \left( N_{act} \sqrt{\frac{\ln(1/S)}{A}} \right)^{5/6} \quad (5.23)$$

# Chapter 6

## Data and Methology.

*The most exciting phrase to hear in science, the one that heralds new discoveries, is not "Eureka!" ("I found it!") but rather "hmm....that's funny..."*

*Isaac Assimov*

---

### 6.1 Overview.

This chapter provides a description of the meteorological and astroclimatological database. The origin and properties of each dataset and how they were created are given in turn. This is followed by a brief discussion of the quality of each dataset and its importance for site selection of telescopes. For a detailed statistical discussion regarding each dataset, please turn to Chapter 7.

### 6.2 The Data.

The data used are distributed mainly into three sets with two different instruments: the meteorological parameters (vertical distribution of temperature and wind speed), the astroclimatological parameter (seeing, isoplanatic angle and coherence time) and the vertical profiles of the refractive index parameter  $C_n^2(h)$ . The sources of these series of data are; the radiosonde measurements stored in the database and the measurements from turbulence monitors such as DIMM and MASS-DIMM instruments.

A radiosonde is a meteorological instrument carried by a balloon to measure pressure and temperature etc. up to an altitude of about 30 km. The Canary Islands has one meteorological observatory to launch such radiosondes every 12 hours and the data packaged in a low resolution are available through the World Wide Web. In this analysis, the meteorological data are used from a station in Tenerife which is about 120km away from the observatory site. The DIMM and MASS-DIMM instruments are two different optical turbulence monitors which can retrieve the astroclimate parameters associated with the optical turbulence such as: total seeing, free seeing, isoplanatic angle and coherence time can build a vertical profile of the optical turbulence parameter  $C_n^2(h)$  (with vertical slabs: 0.5,1,2,4,8 and 16 km). The seeing data and the astroclimate measurements can be retrieved over a long term making available data suitable for a statistical analysis including yearly behaviours. The use of this set of data as the input to the model shows whether or not the simple standard models represent realistic optical turbulence values over variations in climatology conditions. The table 6.1 summarizes the number of nights with data available to perform the statistical analysis in this thesis.

Instrument	Periods
Radiosonde (database)	2144 nights (March 2002 to December 2008)
Robodimm	1404 nights (September 2002 to December 2008)
MASS-DIMM	117 nights (January 2008 to December 2008)

Table 6.1: Summary of the data available to perform post-processing statistical analysis

### 6.2.1 Meteorological data.

The meteorological data used in this research came from several sources ranging from basic equations found in textbooks to more complicated databases and computer programs. Since they are versatile, the equations governing the standard models are easily programmable into any of the more complicated models. The standard profiles are part of both the statistical model and the forecast. The reconstructed

output data are in the form of two vectors: one of  $C_n^2(h)$  values versus the corresponding altitude and the potential temperature  $\theta$  or the Richardson number  $R_i$ . Also available are the astroclimate parameters such as; seeing and isoplanatic angle that can be obtained from the reconstructed  $C_n^2(h)$  profiles from the models.

The vertical measurements of the meteorological parameters can be retrieved from local radiosonde balloon launches as has been done during site testing campaigns conducted by Vernin (Vernin et al, 1992) and others such as; Chun et al. 2009 and McHugh et al. 2008 (Hawaii ) and Sarazin (Paranal, Chile) at many site locations worldwide. Those campaigns are mostly characterized by a short number of launches during specific days and the data were used to give a first approximation to the site characteristics. These profiles have the inconvenience that they cannot be used for long-term statistical analysis. The high cost of balloon launches makes this technique unsuitable for a long period of analysis of the vertical atmosphere and its corresponding astroclimate parameters.

This thesis is based on the collection of free meteorological data from any worldwide meteorological center via free internet access, by which the data can be retrieved from any location given the latitude and longitude e.g., Roque de los Muchachos at lat:  $28^\circ 45'$  and long: W  $17^\circ 53'$ ) or the launch station number, e.g, Canary Islands, Tenerife 60018. To give an idea of the distance between the radiosonde station and the astronomical observatory, a diagram of the Canary Islands is shown in the figure 6.1. The distance between the launch site in Tenerife and the Astronomical observatory at La Palma is about 120 km.

The meteorological data collected come from two main sites;

- The Wyoming University meteorological department has a website: [[http :  
://weather.uwyo.edu/upperair/sounding.html](http://weather.uwyo.edu/upperair/sounding.html)] where a large database of radiosonde data for any site around the world can be searched and retrieved. For the Canary Islands the radiosonde data are retrieved for the station number 60018. These data are stored at two synoptic times: 18:00 UT and 00:00 UT.
- The NCEP center where the meteorological data can be retrieved from any worldwide location given the latitude and longitude of the place of interest.

The data are refined from the NCEP/GFS model and it can be retrieve in the website; [<http://ready.arl.noaa.gov/READYcmet.php>].

The access to the data is via the internet and Figures 6.2 and 6.3 show the web pages to search the data for any date of any year. The output data are saved in a readable ASCII format which can be read by any analysis software such as IDL, matlab or R. The tables 6.2 and 6.3 give a summary of the output data.



Figure 6.1: Location of La Palma and Tenerife, Radiosonde launch site (A) at Tenerife and the La Palma Observatory site at 120 km from the launch site and an altitude of 2400 meters above sea level. Credit. Adapted from Google Earth.

The parameters which can be extracted from the stations are saved in tables with many meteorological parameters versus the altitude. The output data are reduced to the columns with the meteorological parameters used in this thesis, that are; the temperature in (C), altitude (meters), pressure (mb), wind direction (degrees) and wind speed (knots).

### Potential temperature $\theta$ calculated.

The potential temperature ( $\theta$ ) is calculated from the meteorological data using the equation 6.1, that is shown below. And a vertical profile against height is built.

$$\theta = T \left( \frac{1000}{P} \right)^{-0.288} \quad (6.1)$$

Where T is the temperature in Kelvin and P is the atmosphere pressure in millibar (mbar) per each vertical slab.

Pres	Hgth	Temp	Dwpt	Relh	Mix	Drct	Wspd	THAT
[mb]	[m]	[C]	[%]	[%]	[g/kg]	[degree]	[Knots]	[K]
700	3222	13.2	-8.8	21.0	2.82	155.0	8.0	317.1
695	3282	12.8	-8.2	22.0	2.98	155.0	8.0	317.3
635	4030	5.8	-9.9	31.0	2.84	150.0	10.0	317.6
627	4135	4.8	-10.2	33.0	2.82	141.0	11.0	317.6
626	4148	4.7	-10.2	33.0	2.82	140.0	11.0	317.6
582	4731	-0.9	-10.9	47.0	2.89	170.0	13.0	317.8
570	4898	-2.5	-11.0	52.0	2.9	155.0	11.0	317.8

Table 6.2: Example of the output of sounding profile cut from 700 to 570 mb of the data from the station 60018 (Tenerife, Canary Islands ) on 21<sup>st</sup> July 2008 showing the vertical profile for pressure (hPa), temperature (C), wind speed (knots), wind direction (degrees) in significant levels (meters). The data are available for two synoptic time at 12 and 00 UT. The values in the table are; Pres-Pressure, Hgth-Height, Temp-Temperature, Dwpt-Dew point, Relh-Relative humidity, Mix, Drct-wind direction, wsp-wind speed, THAT-Potential temperature (K). Convert knots to  $ms^{-1}$  (1 knots =  $0.514ms^{-1}$ ).



Figure 6.2: Access webpage of the Wyoming Meteorological department. The nearest station is situated in Tenerife ( station number 60018) at 120 kilometer east from the Roque de Los Muchachos Observatory (La Palma Island). Credit <http://weather.uwyo.edu/upperair-sounding.html>

Pres	Hgth	Temp	Dwpt	Drct	Wspd
[mb]	[m]	[C]	[%]	[degree]	[ms <sup>-1</sup> ]
1012	0	21.5	17.9	259.3	3.6
1000	102	20.9	17.0	260.8	4.0
975	321	18.9	15.9	258.6	4.5
950	544	17.3	14.6	255.0	5.3
925	772	15.6	12.9	247.4	6.2
900	1004	14.3	11.1	234.2	7.5
850	1486	12.7	6.3	216.9	11.5
800	1993	10.5	-2.0	214.9	15.1
750	2527	7.3	-9.6	213.5	17.7
700	3090	3.8	-20.7	214.0	19.2
650	3687	-0.3	-32.1	220.8	19.1
600	4322	-4.3	-35.9	235.2	21.3
550	5002	-8.2	-41.3	242.3	25.2
500	5734	-12.9	-40.3	241.5	28.7
450	6529	-18.5	-38.9	242.0	32.9
400	7396	-25.0	-41.6	240.7	36.4
300	9416	-41.5	-51.7	239.1	38.4
250	10628	-50.5	-58.3	245.2	39.5
200	12052	-58.5	-65.4	257.8	42
150	13856	-60.3	-70.9	236.6	32.8
100	16368	-64.8	-81.5	256.1	16.5
50	20501	-65.9	-88.9	346.5	4.4
20	26175	-54.5	-273.1	322.3	6.1

Table 6.3: Output file of sounding profile showing the data vertical distribution using the GFS Sounding for location: 28.45 North 17.48 West, the data are vertical distributed with the temperature, relative humidity, wind speed and wind direction per each vertical value. The data are available for two synoptic times at 12 and 00 UT.

### 6.2.2 Refractive index parameter $C_n^2(h)$ and astroclimato-logical data on site.

In the ORM are many seeing monitors which have been running since 2002 by different institutions and for different purpose; the ING operates one of those DIMM monitors (Robodimm), with the aim of supporting the observations at the ING telescopes. The data on the seeing from the Robodimm measurements are freely available and they can be retrieved from the ING web page. Due to the long period of operations, the values from the Robodimm can be used to do a statistical analysis

Figure 6.3: Using the ARL web interface to retrieve meteorological data. The case of La Palma has longitude and latitude coordinates: latitude: 28.45 degrees, longitude W 17.48 degrees.

of the seeing evolution at the site. This work will use the Robodimm data to compare with the free atmosphere meteorological parameters (temperature and wind speed) where a long term statistics can be obtained. Figure 6.4 shows the two instruments already set up in the tower. In the year 2008 the ING installed a turbulence profiler MASS-DIMM (Tokovinin, 2002) with the aim of obtaining some statistics of the vertical profile of the optical turbulence strength and to help during the observations using the Rayleigh Laser Guide Star (GLAS). The use of LGS is a novel AO technique that helps to correct the wavefront in those fields where there is not a suitable correcting star (NGS). Appendix **D** shows the results obtained during GLAS campaigns. The data from the MASS-DIMM instrument are not freely available but they can be used in this work as part of my current employment with the Isaac Newton Group of Telescopes (ING).

The data from the Robodimm and the MASS-DIMM instrument are stored in a timestamped format with much additional information about the instrument and observing parameters. To work with these data set, they have to be filtered for wrong data acquisition (spikes) or bad computing values and then the interesting

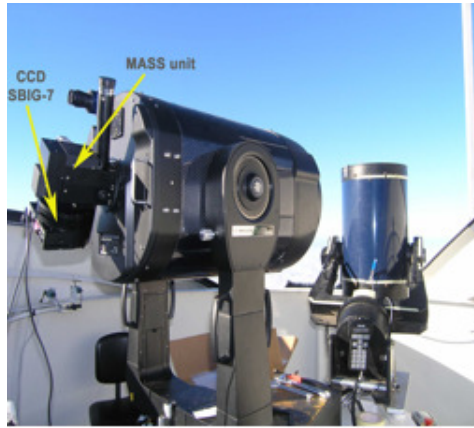


Figure 6.4: MASS-DIMM set up in the tower side by side to the Robodimm.

parameters must be output in a computer-readable manner.

The data retrieved from the Robodimm database and the MASS-DIMM archive are reordered in columns with the values that will be used in the *a posteriori* statistical analysis and modeling. Appendix C shows an example of the raw data format for the Robodimm and MASS-DIMM instruments. The Robodimm output file shows the timestamp column (with date and time) and the median seeing calculated from the longitudinal and transversal values of the seeing. The table 6.4 shows how the final data look, and the storage format.

For the MASS-DIMM, the data are stored in two different archives: one for the DIMM channel and another one for the MASS channel. The DIMM channel gives two seeing measurements which correspond with the transversal values of the seeing, the data are stored in a time stamp format which is shown in the table 6.5, which shows an extracted part of the measurements by the DIMM channel. The MASS channel gives an output file that contains many instruments results, including a part of the free seeing, isoplanatic angle, coherence time and the refraction index for the six height slabs. The filtered data are saved in two new output files which have:

- The timestamp, the free seeing and the  $C_n^2(h)$  values for the height slabs.
- The timestamp, free seeing, isoplanatic angle and the coherence time.

The table 6.4, 6.5, 6.6 and 6.7 show the extracted information for the two MASS-DIMM channels after filtering the dataset.

The seeing data from the robodimm and the DIMM channel are filtered following the 1.5 rms, this remove any possible spikes on the data. For the MASS channel the filtering (Kornilov et al, 2007) procedure takes account of the measurements of the channel D of the photomultipliers which has to be above 100 *pulses*<sup>-1</sup>.

Date	Time	Seeing (arcsec)
3/12/08	20:50:26	2.73
3/12/08	20:53:17	2.38
3/12/08	20:58:54	1.87
3/12/08	21:01:34	1.65

Table 6.4: Seeing measured with the Robodimm after filtering and extracting the median value of the longitudinal and transversal seeing.

Date	Time	<i>Seeing</i> <sub>1</sub>	<i>Seeing</i> <sub>2</sub>
22/4/08	02:47:48	0.97	0.96
22/4/08	02:48:58	0.91	0.92
22/4/08	02:50:08	1.02	1.03
22/4/08	02:51:14	1.07	1.08
22/4/08	02:52:19	1.21	1.23

Table 6.5: Seeing measured from the DIMM channel (MASS-DIMM instrument) This is an extracted portion of the time series for the day 22<sup>nd</sup> April 2008.

## 6.3 Methodology.

The following section describes the background work that had to be completed before the analysis work could begin. It discusses how the data mentioned above are used to produce optical turbulence profiles and other astroclimate statistics and plots, so that the desired comparisons could be made, and it also describes the statistical methods used to quantify these differences.

Date	Time	Fsee	$Cn_1$	$Cn_2$	$Cn_3$	$Cn_4$	$Cn_5$	$Cn_6$
1/7/08	21:55:18	0.4	1.22E-13	1.32E-21	4.28E-18	6.19E-16	9.79E-15	1.72E-14
1/7/08	21:56:26	0.62	2.70E-13	5.37E-23	4.18E-17	6.33E-15	2.45E-15	2.46E-14
1/7/08	21:57:30	0.41	1.32E-13	6.93E-23	2.10E-17	5.09E-16	6.14E-15	1.74E-14

Table 6.6: Output file from the MASS measurements taken on 1st on april 2008, after filtering the file and selecting the interested variables for the post-process analysis. The vertical distribution of the  $C_n^2(h)$  for the 6 six height slabs are represented with  $Cn_1$  corresponds to the height 0.5km and so on. The height slab are; 0.5, 1, 2, 4, 8 and 16 km.

Date	Time	Fsee (arcsec)	Isoplanatic (arcsec)	Coh. time(ms)
19/2/08	21:24:14	0.26	2.59	2.14
19/2/08	21:26:56	0.24	2.65	2.22
19/2/08	21:27:58	0.23	2.6	2.1
19/2/08	21:29:01	0.25	2.36	1.98
19/2/08	21:30:03	0.26	2.3	2.13

Table 6.7: Free seeing, isoplanatic angle ( $\theta$ ) and the coherence time ( $\tau$ ) extracted from MASS-DIMM data on 19<sup>th</sup> February 2008. The output file is filtered and saved to the new output file for the MASS channel.

The scenario of the data presented in the study is shown in table 6.8 and a diagram scheme is presented in figure 6.5, which shows the way to process the data which go through to different statistical analyses and modeling.

Location	Instrument	Season	Local time(UT)	Turb.Profiler	Altitude(Km)
Tenerife	Radiosonde	2002 to 2008	00:00 to 03:00	Climatology	3 to 25
				HV 5/7 and AXP	3 to 25
La Palma	MASS	2008	night to morning twilight	MASS profiler	slabs: 0.5,1,2,4,8,16

Table 6.8: Modelling scenarios for the data.

The models reconstruct the  $C_n^2(h)$  profiles and calculate the  $r_0$  values per radiosonde data every night (00 UTC) and the results are compared with the  $C_n^2(h)$  profiles obtained on site.

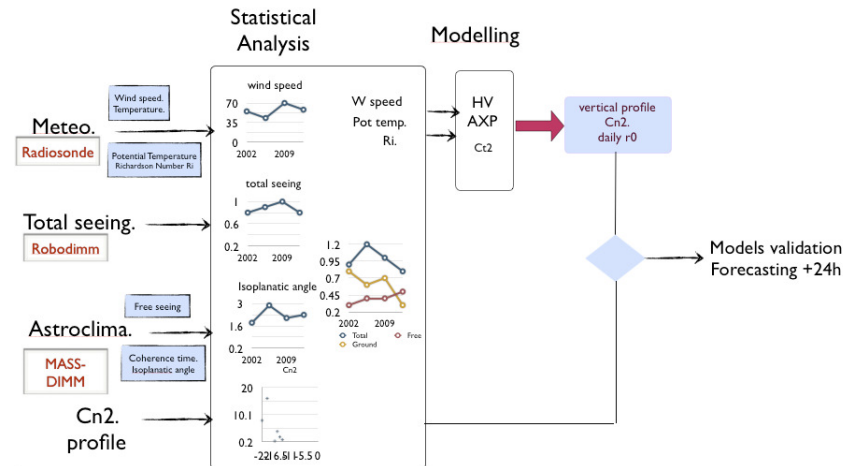


Figure 6.5: Schematic diagram showing the methodology to manipulate the data.

In summary the following step-by-step approach was used for each low-resolution radiosonde data point:

- Calculate the potential temperature.
- Calculate the Potential refractive index gradients  $M$ .
- Create a data subset for wind speed, temperature and potential temperature with height resolution of 1km.
- Calculate the structure constant  $C_n^2(h)$  profile using H-V and AXP models.

As radiosonde measurements do not have values for the same heights, performing statistics on the dataset requires mapping of the  $C_n^2(h)$  to fixed heights with 1000 meter spacing. This makes it possible to arrange all data in a histogram per short periods (days and months) or large periods (years) and making it readily apparent at which values the various percentiles are and how they compare to each other. Moreover, probability distribution functions (pdf) may easily be derived for each height as cross-sections of this histogram.

The potential refractive index "vertical gradient",  $M$ , is needed to compute the refractive index structure constant  $C_n^2(h)$ . This is not a "full" gradient, meaning it does not comprise all derivatives with respect to all variables which the refractive

index is dependent on. This is because the only relevant gradient, or variation of the refractive index, is the one due to turbulence alone.

The expression for the potential refractive index can be expressed following the Warnock and VanZandt (1985) equations, where  $M$  is defined as;

$$M = -\frac{77.6^{-6}p}{T} \frac{\partial \ln \theta}{\partial z} \left(1 + \frac{15000}{T} q - \frac{15000}{2T} \frac{d\theta/dz}{\partial \ln \theta / \partial z}\right) \quad (6.2)$$

where  $\theta$  is the potential temperature,  $p$  is the pressure and  $q$  the specific humidity; in a dry adiabatic atmosphere the parameter  $q$  can be neglected.

With this expression,  $C_n^2(h)$  can be calculated using Tatarski (1971) and it forms the base for most of the modeling analysis:

$$C_n^2 = a^2 A L_0^{4/3} M^2 \quad (6.3)$$

where  $a^2$  is a dimensionless constant between 1.5 and 3.5, but most commonly used with a value of 2.8 (Monin and Yaglom, 1971),  $A = \frac{k}{k_m}(1 - R_i)$  is a numerical constant generally considered equal to unity.  $L_0$  is the outer scale of turbulence, which has been set equal to the resolution of the radiosonde data. The outer scale has been nominally defined for La Palma as equal to 11.9m (Abahamid, et al. 2004).

The total seeing data, the astroclimate parameters and the  $C_n^2(h)$  profiles from the MASS channel are analysed and normalized to the total energy of the turbulence. The ground contributions are calculated and normalized to the total atmosphere turbulence. The following sections described the mathematical equations used to retrieve and normalize the refractive index values.

### 6.3.1 Seeing from the refractive index values.

The MASS measures the turbulence distribution at six heights (0.5, 1, 2, 4, 8 and 16 km) where each layer represents an integral of the turbulence  $J_i$  measured in  $m^{1/3}$  where the refraction index structure constant  $C_n^2(h)$  is measured in  $m^{-2/3}$  and with a weight function  $W(h)$  that is characterized by the instrument response (Tokovinin et al. 2003).

$$J_i = \int_{layer} C_n^2(h)W(h)dh \quad (6.4)$$

The seeing can be calculated for each atmosphere layer using the following expression;

$$\theta_i = \left( \frac{J_i}{6.8 \cdot 10^{-13}} \right)^{0.6} \quad (6.5)$$

### 6.3.2 Surface layers seeing.

The surface layers seeing is retrieved from the measurements of the free seeing (above 0.5 km) calculated by the MASS channel and the total seeing measured by the DIMM channel, the mathematical relationship that relates the two quantities is;

$$\varepsilon_{surface} = \left( \varepsilon_{total}^{5/3} - \varepsilon_{free}^{5/3} \right)^{3/5} \quad (6.6)$$

### 6.3.3 Normalization of the Turbulence energy.

The DIMM delivers the total integral turbulence energy  $C_n^2(D)$  in the column of atmosphere observed. This means that  $C_n^2(D)$  and the sum of the  $C_n^2(i)$  of the restored layers must be equal. The energy of the ground layer can be defined as;

$$C_n^2(GL) = C_n^2(D) - \sum_{i=1}^6 C_n^2(i) \quad (6.7)$$

so the normalization of the layers proportionally to their fraction of the layers is defined as;

$$f_{racGL(i)} = \frac{C_n^2(i)}{\sum_{i=1}^6 C_n^2(i)}, \quad for \ i = 1, 2, 3 \quad (6.8)$$

Thus, the final values of the energy of the layers 1 to 6 becomes;

$$C_n^2(i) = C_n^2(GL) \cdot f_{rac,GL(i)}, \quad for \ i = 1, 2, 3 \quad (6.9)$$

### 6.3.4 Turbulence profile.

The turbulence profile is normalized by the thickness  $\Delta h_i$  of each layer, dividing the integral of the energy  $C_n^2(h)$  in  $(m^{1/3})$  and by  $\Delta h_i$  in (m). Then;

$$\langle C_n^2(i) \rangle = \frac{C_n^2(i)}{\Delta h_i}, \text{ for } i = 1, 2, 3, 4, 5, 6 \quad (6.10)$$

### 6.3.5 Percentage of energy in each layer.

The percentage of turbulent energy in each layer is calculated using the elementary expression;

$$\%C_n^2(i) = \frac{C_n^2(i)}{\sum_{i=1}^6 C_n^2(i)} 100, \text{ for } i = 1, 2, 3, 4, 5, 6 \quad (6.11)$$

We also calculate the total percentage of energy in the ground layer and in the free atmosphere as follows;

$$\%C_n^2(GL) = \frac{\sum_{i=1}^3 C_n^2(i)}{\sum_{i=1}^6 C_n^2(i)} 100 \quad (6.12)$$

$$\%C_n^2(FA) = \frac{\sum_{i=4}^6 C_n^2(i)}{\sum_{i=1}^6 C_n^2(i)} 100 \quad (6.13)$$

### 6.3.6 Fried Parameter ( $r_0$ ).

The Fried radius in (cm) is calculated applying known formulas from Roddier (1981) and Roddier (1989).

$$r_0 = \left[ (6.6729 \cdot 10^{13}) \sum_{i=1}^6 C_n^2(i) \right]^{-3/5} \quad (6.14)$$

### 6.3.7 Total seeing ( $\varepsilon$ )

The total seeing in (arcsec) is retrieved directly from the DIMM channel and the Robodimm instrument. The seeing measurements are taking the wavelength 550nm and corrected to zenith.

$$\varepsilon = 0.98 \left( \frac{\lambda}{r_0} \right) \quad (6.15)$$

where  $\lambda = 550nm$ .

### 6.3.8 Cumulative ascending and descendant seeing.

The calculation of the cumulative seeing starts from the ground layer (ascending, +), and from the free atmosphere (descendant, -). For a j-th layer ( $j = 1, 2, \dots, 6$ ) the considered  $C_n^2(h)$  for the calculation of  $r_0$  and therefore the seeing is expressed by the following formulas;

$$C_{n,+}^2 = \sum_{i=1}^j C_n^2(i) \quad (6.16)$$

$$C_{n,-}^2 = \sum_j^{i=6} C_n^2(i) \quad (6.17)$$

# Chapter 7

## Data and Analysis

*"Nor is it strange if the Earths exhalation is of every sort and diverse, when in the sky too color of objects is not uniform, but rather the red of the Dog Star is piercing, while that Mars is mild and Jupiter has none, its glow being translated into clear light."*  
*Seneca, "Naturals Quaestiones 1.1.7" (225 a.c.)*

---

### 7.1 Overview.

To characterize the optical turbulence and the quality of an astronomical site the value of the seeing is normally used as an indicator of the sky quality, but there are other values such as the astroclimate parameters that have to be considered. Those parameters include the isoplanatic angle ( $\theta$ ), the coherence time ( $\tau$ ) and the wavefront outer scale  $L_0$ . Taking long term measurements of meteorological data (e.g., in the upper atmosphere) and comparing those with astroclimate parameters the evolution of the sky conditions and the optical turbulence can be determined. Also the data can be analyzed and used to determine the dominant parameter for the astronomical image quality. The meteorological parameters can be defined at ground level or in the upper air with each having a different contribution to the image quality. But considering the upper atmosphere and the wind in that region as the

main meteorological parameter, a long term analysis can be built and compared with the astroclimate parameters.

This Chapter analyses the statistics for the astroclimate parameters (seeing, isoplanatic angle and coherence time) and the meteorological vertical profiles for the wind speed and temperature. Also it shows the relationship between the meteorological parameters and the astroclimate parameters and its influence on the optical turbulence.

The first approach is the summary of the seeing statistics from the Robodimm measurements covering 7 years starting in 2002 and finishing in 2008, and the MASS-DIMM measurements of the astroclimate parameters (free seeing, isoplanatic angle and coherence time) and refractive index  $C_n^2$  profiles for the year 2008. The statistics results are plotted in different way to show the seasonality of the seeing and the time evolution over the years. A correlation plot of the astroclimate parameters is shown. The second part gives the statistics of the wind speed and its correlation with the astroclimate parameters. The third part shows the relationship of the temperature variation with the refractive index and the use of the Heffter criteria to determine a possible model correlation between the temperature and the  $C_n^2$ .

## 7.2 Turbulence measurements.

### 7.2.1 Astroclimate coherence length "Seeing". Robodimm data.

The seeing data are collected from the ING seeing database with a total of 161995 measurements on 1059 nights of 6 years observations (from 2003 to 2008). The measurement of the seeing has been in automated operation since the middle of 2002 and has been working all year around. The instrument has shown a robustness in operations giving good long term data recording with a loss of 5% of the operational time due to bad weather and technical problems. Table 7.1 shows the monthly statistics of seeing and its standard deviation for the years 2002 to 2008.

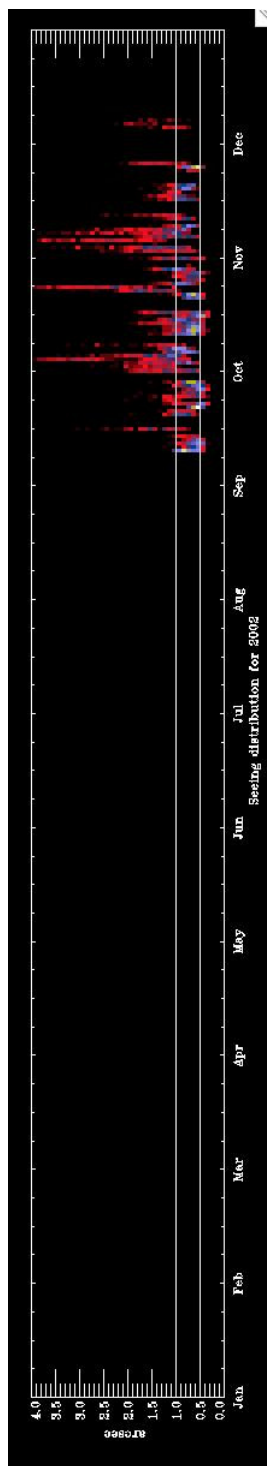
The DIMM instrument is a suitable tool for the statistical analysis of the evo-

lution of the atmospheric turbulence over the years due to its easy method of operation such that it can be remotely or robotically operated, giving long term of data which cover more than 5 years. The seeing measurement from the Robodimm is archived and is available for all user (public access) via the web page (<http://catsserver.ing.iac.es/weather/index.php?zoom=robosee>). The public access to the raw data makes the post-processing analysis more interesting, where the data can be extracted and processed with many analysis algorithms and the results of the analysis can be different from those data where the access to the data is restricted and the data available is already processed.

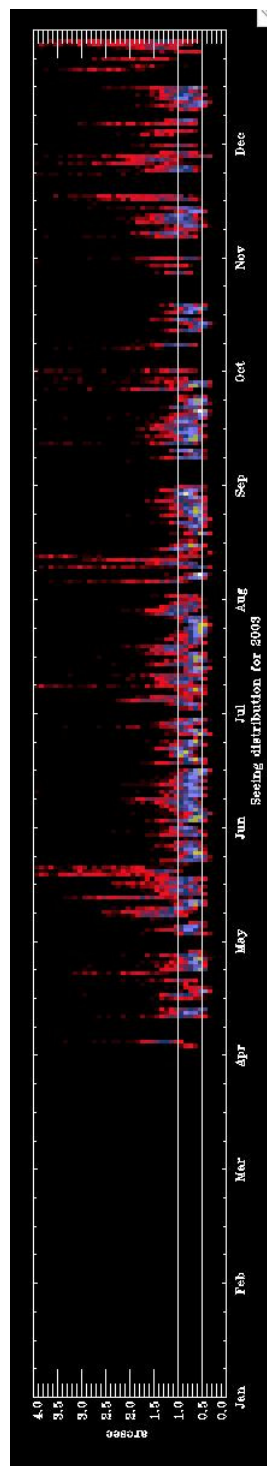
In order to have a visual view of the seeing evolution, the seeing measurements are analyzed using the daily distribution for all the years and representing them in a 2D distribution. The set of plots in Figure 7.1 shows the 2D distribution of the seeing for every day through the years where the values of the daily seeing are reduced to a histogram and the result is fitted to a gaussian giving the maximum density of the daily seeing. The density of the seeing values is represented in color gradient where the low density is represented in red to high density in white.

Month	2002	2003	2004	2005	2006	2007	2008
Jan	No data	No data	No data	$1.13 \pm 0.68$	$1.72 \pm 0.72$	$1.58 \pm 0.79$	$1.12 \pm 0.4$
Feb	No data	No data	$1.48 \pm 0.85$	No data	$0.77 \pm 0.28$	$1.13 \pm 0.58$	$1.25 \pm 0.5$
Mar	No data	No data	$1.09 \pm 0.43$	$1.11 \pm 0.67$	$1.15 \pm 0.62$	$1.16 \pm 0.46$	No data
Apr	No data	$0.91 \pm 0.43$	$1.0 \pm 0.36$	$0.98 \pm 0.42$	$1.06 \pm 0.57$	$1.02 \pm 0.38$	$1.32 \pm 0.5$
May	No data	$1.17 \pm 0.79$	$1.13 \pm 0.47$	$1.00 \pm 0.50$	$0.87 \pm 0.14$	$1.17 \pm 0.64$	$0.93 \pm 0.5$
Jun	No data	$0.83 \pm 0.25$	$0.96 \pm 0.42$	$0.9 \pm 0.47$	$0.89 \pm 0.35$	$0.97 \pm 0.53$	$0.91 \pm 0.3$
Jul	No data	$0.88 \pm 0.40$	$0.94 \pm 0.49$	$0.89 \pm 0.38$	$0.88 \pm 0.31$	$0.90 \pm 0.55$	$0.73 \pm 0.3$
Aug	No data	$0.92 \pm 0.56$	$0.80 \pm 0.35$	$0.84 \pm 0.36$	$0.89 \pm 0.41$	$0.80 \pm 0.44$	$0.72 \pm 0.2$
Sep	$0.76 \pm 0.28$	$0.91 \pm 0.63$	$0.99 \pm 0.52$	$0.86 \pm 0.51$	$0.78 \pm 0.30$	$0.76 \pm 0.37$	$0.78 \pm 0.3$
Oct	$1.11 \pm 0.62$	$1.05 \pm 0.74$	$1.15 \pm 0.65$	$0.68 \pm 0.18$	$0.77 \pm 0.42$	$1.02 \pm 0.55$	$1.45 \pm 1.0$
Nov	$1.274 \pm 0.73$	$1.20 \pm 0.53$	$1.17 \pm 0.86$	$1.0 \pm 0.56$	$0.93 \pm 0.57$	$1.01 \pm 0.32$	$1.35 \pm 0.7$
Dec	$1.35 \pm 0.35$	$1.23 \pm 0.62$	$1.99 \pm 0.90$	$1.19 \pm 0.57$	$1.22 \pm 0.50$	$1.42 \pm 0.47$	$1.41 \pm 0.8$

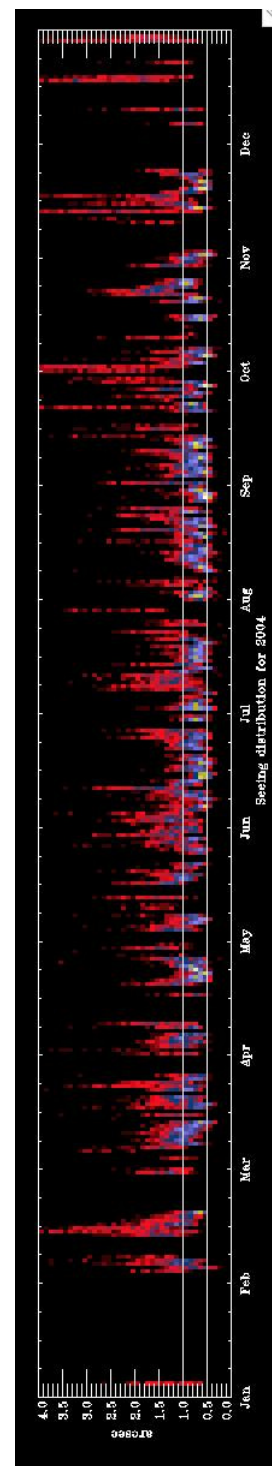
Table 7.1: Monthly distribution of the seeing (arcseconds) through the years 2002 to 2008. The months with no data available are due to the Robodimm either not running or a performing only a few sporadic data acquisitions per night.



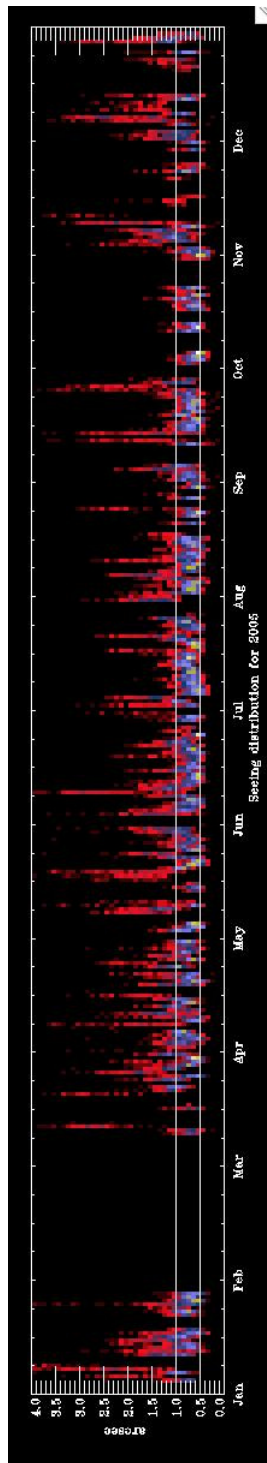
(a) 2002



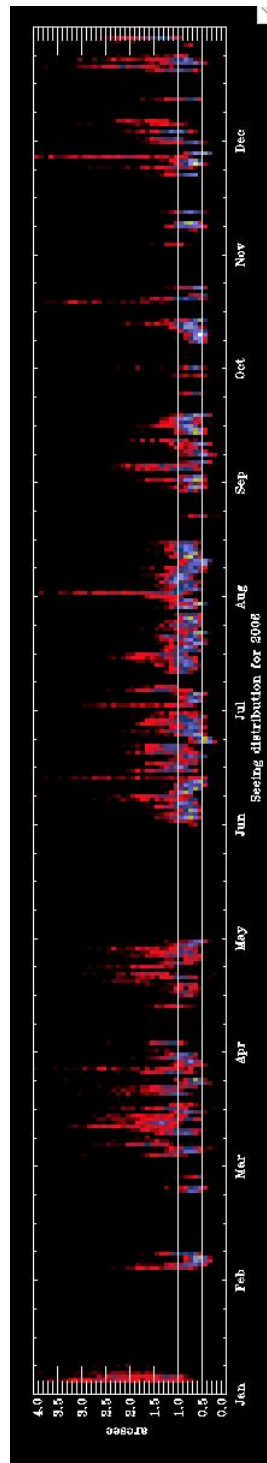
(b) 2003



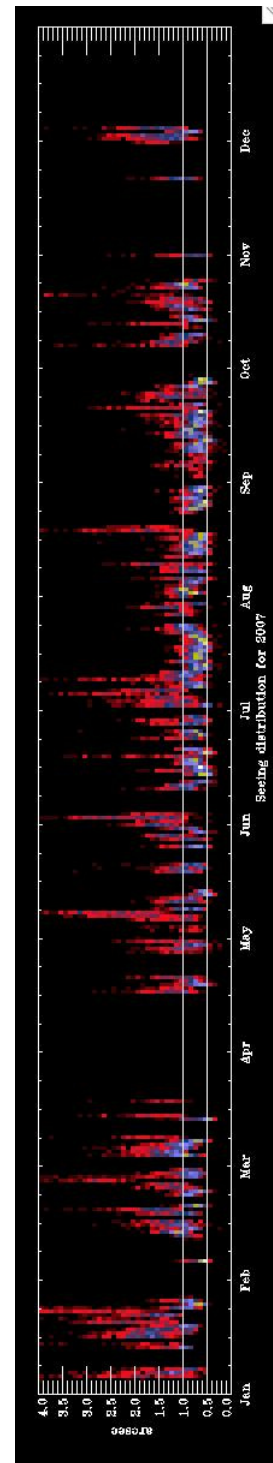
(c) 2004



(d) 2005



(e) 2006



(f) 2007

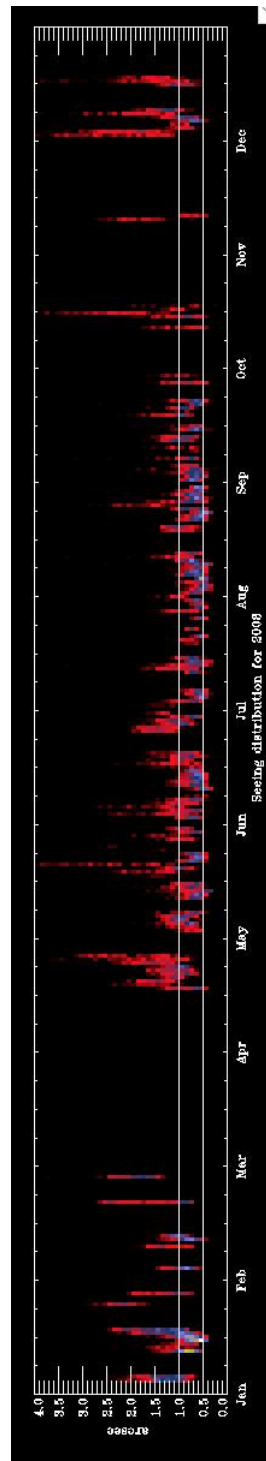


Figure 7.1: 2D distribution of the evolution of the seeing through the years 2002 to 2008. The gradient colors show the intensity of the distribution of the measurements.

A summary of the seeing evolution over the years is provided in figure 7.2, which shows the monthly mean along with the standard deviation. The statistical analysis

is carried out by grouping the measurements for each month and filtering the data with a value of 1.5 sigma deviation (described in Chapter 6) to avoid any artifacts in the time series. A more extended statistical analysis is shown in Appendix C.

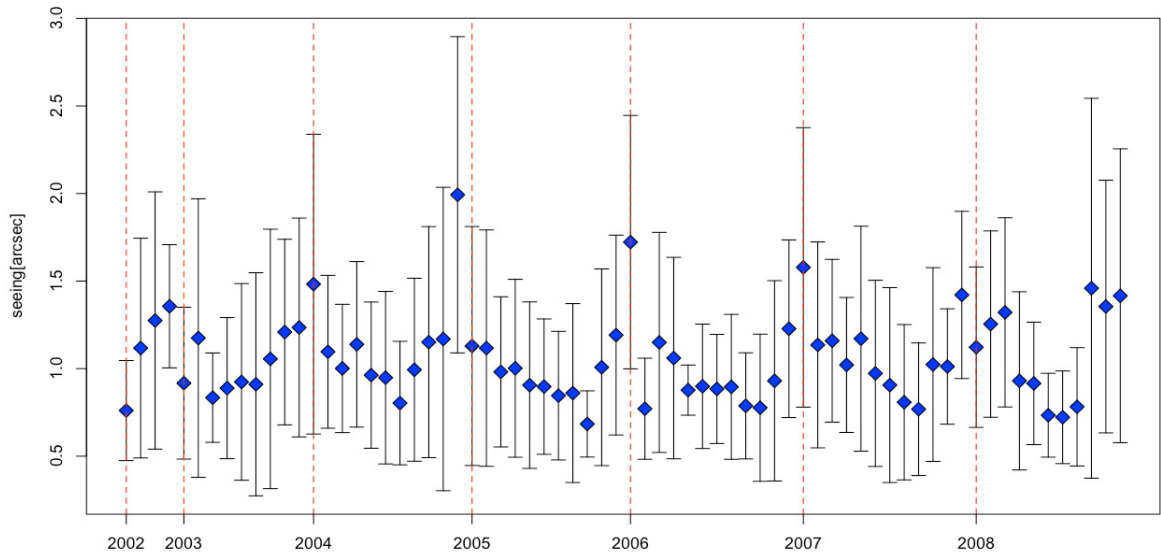


Figure 7.2: Monthly seeing distribution retrieved from the Rododimm data from September 2002 to December 2008 showing the standard deviation in vertical bars.

The statistics of the time series of the seeing measurements can be represented in many ways and a useful plot is shown in figure 7.3, where the monthly seeing is grouped per year, and fitted with a regression linear shown as a smooth line for the median monthly seeing. This representation shows an interesting figure showing the minimum of the fitting line in the year 2005. The grey shadow regions shows the 95% confident interval.<sup>1</sup>

A common way to present the statistics of the seeing yearly distribution is a cumulative distribution; the following figure 7.4 shows this cumulative distribution for the daily mean seeing of the whole dataset (2002 to 2008) and for two distinct periods which are summer (June to September) and winter (November to March).

<sup>1</sup>Assuming the error term in the linear regression model is independent of  $x$  and is normally distributed with zero mean and constant variance. For a given value of  $x$ , the interval estimate for the mean of the dependent variable  $y$  is the confidence interval.

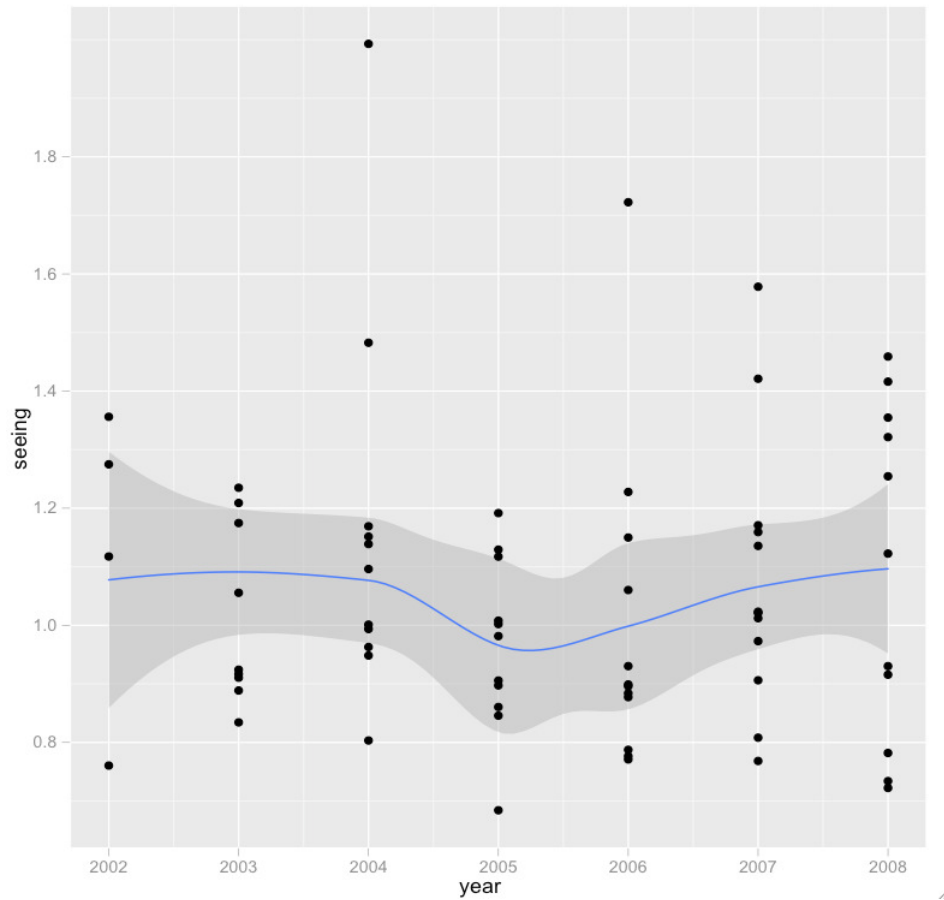


Figure 7.3: Representation of the monthly seeing distribution for 2002 to 2008. The blue line represent the median values and the shadows are the 95% confident intervals.

Table 7.2 summarizes the median, the first and third quartiles for the whole daily median for the total and these two periods.

The macro-data values for the seeing give a yearly evolution and show the possible changes in the seeing patterns over the years. There is a clear seasonal contribution to the seeing during the year with a good and stable seeing during the summer time. The cumulative distribution of the seeing split into two terms, summer and winter, shows better seeing conditions during the summer term. This result can

Quartile seeing		
Whole year	25%	0.68
	50%	0.86
	75%	1.16
Winter	25%	0.78
	50%	1.02
	75%	1.41
Summer	25%	0.63
	50%	0.78
	75%	0.99

Table 7.2: Statistical values for the median (50%), first (25%) and third quartiles (75%) of the total daily average seeing (arcseconds) parameter above Roque de Los Muchachos Observatorio. The two periods summer and winter represents the months; Summer (June to September ) and winter (November to March).

be seen in figure 7.5, which is a representation of the Box-Whisker boxplot <sup>2</sup>of the monthly distribution of the seeing and its variability by months for all the seeing data measured years. The seeing values are grouped per month showing clearly the better conditions during the summer time.

### **7.3 Astroclimate parameters; seeing, isoplanatic angle and coherence time. MASS-DIMM data.**

The astroclimate parameters were obtained during the MASS-DIMM campaigns in the year 2008 where the instrument was running in continuous operation. A MASS-DIMM instrument description is given in Chapter 4 and the data retrieved for the two channels instrument are: the total seeing, isoplanatic angle, coherence time,

---

<sup>2</sup>A way of representing the distribution of a set of data; a solid box is drawn whose left and right edges correspond to the quartiles, with a mark inside it to show where the median is. Two 'whiskers' are attached to the sides of the box, to show the overall range of the data.

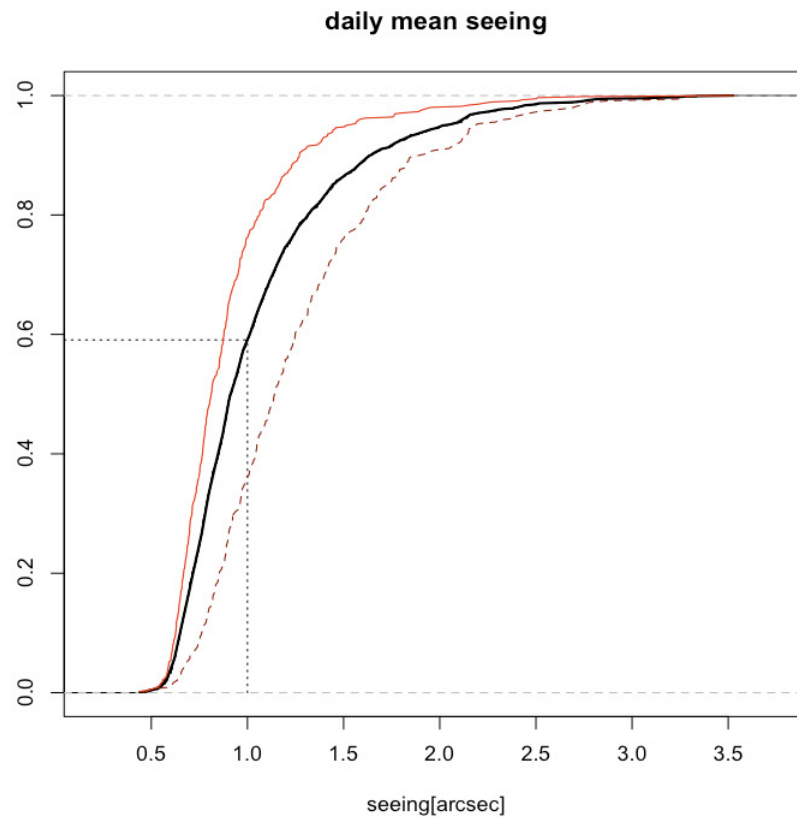


Figure 7.4: Cumulative distribution of the seeing parameter for a daily average of the whole data set. The red line: summer time. The red dash line: winter time.

the restored free seeing and the vertical profile of the refractive index turbulence parameter.

### 7.3.1 Data-Set.

The data collected and analyzed so far are for observations related to 148 useful nights (Table 7.3) spread out over 2008. The MASS-DIMM operation is scheduled depending on the ING observational requirements and to cover most of the year with good sampling. The instrument is not so robust as to operate during strong wind (more than  $30 \text{ kmh}^{-1}$ ) conditions and the measurement acquisition is halted until the weather conditions improve, also the sky transparency is an important issue and for nights with thick cloud passing or partially covered sky the instrument stops and it will restart the operations when the sky improves in transparency or

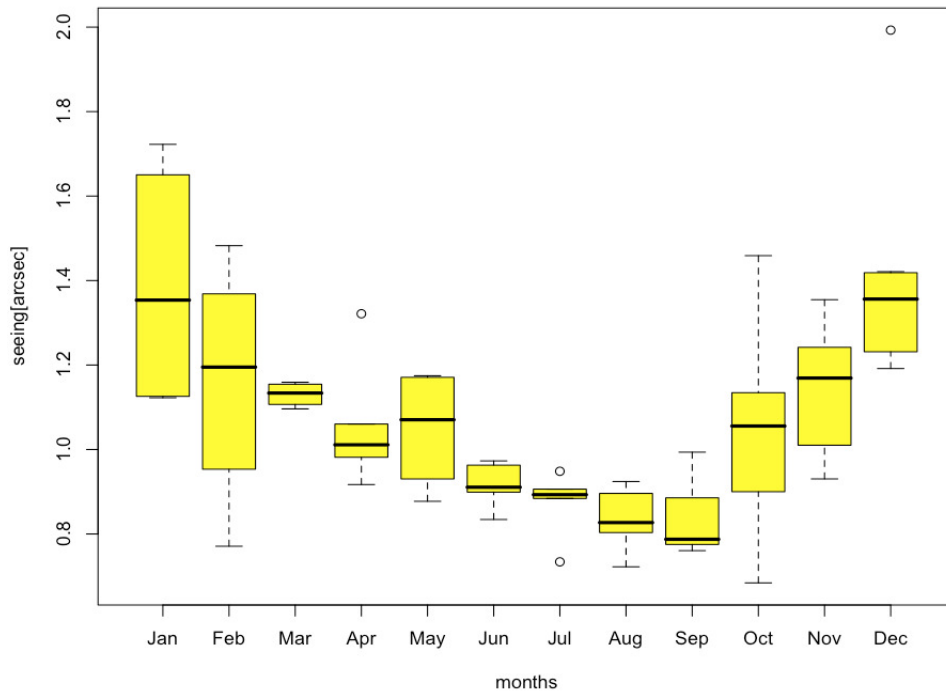


Figure 7.5: Boxplot representation of the whole dataset of the seeing values from 2002 to 2008 with a monthly distribution for all the years. The best months are August and September with the lowest median values, but July show a less variability.

stop for the rest of the night. These kind of sky conditions lead to non-continuous data acquisition and introduce gaps (spikes) in the data saving.

The weather conditions are the bigger constraints on the observations of the MASS-DIMM instruments and depending on the weather during a year the number of useful nights increases or decreases.

### 7.3.2 MASS Channel.

The statistics of the free seeing, isoplanatic angle and the coherence time for the year 2008 are shown in a boxplot representation, which gives a good view of the statistical evolution of the parameters. Looking at the set of figures; figures 7.6, 7.7 and 7.8 for free seeing, isoplanatic angle and coherence time respectively a seasonal behavior can be observed showing better values during the summer term.

A summary of the astroclimatic parameters for the median, first quartile and

Observing Nights	
January	12
February	8
March	Out of operations
April	6
May	16
June	14
July	19
August	22
September	11
October	9
November	13
December	14

Table 7.3: Number of suitable nights observed during the year 2008 with the total of 148 nights.

third quartile is shown in table 7.4 for the total number of samples for the whole year and for the two periods (summer and winter).

A statistical summary of the astroclimate parameters, including the total seeing measured with the DIMM channel, is collected in table 7.5 for the measurements over the year 2008. The monthly median values are shown.

Looking at the figures 7.6, 7.7 and 7.8, a clear seasonal variation appears evident for all the integrated astroclimatic parameters. Identifying periods of extreme good conditions (e.g. June with a low free median seeing and large isoplanatic angle.) over such long time during the same periods of the years indicates that there is a highly probability of having a better turbulence conditions at such time.

Comparing this result with a synoptic area (or macroscale area) of the wind speed at the troposphere about 15 km, there is an agreement with upper wind speed. Under these conditions there is a low probability of triggering optical turbulence in the high atmosphere confirmed by the weaker  $C_n^2$  values (next Section) and large isoplanatic angle. The tables 7.6 and 7.7 summarize the monthly statistics for the

Quartile		Free seeing(")	Iso angle(")	Coh.time(ms)
Whole year	25%	0.27	1.85	2.8
	50%	0.36	2.21	5.88
	75%	0.51	2.75	8.58
Winter	25%	0.3	1.74	2.2
	50%	0.4	2.0	3.28
	75%	0.58	2.44	5.48
Summer	25%	0.24	1.9	5.64
	50%	0.315	2.49	7.89
	75%	0.39	3.1	11.18

Table 7.4: Statistics of the astroclimate parameters (free seeing, isoplanatic angle and coherence time) obtained with the MASS channel for the 1<sup>st</sup> (25%), 2<sup>nd</sup> (median) and 3<sup>rd</sup> (75%) quartiles. Statistics are applied to the whole year and two different periods. Summer(June, July, August and September) and winter (November, December, January, February and March). The free seeing and isoplanatic angle are measured in arcseconds and the coherence time in milliseconds.

astroclimate parameters, isoplanatic angle and coherence time for the year 2008.

The isoplanatic angle (see figure 7.7) shows a yearly seasonal behavior where the best period is during the summer months. Table 7.5 shows the vales of the mean of the monthly astroclimate parameter for the year 2008 and it is indicating that the atmospheric stability in the upper layers is consistent with the summer anticyclonic settled in the Azores Islands<sup>3</sup> producing less influence of the jet stream on the upper atmosphere above the Canary Islands and especially on the ORM.

The MASS-DIMM instrument and its measurements of the vertical profiles of the  $C_n^2$  provides the possibility of integrating the seeing in different vertical slabs. Considering that the MASS-DIMM gives measurements for the vertical slabs (0.5, 1, 2, 4, 8 and 16 km), the free seeing could be split into; Boundary seeing and Free seeing. The Boundary seeing is the integral of the seeing for the first 2 km and the

<sup>3</sup>Azores Islands are located in the North West from La Palma at a distance about 500 km away in the Atlantic Ocean.

Month	Total seeing(")	Free seeing(")	Iso angle(")	Coh.time(ms)
January	1.16	0.44	1.9	4.12
February	1.05	0.47	1.8	1.6
April	1.2	0.58	2.4	7.7
May	0.84	0.4	1.9	2.5
June	0.75	0.26	3.1	8.4
July	0.8	0.31	2.7	9.0
August	0.78	0.35	2.2	7.7
September	0.8	0.35	1.7	6.0
October	0.87	0.48	2.2	9.7
November	1.1	0.32	2.3	2.8
December	1.05	0.37	2.2	4.1

Table 7.5: Statistics of the astroclimate parameters (free seeing, isoplanatic angle and coherence time) obtained with the MASS channel for the 1<sup>st</sup>(25%), 2<sup>nd</sup> (median) and 3<sup>rd</sup> (75%) quartiles. Statistics are applied to the whole year and two different periods. Summer(June, July, August and September) and winter (November, December, January, February and March). The free seeing and isoplanatic angle are measured in arcseconds and the coherence time in milliseconds.

Free seeing is the integral of the optical turbulence above 2km (slabs: 2, 4, 8 and 16 km). The monthly statistics of these two free seeing components is shown in the table 7.8 (below).

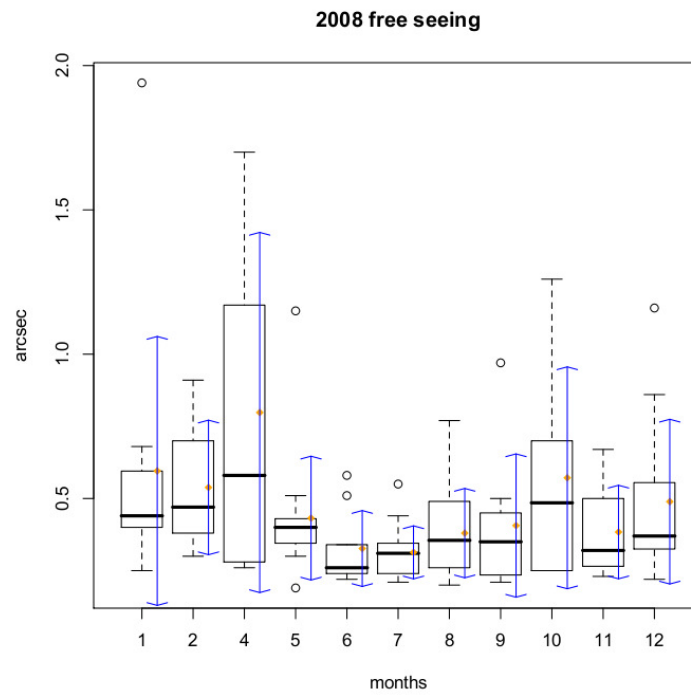


Figure 7.6: Boxplot of the free seeing for the whole year 2008 showing the monthly distribution. The orange dots represent the median and the blue bars are the standard deviation. The x-axis represents the months by numbers (1 to 12; January to December), the y-axis represents the free seeing in arcsecs retrieved from  $C_n^2$  profiles obtained with the MASS-DIMM instrument. There is no data for the month 3 (March).

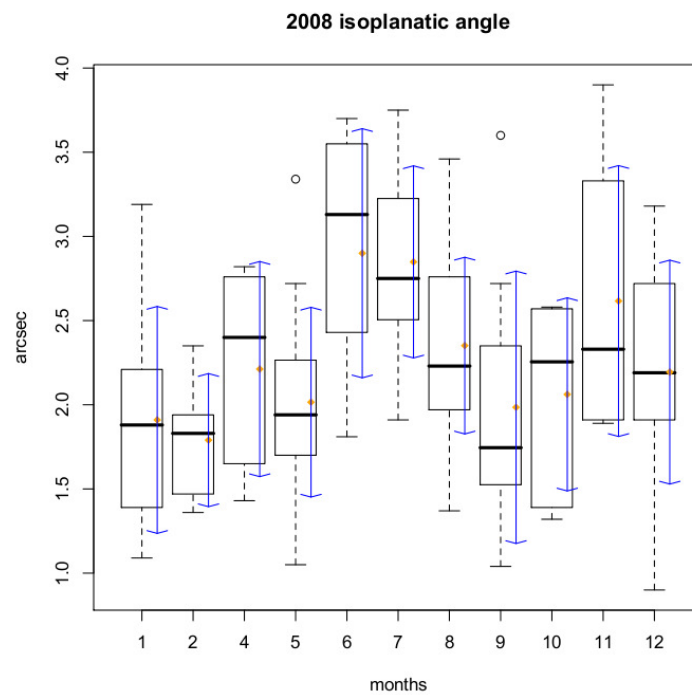


Figure 7.7: Statistical analysis of the isoplanatic angle for the year 2008. Data retrieved from the MASS-DIMM instrument. The x-axis represents the months ( 1- January to 12- December) and y-axis represents the isoplanatic angle measured in arcseconds. There is no data for March (3).

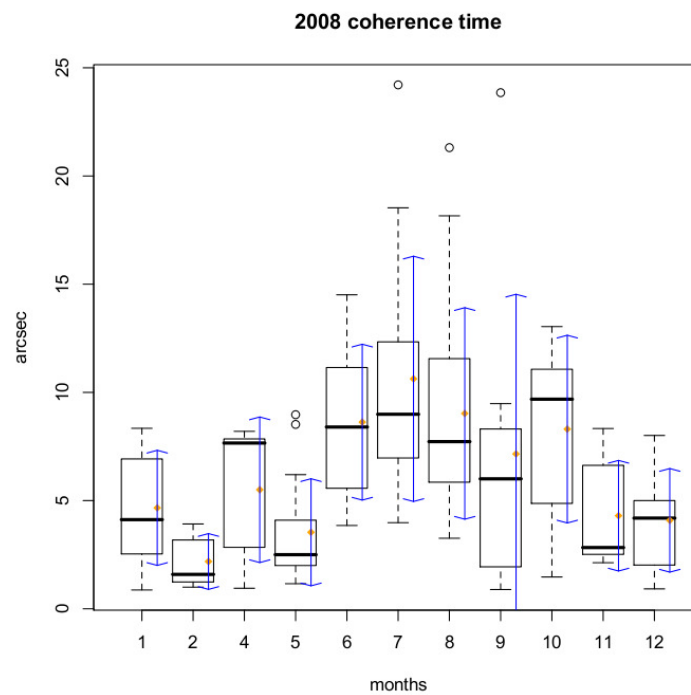


Figure 7.8: Statistical analysis of the coherence time for the year 2008. Data retrieved from the MASS-DIMM instrument. The x-axis represents the months (1- January to 12- December) and y-axis represents the coherence time in seconds. There is no data for March (3).

Month	1 <sup>st</sup> Quartile	Median	3 <sup>rd</sup> Quartile	St.dev
January	1.39	1.88	2.21	0.67
February	1.47	1.83	1.94	0.39
March	No data	No data	No data	No data
April	1.65	2.4	2.76	0.63
May	1.70	1.94	2.26	0.56
June	2.43	3.13	3.55	0.74
July	2.50	2.75	3.22	0.57
August	1.97	2.23	2.73	0.52
September	1.52	1.74	2.16	0.81
October	1.57	2.25	2.52	0.57
November	1.92	2.33	3.2	0.80
December	1.95	2.19	2.61	0.66

Table 7.6: Summary of the monthly statistics of the isoplanatic angle for a time series evolution of the parameter through 2008.

Month	1 <sup>st</sup> Quartile	Median	3 <sup>rd</sup> Quartile	St. dev
January	2.53	4.12	6.92	2.65
February	1.24	1.59	3.18	1.28
March	No data	No data	No data	No data
April	2.84	7.66	7.85	3.36
May	6.58	8.6	12.0	5.55
June	2.0	2.5	4.09	2.47
July	6.97	8.99	12.33	5.66
August	5.86	7.72	11.25	4.88
September	2.54	2.83	6.0	2.55
October	5.84	9.68	10.95	4.33
November	2.54	2.83	6.0	2.55
December	2.21	4.19	4.95	2.39

Table 7.7: Summary of the monthly statistics of the coherence time for a time series evolution of the parameter through 2008.

6 Layers (Boundary + Free)						4 Layers (Free)				
Month	Min	1 <sup>st</sup> Q	Median	3 <sup>rd</sup> Q	Max	Min	1 <sup>st</sup> Q	Median	3 <sup>rd</sup> Q	Max
January	0.129	0.332	0.465	0.641	5.26	0.0760	0.25	0.375	0.564	1.556
February	0.164	0.321	0.43	0.678	2.41	0.159	0.294	0.385	0.539	1.92
March	No Data	No Data	No Data	No Data	No Data	No Data	No Data	No Data	No Data	No Data
April	0.135	0.32	0.670	1.25	5.43	0.079	0.184	0.244	0.664	1.52
May	0.104	0.343	0.435	0.543	2.43	0.092	0.251	0.331	0.421	1.424
June	0.093	0.242	0.297	0.405	3.8	0.067	0.145	0.195	0.292	1.909
July	0.0748	0.25	0.320	0.424	1.94	0.053	0.163	0.245	0.348	1.435
August	0.125	0.253	0.329	0.478	2.09	0.083	0.218	0.29	0.402	1.563
September	0.11	0.277	0.381	0.55	1.73	0.087	0.232	0.347	0.510	1.613
October	0.12	0.305	0.455	0.799	6.38	0.11	0.221	0.272	0.408	1.605
November	0.140	0.27	0.365	0.5	3.45	0.104	0.206	0.270	0.377	0.9041
December	0.126	0.310	0.407	0.69	5.36	0.108	0.245	0.331	0.517	1.624

Table 7.8: Statistical analysis of the free seeing through 2008 with the contribution of the boundary seeing and free seeing. The 1<sup>st</sup> Q. and 3<sup>rd</sup> Q. represent the first and third quartiles. The free seeing is measured in arcseconds.

### 7.3.3 DIMM Channel.

The DIMM channel provides the seeing measurements at the same time on the MASS channel is getting the  $C_n^2$  profile and the integrated astroclimate parameters. We consider the same number of suitable nights as when the MASS channel is used to perform the statistics analysis. The seeing statistics for the year 2008 is summarized in table 7.9 with the first and third quartiles, and it is represented in figure 7.9 showing seasonal behaviors with the best values during the summer time and the best month July; the worst seeing is during the winter term and the worst month is April.

Month	1 <sup>st</sup> Quartile	Median	3 <sup>rd</sup> Quartile	St. dev
January	0.78	1.01	1.40	0.46
February	0.86	1.06	1.59	0.53
March	No data	No data	No data	No data
April	0.93	1.32	1.65	0.56
May	0.71	0.87	1.1	0.44
June	0.64	0.79	1.20	0.36
July	0.64	0.78	0.97	0.37
August	0.64	0.76	0.95	0.64
September	0.73	0.84	1.05	0.29
October	0.73	0.92	1.44	0.64
November	0.75	0.96	1.32	0.44
December	0.81	1.06	1.54	0.56

Table 7.9: Statistics summary of the seeing measured with the DIMM channel for measurements in the year 2008. Measure in arcseconds

The instrument measures the seeing every minute and the statistical analysis can be set from the mean value of 10 minutes. Pooling the total data into different time bins (10,20,30,40,50 and 60 minutes), the variance of the seeing in those bin indicates the stability period where the atmosphere turbulence is more steady. Table 7.10 shows the variance over the time. This value of stability of the atmosphere is depending of the local orography and the wind direction for the measurements taken

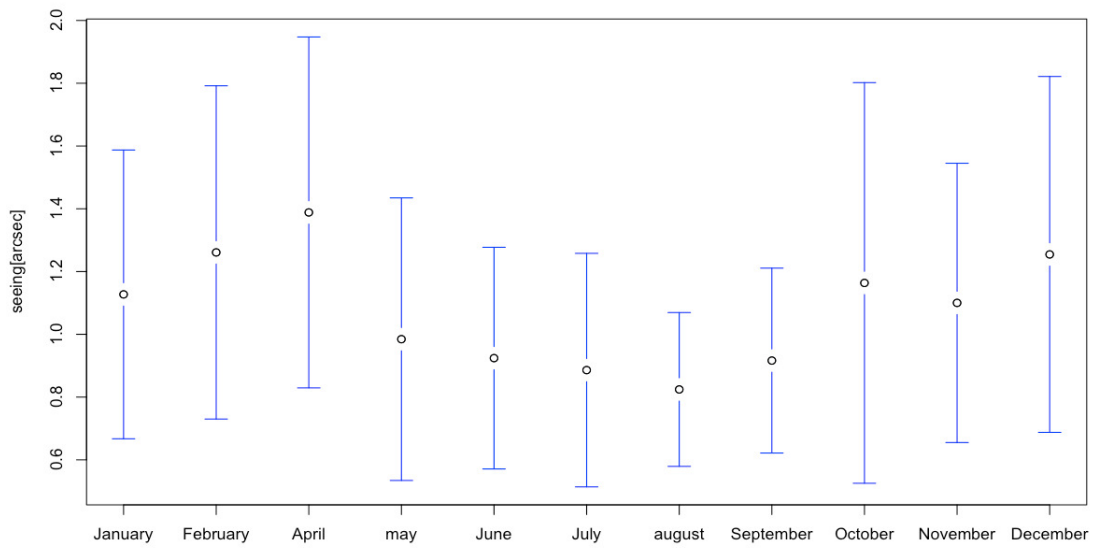


Figure 7.9: Temporal evolution of the total seeing measured with the DIMM channel.

at La Palma. Taking the 10 minutes mean interval and the total data plotted in cumulative distribution doesn't shows a strong discrepancy. Figure 7.10 shows the two cumulative curves. It can be then considered that the statistics of the seeing reduced every 10 minutes doesn't have an impact in the year statistics.

Time (minutes)	Variance
10	0.096
20	0.102
30	0.104
40	0.107
50	0.113
60	0.115

Table 7.10: Seeing variance of the measurements in the year 2008 over time scale from 10 minutes to 1 hour. Variance (*arcseconds*)<sup>2</sup>

To identify the monthly seeing distribution the data set is split for each month and a histogram plot is produced. Figure 7.11 compiles all the monthly histograms for the seeing and illustrate the differences in the distributions for the month April

and September. More extended daily seeing histograms are shown in the Appendix B for measurements since 2002 to 2008.

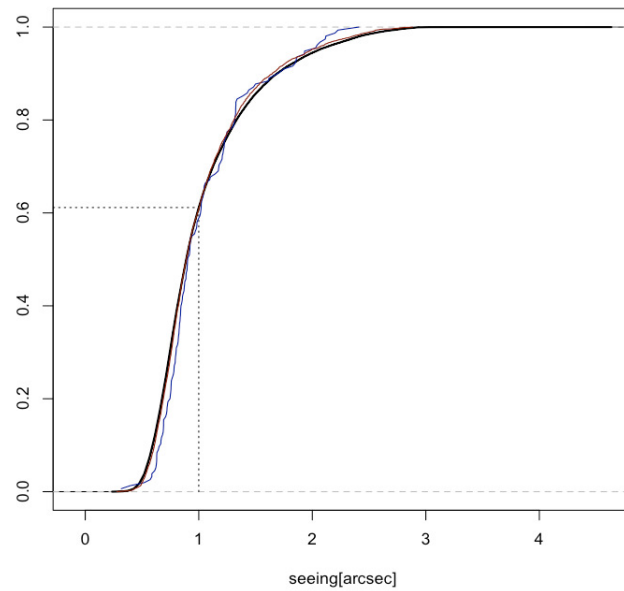


Figure 7.10: Cumulative distribution calculated from the seeing measured with the DIMM channel. A 10 minutes median value per day is calculated (red line) and the daily median value is plotted (blue line).

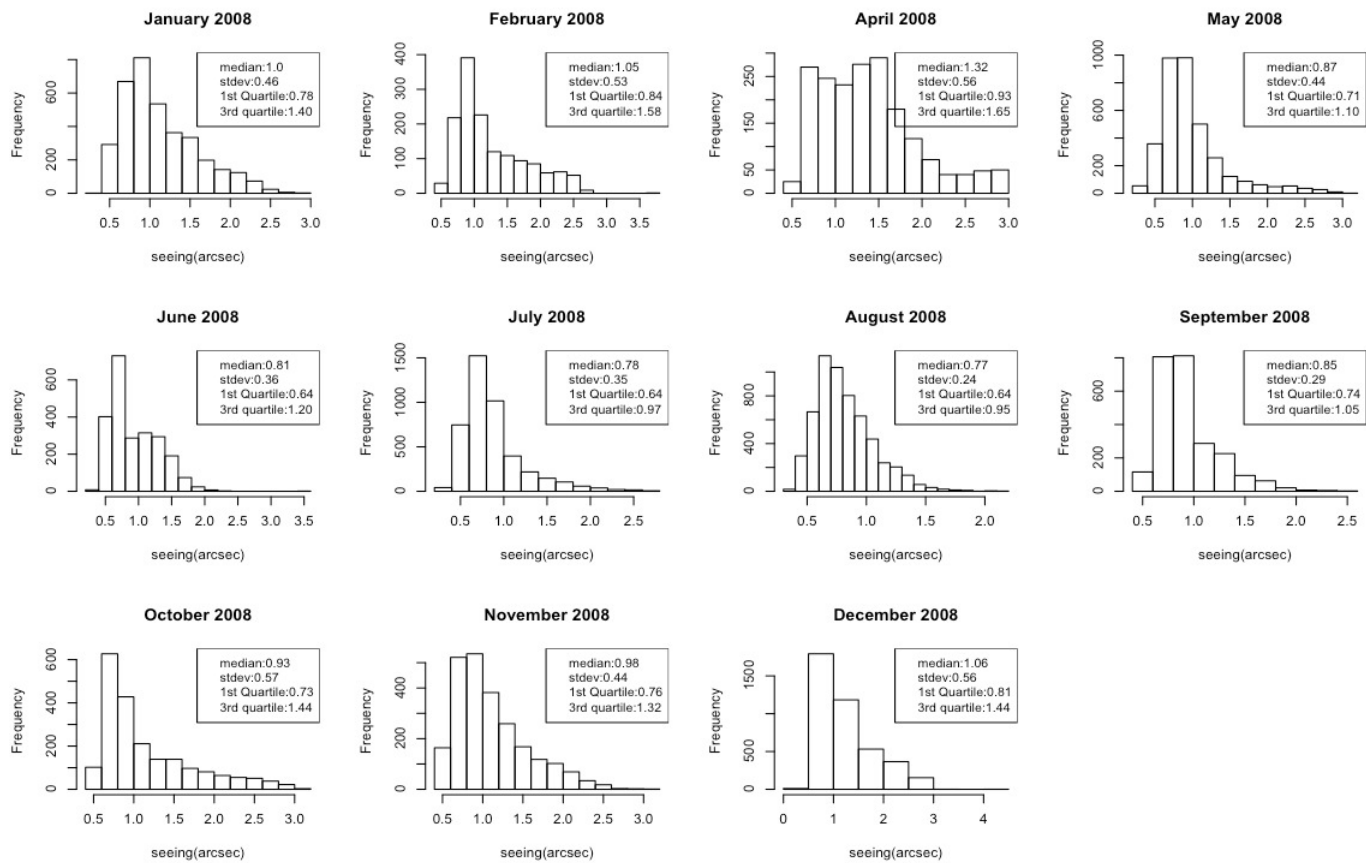


Figure 7.11: Histogram of the seeing distribution per month during the year 2008. This shows the histograms of the total seeing per month.

### 7.3.4 Surface layers seeing. Combine the MASS and DIMM channels.

The two seeing measurements can be combined to get the value of the surface layer seeing using the equation 6.6 (Section 6.3.2). With the surface layer seeing (below 0.5 km) it is possible to determine the contribution of the different layers to the total seeing and how it changes during the year. The restoration of the surface layer seeing by the MASS-DIMM is not a direct measurement and it provides a low resolution vertical profile measurement. A better instrument has to be used to get a better measurement of the surface layers; this is the optimized surface layer SLODAR (Osborn, 2009) that provides a vertical resolution of meters from the surface to a few hundred meters. Other instruments resembling meteorological instruments such as temperature sensors placed at different heights on a mast or the use of balloon radiosondes, can also provide a good vertical resolution of the surface seeing.

Restoring the surface seeing using equation 6.6, and plotting the results as the median value for the three seeing components; total, free and surface seeing shown in figure 7.12, we see that the total seeing data show a seasonality of the seeing that is repeated every year with more or less strength. Two different periods can be identified; one in winter+spring and another one in summer with the worst seeing during the winter+spring time and the best seeing occurring during the summer time. Looking at Autumn one sees a ramp up of the seeing values, with a reduction of the surface seeing and an increase in the free seeing. This may be due to the seasonal change from summer to autumn and the changes in the upper air wind speed or it could be an isolated event for the year 2008.

### 7.3.5 The Refractive Index parameter. The $C_n^2$ profiles.

The vertical profile of the atmospheric turbulence refraction index  $C_n^2(h)$  measured with the MASS instruments are stored and filtered in a post-processing analysis to avoid bad data in the statistics. The statistical analysis is performed using the daily data set shown in table 7.3 with at least of 4 hours of measurements in order to have continuous statistics of the refractive index ( $C_n^2(h)$ ) evolution during the nights.

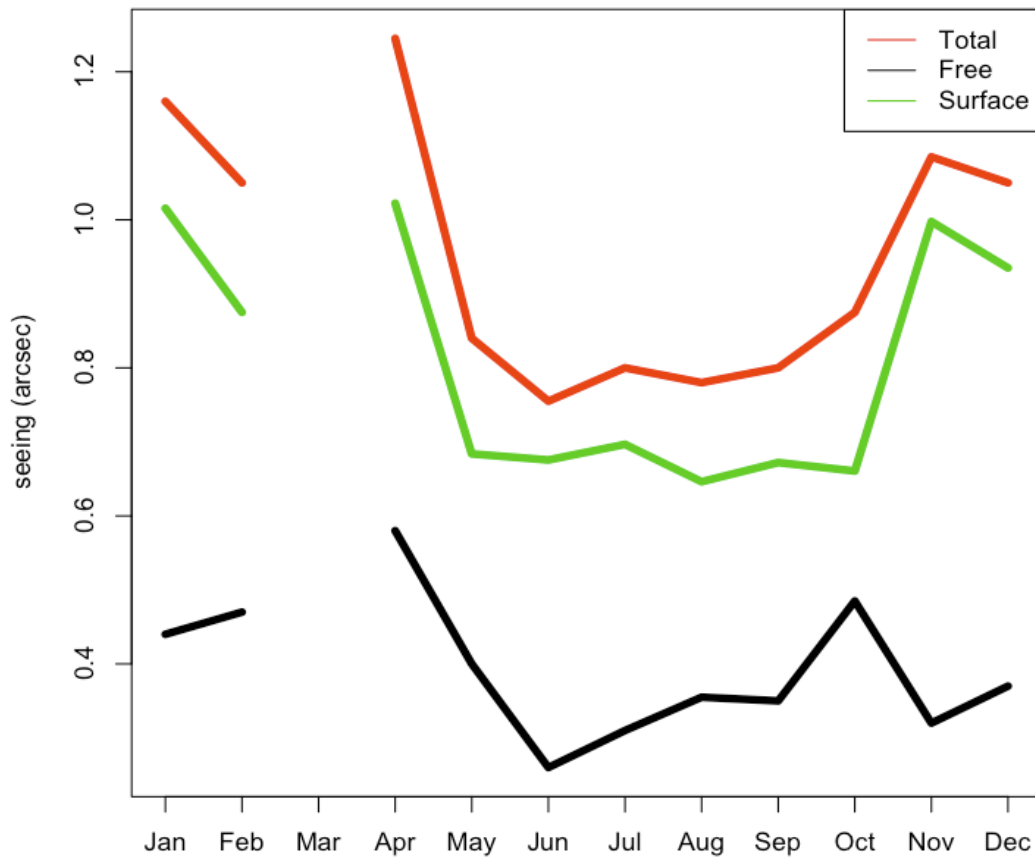


Figure 7.12: Monthly median seeing for the surface, free and total seeing. The data considered are filtered with a minimum integration of 4 hours of measurements.

A monthly summary of the median value of the  $C_n^2(h)$  at the height slabs for the year 2008 is shown in table 7.11 with the integrated free seeing, and the figure 7.13 shows the daily median statistics of the  $C_n^2(h)$  values calculated through the year and plotted as a boxplot, which summarizes the distribution of the time series of the data with respect to the heights slabs; 0.5, 1, 2, 4, 8 and 16 km.

The MASS-DIMM instrument can't measure the surface layers, but this value can be calculated from the combination of the free and the total refractive index parameter; this last value can be calculated from the total seeing using equation 6.6. Now with the knowledge of the refractive index throughout the atmosphere it is an important issue to determine the strength of each layer relative to the total refractive index, and plotting them together it is possible to identify the behaviors

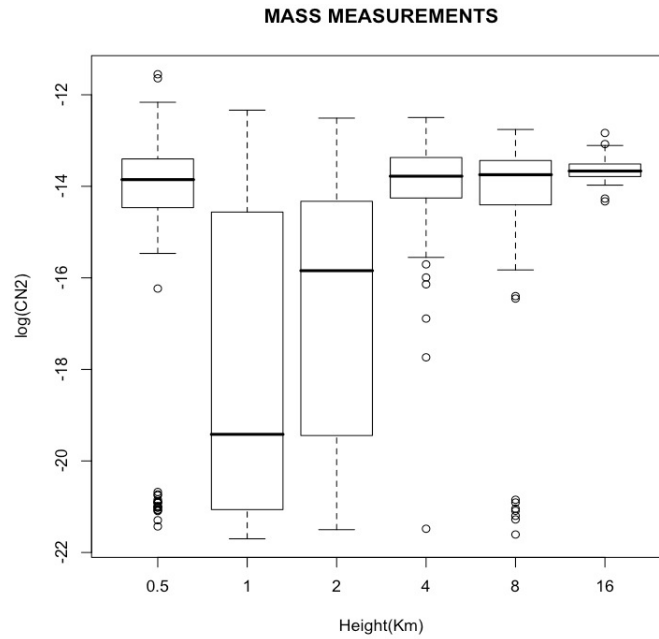


Figure 7.13: Statistics of the refractive index parameter  $C_n^2$  during the year 2008. The  $C_n^2$  vales are in logarithm. The logarithm of the refractive index  $C_n^2$  shows a weak turbulence for values -20 and strong turbulence for values -14.

Month	Free seeing	0.5km	1km	2km	4km	8km	16km
January	0.47	$9.94e^{-15}$	$1.15e^{-21}$	$2.50e^{-18}$	$1.69e^{-14}$	$7.20e^{-14}$	$2.80e^{-14}$
February	0.46	$4.2e^{-15}$	$2.02e^{-19}$	$6.015e^{-16}$	$4.25e^{-14}$	$5.19e^{-14}$	$2.68e^{-14}$
March	No Data	No Data	No Data	No Data	No Data	No Data	No Data
April	0.63	$9.70e^{-14}$	$2.35e^{-14}$	$2.90e^{-15}$	$1.69e^{-14}$	$1.760e^{-15}$	$1.95e^{-14}$
May	0.43	$2.69e^{-14}$	$2.87e^{-16}$	$9.46e^{-17}$	$1.79e^{-14}$	$2.710e^{-14}$	$3.55e^{-14}$
June	0.31	$2.72e^{-14}$	$1.26e^{-19}$	$7.99e^{-16}$	$9.50e^{-15}$	$2.485e^{-15}$	$1.69e^{-14}$
July	0.32	$1.79e^{-14}$	$1.13e^{-16}$	$5.29e^{-16}$	$1.35e^{-14}$	$2.480e^{-15}$	$1.95e^{-14}$
August	0.33	$2.99e^{-15}$	$1.28e^{-21}$	$2.75e^{-18}$	$3.15e^{-14}$	$2.045e^{-14}$	$2.04e^{-14}$
September	0.36	$1.08e^{-15}$	$1.02e^{-21}$	$9.02e^{-19}$	$8.33e^{-15}$	$3.495e^{-14}$	$3.974e^{-14}$
October	0.43	$3.53e^{-14}$	$7.78e^{-15}$	$1.64e^{-15}$	$2.19e^{-14}$	$1.27e^{-14}$	$2.63e^{-14}$
November	0.37	$2.85e^{-14}$	$1.72e^{-16}$	$2.12e^{-16}$	$1.60e^{-14}$	$2.40e^{-14}$	$2.32e^{-14}$
December	0.41	$2.43e^{-14}$	$6.80e^{-19}$	$1.84e^{-16}$	$2.81e^{-14}$	$3.97e^{-14}$	$2.34e^{-14}$

Table 7.11: The monthly median value for the  $C_n^2$  parameter and the free seeing. The atmosphere turbulence is considered turbulent for  $C_n^2$  values of  $10^{-14}$  and weak for values about  $10^{-20}$ .

of each layer, identifying trends and seasonality. This is shown in figure 7.14 for the monthly distribution for the year 2008. The surface layer (below 0.5km) is the major

contributor to the total  $C_n^2(h)$  during all the year, showing two stages in summer with a dominant surface contribution, and in winter with an increase of the free contribution during the winter months with the highest point during April and it ramps up to the 20% during the Autumn term. During the summer time (June to August) the surface contribution to the total turbulence is predominant, which could be consistent with a lesser influence of the jet stream as it moves to the northern hemisphere making the atmosphere more stable and reducing its contribution to the local weather conditions.

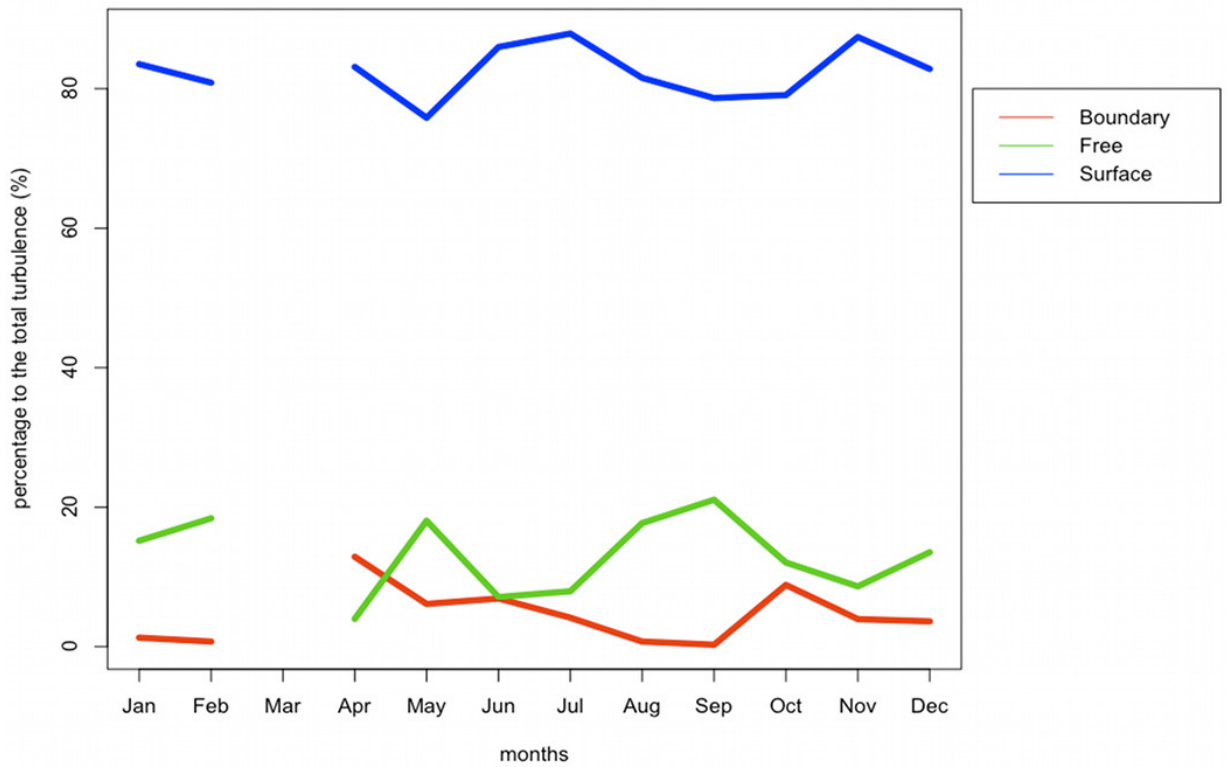


Figure 7.14: Percentage of the ground layer and the free (boundary and boundary+Free) contribution to total  $C_n^2(h)$  retrieved from the total seeing (DIMM measurements) and the free seeing (MASS measurements). The free is measured with the MASS channel in 6 height slabs (0.5, 1,2,4,8 and 16 km) and the boundary is taking the first three slabs (0.5,1 and 2 km).

The determination of the layers contributions to the total turbulence in terms of percentage of energy and seeing with respect to the altitude can help to statistically

determine the major contributors (turbulence heights) to the optical turbulence. Figure 7.15 shows an example of a median vertical refractive index parameter  $C_n^2$  and how this information of the vertical distribution clearly predicts the image quality that the observatory can reach and the hypothetical performance of the Adaptive Optics system. The distribution of the atmosphere turbulence has a special interest for Multi-Conjugated AO (MCAO) systems, which can use it to setup the right deformable mirrors at the predominant heights or in the Ground Layer AO (GLAO) where the correction system is optimized to correct mostly the lower part of the atmosphere giving an improvement of the image quality in a wider field of view.

To conclude, the technique shown in the present chapter constitutes a powerful tool in real-time studies of the turbulence evolution during Multi-Conjugated Adaptive Optics observations.

## 7.4 Wind and the Refraction Index parameter.

The wind data are retrieved from the web database described in Chapter 6; the data sets are represented in a 2D distribution plot in order to have a better view of the yearly distribution which is shown in the figure set 7.16. Having data from 2002 to 2008, a 7 years of statistics, which represents a good sampling; and it can be shown that there exists a seasonality. The wind speed can be associated with changes in the light propagations through a mixing process of the different cells of different refraction index. Then we can say that the wind speed is a process that affects the optical turbulence and it can be correlated with the seeing measurements in the sense of finding a common behavior. The influence of the wind on the optical turbulence could be considered with respect to the local wind speed or with the wind in the upper atmosphere in the jet stream altitude (about 12km asl.)

The wind speed data set is represented in a 2D distribution in order to visualize the evolution through the years, where each column of the radiosonde data is the collection of the daily profiles; missing columns are due to lack of data. The figure shows clearly how the strength of the wind speed in the upper atmosphere (jet stream) changes in strength and location. The analysis is focused on the wind speed

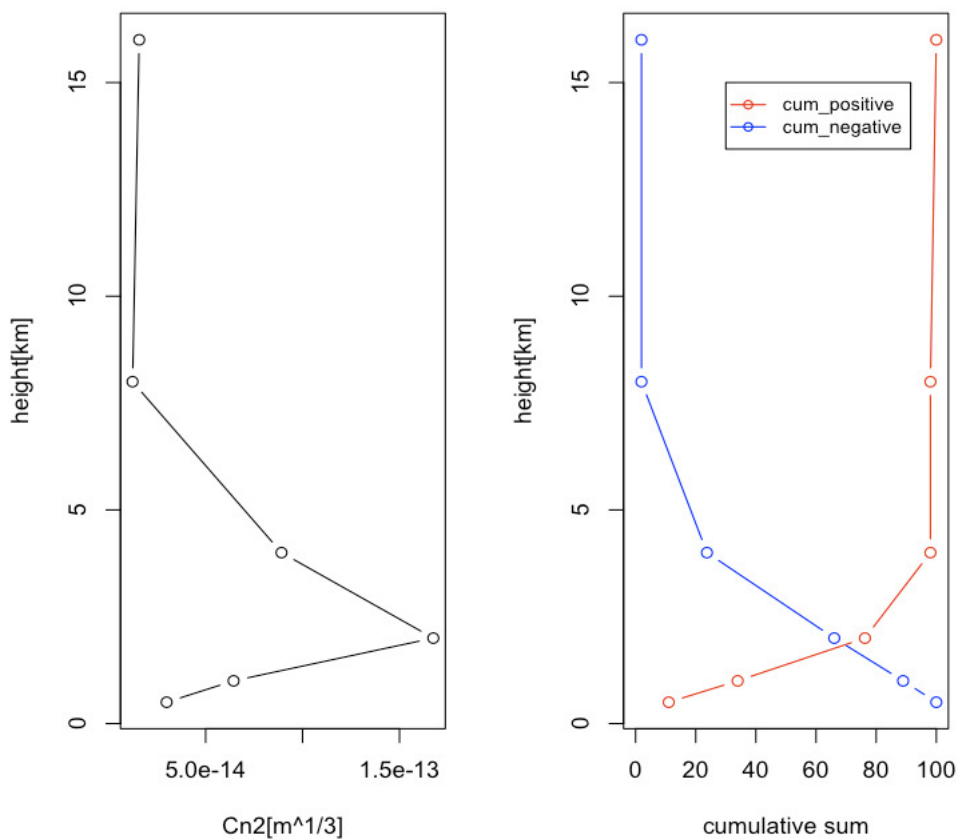


Figure 7.15: Example of turbulence profile restored from the MASS profiles. The Figure shows one frame of the whole sequence of the atmospheric profile obtained in real time during the acquisition process. The right plot shows the median value of the  $C_n^2$  for the measured height slab and the left plot shows the positive and negative cumulative sum of the  $C_n^2$  indicating that the predominant strength occurs about 2 km. The plot reports all the parameters calculated from the recombination of the free and the total atmosphere.

in the upper atmosphere and the possible impact on the local conditions of Roque de los Muchachos Observatory. The local conditions are determined by the seeing measurements.

The wind speed at the jet stream altitude can be a factor of seeing changes as mentioned by Sarazin (Carrasco et al, 2003,) in previous works and its time evolution can be linked with the variation of the strength and distribution at the jet stream altitude. The figures 7.17 represents a short term of 7 years of statistics where at

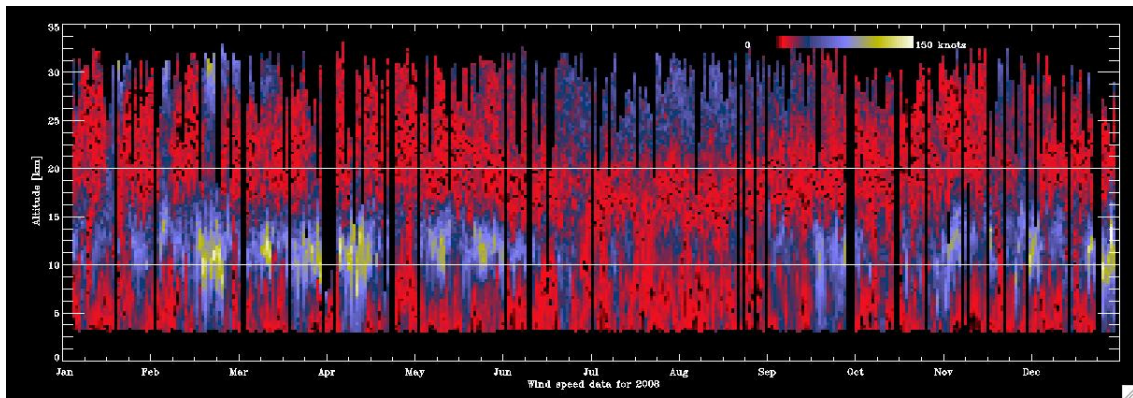
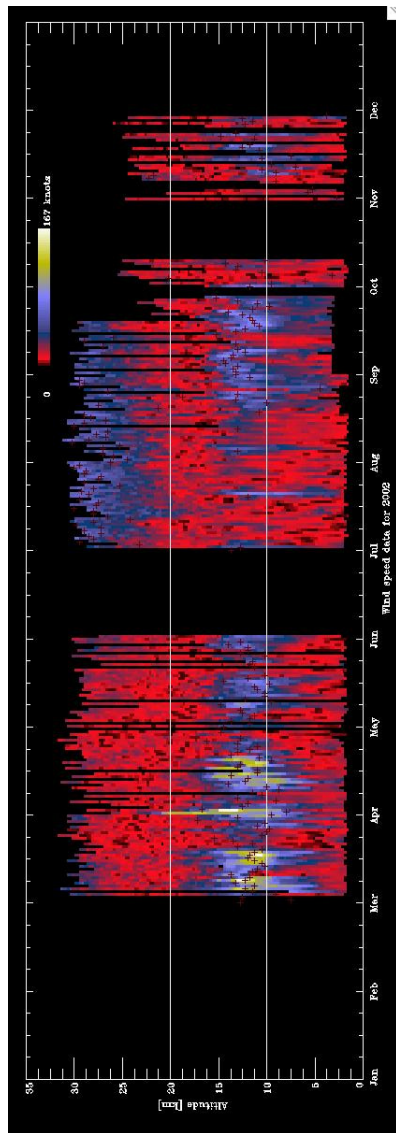


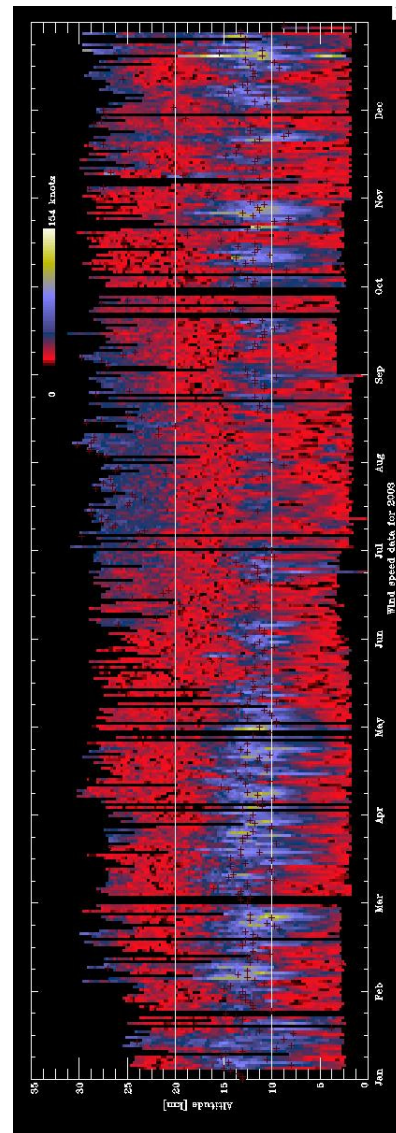
Figure 7.16: Retrieved the profiles of the wind speed from the radiosonde data station 60018 (Tenerife) for the year 2008. The balloons are launched at midnight (00 UT) every day and the plot represents a 2D profile of the vertical wind speed through the year. The height goes from 3 to 30 km.

the first view the significant variation of the wind speed strength distribution during the winter terms.

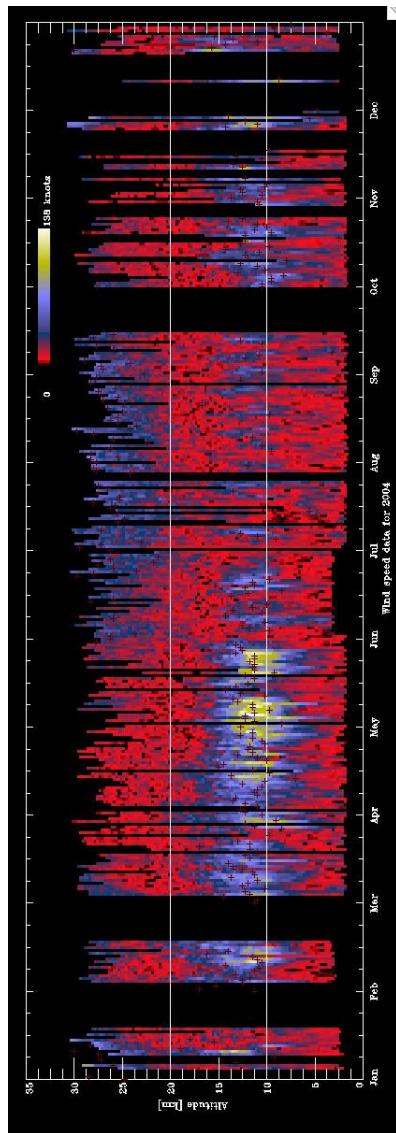
This series of plots shows evident changes in the evolution of the jet stream and a seasonal pattern. Starting from 2003, we can see from the available data that the coincidence of the maximum of the wind speed with the jet stream altitude finished in the middle of April, in 2004, while the incidence of the maximum of the jet stream is extended until the end of May. In 2005 we can observe a reduced concentration of points in the jet stream region and a major distribution of the wind speed during the months March, April and May. During the same period the seeing data show a strong variability (see figure 7.2). This may be partly due to the higher temporal resolution of the DIMM measurements compared to the radio-sonde data.



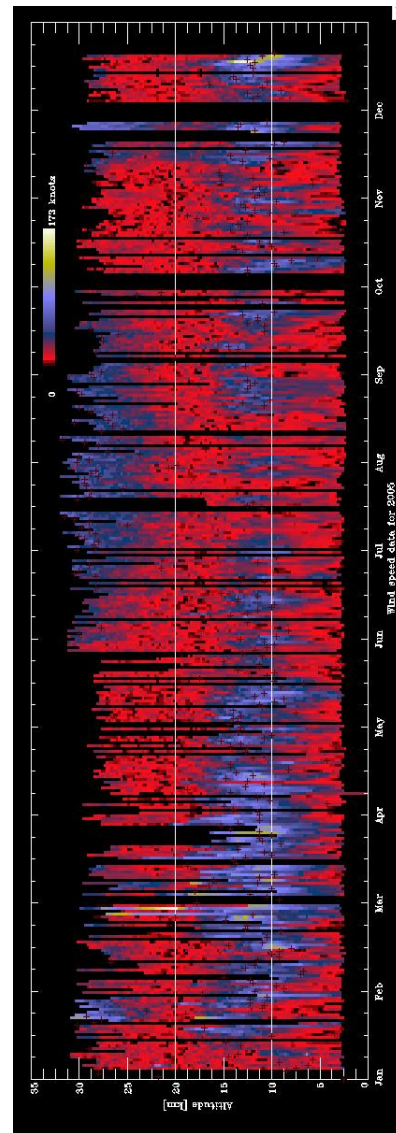
(a) 2002



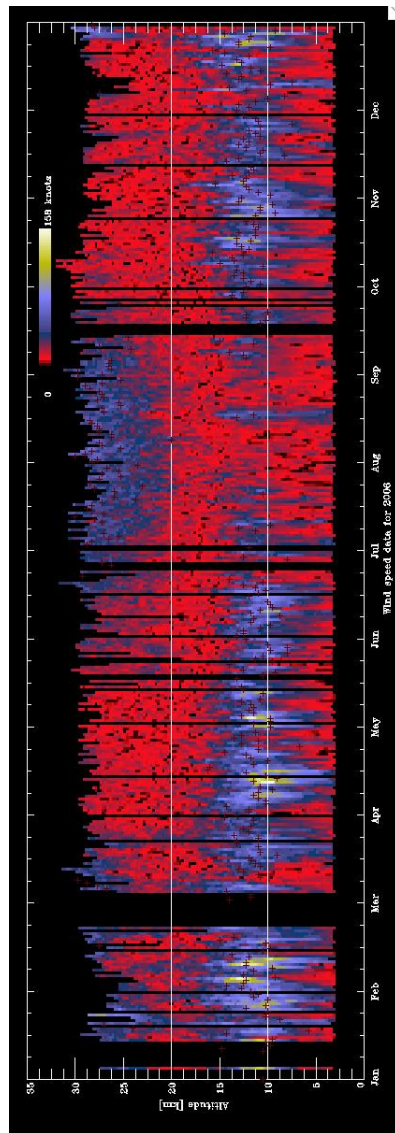
(b) 2003



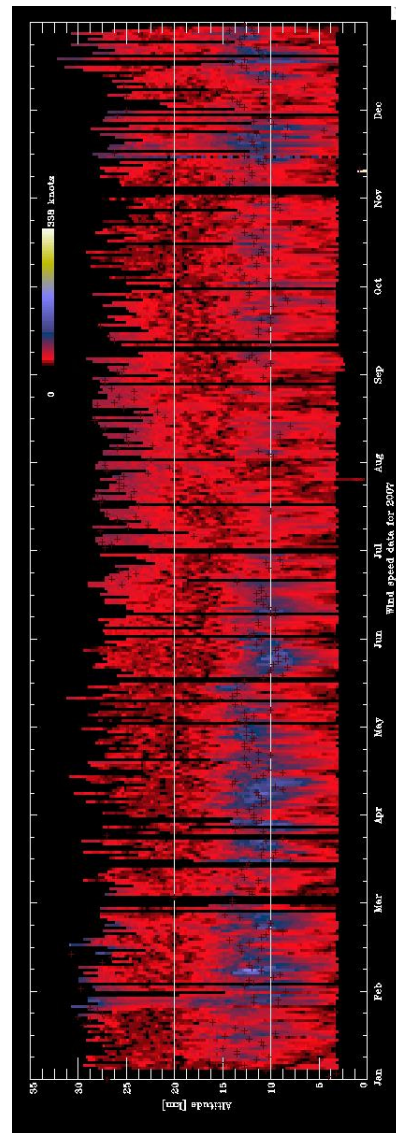
(c) 2004



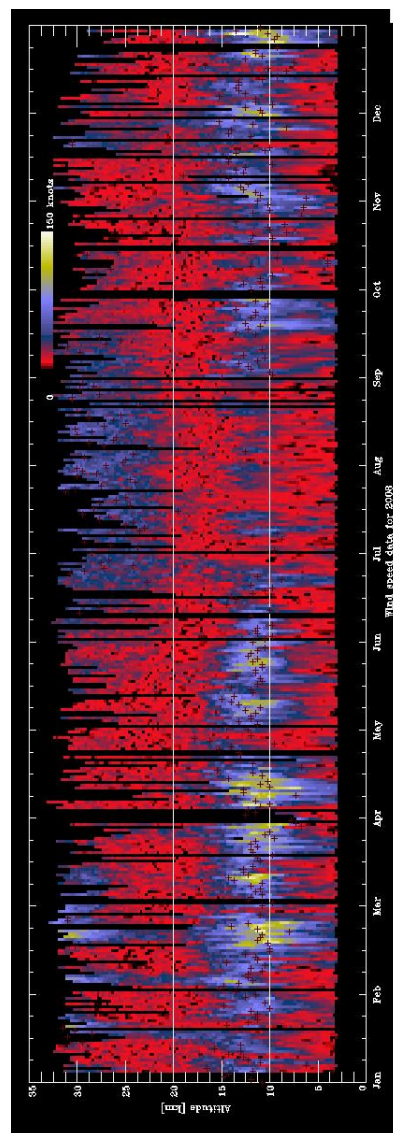
(d) 2005



(e) 2006



(f) 2007



(g) 2008

Figure 7.17: 2D image of the daily distribution of wind speed measurements starting in the years 2002 to 2008, the daily distribution is represented in a gradient colors. With the strong wind speed is representing in white. Day without data are represented has black columns. Data taken from radiosonde database.

Taking the wind speed value at the jet stream height as the influence region to contribute to the optical turbulence and looking at the period from 2004 to 2008 we perform a statistical analysis, which is shown in the Figure 7.18. The monthly median distribution of the wind speed and the values summarized in the table 7.12. The wind speed shows a seasonal pattern with an increase trend after 2005. Looking at Figure 7.19 there is an interesting event during 2005 with a weak jet stream distribution. A fitting of a local regression polynomial (loess)<sup>4</sup>(Cleveland, 1979) with a span of 0.75 line is added to the plot to improve the visual effect of the evolution of the parameters. The figure 7.19 shows that the year 2005 is weak and with a low variance of the median values along the year.

---

<sup>4</sup>Loess is a method that is (somewhat) more descriptively known as locally weighted polynomial regression. At each point in the data set a low-degree polynomial is fit to a subset of the data, with explanatory variable values near the point whose response is being estimated. The polynomial is fit using weighted least squares, giving more weight to points near the point whose response is being estimated and less weight to points further away. The value of the regression function for the point is then obtained by evaluating the local polynomial using the explanatory variable values for that data point.

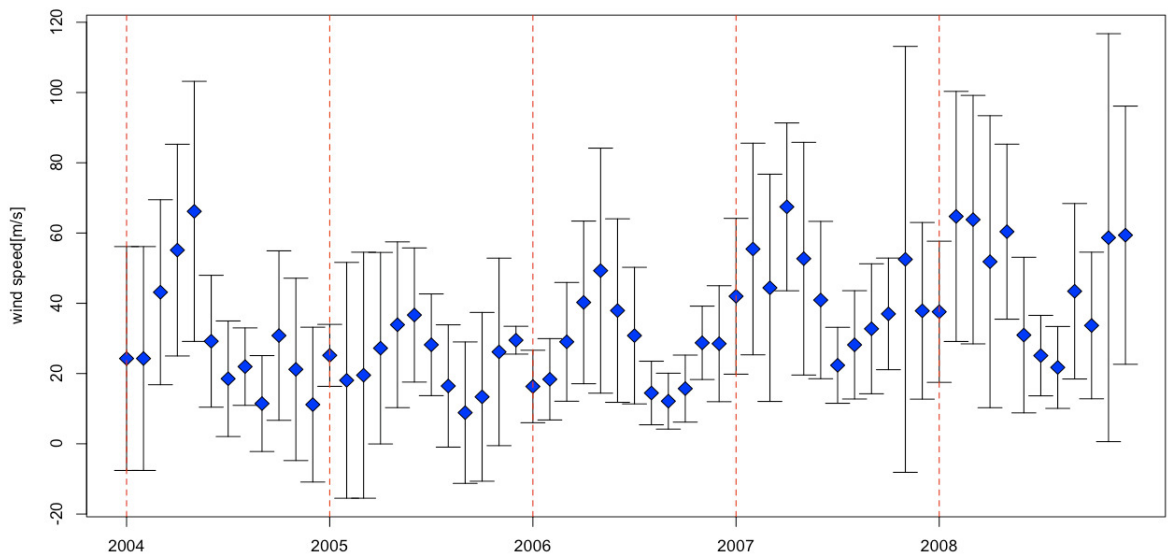


Figure 7.18: Monthly distribution of the wind speed at a height between 9 to 12 km for the years from 2004 to 2008. The height analyzed is just in the region of the jet stream.

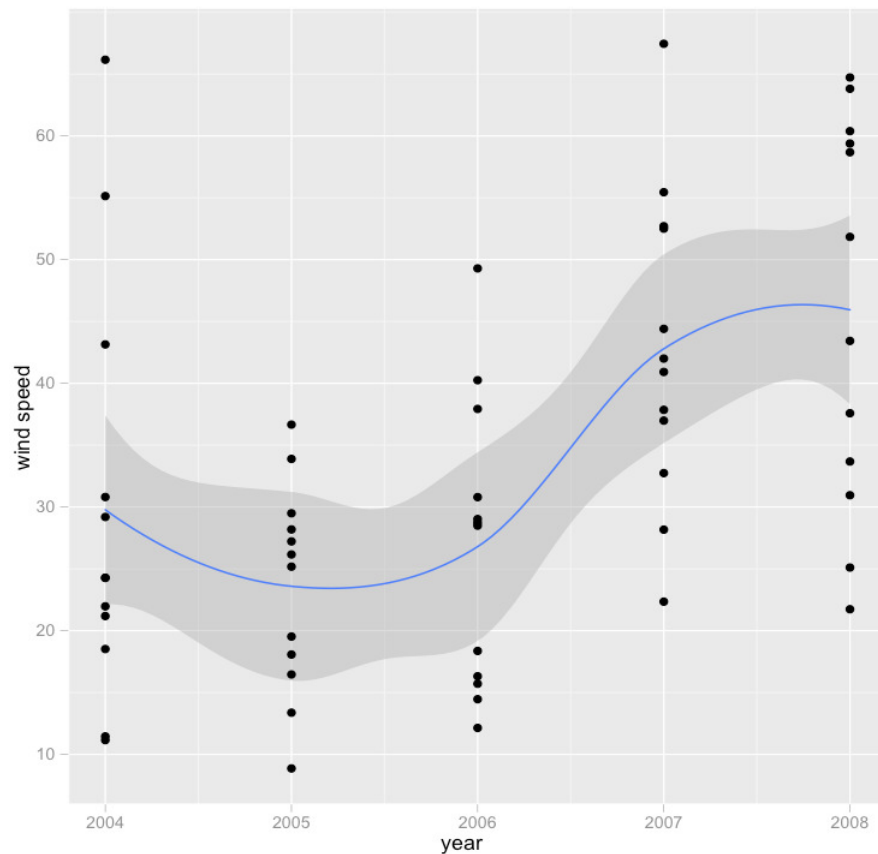


Figure 7.19: Wind speed distribution of the tropospheric wind in a height slab between 9 to 12 km. The blue line is the fitting of the local regression polynomial to the data and the grey zone is the 95% confidence interval region. Data obtained from the radiosonde launched at 120 km from the Roque de los Muchachos Observatory.

month	2004	2005	2006	2007	2008
Jan	NA	25.17±8.81	16.31±10.31	42.0±22.1	37.58±20.09
Feb	24.27±31.8	18.07±33.56	18.36±11.57	55.45±30.1	64.72±35.60
Mar	43.14±26.3	19.52±35.01	29.02±16.90	44.4±32.3	63.81±35.36
Apr	55.13±30.13	27.21±27.26	40.25±23.15	67.45±23.88	51.83±41.56
May	66.16±37.02	33.88±23.59	49.29±34.87	52.7±33.12	60.38±24.91
Jun	29.19±18.77	36.66±19.09	37.92±26.12	40.91±22.39	30.95±22.15
Jul	18.51±16.44	28.18±14.48	30.79±19.43	22.34±10.81	25.10±11.45
Aug	21.96±11.02	16.45±17.40	14.59±9.05	28.16±15.42	21.73±11.66
Sep	11.45±13.62	8.86±20.13	12.13±7.95	32.74±18.50	43.42±24.97
Oct	30.86±24.12	13.37±24.02	15.71±9.53	36.98±15.89	33.67±20.87
Nov	21.18±25.96	26.16±26.69	28.74±10.44	52.50±60.62	58.68±58.07
Dec	11.15±22.03	29.49±3.96	28.49±16.50	37.85±25.14	59.38±36.75

Table 7.12: Summary of the tropospheric wind speed (knots) with the median and standard deviation.

Analyzing a single year, the year 2008 which corresponds with the periods of data available for the MASS-DIMM instrument, the tropospheric wind speed (see figure 7.20) shows a seasonal pattern with a minimum contribution during the summer time and the maximum during the winter time and also it shows better conditions during the Autumn than the spring time.

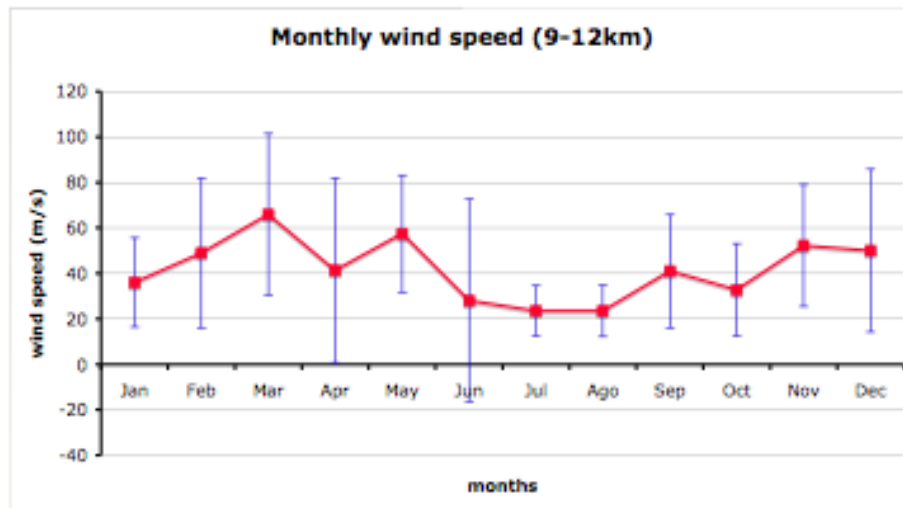


Figure 7.20: Monthly median wind speed distribution for the year 2008. The plot data are retrieved from the table 7.13. The wind speed has been taken from median value in the altitude slab between 9 to 12 km where the jet stream is located; the monthly distribution show a more stable conditions during the summer period extended to the autumn (October and November). The bars represent the standard deviation

The optical turbulence measured as "seeing" is an important input to knowledge of the real time optical atmosphere turbulence analysis, and a relationship has been studied between the wind speed at these heights. The following analysis takes the monthly statistics of the seeing and the upper air free seeing and plots them with the tropospheric wind speed shown in the figure 7.21; one can recognise a seasonal pattern of all the components in the plot with two different scenarios, one during the summer time (from June to September) with best values of the free seeing and low values of the wind speed.

The low values for the wind speed may mean a stability of the upper atmosphere

Months	Average ( $ms^{-1}$ )	Median ( $ms^{-1}$ )	Stdev ( $ms^{-1}$ )
Jan	36.5	36.0	19.57
Feb	63.0	49.0	32.8
Mar	62.1	66.0	35.5
Apr	50.6	41.3	40.6
May	58.9	57.5	25.7
Jun	35.8	28.0	44.5
Jul	24.3	23.5	11.1
Ago	20.8	23.5	11.4
Sep	43.2	41.0	24.8
Oct	33.2	32.8	20.3
Nov	48.2	52.25	26.8
Dec	56.3	50.0	35.78

Table 7.13: Monthly statistics of the tropospheric wind speed at an altitude between 9 and 12 km.

with a low probability to trigger turbulence and decrease the wavefront coherence time. Also it could be considered as a low contribution to the local wind conditions as showed in the relationship from Sarazin 3.1. The tropospheric wind speed and the seeing distribution follow the same temporal series with a seasonal pattern.

The seeing is an important parameter used to identify changes in the optical turbulence and it is a parameter that can be correlated with the wind speed at jet stream height (200 mb), where the variation of the strength and its distribution can affect the local conditions, hence altering the low atmosphere and increasing the low altitude turbulence. But the seeing is not the only parameter to consider, there is another important astro-climate parameter called **Isoplanatic angle**. As previously defined in Chapter 3, the isoplanatic angle is a parameter which is influenced by the upper atmospheric turbulence and it may have a relationship with the wind speed at a height of 200mb. A large isoplanatic angle gives a large correction field and indicates a low free atmosphere seeing. The MASS-DIMM instrument can measure the isoplanatic angle every minute, and statistics of the monthly median isoplanatic

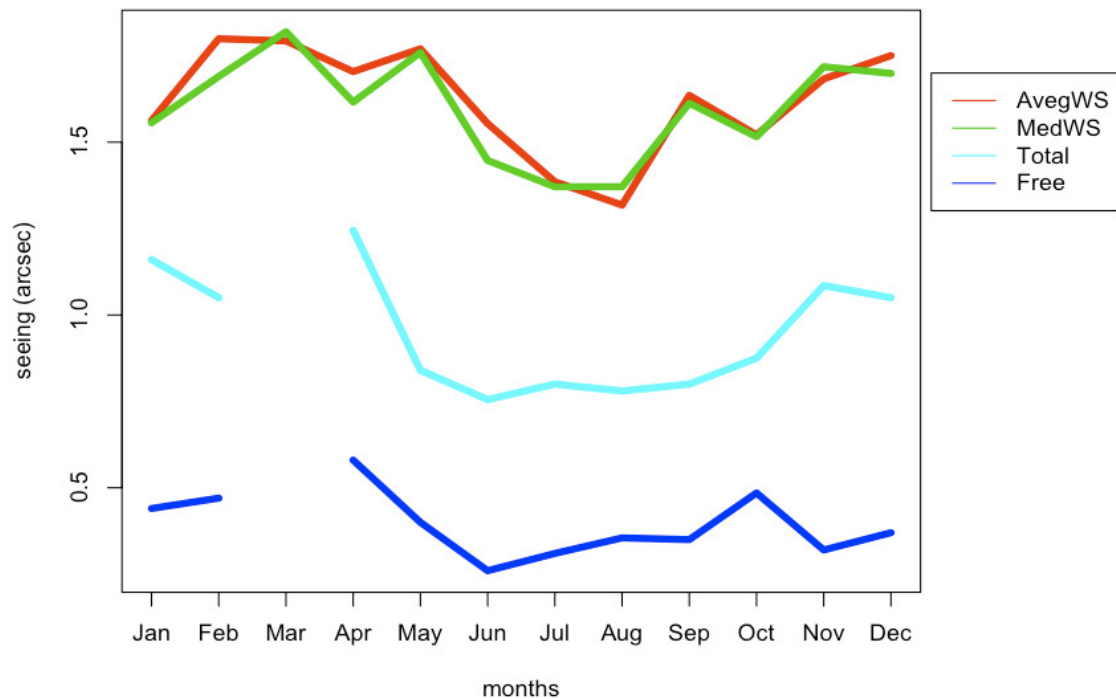


Figure 7.21: Plot of the median wind speed, the whole seeing measured by a DIMM and free atmosphere seeing (above 0.5km) measured by the MASS. Statistics is referred to the year 2008. To scale the whole set of data for representation purpose, the wind speed is in logarithm scale. The total seeing and free seeing are in normal scale. Seeing measured in arcseconds and wind speed in  $ms^{-1}$ .

angle for 2008 is summarized in table 7.14, with the wind speed at altitudes between 9 and 12 km. It has been seen in figure 7.7 that the isoplanatic angle shows a seasonal pattern, and comparing this with the tropospheric wind speed it can be seen that the large isoplanatic angle corresponds with the lower wind speed values, showing better conditions during the summer time.

The figure 7.22 shows the median values for the isoplanatic angle plotted with the median value of the tropospheric wind speed for the year 2008. In the same way as the seeing, the isoplanatic angle has a daily variability due to changes in the atmosphere turbulence and it shows a seasonal behavior which may depend on the yearly fluctuations of the macro-scale weather.

The wind speed at the tropospheric height (200 mb) has shown a relationship

Month	Average wind spd [ $ms^{-1}$ ]	Median wind spd [ $ms^{-1}$ ]	Median isoplanatic angle [arcsec]
January	36.5	36.0	1.88
February	63.0	49.0	1.83
March	62.1	66.0	NA
April	50.6	41.3	2.4
May	58.8	57.5	1.94
June	35.8	28.0	3.13
July	24.3	23.5	2.75
August	20.8	23.5	2.23
September	43.2	41.0	1.74
October	33.2	32.8	2.25
November	48.2	52.25	2.33
December	56.3	50.0	2.19

Table 7.14: Monthly statistics for the median isoplanatic angle and wind speed at 200mb during the year 2008.

with the astroclimate parameters measured from 120 kilometers away at the radiosonde launch site. The circulation of the upper air is related to the displacement of the jet stream, which has a clear seasonal behavior. Then, knowing the relationship between the tropospheric wind speed to the local optical turbulence, the tropospheric wind speed may an important parameter to be considered during AO observing set up, and also for laboratories modeling the local optical turbulence of an observatory during the optimization and design of an AO system.

Can this relationship be applied to other observatories.? The global circulation of the air is known and the displacements of the air masses follow those wind circulations, the only difference is the location of the site. Work done by Varela (Varela et al. 2006) has performed the correlation at different sites (Mauna Kea, Paranal, La Silla, San Pedro Martir and the Roque de Los Muchachos) of the tropospheric wind, finding a good correlation of the wind at 200mb with the wind at lower altitude, which is affected by the local orography. Figure 3.4 (Section 3.4), which is retrieved

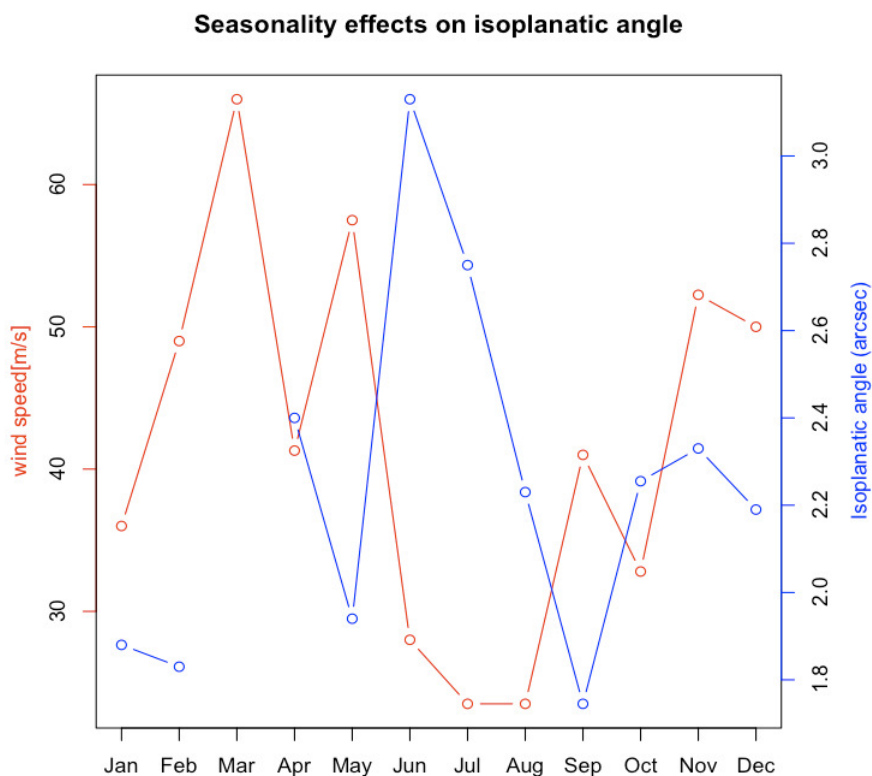


Figure 7.22: Seasonal effect of the isoplanatic angle in relationship with the seasonal effects of the wind speed at the tropospheric height (200mb). Data for the year 2008. March doesn't have MASS-DIMM measurements. The blue line represents the isoplanatic angle with the y-axis on the left and the red lines represents the wind speed with the y-axis on the rights.

from work (Garcia-Lorenzo et al. 2005), shown the Pearson correlation coefficients of the different sites.

#### 7.4.1 Applying to a daily case.

A daily approach could be useful to determine a "nowcast" of the sky conditions and with long statistics over many years, it could be possible to build an accurate model. Taking, for example, the wind speed measurements spread out in four months (January, May, August and November) which represents the different seasons (spring, summer, autumn and winter) during the year 2008, and performing a daily analysis of the data, we obtain the results summarized in tables 7.16, 7.17, 7.18

and 7.19 and plotted in figures 7.23 showing the wind speed, free seeing and total seeing for a daily median values with a significant similarity between the graphs. A Pearson correlation is calculated for free seeing and total seeing for those months (January, May, August and September ) and it gives results of 0.86, 0.65, 0.76 and 0.86 respectively. The Pearson correlation for the seeing data set with respect to the wind speed gives the results shown in table 7.15 ;

Months	Troposp. vs Fseeing	Troposp vs Total seeing
January	0.30	0.27
May	0.18	-0.36
August	0.17	0.10
November	0.0	0.34

Table 7.15: Pearson correlation values for the tropospheric wind speed respect the free seeing (arcsec) and the total seeing (arcsec ).

Date	Total seeing	Free seeing	Wspd(9-12km)
January 1	1.27	0.58	38.3
January 2	1.24	0.68	34.8
January 9	0.83	0.28	49.5
January 10	1.18	0.56	49.0
January 11	0.80	0.40	35.8
January 12	0.63	0.25	33.0
January 13	0.82	0.61	27.5
January 14	1.12	0.40	32.3
January 15	1.45	0.44	28.5
January 22	2.18	1.94	50.5
January 25	1.16	0.41	59.0

Table 7.16: January data for the statistical median; total seeing (arcsec), free seeing (arcsec) and tropospheric wind speed ( $ms^{-1}$ ).

Date	Total seeing	Free seeing	Wspd(9-12km)
May 3	0.75	0.30	53.5
May 4	0.94	0.50	71.2
May 5	0.84	0.40	71.0
May 6	0.65	0.43	60.0
May 12	0.51	0.19	33.7
May 13	0.70	0.41	32.75
May 14	0.64	0.51	62.0
May 16	1.08	0.35	92.0
May 17	1.40	0.34	95.0
May 18	0.84	0.43	54.2
May 19	2.08	1.15	32.7
May 27	1.29	0.30	69.5
May 28	0.63	0.57	28.7
May 29	0.42	NA	78.5
May 31	0.96	0.35	NA

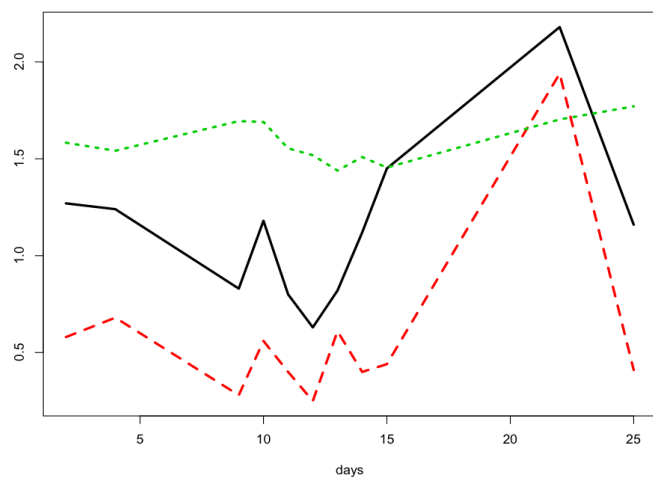
Table 7.17: May data for the statistical median; total seeing (arcsec), free seeing (arcsec) and tropospheric wind speed ( $ms^{-1}$ ).

Date	Total seeing	Free seeing	Wspd(9-12km)
August 4	0.74	0.31	18.8
August 5	0.58	0.30	33.0
August 6	0.70	0.20	38.0
August 7	0.66	0.20	16.0
August 8	0.49	NA	22.5
August 9	0.52	0.27	18.0
August 10	0.84	0.26	24.5
August 11	0.14	0.22	30.3
August 16	0.83	0.51	24.3
August 17	0.96	0.52	21.0
August 18	1.10	0.64	31.0
August 19	1.13	0.77	35.3
August 21	0.78	0.46	NA
August 22	0.75	0.38	40.3
August 23	0.53	0.26	NA
August 24	0.82	0.61	12.3
August 26	0.82	0.24	9.7
August 27	0.70	0.37	NA
August 28	0.83	0.37	24.3
August 29	0.73	0.27	30.0
August 30	0.85	0.36	26.8
August 31	0.61	0.35	NA

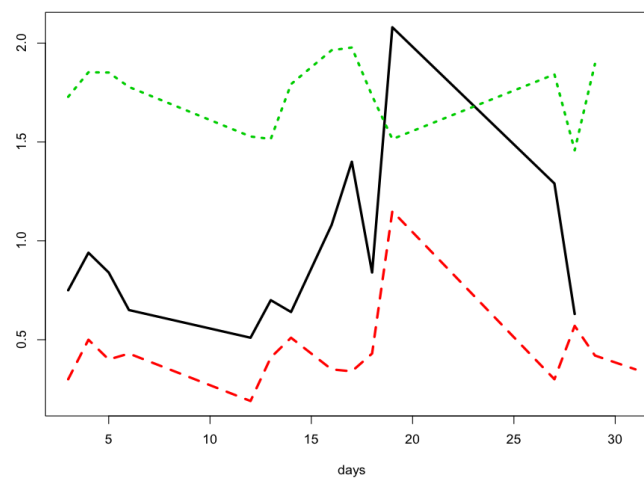
Table 7.18: August data for the statistical median; total seeing (arcsec), free seeing (arcsec) and tropospheric wind speed ( $ms^{-1}$ ).

Date	Total seeing	Free seeing	Wspd(9-12km)
November 3	1.20	0.34	13.5
November 9	1.15	0.42	11.0
November 10	0.81	0.24	53.25
November 11	1.40	0.67	64.2
November 12	1.0	0.29	50.5
November 14	0.67	0.23	38.5
November 18	1.20	0.58	54.5
November 29	0.70	0.30	43.7

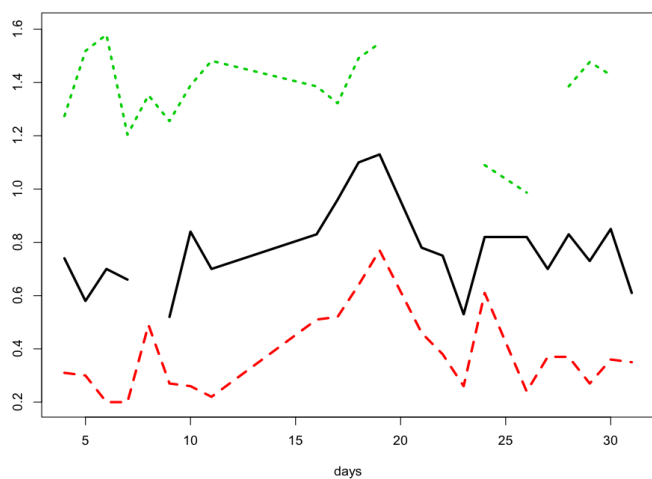
Table 7.19: Table set of the daily median values of the seeing; total seeing (arcsec) and free seeing (arcsec ) and the wind speed at the altitude between 9 to 12 km. Measurements for the months January, May, August and November of the year 2008.



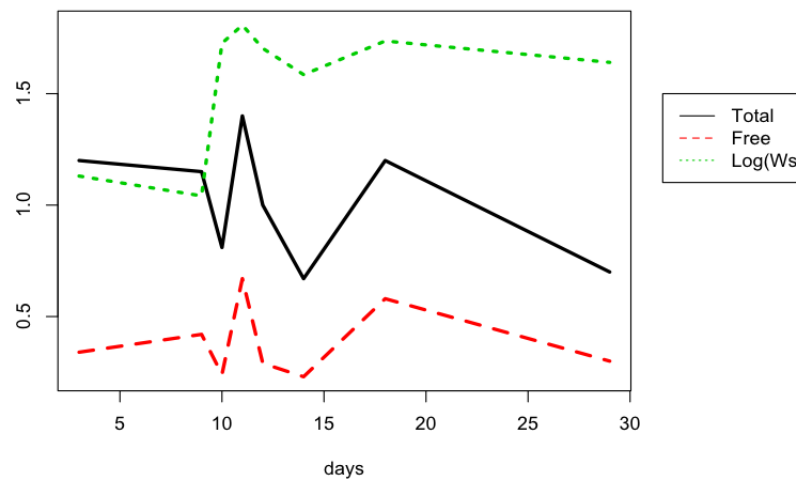
(a) January



(b) May



(c) August



(d) November

Figure 7.23: Four months figures set for the median daily; total seeing, free seeing and wind speed at the troposphere altitude (9 to 12 km) for measurements collected in January, May, August and November of the year 2008. The wind speed is shows in a logarithmic

This statistical analysis can give an indicator for the possible contribution of the wind speed at the jet stream height to the total atmosphere turbulence sensed by the seeing parameter. The jet stream can trigger possible turbulence at low altitudes and this can affect the seeing, and can be seen as an "explosion" which disturbs the atmosphere. An example is shown in figure 7.24 of a reduced  $C_n^2$  profiles measured by the MASS-DIMM.

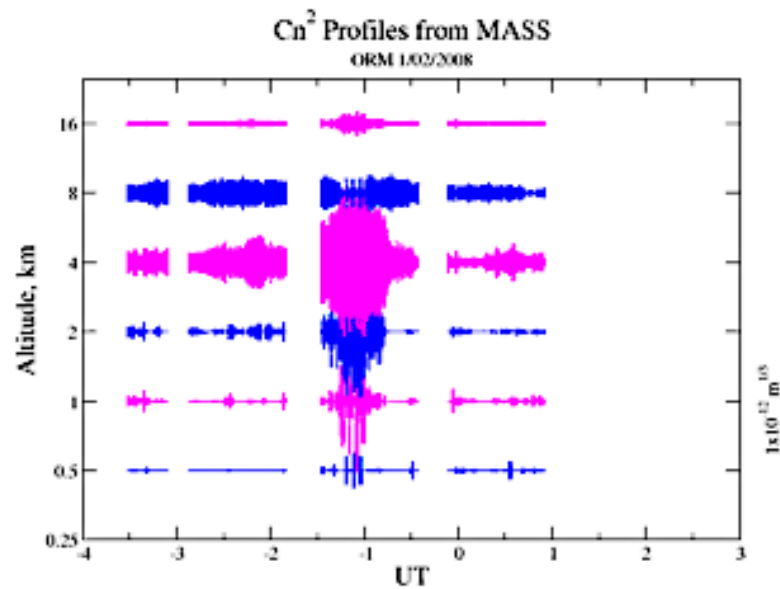


Figure 7.24: Reconstructed  $C_n^2$  profile from the MASS measurements. It shows an explosion in the middle altitude below the 4 km that propagates down to the lower layers. Also it can be seen at 16 km. This event occurs on the 1<sup>st</sup> of February 2008

The movements of masses of air can affect the local weather conditions, but it is the local conditions which can give bigger changes in the atmosphere conditions. The tables 7.16, 7.17, 7.18 and 7.19 are extended to the surface layer seeing and a new set of results, see table 7.20, 7.21, 7.22 and 7.23 and plot them against the free seeing where the contribution of the surface layers to the free atmosphere seeing will be clearly seen. Looking at figure 7.12 the surface seeing is the bigger contribution to the total seeing, following the total seeing curve, with an exception during October, where there is an increase in the contribution of the free seeing and a decrease in

the surface layer. This may be an indicator of the influence of the free atmosphere being dominant during this month.

We have been discussing monthly median values, but the real atmosphere can change daily due to local conditions or may be stable for short periods of days. Having as a reference the four months selected before, the daily distribution of the seeing may be different, we look at August (month number 8), where the free seeing ramps up whilst the surface seeing ramps down; the results can be seen in figure7.25, showing August seeing plots.

Date	Total seeing	Free seeing	Surface seeing
January 2	1.27	0.58	1.05
January 4	1.24	0.68	0.94
January 9	0.83	0.28	0.74
January 10	1.18	0.56	0.96
January 11	0.80	0.40	0.63
January 12	0.63	0.25	0.54
January 13	0.82	0.61	0.46
January 14	1.12	0.40	0.99
January 15	1.45	0.44	1.32
January 22	2.18	1.94	0.77
January 25	1.16	0.41	1.03

Table 7.20: Daily median seeing for the total (arcsec), free (arcsec) and computed surface seeing (arcsec). Data taken on January 2008.

Date	Total seeing	Free seeing	Surface seeing
May 3	0.75	0.30	0.64
May 4	0.94	0.50	0.72
May 5	0.84	0.40	0.68
May 6	0.65	0.43	0.42
May 12	0.51	0.19	0.44
May 13	0.70	0.41	0.51
May 14	0.64	0.51	0.32
May 16	1.08	0.35	0.97
May 17	1.40	0.34	1.32
May 18	0.84	0.43	0.66
May 19	2.08	1.15	1.57
May 27	1.29	0.30	1.22
May 28	0.63	0.57	0.2
May 29	NA	0.42	NA
May 31	0.96	0.35	0.84

Table 7.21: Daily median seeing for the total (arcsec), free (arcsec) and computed surface seeing (arcsec). Data taken on May 2008.

Date	Total seeing	Free seeing	Surface seeing
August 4	0.74	0.31	0.63
August 5	0.58	0.30	0.45
August 6	0.70	0.20	0.64
August 7	0.66	0.20	0.60
August 8	NA	0.49	NA
August 9	0.52	0.27	0.41
August 10	0.84	0.26	0.76
August 11	0.14	0.22	0.63
August 16	0.83	0.51	0.58
August 17	0.96	0.52	0.73
August 18	1.1	0.64	0.80
August 19	1.13	0.77	0.72
August 21	0.78	0.46	0.56
August 22	0.75	0.38	0.59
August 23	0.53	0.26	0.42
August 24	0.82	0.61	0.46
August 26	0.82	0.24	0.75
August 27	0.70	0.37	0.54
August 28	0.83	0.37	0.69
August 29	0.73	0.27	0.64
August 30	0.85	0.36	0.72
August 31	0.61	0.35	0.45

Table 7.22: Daily median seeing for the total (arcsec), free (arcsec) and computed surface seeing (arcsec). Data taken on August 2008.

The surface seeing follows the total seeing very well, but we can see some bursts (from the 14<sup>th</sup> until 22<sup>nd</sup>) where the free seeing is contributing more to the total seeing, which means a bigger contribution of the free atmosphere. This burst can be detected from the radiosonde data and its duration will be dependent on the

Date	total seeing	Free seeing	Surface seeing
November 3	1.20	0.34	1.1
November 9	1.15	0.42	1.0
November 10	0.81	0.24	0.74
November 11	1.40	0.67	1.13
November 12	1.0	0.29	0.92
November 14	0.67	0.23	0.6
November 18	1.20	0.58	0.97
November 29	0.70	0.30	0.6

Table 7.23: Daily median seeing for the total (arcsec), free (arcsec) and computed surface seeing (arcsec). Data taken on November 2008.

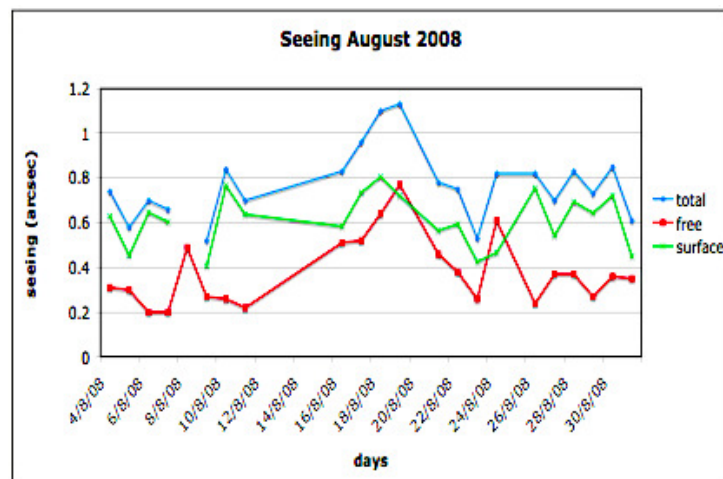


Figure 7.25: Daily median seeing values for the total seeing and free seeing with the calculated surface seeing for measurements taken during August of the year 2008.

macro-scale weather evolution. Looking the figure 7.26 that shows the seeing values and wind speed for August 2008 shows when the wind speed increases there is an increase in the free seeing, but with a low effect in the surface seeing which remains low.

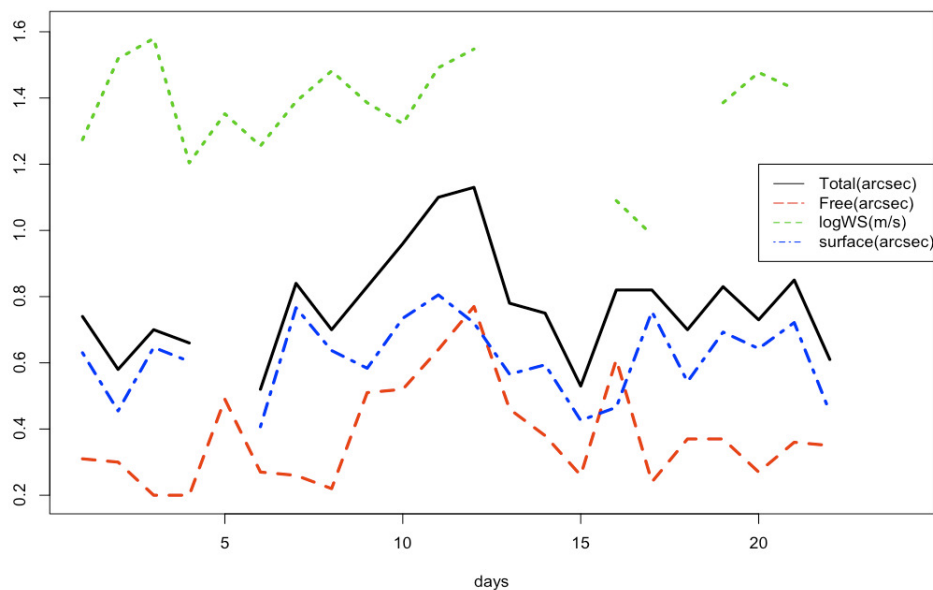
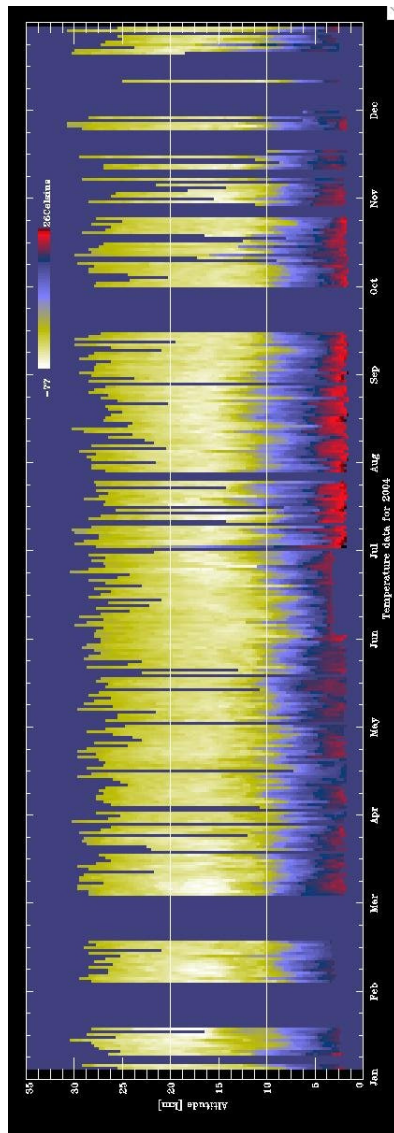


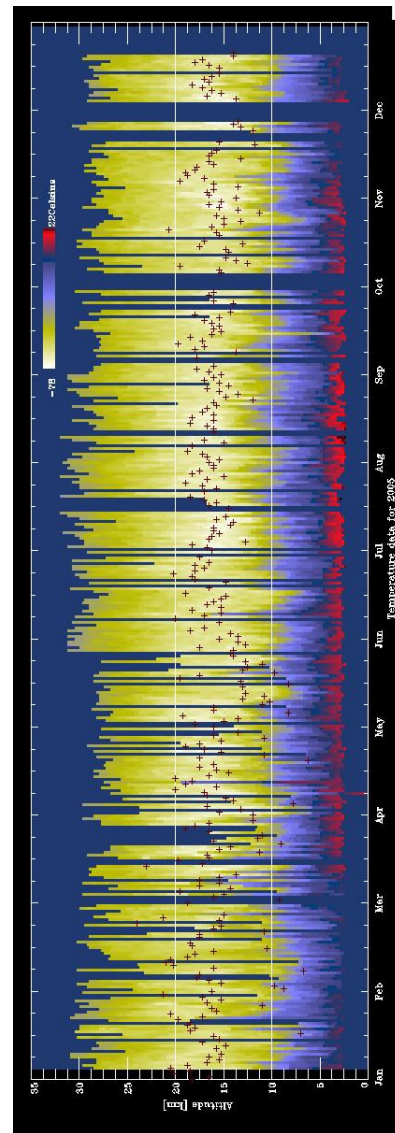
Figure 7.26: Daily median values for the seeing (total, free and surface) and the tropospheric wind speed, showing events where increase of the wind speed in the upper layers affects the seeing evolution with increase of the free seeing contribution to the total. The peak of this event took about 3 days to disappear with an increase of the free seeing values. The wind speed has a logarithmic scale for visual comparison with the seeing values.

## 7.5 Temperature and the optical turbulence.

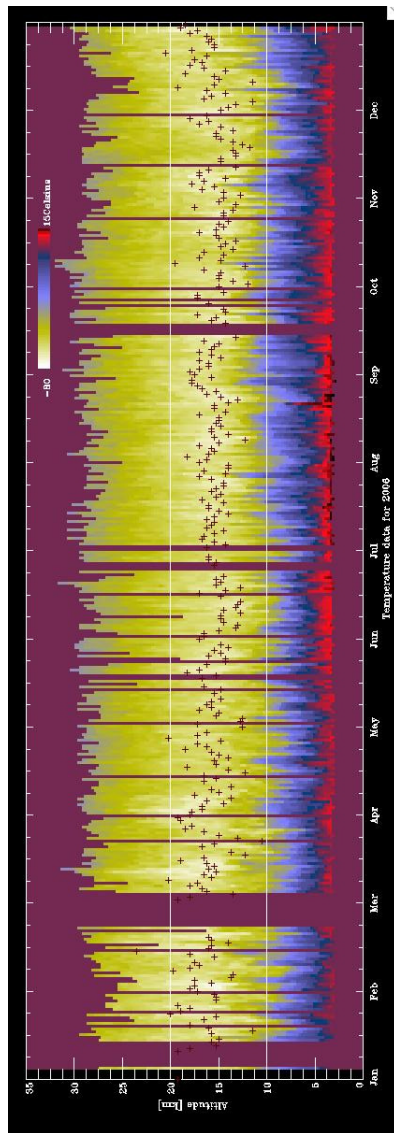
The optical turbulence can be defined as a fluctuation of the refractive index as a result of small changes in the temperature. This can be seen in the equation 3.9 (Chapter 3) that shows the relationship between the gradient of the potential temperature and the refractive index value. The changes in space and time of these cells with different refractive index causes effects in the light propagation like the scintillation and the phase fluctuations. The following figures (figure 7.27) show the vertical distribution of the temperature retrieved from the radiosonde data for the years from 2004 to 2008.



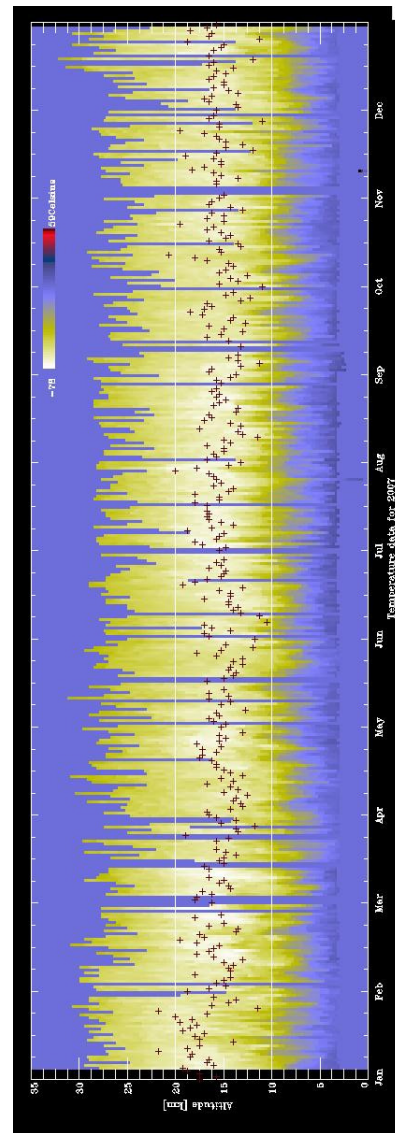
(a) 2004



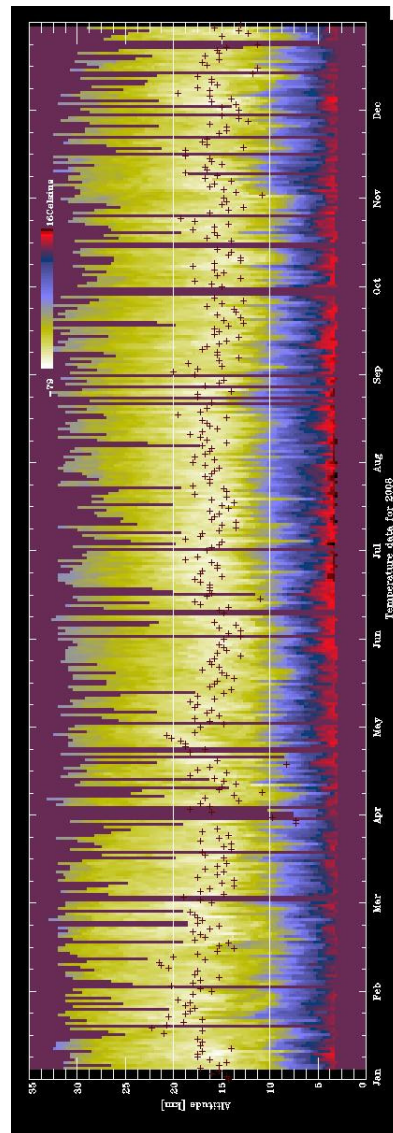
(b) 2005



(c) 2006



(d) 2007



(e) 2008

Figure 7.27: Figure set of the temperature profiles for the data collected from the radiosonde database and it shown in a gradient color profile that goes from blue to white, the crosses indicate where the troposphere inversion layer is produced.

The analysis of the temperature with respect to the optical turbulence is centered on the fluctuations of the gradient of the potential temperature  $\theta$  with the Heffter criteria as an index to determine the atmosphere status (turbulent or calm). The resulting values can be correlated with the local measurements of the optical turbulence by the MASS-DIMM instrument. To quantify the Heffter criteria, the temperature data are transformed into the gradients of the potential temperature,

and the criteria are applied to calculate the statistics of the monthly frequency of occurrence of calm and active layers. The data are grouped in four vertical slabs (3-5, 5-8, 8-11 and 11-16 km) to match the heights slabs of the  $C_n^2$  profiles; the monthly frequency for the year 2008 is shown in figures 7.28.

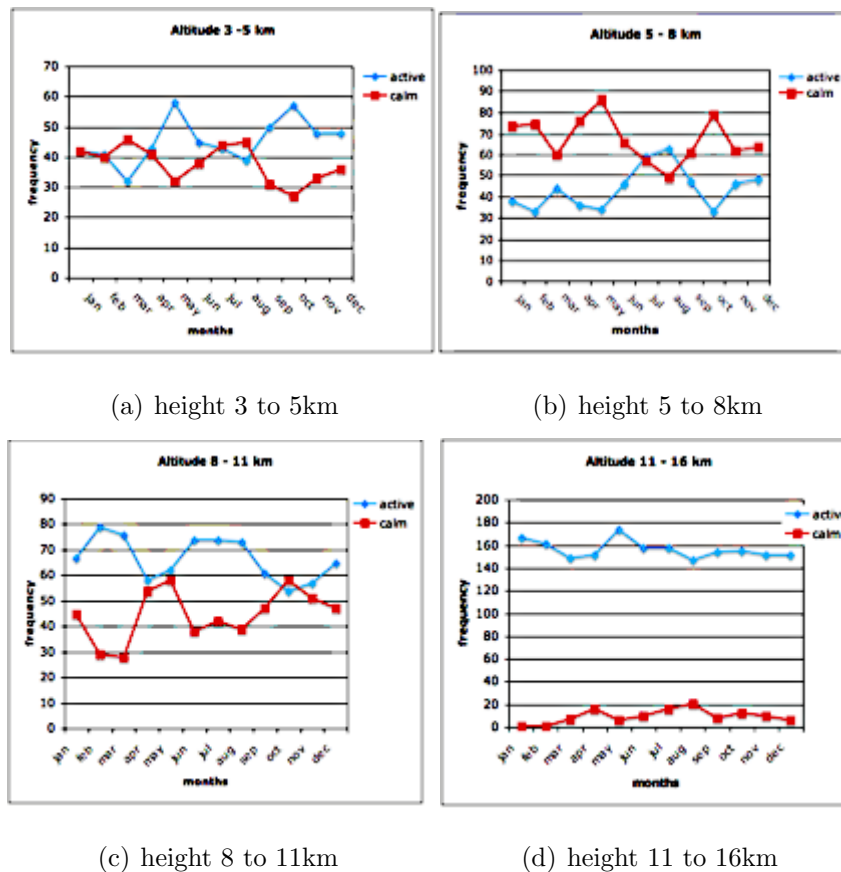


Figure 7.28: Frequency of occurrences of calm and active turbulence states at four height slabs. The data represent the monthly median of the data taken for the year 2008.

From the figure 7.28 can be identified a calm altitude slab which corresponds with the range from 5 to 8 km during most of the year with the exception that during the summer months July and August becomes more active which means that there is more probability to develop turbulence. Another significant condition is that the altitude slab 11 to 16 km shows an active state through all the months with a slight reduction during the summer. This altitude slab represents the region where the jet stream is located and it shows the high probability to trigger a turbulent

state. The slight reduction in summer is due to the low influence of the jet stream during the summer period, this effect can be seen in the  $C_n^2$  profiles from the MASS-DIMM instrument that detects the upper layer (16 km) with a persistent value of  $10^{-14}$  which makes references to a turbulent layer. The layer slab below shows a predominantly active conditions, this can be related to the fact that the edge of the jet stream moves faster than the air masses at this heights, producing a mixing of the air masses with a different temperature.

The calm layer is about 5 to 8 km which is in the middle of the atmosphere where the turbulence from the upper layers can not go down making this region more stable. We can see that during the summer time this region is getting more active which means that it can be possible that warm airmasses are in collision with the cooler air masses and start to mix the layers.

For the vertical slab from 3 to 5 km the Heffter index gives an active layer with a drop from April to August. The same effect can be seen in the  $C_n^2$  plot (figure 7.13) where the layer at 0.5km (3 km) drops clearly from April to September, also the layer at 1km (3.5 km) shows the same drop. The figure 7.28 for the slab between 5 to 8 km the Heffter index gives a very calm layers with the difference during the summer months (May to August) where there the active layers rise up, for the  $C_n^2$  figure we can see that slab 4 and 5 km rise up from May to September increasing the strength of those layer to the turbulence.

The MASS instrument is getting profiles every minute, and to compare those measurements with the Heffter criteria index, the  $C_n^2$  values from the MASS instrument is analysed taking the monthly percentage of the strength per every layer. This makes a distribution of the layers per month. The figure 7.29 shows the monthly strength contribution of the  $C_n^2$  per year 2008.

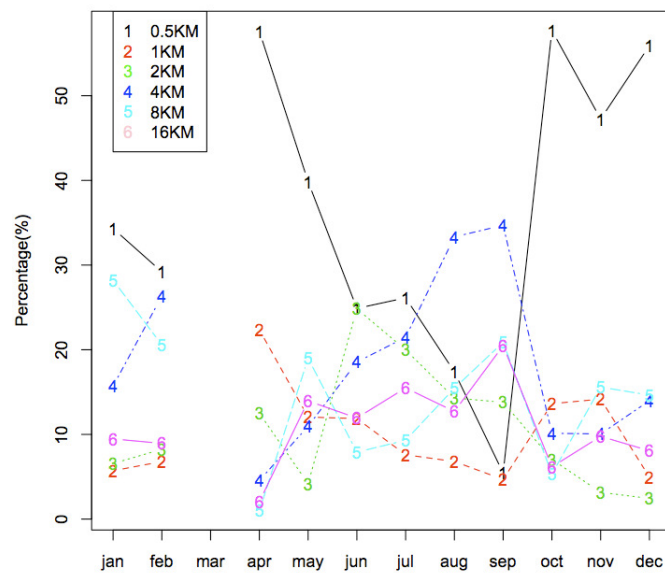


Figure 7.29: Percentage of the monthly distribution of the turbulence strength for the year 2008. Different colors to express the height slabs measured with the MASS instrument (0.5,1,2,4,8 and 16 km). No data available for March.

# Chapter 8

## Optical Turbulence Modeling

*"We can hope that the time will soon come when either as a daily routine, or for certain designate days a complete diagnosis of the state of the atmosphere will be available. The first conditions for putting forecasting on a rational basis will then be satisfied".*

*Vilhelm Bjerknes, 1900*

---

### 8.1 Overview.

Lewis Fry Richardson in England (1881-1953) was the first scientist to develop a numerical weather prediction system based in the division of space into a grid and using the finite approximation (primitive differential equations) proposed by Bjerknes's<sup>1</sup>. When Richardson tried to run a single model with a period of 8 hours it took about six weeks of real work to perform the analysis and at the end failed. This primitive model required such an enormous calculations that Richardson proposed a solution to manage all the calculations and he proposed something that

---

<sup>1</sup>Vilhelm Bjerknes.(1862-1951)Physicist and meteorologist norwegian argued that atmospheric physics had advanced sufficiently to allow weather to be forecast using calculations. He developed a set of seven equations whose solution would, in principle, predict large-scale atmospheric motions.

he called the "forecast-factory". The "factory" would have involved filling a vast stadium with 64000 people where each one is calculating and would be part of the flow calculations. A leader in the middle would manage all the communication and at the end coordinate the forecast.

Today the weather forecast takes a supercomputing process to run the meteorological models like the European Center Meteorological Weather Forecast (ECMWF), which can forecast the weather in periods of up to 78 hours for any region in Europe. Much effort has been put into the use of meteorological forecasts for the determination of the optical turbulence (Masciadri, 2006). This could be used a useful tool in many fields of application such as site testing or supporting the observations of any AO or MCAO system depending upon the atmosphere turbulence profiles. Also it is an important issue for the management of observing time (allocating the best sky conditions, i.e. better seeing and  $C_n^2(h)$  profiles) to the AO observing schedule. This Chapter gives a description of the modeling techniques used to obtain a  $C_n^2(h)$  profile using meteorological parameters applying the Hufnagel-Valley model and a proposed model by Trinquet (Trinquet et al, 2006).



Figure 8.1: Richardson's artistic vision of how should be the forecast "factory". Credit. Franc Schuiten.

## 8.2 Introduction.

The use of the meteorological data to estimate the  $C_n^2(h)$  profile from the different model equations which can be large values compared with those derived from other on-site systems with a better spatial and temporal resolution. But the atmosphere modeling can be done assuming a statistically stationary regime for well developed homogeneous turbulence following the Kolmogorov law giving the refractive index structure constant  $C_n^2(h)$ . The following equation is mainly used in different synoptic models related here;

$$C_n^2(h) = \alpha^2 L_0^{4/3} M^2 \quad (8.1)$$

where  $\alpha = 4.8$ ,  $L_0$  is the outer scale parameter and  $M$  is the buoyancy relationship. The buoyancy is the dynamic process that drives the vertical motions in the atmosphere, and this is determined by the vertical gradient of temperature.

Consider the buoyancy coefficient given by the equation;  $B = (g/\theta)d\theta/dz$ , where  $g$  is the gravity acceleration,  $\theta$  is the potential temperature and  $z$  is the altitude. It has been defined that  $C_n^2(h)$  is mainly related to the local vertical gradients of temperature and humidity. We take a large area and assume that the local meteorological quantities, pressure, humidity and temperature, do not vary appreciably over large scales to affect the values of  $C_n^2(h)$ . The Canary Islands are an example where the free atmosphere turbulence cannot vary too much from one island to another due to the stability of the atmosphere caused by the ocean between the islands and the short distances between the islands.

In this simple model of the  $C_n^2(h)$  there is a factor of the outer scale  $L_0$  which can be in the range from centimeters to several hundred meters. To identify the outer scales with the low radiosonde values obtained from the radiosonde database is a very difficult task and with only a high resolution instrument can this parameter can be identified. VanZandt (VanZandt et al, 1978) found that the outer scale values can be parameterized in the free atmosphere where it usually takes values between 10 and 100 meters. By examining the backscatter from the free atmosphere, VanZandt estimated the average of the outer scale as  $L_0=10$  m and others have been working on

estimating the  $C_n^2(h)$  by the means of equation 8.1 (Karasawa et al,1988). Recently an instrument has been proposed (Tokovinin et al,1998) to determine the outer scale at observatories with high temporal resolution. This is the Grating Scale Monitor (GSM)<sup>2</sup>

It has been mentioned before how the modeling of the atmospheric turbulence ( $C_n^2(h)$  modeling) can help many aspects in the astronomy field, but this knowledge of the  $C_n^2(h)$  can be extended to the laboratory at the point when AO systems are starting to be optimized to operate in real situations. As an example one may consider the Large Binocular Telescope (LBT) AO system ( Esposito et al, 2010) which has used knowledge of the  $C_n^2(h)$  and astroclimate parameters on Mt. Graham to perform tests of the system in a scenario similar to where the system will be deployed. The importance of the prior knowledge of the astroclimate parameters at Mt. Graham (LBT site) has allowed to performs the system tests under similar conditions that the site. The particular conditions of the LBT AO system which basically consists in a 91cm adaptive secondary mirror (ASM) with a pyramid wavefront sensor. The AO system is calibrated using the 14 meters solar tower sited at Arcetri observatory (Italy) to place the secondary mirror and the system is calibrated using the ASM has a turbulence generator which run a phase screen associated to a specific disturbance which is added to the final position of the secondary. The system lock the loop in this emulated disturbance running in the secondary where the mirror shape is following the residual wavefront and other external disturbance such as; thermal convections or tower bending. The phase screens are generated with the median atmospheric condition for the observatory with the median seeing of 0.8" a wind speed of  $15ms^{-1}$  and an outer scale of 20 meters. Looking the statistics of the site other phase screens can be generated and it can be tested the performances of the AO system and improve his performances for some special atmospheric scenarios.

The following models will retrieve the  $C_n^2(h)$  from the radiosonde and it shows the possibility of using them as a low computing time consuming method to generate

---

<sup>2</sup>Grating Scale Monitor (GSM). GSM is an instrument which measures the covariance of the angle of arrival fluctuation simultaneously detected at several points on the wavefront.

$C_n^2(h)$  profiles in advance ( forecasting ). It is not the scope of this work to perform an analysis of the reconstructed phases. The figure 8.2 details a block diagram of the atmospheric turbulence propagation and this is injected into the model to retrieve the optical imaging performances.

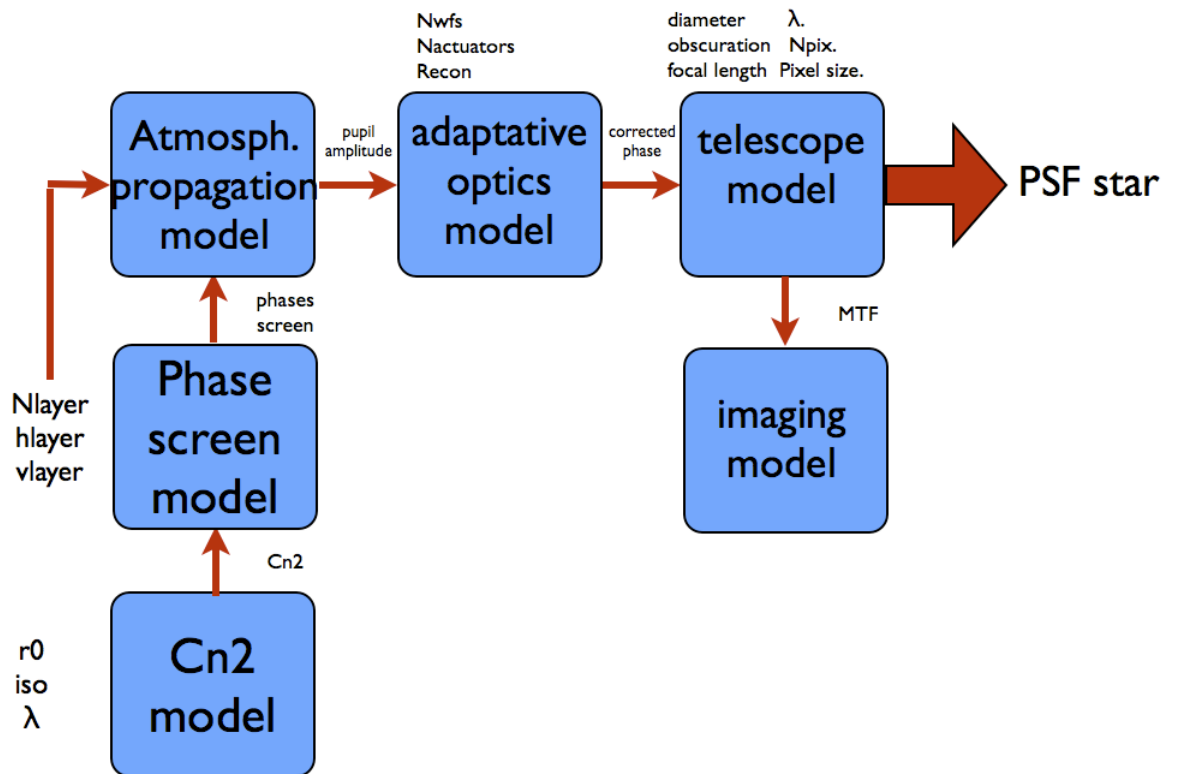


Figure 8.2: Schema of the information from the model of  $C_n^2$  and how many parameters can be added to the whole system to retrieve a performance of the system measuring the PSF of the source through the turbulent medium. The values are identified as; "r0" coherence length (Fried parameter), "iso" isoplanatic angle, "λ" wavelength, " $C_n^2(h)$ " refractive index coefficients. "Nlayer" number of turbulent layers determined, "Hlayer" height of the turbulent layers, "Vlayers" velocity of the layers, "Nwfs" number of wavefront sensors used, "Nactuators" number of actuator, "Npix" number of pixels of the detector.

## 8.3 Synoptic analysis of models.

The models are dependent on meteorological parameters. This dependency is on the pressure, wind speed and temperature as the most common parameters to apply in the models. Taking those parameters obtained from the meteorological database, the model can be built using the meteorological data set and applying the model to the night time at a synoptic time of 00:00 (midnight); the profile of  $C_n^2(h)$  is computed for each data set and other astroclimate parameters such as coherence length and isoplanatic angle can also be retrieved.

Using the  $C_n^2(h)$  profile retrieved from the model (equation 8.1) the coherence length and the isoplanatic angle can be calculated using the equations 3.18 and 3.21 where it is assumed that there is a Kolmogorov spectrum of the turbulence (zero inner scale and infinite outer scale). Those parameter can be retrieved using the  $C_n^2(h)$  via integrals over the optical path.

The following models are considered for their low cost in computing time, with simple mathematical equations and a reasonable correlation with real on-site  $C_n^2(h)$  profiler instrumentation. For the model, the surface layer is not considered and only the upper atmosphere is analyzed in terms of its variation as a coefficient contribution

### 8.3.1 Hufnagel-Valley Model.

As an example of a vertical profile model we consider the H-V model, which is a single-parameter model determined from the upper altitude wind speed. This model (Beland, 1993), consists of a fusion of the original Hufnagel (Hufnagel, 1978) model, and its extension to the ground by Ulrich (Ulrich, 1988), based on a suggestion by Valley (Valley, 1980). The H-V model is very well known and often cited (Beland, 1993; Roggemann and Welsh, 1996; Andrews and Phillips, 2005). The H-V model is very popular due to its simplicity and that only using the upper level wind speed,  $U$ , given as the Root Mean Square (rms) windspeed ( $ms^{-1}$ ) averaged over the 5 to 20 km vertical range. The H-V model also has a very simple form which has been mathematically described in Chapter 3 and is here summarized by the equation:

$$C_n^2(h) = \left[ 5.94 \cdot 10^{-53} h^{10} \left( \frac{W}{27} \right)^2 e^{-h/1000} + 2.7 \cdot 10^{-16} e^{-h/1500} + A e^{-h/100} \right] \quad (8.2)$$

### Data and Analysis

Using the modified H-V model for La Palma described in the Section 3.7 by the equation 3.30, to describe the optical turbulence, and evaluating it in the free atmosphere, a profile of the refractive index parameter  $C_n^2(h)$  can be built. The statistics of the wind speed for the year 2008 (median, 1<sup>st</sup> and 3<sup>rd</sup> Quartile ) is summarized in the table 8.1 and it is used to build the yearly median  $C_n^2(h)$  profile. The statistics of the wind speed for the median, 1<sup>st</sup> quartile and the 3<sup>rd</sup> quartile are calculated for the height slab between 5 to 15 km.

Wind speed [m/s]	Jan	Feb	Mar	Apr	May	Jun	Jul	Aug	Sep	Oct	Nov	Dec
1st Q	27.5	38.25	36.5	18.5	39.0	16.5	14.0	14.0	9.5	20.5	25.0	29
Median	31.5	49.0	50.0	33.0	50.0	28.0	18.0	16.5	13.8	26.0	43.0	43.5
3rd Q	38.5	69.0	65.0	67.0	54.0	34.0	27.75	19.0	17.5	37.5	53.5	65.25

Table 8.1: Summaries of the statistics of the wind speed taking the height slab between 5 to 15 km. The wind data are retrieved from the radiosonde database. The launch site is 120km away from the observatory. The 1<sup>st</sup> Q and the 3<sup>rd</sup> Q are the first and the third quartiles.

A monthly  $C_n^2(h)$  profiles can be built using the data summarised in the table 8.1 for the monthly tropospheric wind speed and it shown in the figure 8.3. The Huffnagel-Valley model gives a  $C_n^2(h)$  profile with 1 km vertical resolution starting at 3 km which is above the Observatory Roque de los Muchachos (2400m asl) to 30 km.

The model can be compared with the median  $C_n^2(h)$  profile retrieved from the MASS measurements and calculating a correlation of the two data sets. It has been stated that the MASS instrument only gives a low vertical resolution of the  $C_n^2(h)$  measurements with the vertical slabs; 0.5, 1, 2, 4, 8 and 16 km above the observatory, and these heights are 3, 3.5, 4.5, 6.5, 10.5 and 18.5 km when situated at the Observatorio Roque de los Muchachos. Taking the median H-V profiles to

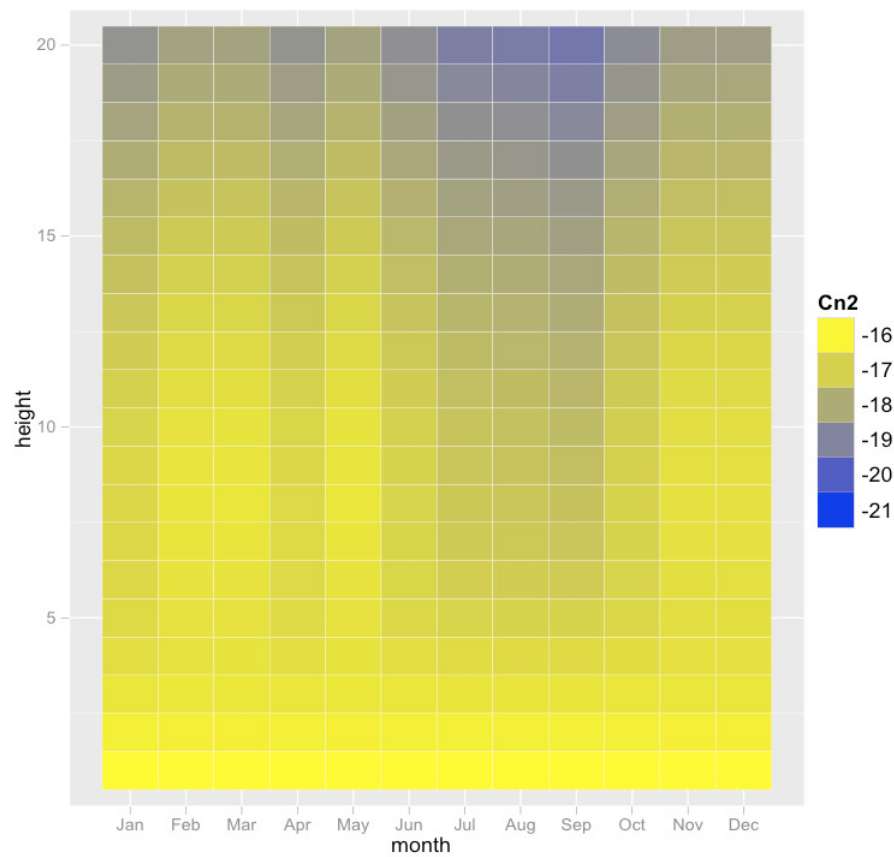


Figure 8.3: Representation in gradient color image of the vertical  $C_n^2(h)$  profile from the modified H-V model, applying the monthly median wind speed between the heights 5 to 15 km. The scales goes from -21 to -16 that represents: -21 a stable (weak) atmosphere and -16 a turbulent state. The  $C_n^2(h)$  is measured ( $m^{-2/3}$ ). The x-axis is represented by the months (January to December) and y-axis is the height (Km).

get the same height slabs, the two data set gives a Pearson correlation of -0.1 which is poor correlation factor.

Looking at the figures 8.3 and 8.4 some visual relationship can be find during the summer periods where the MASS profiles shows a weak turbulence around 4 and 6 km which corresponds with weak turbulence in the Huffnagel-Valley profiles.

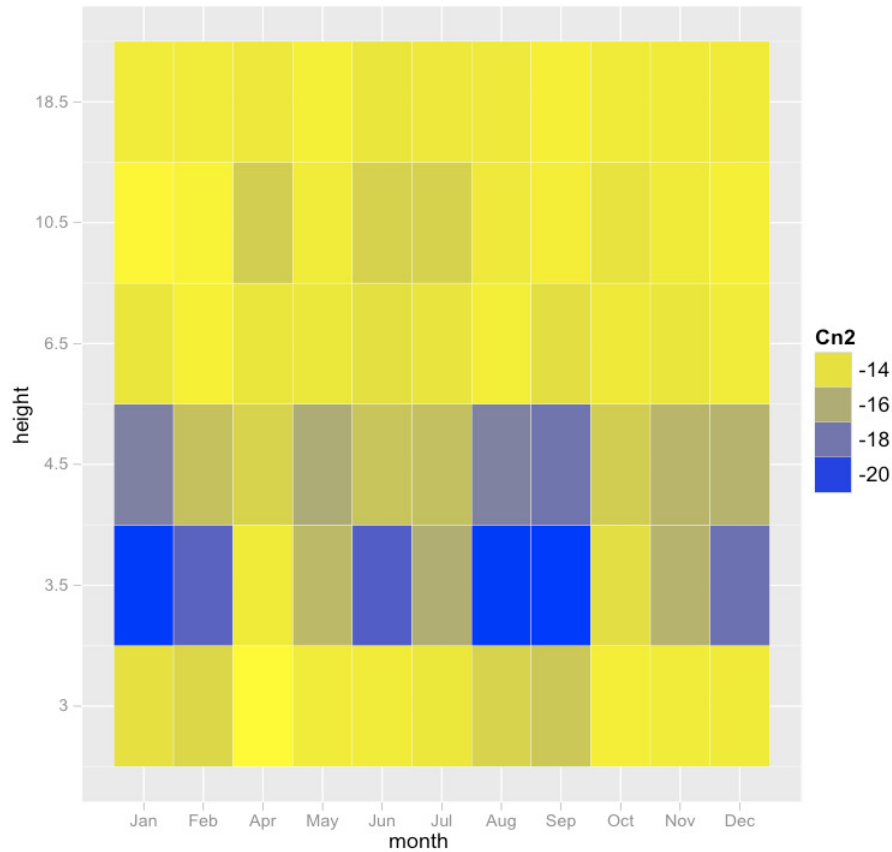


Figure 8.4: Statistical median monthly  $C_n^2(h)$  profiles retrieved from the MASS measurements located at Observatorio Roque de los Muchachos (La Palma) with a distance of 120 km away from the radiosonde launch (Tenerife). The MASS gives 6 heights slabs; 0.5,1,2,4,8 and 16 km where are represented in the y-axis by; 3,3.5,4.5,6.5,10.5 and 18.5 Km.respectively. The x-axis gives the month with an empty 3 (March) due to the fact that the MASS instrument was out of operation.

### 8.3.2 AXP Model.

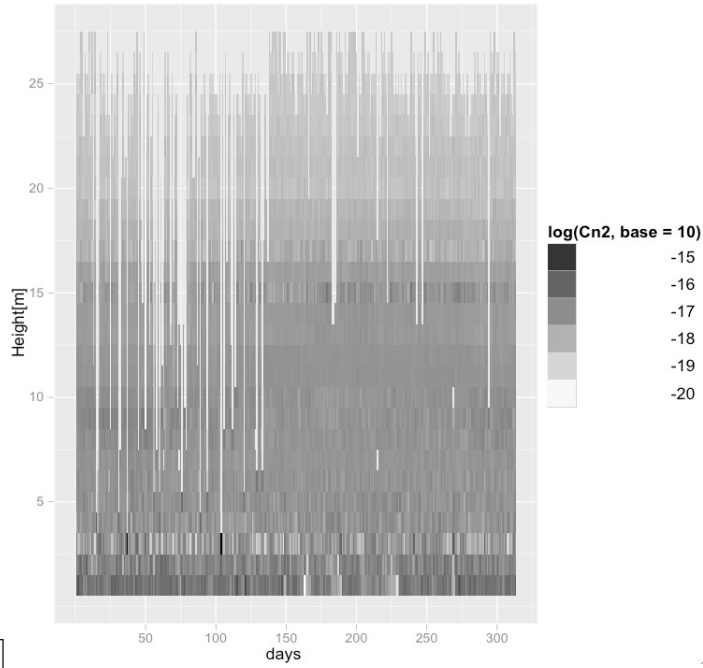
The AXP model is a model based on the knowledge of the potential temperature gradient and on the wind distribution. This model has been described in Section 3.6.3. The physical phenomena caused by the atmosphere turbulence can be associated with the case where large scale atmospheric features, such as the wind, form turbulent eddies and where the energy is input into the turbulence system from the thermal and the kinetic energy of the turbulence. The affected temperature and wind speed of the atmosphere are determined by the state of the atmospheric profile

and using the algorithm described in Chapter 3 as a feasible method to build refractive index parameter profiles. The data set (meteorological parameters) is limited to one measurement per night but with good sampling through the years. To analyse the model feasibility with the local real time turbulence monitor, only a fraction of the atmosphere is of interest to correlate and this is the upper atmosphere (above 5 km). Taking the radiosonde data from the database and using the AXP model equations, the refractive index parameter is retrieved in a daily profile for the whole year as a daily  $C_n^2$  vertical profile.

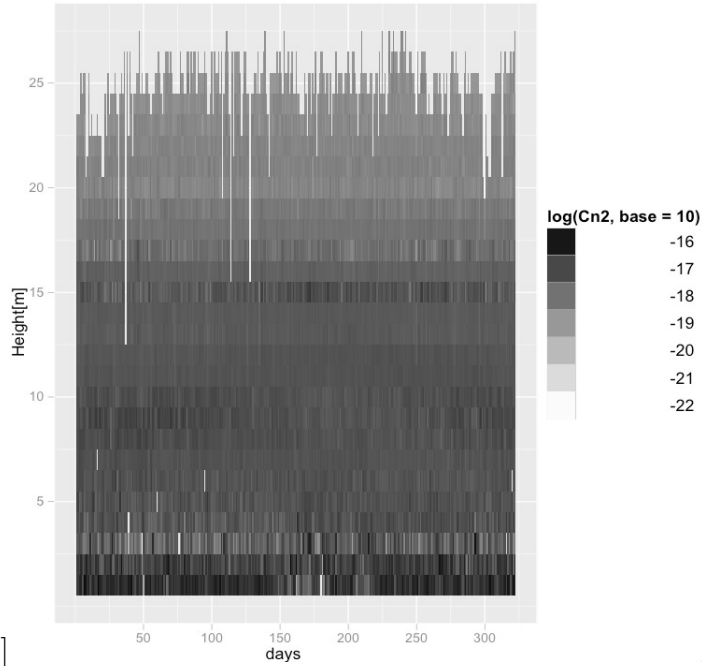
### Data and Analysis.

The meteorological parameters used for the AXP model have been described in Chapter 7 where a series of meteorological parameters such as; temperature, wind speed, humidity and wind direction are identified in daily vertical profiles. The daily data from the radiosonde is binned with one kilometer resolution to match the vertical resolution of the AXP equations (see table 3.4, Section 3.7.3). Then a  $C_n^2(h)$  profile computed can be plotted on a daily distribution along the year or months identifying possible seasonality of the  $C_n^2(h)$  values and its vertical distribution. A set of figures is showed in the Figure 8.5 where it is shown the constructed  $C_n^2(h)$  profiles for the years from 2005 to 2008 in a 2-D temporal distribution in a days basis.

It is known that the H-V is one the most utilized  $C_n^2(h)$  profiles to elaborate models of the optical turbulence and the values are often used as input to the error budget in AO system design. Having the assumption of the H-V as a useful optical turbulence model, the AXP model can be compared and correlated with the H-V profiles to provide an index of the feasibility of this model. Building a monthly series of  $C_n^2(h)$  profiles using the AXP model and the modified H-V model during the year 2008 and plotting the statistics of the median, first and third quartile together as is shown in figure 8.6, a first glance shows a strong correlation between the two time series for the whole year. The monthly Pearson correlation is summarized in table 8.2 and figure 8.7 shows the scatter distribution of the yearly  $C_n^2(h)$  for the two models with linear fitting and smooth line.



[(a)2005]



[(b)2006]

Month	Jan	Feb	Mar	Apr	May	Jun	Jul	Aug	Sep	Oct	Nov	Dec
Pearson correlation	0.89	0.90	0.90	0.88	0.94	0.92	0.89	0.91	0.92	0.91	0.92	0.95

Table 8.2: Pearson correlation values for the  $C_n^2(h)$  profiles obtained using the H-V and AXP model with the same meteorological parameter.

In order to improve the feasibility of the model, it can be correlated with the  $C_n^2(h)$  profiles measured with the MASS instrument on site. It is important to

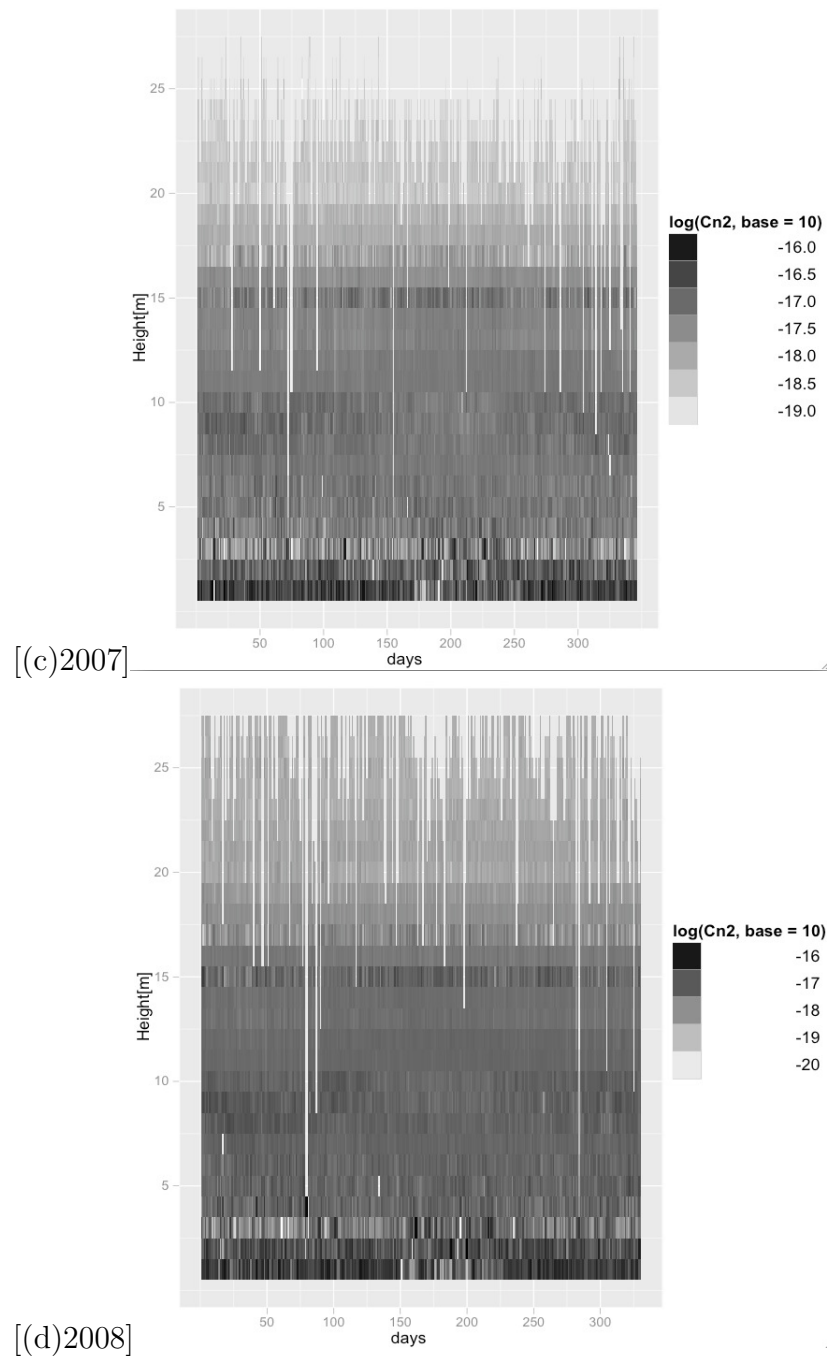


Figure 8.5: Set of figures representing the temporal variation of the  $C_n^2(h)$  profiles obtained from the AXP model for 4 years of meteorological data retrieved from the database (Chapter 6). The figure represents a 2D gradient of the logarithm of the  $C_n^2(h)$  values with the x-axis for the days and the y-axis for the altitude. (a) the year 2005, (b) year 2006, (c) year 2007 and (d) year 2008.

## H-V and AXP models

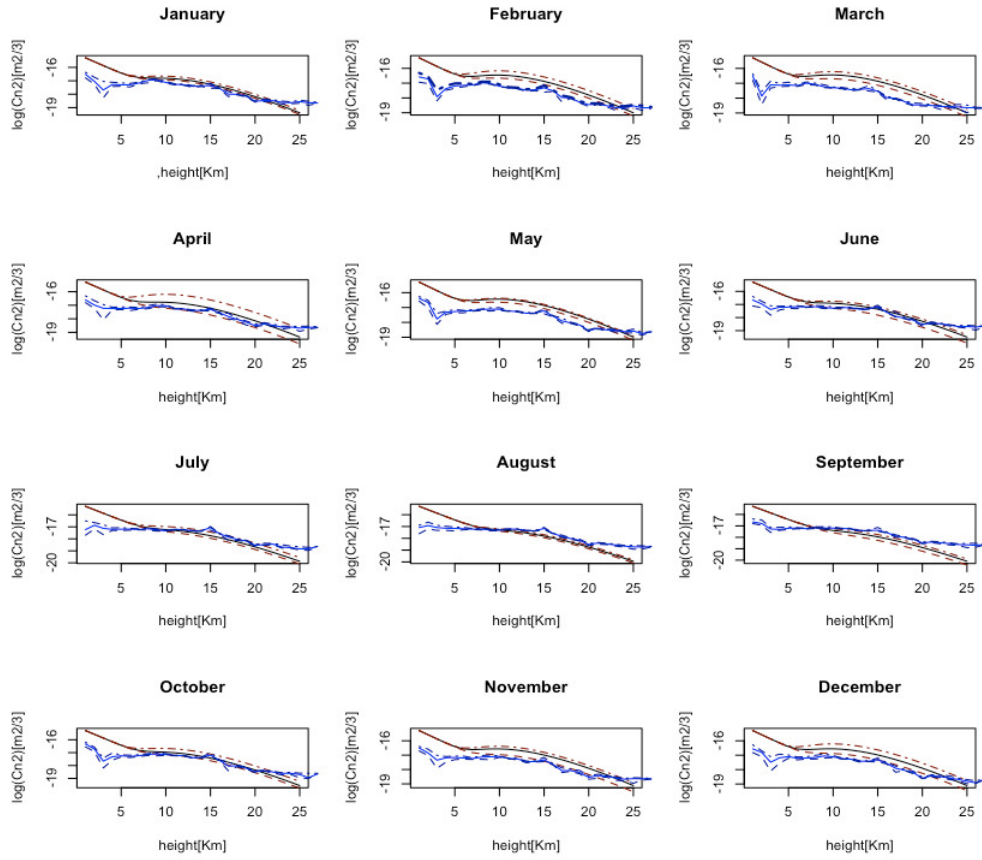


Figure 8.6: Monthly statistics plots of the  $C_n^2(h)$  retrieved from two models; the Hufnagel-Valley and the AXP. The solid blue line is the median value for the AXP model and the dashed lines are the 1<sup>st</sup> and 3<sup>rd</sup> quartiles. The solid black line is the median for the H-V model and the dashed red lines are the deviation formed by 1<sup>st</sup> and 3<sup>rd</sup> quartiles.

remember that the AXP model generates a  $C_n^2(h)$  profile using meteorological parameters taken about 120 km away from the MASS site and uses only one profile per night (synoptic time at 00 UT). The data sets available from the MASS instrument are distributed through the year 2008 in a different way, with the following monthly distribution summarized in the table 8.3. The same dates are taken for the  $C_n^2(h)$  profiles from the AXP model.

The profile obtained with the AXP model has a vertical resolution of one kilo-

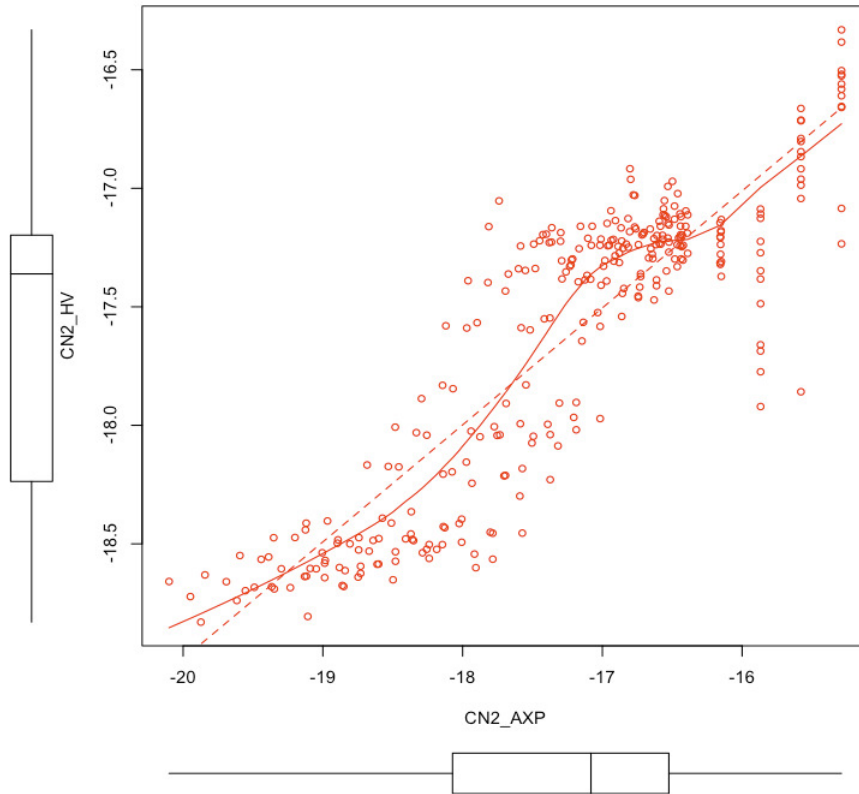


Figure 8.7: Scatter plot for reconstructed  $C_n^2(h)$  profiles obtained from the AXP and HV model. The x and y -axis shows the logarithm of the  $C_n^2(h)$  vales ( $m^{-1/3}$ ). The red dash line shows the linear fitting and the solid red line is the smooth series. The figure includes two boxplots with the distribution of the series and with the median value displacement.

Month	Jan	Feb	Mar	Apr	May	Jun	Jul	Aug	Sep	Oct	Nov	Dec
N nights	4	3	NA	3	6	8	17	16	6	4	5	9
Total	81 nights											

Table 8.3: Summary of the number of observing nights used to perform the correlation of the MASS measurements with the  $C_n^2(h)$  profiles retrieved from the AXP model using the data for the year 2008.

meters that it is different to the MASS profiles vertical slabs. To compare the two profiles the AXP one has to be sampled in the same way as the MASS heights sampling. The new profiles are built with the median value of the  $C_n^2(h)$  for the height

slabs; 3, 4, 5, 7, 11 and 16 km.

Figure 8.8 shows the distribution for the two  $C_n^2(h)$  profiles grouped by the heights for the yearly distribution and from a first look at the plot a correlation of the distribution can be determined, with a large variability below 16 km. Table 8.4 summarizes the correlation of the statistics of the  $C_n^2(h)$  per month. Due to the lack of observations a correlation factor cannot be considered as good as if the sampling of the two series were larger.

Month	Jan	Feb	Mar	Apr	May	Jun	Jul	Aug	Sep	Oct	Nov	Dec
Corr.	-0.23	0.49	NA	0.52	0.02	0.02	0.14	-0.17	-0.25	0.18	0.17	-0.24

Table 8.4: Summary of the monthly Pearson correlation for the AXP and MASS  $C_n^2(h)$  values.

Once the  $C_n^2(h)$  profiles are obtained, the other astoclimate parameters like the coherence length can be calculated. Taking the integrated  $r_0$  for each daily profile during the year 2008 and retrieving the seeing from the  $r_0$  values it is possible to deploy the statistical analysis for the seeing retrieved from the radiosonde data for the AXP model. The seeing obtained with the AXP model refers to the upper atmosphere seeing, which can be correlated with the free seeing measurements with the MASS instrument. With the knowledge of the  $C_n^2(h)$  values, the  $r_0$  can be calculated and taking all the  $C_n^2(h)$  profiles for the year 2008 and calculating the  $r_0$  for each profile, the monthly distribution can be built and is shown in figure 8.9 as a boxplot representation. The values obtained with the AXP model suffer a bias due to that model approximation equation 3.34 reduce the accuracy of  $C_n^2(h)$  profiles to about 50% of the real measurements. Also the data are smoothed by the mean every kilometer height slab to match the vertical resolution of the AXP model (one kilometer). The model can quantify the parameter changes through the year. The monthly median value of the free seeing calculated from the AXP model  $C_n^2(h)$  and the free seeing measured with the MASS-DIMM instrument is shown in figure 8.10.

The free seeing calculated from the AXP has a short variability around 0.51 arcsec and this is different from the variability shown in the measurement of the free seeing with the MASS instrument, but looking at the statistical approach in

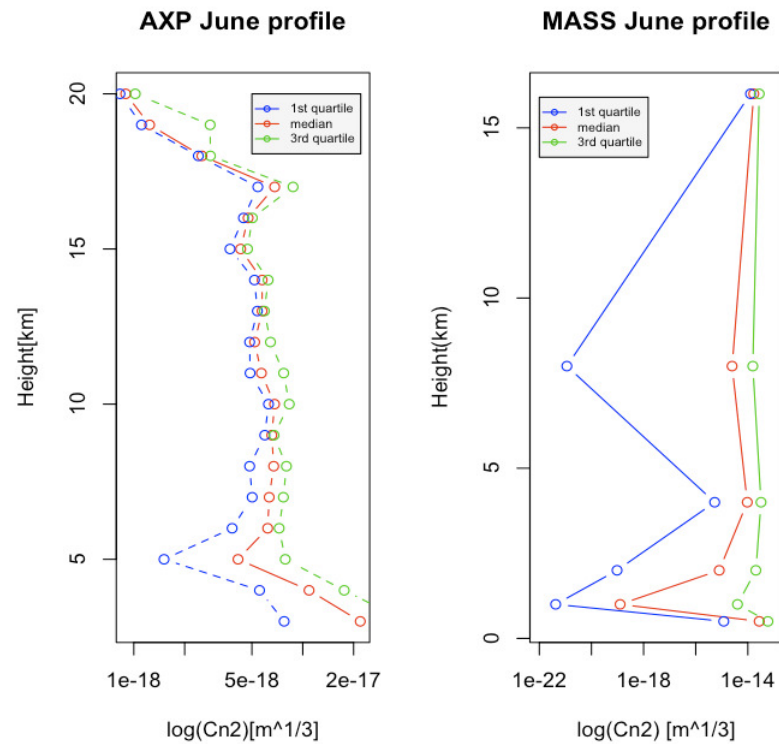


Figure 8.8: Comparison of the median distribution of the  $C_n^2(h)$  profiles from the MASS measurements and the  $C_n^2(h)$  profiles retrieved from the AXP model. x-axis ( $\log C_n^2(h)$ ), y-axis is the heights (Km). The data shows the data compiled for June 2008.

the figure 8.10 the two time series have a similar behavior, which can contribute to determine that the free seeing from the AXP model can detect the variability (seasonality) of the real measurements

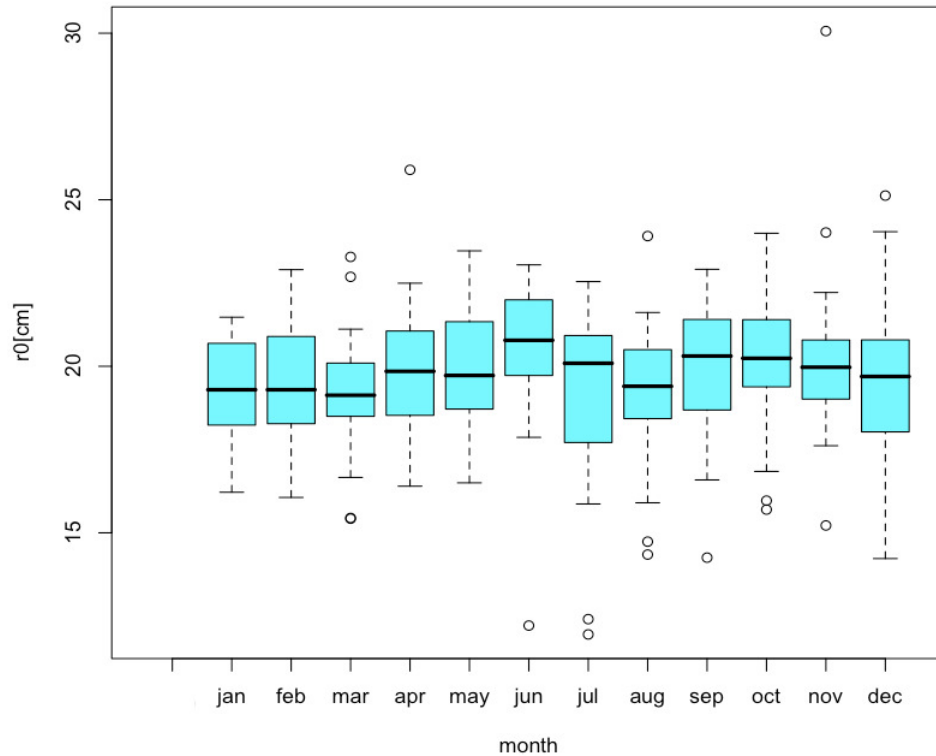


Figure 8.9: Boxplot representation of the monthly distribution of the  $r_0$  parameter obtained with the AXP model for the year 2008.

### 8.3.3 Qualitative evaluation of the refraction index profile obtained with the model AXP (thermosode data) and SCIDAR profiles.

To get a qualitative evaluation of the refraction index profiles obtained through the model it will necessary to provide  $C_n^2(h)$  profiles to compare with a reasonable vertical distribution. The MASS instrument gives the  $C_n^2(h)$  profiles for 6 heights slabs hence requiring that the results from the model has to be adapted to those height slabs. We have retrieved two plots, figure 4.13a and figure 4.13b, of the median  $C_n^2(h)$  profiles obtained with the SCIDAR which has been mentioned in the Chapter 4. Taking the  $C_n^2(h)$  profiles obtained through the AXP model and calculating the median values for the same number of nights and putting these together with the SCIDAR profiles, we obtain figures 8.11 and 8.12. The data to

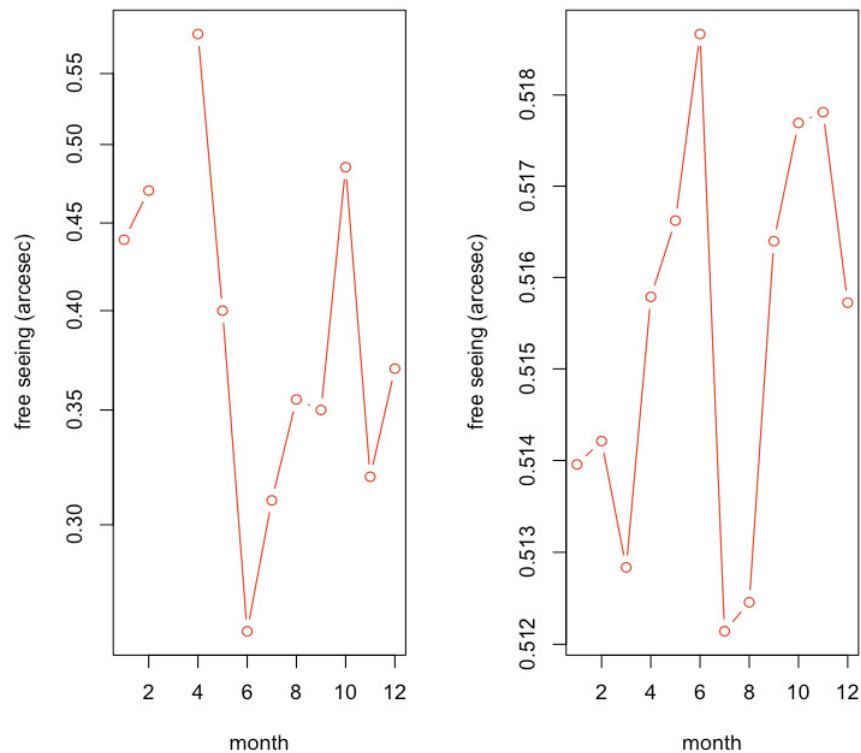
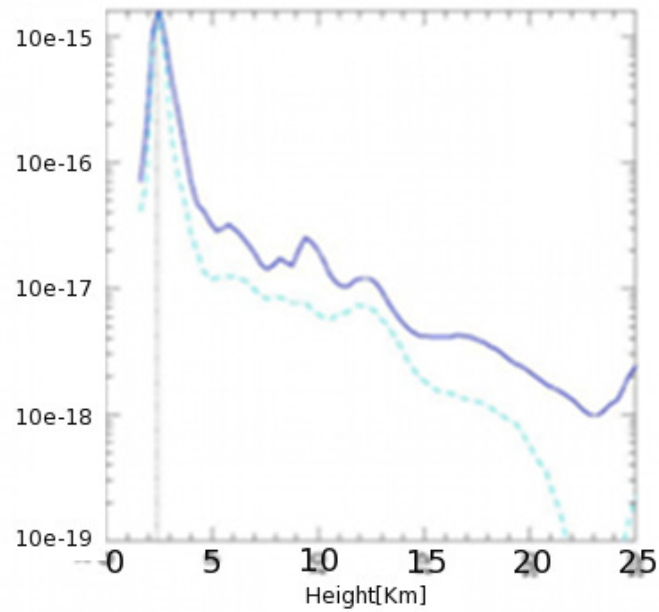
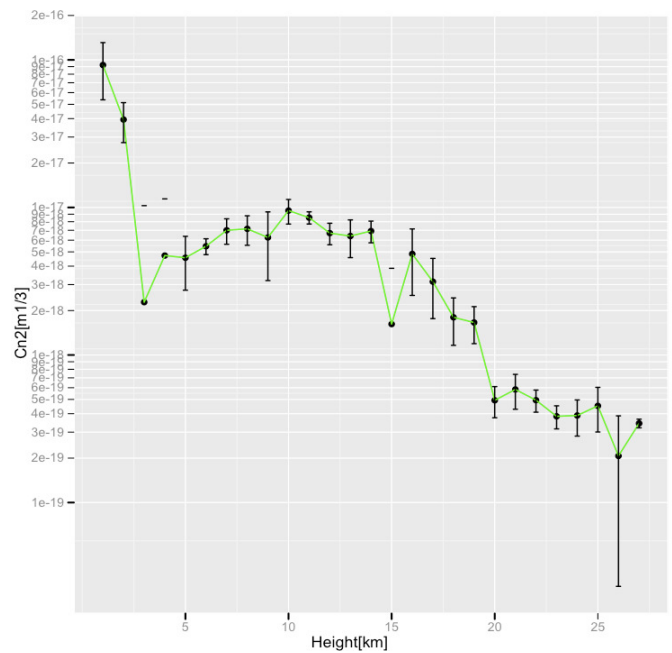


Figure 8.10: Comparison between the MASS and AXP free seeing. The AXP model free seeing is represented in the left and the MASS free seeing is represented in the right side of the figure. The x-axis represents the months by 1 to 12 which corresponds ; January to December).

build those SCIDAR plots are not available and in this section we are going to compare those figures with the plots generated with the AXP model. This is a visual comparison of the profiles. The poor resolution of the SCIDAR figures is due to the fact that the images are retrieved from the Fuensalida work (Fuensalida et al., 2004) and it was not possible to obtain a better image or the raw data to plot.

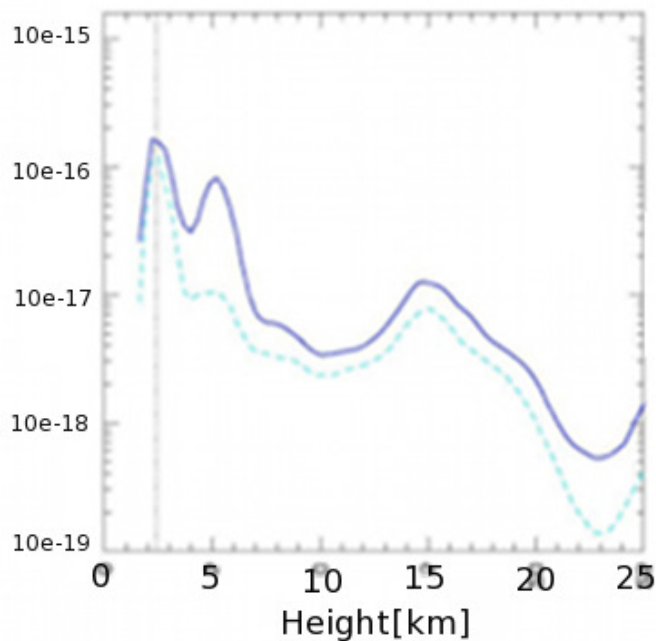


(a) SCIDAR median profile

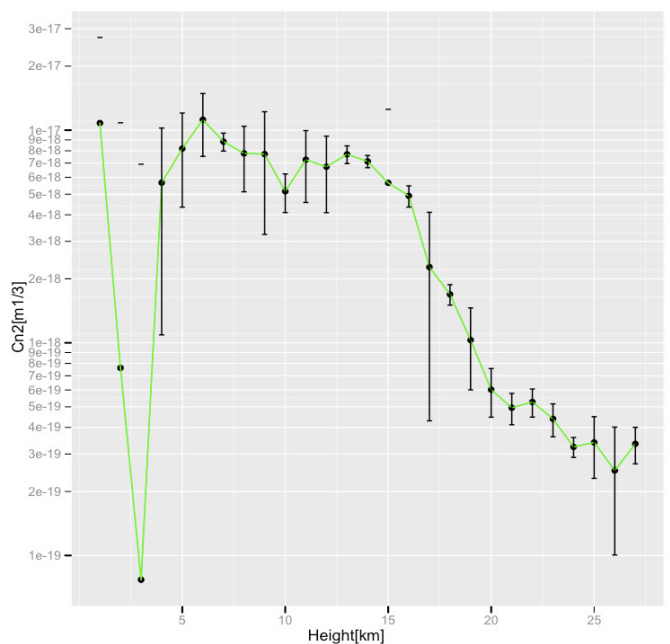


(b) AXP median profile

Figure 8.11: Comparison plots of  $C_n^2(h)$  profiles measured with the SCIDAR instrument set at Roque de Los Muchachos and the  $C_n^2(h)$  profiles calculated from the AXP model using the radiosonde data from the database. The x-axis shows the altitude (Km) and the y-axis shows the  $C_n^2(h)$  ( $m^{1/3}$ ). The two set of plots represent the median values for the  $C_n^2(h)$  profiles from SCIDAR and AXP for 6 nights on March 2004. For the AXP data it has been taken from the meteorological data for the first 6 days of March.



(a) SCIDAR median profile



(b) AXP median profile

Figure 8.12: Comparison plots of  $C_n^2(h)$  profiles measured with the SCIDAR instrument settled at Roque de Los Muchachos and the  $C_n^2(h)$  profiles calculated from the AXP model using the radiosonde data from the database. The x-axis shows the altitude (Km) and the y-axis shows the  $C_n^2(h)$  ( $m^{1/3}$ ). The two set of plots represent the median values for the  $C_n^2(h)$  from SCIDAR and AXP for 7 nights on July 2004. For the AXP data it has been taken from the meteorological data for the first 7 days of July.

# Chapter 9

## Conclusions and Future Work

*"The answer my friend is blowing in the wind..".*

*Bob Dylan*

---

### 9.1 Conclusions.

The classical AO systems which are currently operating use a limited knowledge of the optical turbulence that can be classified as good or bad. The term -good or -bad is based on the knowledge of the seeing parameter and using that information the AO system is setup to compensate during good seeing or bad seeing conditions. Another issue that the classical AO system designer has to consider and to worry about is the stability of the seeing and whether the systems can accommodate changes in the system on-the-fly. The seeing statistics can be used to perform a "nowcast" analysis using Kalman filtering and the predictor can help to predict the seeing during a single night or for two or three nights in advance.

Applying new laser capabilities to the classical AO we see that the knowledge of the optical turbulence is not limited only to "good" or "bad" seeing. These techniques require more information about the optical turbulence distribution and at which altitude the refractive index  $C_n^2$  becomes strong or weak. This is important to know because with the LGS running, such as a Rayleigh laser focused at 15 km, the system theoretically will compensate all the turbulence well below this altitude, such that it should be sufficient to have good correction, but the spatial evolution of the

upper layers can produce a situation such that the AO system is not compensating well due to changes in the upper atmospheric turbulence. The upper turbulence can produce entrainment to the lower layers making those to be in a turbulent state with rapid changes in refractive index making it difficult for the system to follow up and to compensate. Thus the knowledge of the strength of the turbulence and its time evolution is so important both in classical AO+LGS and especially for the new AO systems (MCAO, MOAO or LTAO). A real time turbulence profiler, eg. MASS-DIMM, can feed the system with the required information related to the refractive index vertical distribution.

We have found that the use of the meteorological parameters obtained from the measurements in Tenerife can be a useful tool to evaluate the sky conditions in La Palma. It is necessary to have a long term analysis of the meteorological parameters with the local conditions measured by the seeing in order to provide a good correlation of the two measurements.

The results of the seeing measurements at the Roque de los Muchachos are presented in this work, which started in September 2002 and finished in December 2008 and gave a median seeing of **0.88** arcseconds (no dome seeing). We have taken the same period of years to evaluate the meteorological parameters (wind speed and temperature), which have shown a strong variability between years. The wind speed at jet stream altitude (about 12km or 200mb) has shown a strong median during the periods of March and April ( $43$  and  $51\text{ms}^{-1}$ ) and the weakest during August and September ( $21$  and  $12\text{ms}^{-1}$ ).

The seeing and wind speed at 200mb have shown a seasonal distribution throughout the years, with the better periods during the summer time and the worst periods during the winter time. In the analysis of the years there has appeared an interesting event during the year 2005, which has shown the best median seeing with a low upper wind speed contribution (with a low variability), which means that the atmosphere has shown very stable conditions all year around.

A further topic of this thesis is to use the meteorological parameters to build a simple model of the  $C_n^2$  that can be used to forecast the conditions at the Observatory. There are many models that can be used, and we have selected the Trinquet-

Vernin (AXP model), which has shown interesting results. Comparing this model with another model, the H-V 5/7 model commonly used in AO simulations, has shown a good correlation with a Pearson correlation index of **0.83**. When comparing the profile obtained with the model with the measurements obtained with the MASS-DIMM instrument, a poor correlation is shown. To qualify the model, it was compared with two profiles obtained with the SCIDAR (located at the ORM) and comparing those plots with the plots of the profiles obtained with the AXP model, we can see a common pattern in the plots. Unfortunately, those are the only plots from a high resolution  $C_n^2$  profile available for the thesis. But this opens an interesting topic that can be explored in the future. We have found that the use of the meteorological parameters obtained from the measurements in Tenerife can be a useful tool to evaluate the sky conditions in La Palma. It is necessary to have a long term analysis of the meteorological parameters with the local conditions measured by the seeing in order to provide a good correlation of the two measurements. The way in which the jet stream contributes to the optical turbulence and to the instability of the atmosphere below it, and how these instabilities affect the seeing and its temporal variability, require a further study with an instrument with better spatial resolution. One approach would be to have a Wide-Field SLODAR instrument which could detect the atmosphere instability with a resolution of tens of meters from 100 metres to 20 km. Looking at the overall results for the seeing (see figure 9.1) and the wind speed at the tropospheric height (median between 9 to 12 km) (see figure 9.1) and the modeled  $C_n^2$  obtained from the AXP modeling (see Chapter 8), the first look indicates that the best year was 2005.

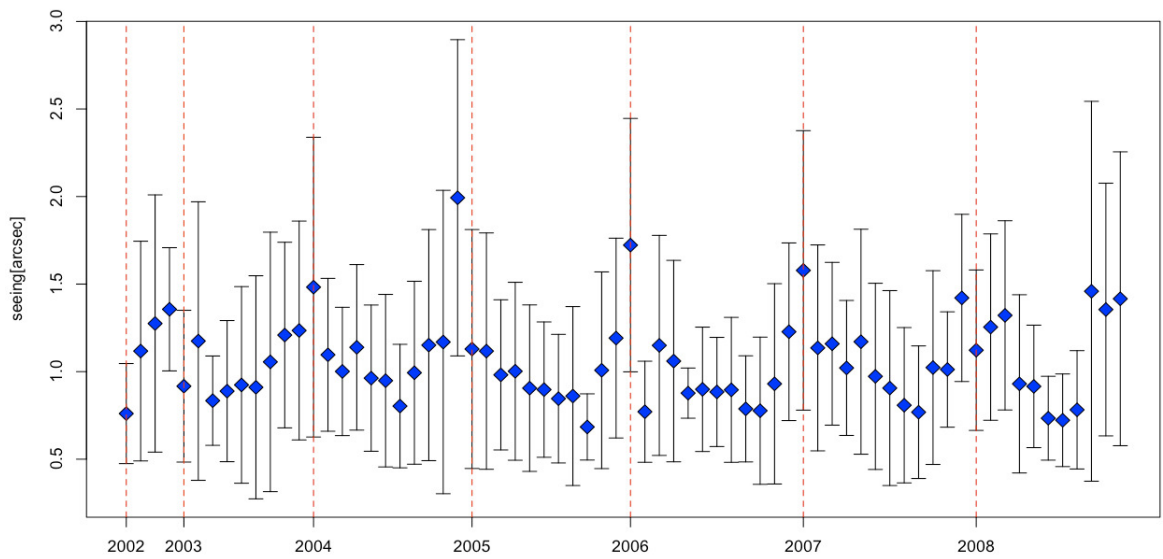


Figure 9.1: Monthly median seeing for all the data set available from the September 2002 to December 2008.

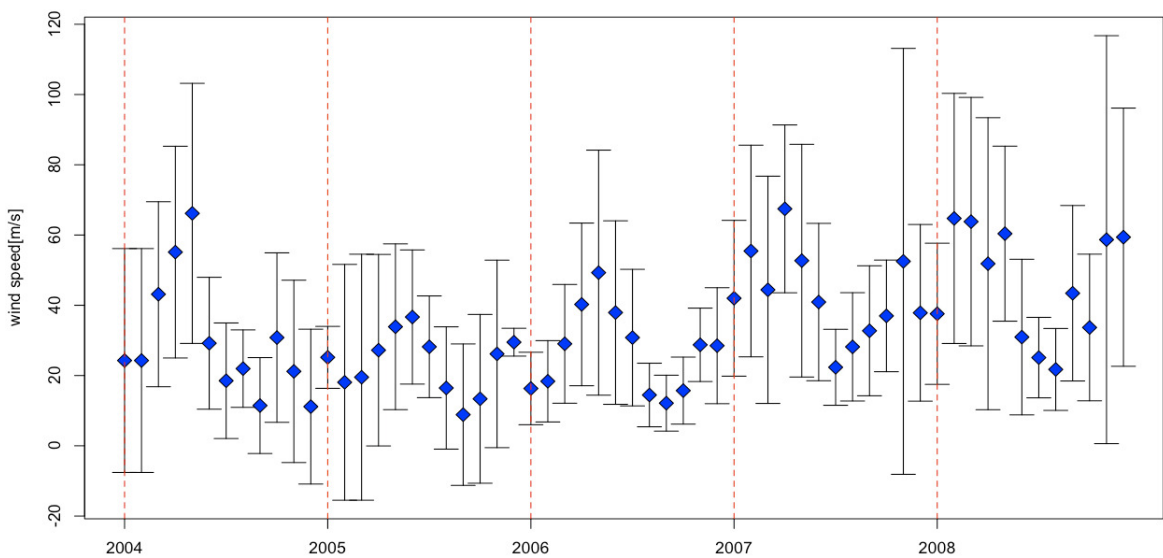


Figure 9.2: Monthly median wind speed at tropospheric heights (9 to 12 km).

## 9.2 Future Work

This thesis has suggested some work which can help in statistical analysis, forecasting and new observations of the optical turbulence.

All of the following "wildcard" proposed techniques can be investigated and applied to new AO systems, which are becoming more sophisticated and requiring more knowledge of the refraction index as an important input to the reconstructor of the wavefront, particularly of the wide field tomography systems. The wildcards proposed are:

- A novel technique to measure the optical turbulence in real time using the LGS backscatter information obtained through a DIMM and Lidar technique. A preliminary experiment has been proposed with a basic setup to run an analysis of the laser plume during a few nights of AO+LGS observing at the William Herschel Telescope. The experiment is reported in the Appendix **A**.
- A second wildcard proposed is to improve the AXP model using high resolution profiles to further quantify the model performance. A SLODAR instrument is a suitable solution due to the portability and easy to use.
- A third wildcard proposed is a novel statistical reduction process for the seeing using the Kalman filtering and Generalize Extreme Values (GEV) distribution.

# Appendix A

## Preliminary results of the Laser Plume DIMM Experiment.

Based on the Differential Image Motion technique (DIMM) and using the capabilities of the new Range-Gated CCD a device was built. This new and novel device could determine the vertical profile of the refractive index structure parameter. Using a Rayleigh laser (GLAS), the atmospheric backscatter and a range-gated receiver.

This preliminary report gives the first images impression of the laser plume experiment at the ORM detecting a Rayleigh laser plume.

### A.1 Experiment set-up.

The experiment has been separated into two steps; the first one was to mount, align and test the equipment on the sky. This first step was done outside of the WHT in order to be free to work around the equipment without any restrictions. The second step was to set the experiment inside of the WHT, synchronising the device to the laser, and to obtain laser plume data. The equipment need to run the experiments are; 14" diameter telescope, and an aperture mask with four 7 cm diameter sub-apertures separated by 15 cm to be mounted in the front of the telescope to separate the incoming wavefront. The four wedge prisms are used to displace the images in the detector. A finder mounted in the telescope is used to improve the pointing. The CCD is mounted with an interface in the back of the telescope and a filter at

580 nm is used to increase the signal to noise ratio of the images of the laser. The CCD has an array of 128x128 pixels with a pixel size of  $25\mu m$  and is connected to a PC through the PCI bus. The acquisition is done by software provided by the manufacture and an external python program was built to calculate different configurations of the range-gate. Also a time delay generator and an oscilloscope are connected to the CCD controller.

The images are stored locally in the PC hard drive for post-processing analysis. The images are saved in its 16-bits raw format and there isnt any image correction during this process. The background, bias or dark subtraction is done during the post-process analysis.

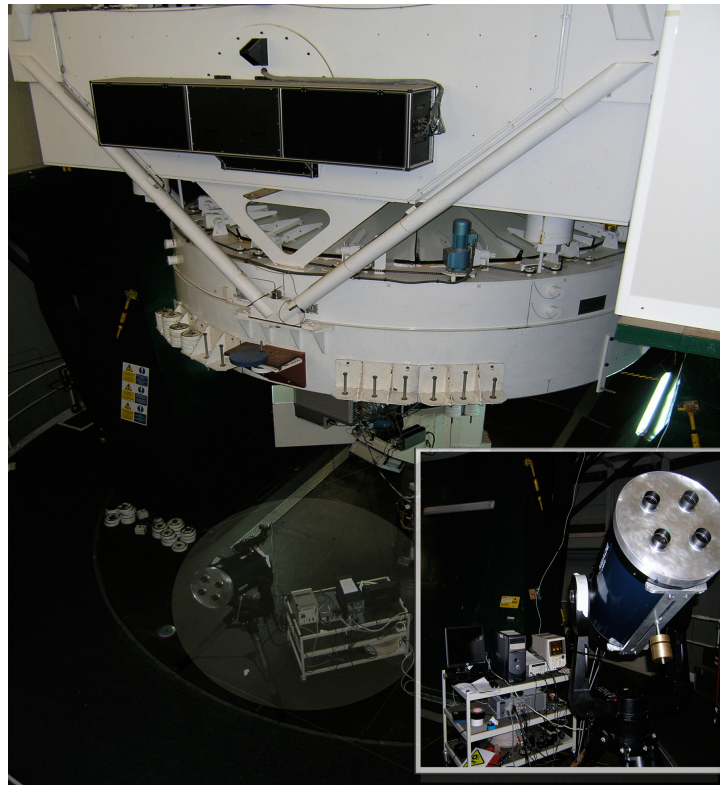


Figure A.1: The system setup at the fork of the WHT.

## A.2 Experiment performances.

The experiment took place during two runs of GLAS+AO observations in the WHT. The first period was to setup the instrument, fix problems and take sky images,

and leave the second run to do tests on sky with the laser. The weather and the requirements of the AO observations have been external factors, which can stop the experiment. The experiment is weather and AO observations conditions dependant.

### A.2.1 First Run.

During this run the weather wasnt too good and the time available was used to check the equipment and to setup the experiment outside of the WHT. In this first approach the telescope was aligned, the camera installed and focused and all the equipment were checked. The detector was focused using the Polaris star and this was the reference star to work with the detector. Two stars were used during the setup of the instrument and they are; Polaris and Shedir that have the following characteristics.

	Polaris	Shedir
Magnitude	V2.02	V2.2
spectral type	F7:1b-IIa	K0IIIa

Table A.1: Tested stars.

To provide a good image quality some calibration images (bias and darks) were taken and they can be used during the data post-processing analysis. The range-gated CCD has the capability to work without the range-gate mode, the images of the stars are taken with the open shutter and the changes of the frame rates are manually. The Polaris and Shedir stars can be detected at a frame rate of 200Hz with a good signal to noise ratio. The first look at the stars is reported in the following set of images and profiles.

A set of 100 images of Polaris and Shedir stars were taken. The frame rate of the images ranged from 100Hz to 500Hz, those images showing a good signal to noise ratio and saturation at frame rates below 150Hz; the saturation value is 16380 counts.

A simple profile of the image is plotted below and it is interesting to see the shape of the spots and how they are more less round. And the Full Width High Maxima

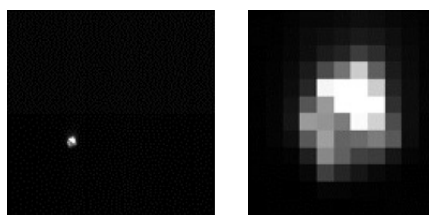


Figure A.2: Polaris star, and a zoomed image.

(FWHM) for the images is calculated giving the X and Y statistics showed in the table A.2.

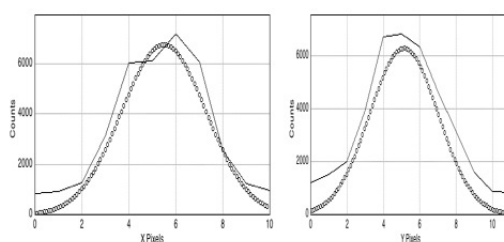


Figure A.3: Polaris star, and a zoomed image.

XFWHM	YFWHM	XCEN	YCEN
4.24 pixel	4.43 pixel	39.49	80.136

Table A.2: X and Y profile for the polaris image

The second star was Shedir, the frame rate could be increased to 500Hz and the star was still visible; the image below corresponds with a frame rate of 300Hz, and a profile plot is also shown. The frame rate was too high so the distribution of the flux in the image is a bit different.

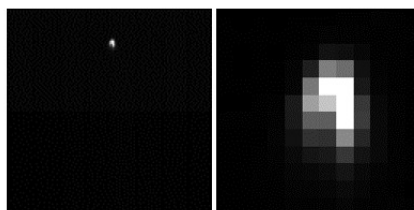


Figure A.4: Shedir star, and a zoomed image.

The table below shows the star FWHM for X and Y direction parameter are:

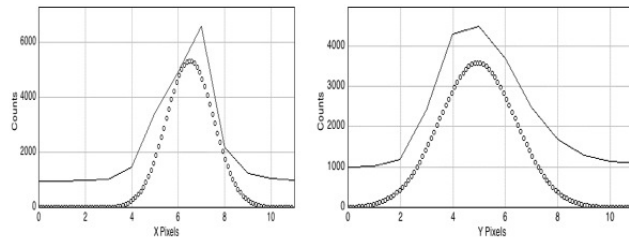


Figure A.5: Shedir FWHM for x and y.

XFWHM	YFWHM	XCEN	YCEN
2.39	3.416	65.518	20.952

Table A.3: Shedir FWHM x and y axis.

### NGS+MASK.

In the AO corrections those two stars could be used as NGS. The mask with four sub-apertures is put in the front of the telescope to detect the star, once the mask is on, the images of the spots were lost, but using the Polaris, which is a good choice as it doesn't move too much in the sky, it is easy to recover it again. Polaris allows one to perform the centering and focus and to track the spots during a long period of time. The flux drops when the mask is on, but it was possible to take a series of images at 75 and 100Hz. The image below shows Polaris with a frame rate of 75Hz.

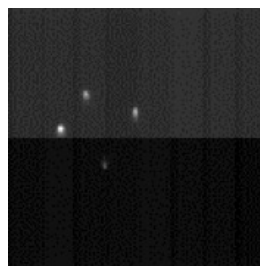


Figure A.6: Polaris image through the mask and reading the range-gated ccd at 75Hz, Not gating.

The spots distribution is important to determine, in the way to establish any effects of the detector.

A surface plot gives a good appreciation of the shape of the spots.

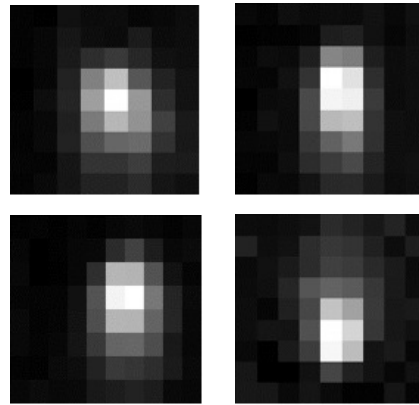


Figure A.7: Polaris star, and a zoomed image.

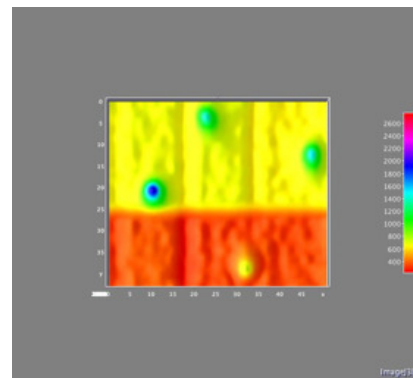


Figure A.8: Surface plot of the Polaris image through the mask and reading the range-gated ccd at 75Hz, Not gating.

Running the CCD at 100Hz the spots are still visible with a difference of the bottom spot which is getting less signal.

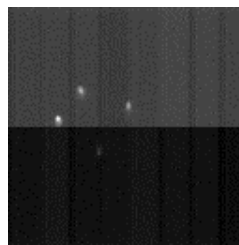


Figure A.9: Polaris image through the mask and reading the range-gated ccd at 100Hz, Not gating.

The surface plot of the image shows this difference in the spots signal.

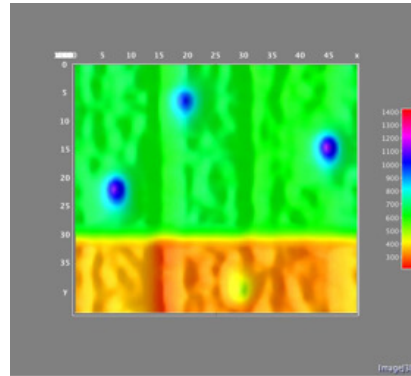


Figure A.10: Surface plot of the Polaris image through the mask and reading the range-gated ccd at 100Hz, Not gating.

### A.2.2 Second Run.

The second run of observations took place inside of the WHT and the equipments were placed in the telescope fork. The delay generator for the plume monitor was connected to the GLAS delay generator to sync the range-gated CCD with the Rayleigh laser. The images took during this run are mainly images of the laser, using the two observing modes of the CCD; the range-gated and the open shutter. The range-gating of the CCD is a tricky process where the timing setup of the delay generator has to correspond with the volume of the laser and the altitude that we want to reach and it is necessary to modify the parameters online. The CCD is triggered with the laser frequency at 5kHz and using a python program to determine the parameters which can be used to configure the Little Joe controller. The parameters, which can be setup using the python program are; the altitude and the range-gated depth and it outputs the time to set in the delay generator and the CCD exposure time. A series of images acquired from the laser in open frame mode were taken, the telescope wasn't tracking so to acquire the laser it was necessary to drop the frame rate to 10Hz and trace the laser plume. The images are in raw format, no post-processing action was taken to minimize images effects, and also the images are converted to GIF.

The images are taken during the same setup, without any change in the frame rate. In the first two images on the left (image A.11(a) and A.11(b)) we can see the

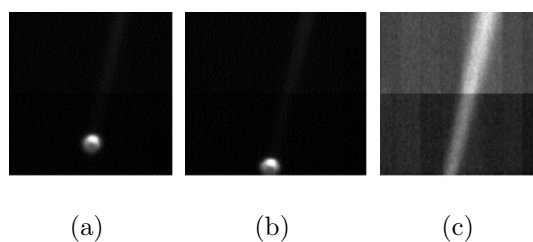


Figure A.11: Polaris ar 10Hz

spot generated for the laser focused at 15 Km. A 3D surface plot of the laser spot is showed in the figures below.

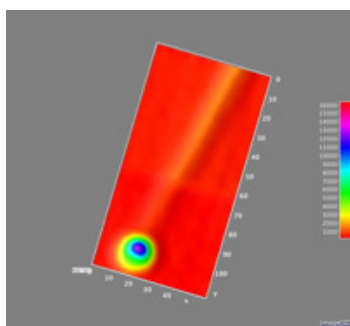


Figure A.12: Image

Observing the image of the surface, we can see that there is a different bias between the top and the bottom of the images. This effect could affect the laser spot image. The following images are taken from the same series of 100 images, the laser spot moves along the CCD in the Y direction with a small angle. Taking two images of the spot; one in the bottom and another one in the top and plotting the profile we can see that the images dont show a big difference in the shape and the intensities.

The profiles of the two images in X and Y are represented in the figures set A.13(a) and A.13(b) with the statistics of the FWHM summarized in the table.

The X and Y FWHM for the two spots are summarised in the table A.4.

The CCD responds very well to the laser showing a high intensity of the spots at 10 Hz.

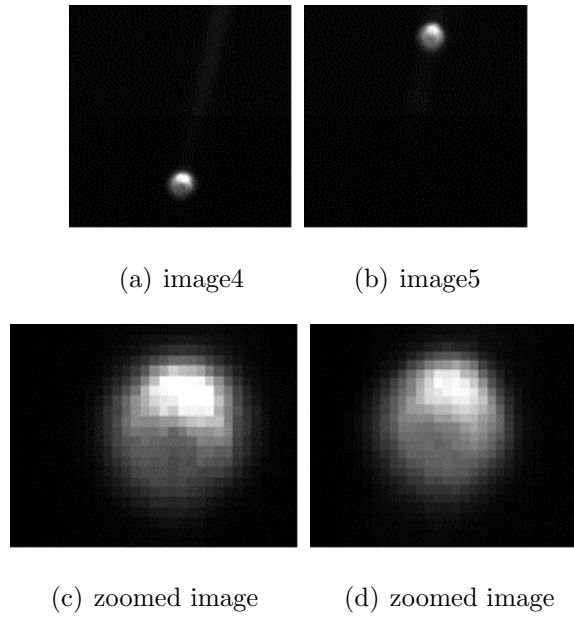


Figure A.13: Polaris at 10Hz

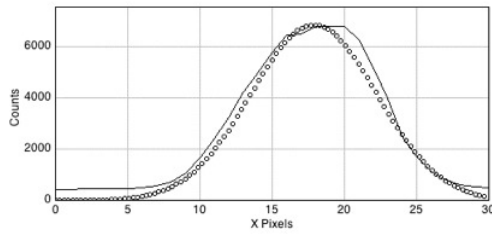
	Image 4(bottom)	Image 5(up)
X FWHM	10.171	10.302
Y FWHM	7.559	9.916

Table A.4: FWHM in X and Y for the images A.13(a) and A.13(b)

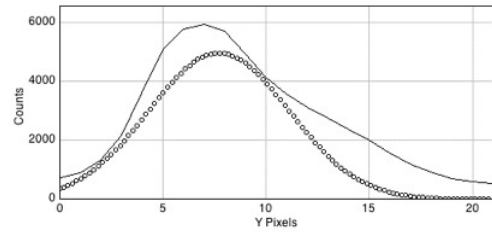
### A.3 Range-Gated operations.

The laser spots are checked using different frame rates, the maximum for visible spots is about 50Hz. With this first approach the device is set to trigger the signal with the laser at 5kHz in different altitudes 2 km, 4km, 8Km, 10Km and a gated depth of 500 meters.

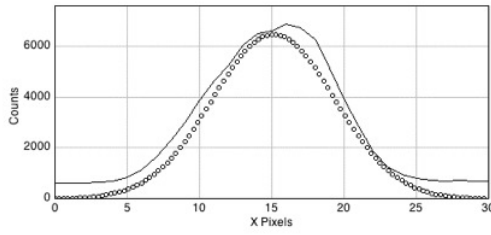
The laser image was hard to identify and to center in the CCD. After tracking manually and pointing to the laser an image of the laser range-gated at 10km with a depth gated of 500m came out. The images have dots which means that it is necessary to modify one of the time delay generator parameters. After changing the parameter which trigger from the laser ( $A = T + 65.5\mu s$ ) by  $0.1\mu sec$  the spots disappear. Running the system at 10Hz laser trace is visible but the laser spot couldnt be seen. The flux detected is not sufficiently high to put the mask on.



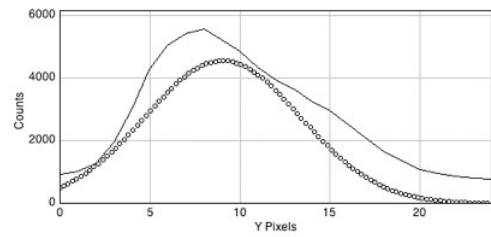
(a) Caption of subfigure 1



(b) Caption of subfigure 2

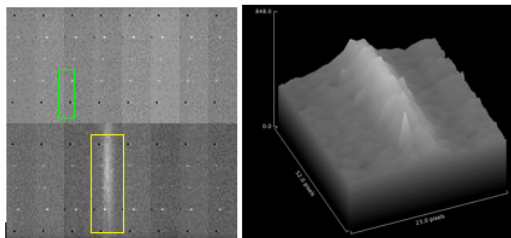


(c) Caption of subfigure 3

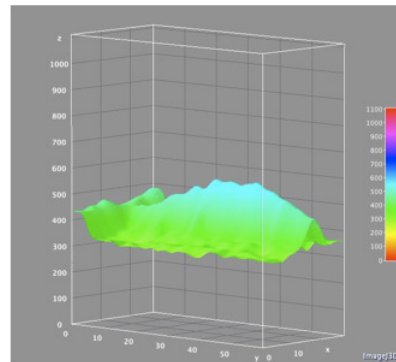


(d) Caption of subfigure 3

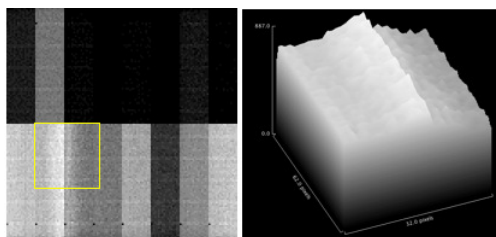
Figure A.14: Caption of subfigures (a), (b) , (d) and (d)



(a)



(b)



(c)

Figure A.15: Polaris image in range gated mode

### A.3.1 LGS + MASK.

Once we have set the times for the CCD in range-gated mode and taken series of images with and without the mask on, the plume spots were too faint to trace and

to center in the CCD. Also we have to consider that the telescope wasn't in tracking and the accuracy of pointing wasn't good. Then, the CCD was setup to run in open shutter mode (no range-gated) with a frame rate of 5Hz. Using this frame rate the spots are visible.

A series of 100 images taken with a rate of 2Hz and 3Hz were taken. The spots were centered and the telescope was correcting its position in elevation allowing one to track the laser during the short time. The misalignment of the spots is clear but it was impossible to leave the telescope control to access the mask.

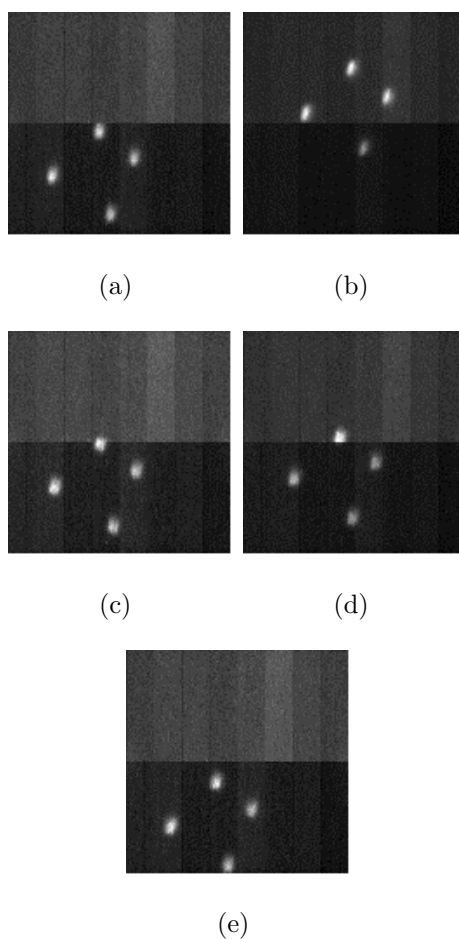


Figure A.16: Polaris Range gated

One spot in the image A.16(b) is analyzed and a profile is plotted, the figure below shows the X and Y profiles for the top spot in the image A.16(b). Looking the series of images presented above, the image A.16(b) is the 2<sup>nd</sup> from a series of 100 images and it looks more elongated than the rest, this effect could be by the

telescope shake, the rest of the series of spots images look more round. A surface plot of the images can give a better view of the spots.

A surface profile is taking from the image A.16(d), it is clear the differences in the bias level of the detector. And a same surface profile is plotted for the image 10.

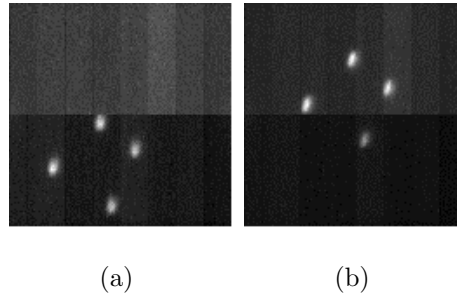


Figure A.17: Surface profile of the image number 9 in the upper part of the CCD.

The image 10 is centered in the bottom image with a lower bias.

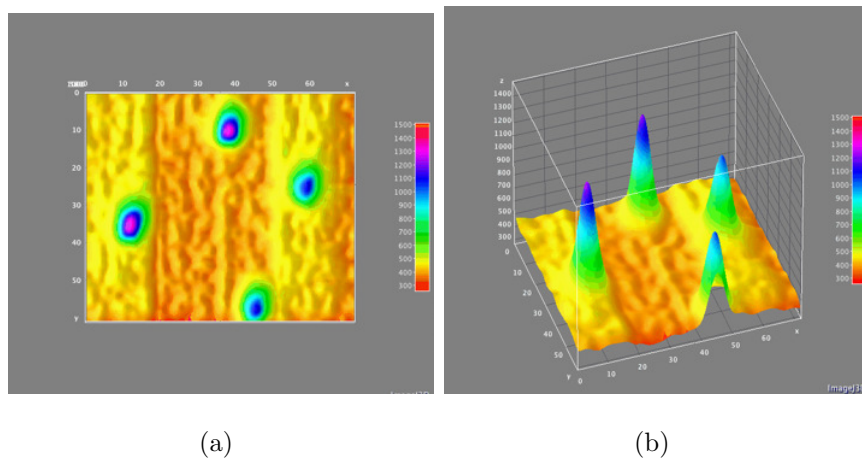


Figure A.18: Surface profile of the image number 10 in the lower part of the CCD.

## A.4 Conclusions and future work.

The Plume monitor demonstrator has shown that it can be accomplished and it could give good results with the laser to determine the Cn2 profiles at different altitudes. The Range-Gated CCD device has given good performance detecting stars or even the laser plume. During the setup of the experiment to work on the sky some stars

were observed: Polaris and Shedir. We could detect these stars with a frame rate at 500Hz, also the laser spot with much less flux could be observed with a frame rate of 100Hz.

The images taken with the mask on for the star and the laser are quite similar in the sense of spot elongation, the surface image of the laser spots looks a bit more elongated than the star image; we dont have enough data to analyze and to clarify this effect which could be due to being out of focus on the laser spots.

During this first try we have observed that the small telescope didnt respond as expected, showing continuous error in tracking, difficulty in setting a good focus and powering off many times. Also we have to consider that the telescope was put in the rotating part of the WHT (fork) and this has meant that the MEADE couldnt be aligned properly.

As well as considering hardware problems, to work in the dome when the laser is on was difficult because we have to wear protecting glasses that makes it difficult to work around with the delay generator or pointing the telescope with the finder

The Range-Gated mode couldnt get good results with the laser plume and the mask on, but it has given good experience of working with the time delay generator at the same time with the laser.

Considering that the main goal couldnt be completed at all, to detect laser spots using the range-gated at different altitudes, the experience gained during this time of the experiment has given us a more confident feeling for the next time. Also it gave the opportunity to think in new ways about how to run and improve this experiment.

#### A.4.1 Future work.

To face the next time that the experiment can be performance a few considerations have to be noticed before to go:

- Improve the telescope performance and in special the tracking, change the focus knob by a more sophisticated system (automatic) or to get a new telescope with the important issue of automatic focus RCX400 14.

- The camera support has to be improved (tilt correction and movements back and forward).
- Additional optics, flip mirror, short eyepiece (12mm) with a cross air.
- The mask apertures have to be bigger. Think in 10 cm apertures.

Most of those consideration could be addressed with a small cost and the main problem is the cable twister for the fiber optic and the Ethernet cable, but with a simple solution which is to get some time during the GLAS nights (eg. first Services night) and to have the WHT stopped with the laser ON. Having the control of the WHT we can change the elevation of the laser and it gives time to one person to drive the MEADE, point to the laser, adjust the focus, check the flux of the laser using different frame rates, adjust the mask and the pupils. And to switch to range-gated mode trace the laser and get finally spots data.

### Appendix A.

Series of the laser spot at 10Hz frame rate and open shutter (not range-gated). Evolution of the spots, the telescope position 25 zenithal angle.

### Appendix B.

Some screenshot of the oscilloscope for different range-gated configuration parameters.

A-B	C-D	SOS controller	Controller
Channel 1	Channel 2	Channel 3	Channel 4

Program 100Hz, at 10Km and a gate depth=500m

Using this configuration with increasing  $A = 64.97$  by 0.1 a white blob in the images disappear.

Program 50Hz at 8km, gate depth=700m, sequence 2 running.

Program 20Hz 8km gated=500m, the small points disappear at  $63.82\mu s$ .

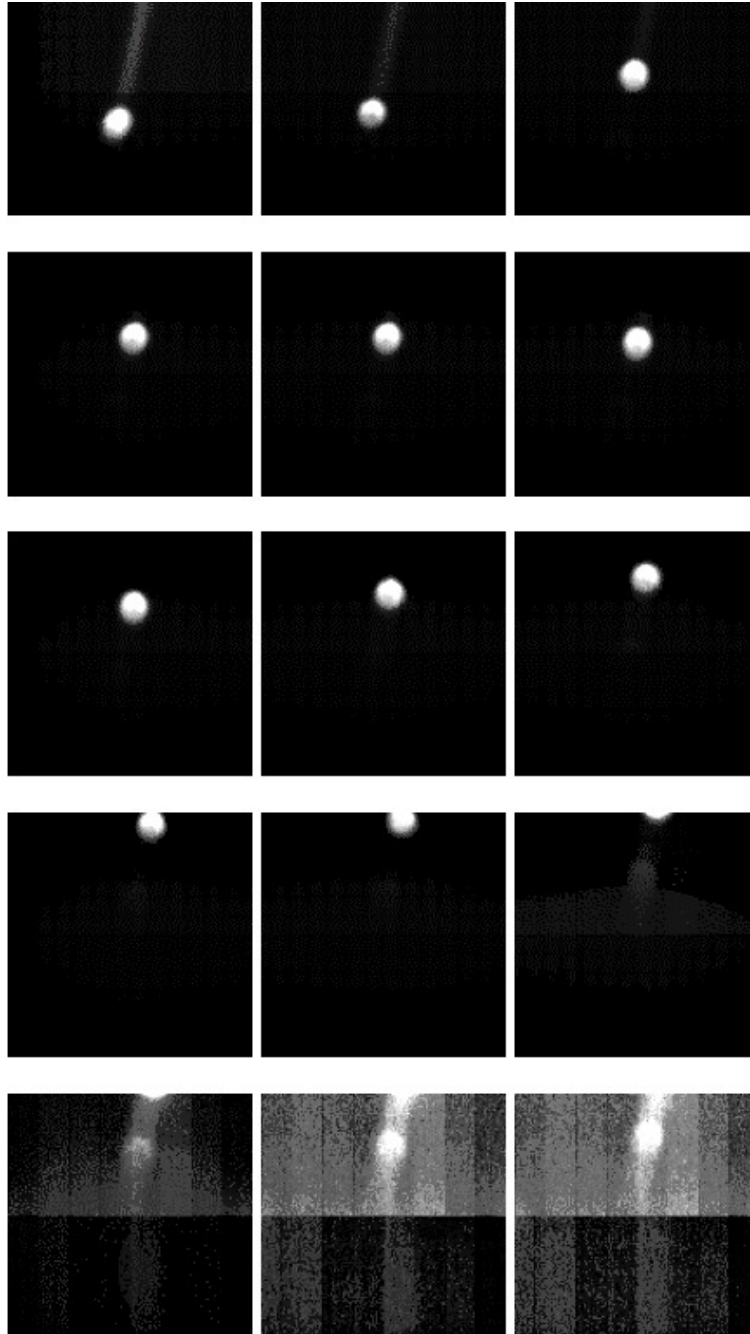


Figure A.19: Set of images of the Rayleigh laser spot



Figure A.20: Oscilloscope screenshot at 100Hz and 10Km gated=500m



Figure A.21: Oscilloscope screenshot at 50Hz and 8km gated=700m



Figure A.22: Oscilloscope screenshot at 20Hz,8km gated=500m

# Appendix B

## Statistical Analysis of the Seeing.

### B.1 Overview.

This Appendix summaries the statistical analysis of the Robodimm seeing measurements series, in this analysis a series of statistical plots that goes from 2002 to 2008 are represented and the statistics are enough to identify any change in the seeing behavior with a change in the climate changes.

Those plots are the baseline to start to understand better the seeing behaviors and it can be useful to use different approach to the analysis using different filtering and forecasting techniques like as; Kalman filter, and a new approach to analyze the outer limit measurements using the Generalized Extreme Value Distributions.

### B.2 Data set. Plots.

The first analysis of the Robodimm data is to show the changes of the seeing condition over the data set using a boxplot representation. The seeing data set is sorted per year as showed in the figure B.1 where a clear variation of the seeing behaviors with changes in the years and there is a remarkable better year, that is the 2005. This year shows a less variability of the seeing data. Unlike the year 2008 which shows a large variability of the seeing data with a large median value. The overall median values showed in the table B.1.

Using the same data set and grouping them per month for the different years

	Total			Summer			Winter		
Quartile	25%	50%	75%	25%	50%	75%	25%	50%	75%
$\varepsilon(arcsec)$	0.68	0.86	1.16	0.78	1.02	1.41	0.63	0.78	0.99

Table B.1: Statistical values for the median (50%), first (25%) and third quartiles (75%) of the total daily average seeing parameter above Roque de Los Muchachos Observatorio. The two periods summer and winter represents the months; Summer (June to September ) and winter (November to March).

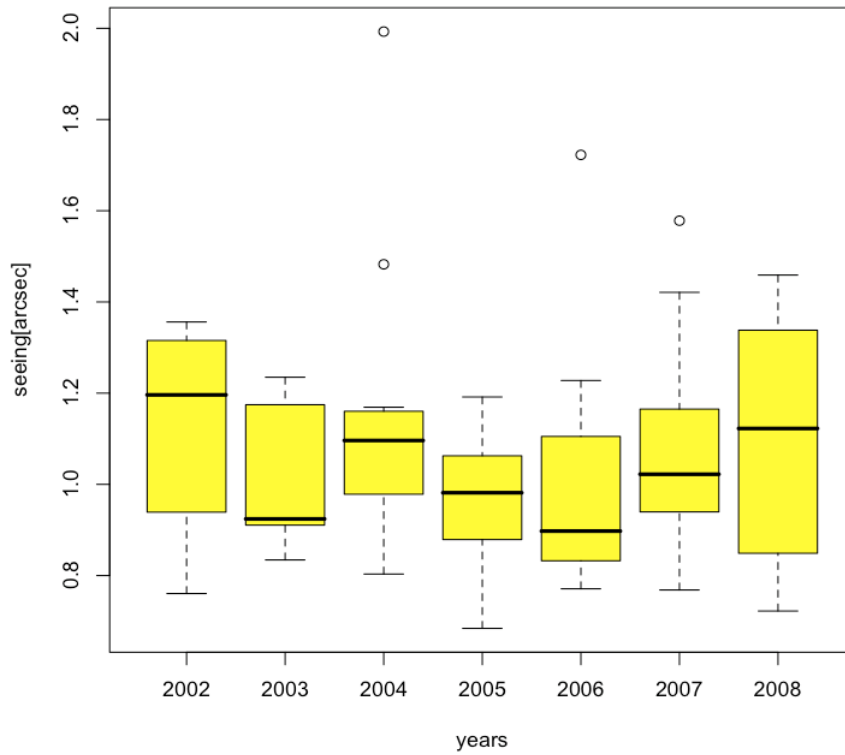


Figure B.1: Boxplot representation of the yearly seeing.

we can get the statistics for the monthly distribution for the whole data set (7 year data), the figure B.1 shows the monthly boxplot representation for the seeing data set. This representation can gives a good help to understand this long-term data series in a monthly manner where it is easy to identify the monthly trends and the distributions of the measurements.

Looking into the figure B.2 a clear good month is July, that is giving a low

variability of the seeing, but the best mean seeing can be seeing during August and September.

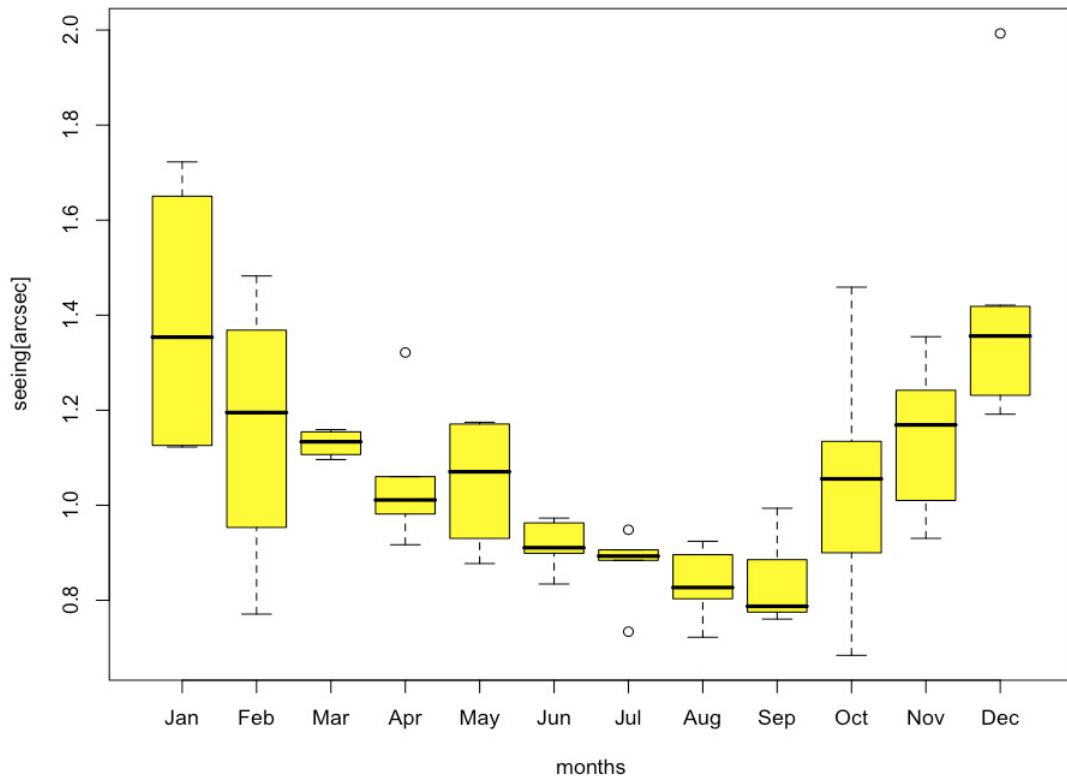


Figure B.2: Boxplot of the monthly seeing

The yearly data set distribution of the seeing can be shown using the daily median seeing histogram. The figure B.3 gives a set of daily histogram for the seeing measurements from 2002 to 2008. It has to be consider that the years dont have the same number of months and the histograms set with the density fitting lines could shows more less the same distributions.

To have a continuous statistics of the data-set and to avoid gaps , the monthly median seeing is calculated from the daily measurements with a minimum of 5 hours observations. Using this filtering technique, the data-set reduces its number of nights to be analyze and the results are showed in the tables below (from B.2 to B.7).

	Jan	Feb	Mar	Apr	May	Jun	Jul	Aug	Sep	Oct	Nov	Dec
Median	Na	Na	0.79	0.79	0.9	0.78	0.76	0.8	0.74	0.81	1.05	1.17
St dev	Na	Na	0.36	0.37	0.63	0.15	0.22	0.3	0.38	0.16	0.32	0.52
Nights	Na	Na	18	18	26	27	29	21	20	8	17	13

Table B.2: Statistics of the seeing for the year 2003.

	Jan	Feb	Mar	Apr	May	Jun	Jul	Aug	Sep	Oct	Nov	Dec
Median	Na	1.22	1.04	0.92	1.06	0.86	0.82	0.72	0.82	0.97	0.92	1.62
St dev	Na	0.42	0.19	0.28	0.27	0.23	0.50	0.23	0.23	0.6	0.55	0.62
Nights	Na	14	20	16	21	27	23	25	22	18	13	6

Table B.3: Statistics of the seeing for the year 2004.

	Jan	Feb	Mar	Apr	May	Jun	Jul	Aug	Sep	Oct	Nov	Dec
Median	0.87	Na	0.85	0.85	0.82	0.71	0.80	0.73	0.77	0.64	0.83	1
St dev	0.42	Na	0.28	0.28	0.40	0.39	0.24	0.20	0.25	0.09	0.45	0.42
Nights	16	Na	25	25	25	26	26	23	23	13	11	15

Table B.4: Statistics of the seeing for the year 2005.

	Jan	Feb	Mar	Apr	May	Jun	Jul	Aug	Sep	Oct	Nov	Dec
Median	1.8	0.72	1.05	1.06	Na	0.83	0.84	0.79	0.66	0.61	0.76	1.03
St dev	0.33	0.20	0.33	0.34	Na	0.23	0.19	0.30	0.21	0.12	0.48	0.41
Nights	2	7	23	9	Na	27	24	17	16	9	9	9

Table B.5: Statistics of the seeing for the year 2006.

	Jan	Feb	Mar	Apr	May	Jun	Jul	Aug	Sep	Oct	Nov	Dec
Median	1.36	0.99	1.09	1.00	0.97	0.81	0.80	0.77	0.73	1.03	0.93	1.56
St dev	0.61	0.51	0.28	0.24	0.47	0.21	0.36	0.28	0.21	0.23	0.18	0.34
Nights	14	17	6	6	18	19	27	22	21	12	2	4

Table B.6: Statistics of the seeing for the year 2007.

	Jan	Feb	Mar	Apr	May	Jun	Jul	Aug	Sep	Oct	Nov	Dec
Median	1.1	1.2	Na	1.27	0.78	0.91	0.67	0.66	0.77	0.89	1.4	1.2
St dev	0.45	0.53	Na	0.4	0.41	0.34	0.17	0.26	0.15	0.86	0.75	0.86
Nights	14	10	Na	10	20	22	17	24	17	8	4	13

Table B.7: Statistics of the seeing for the year 2008.

As a summary of the results from the tables, the following figure (Figure B.4) shows the variation of the yearly median from 2002 to 2008.

### B.3 Daily Median, Maximum and Minimum.

The seeing has a temporal evolution that can vary in a short of time, eg. in minutes. It is in this temporal variability that a daily analysis can give a better picture of the seeing evolution through the years. To represent the daily median seeing, I suggest to use a representation of every daily value in a gradient colour way. To this work I summarize the daily median seeing in a Calendar heat map. This calendar image is showed in the figure B.5. Using this representation of the statistics of the seeing, a researcher can identify the best days in a month to perform high resolution images (trigger AO observations) and it gives an important input of the effects of the weather in the number of observing nights through the years and also it can identify climatological changes in the site

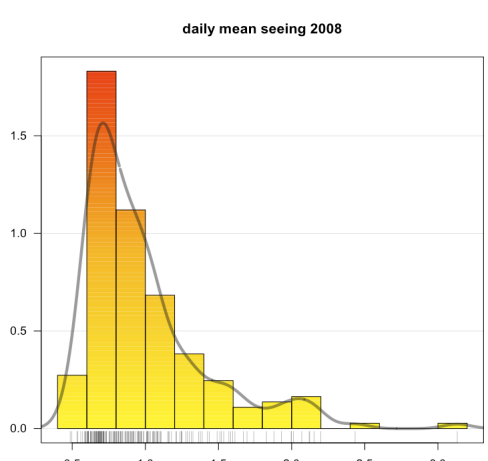
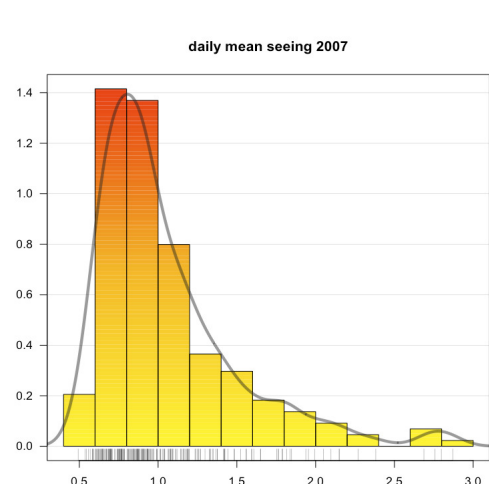
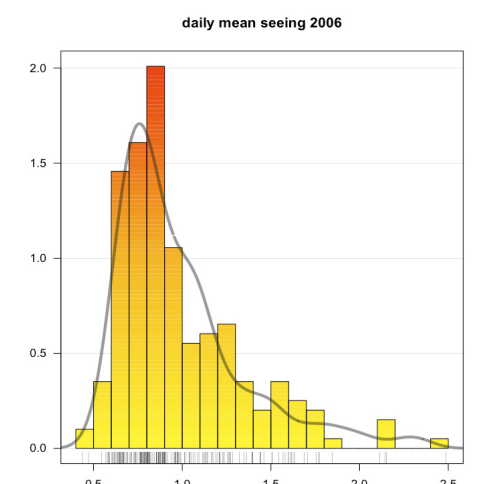
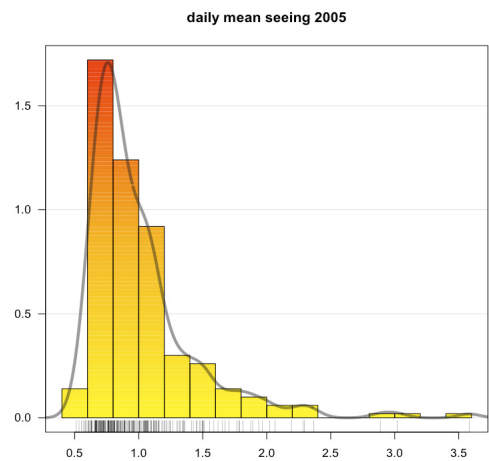
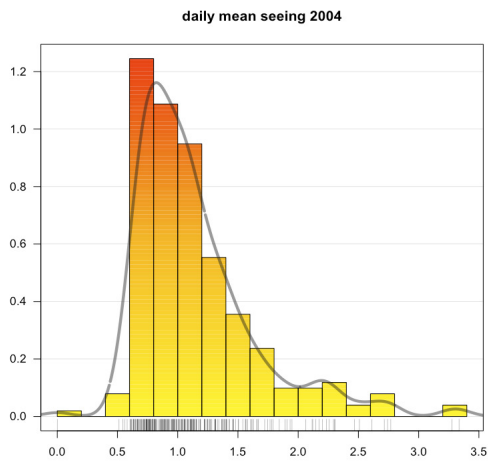
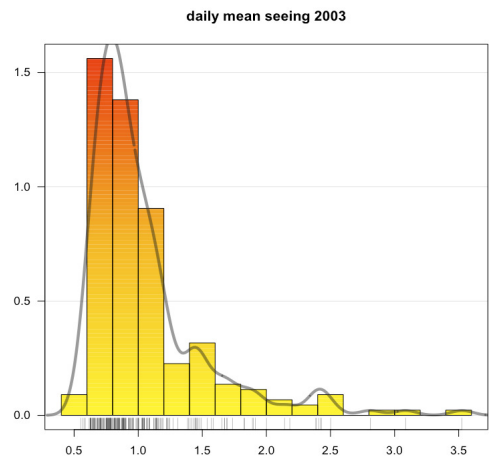
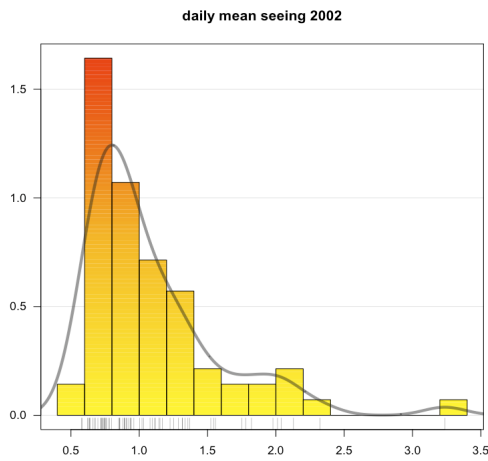
A part of the median seeing distribution is also good to know how the maximum and minimum seeing are distributed along the years. The statistics of the maximum and minimum can be displayed in a boxplot where we can see the variation per month along the years. The maximum plot shows a shape quite similar to the

median monthly seeing (figure B.6), this can help to identify that the maximum median seeing can be also an indicator of the seeing evolution. The minimum seeing doesn't show a clear tendency as the maximum seeing, but it is easy to see a small variation between the winter terms and the summer and from the figure B.6 we can see that the inflection point is around August which is showed in the median seeing and the maximum seeing.

Along the year 2003 to 2008 many nights have showed good seeing with values of 0.4, those registers can be done in any period of the year. But looking the plot of the median minimum seeing it is easy to say this is the minimum value that the site can get is 0.45. In this site the atmosphere can develop free turbulence conditions but during those special nights with a good seeing we cannot get better values than 0.4. It is important to mention that the measurements are taken by a seeing monitor which is limited by its optical resolution and also it is possible to observe nights in a very stable good seeing and the seeing could drop to 0.3.

In a management considerations to allocate AO observing nights we can analyse the graphs from the figure B.5 and figure B.6 where the monthly median seeing is showed for the daily median and the maximum and minimum. From the figures we can determine easily that the best periods is the summer time and looking into two months in summer such as August and September we can analyse the stability of the seeing. Considering those two months for a forward analysis of the hourly statistics of the seeing.

The daily data are sorted per hour in which it is calculated the median, the maximum and the minimum and they are represented in a boxplot format with the x-axis given the time in hours from the 9:00 p.m to 6 am. The figure sets; B.7, B.8, B.9, B.10, B.11, B.12 takes the yearly ( from 2003 to 2008) boxplots for the months August and Septembers.



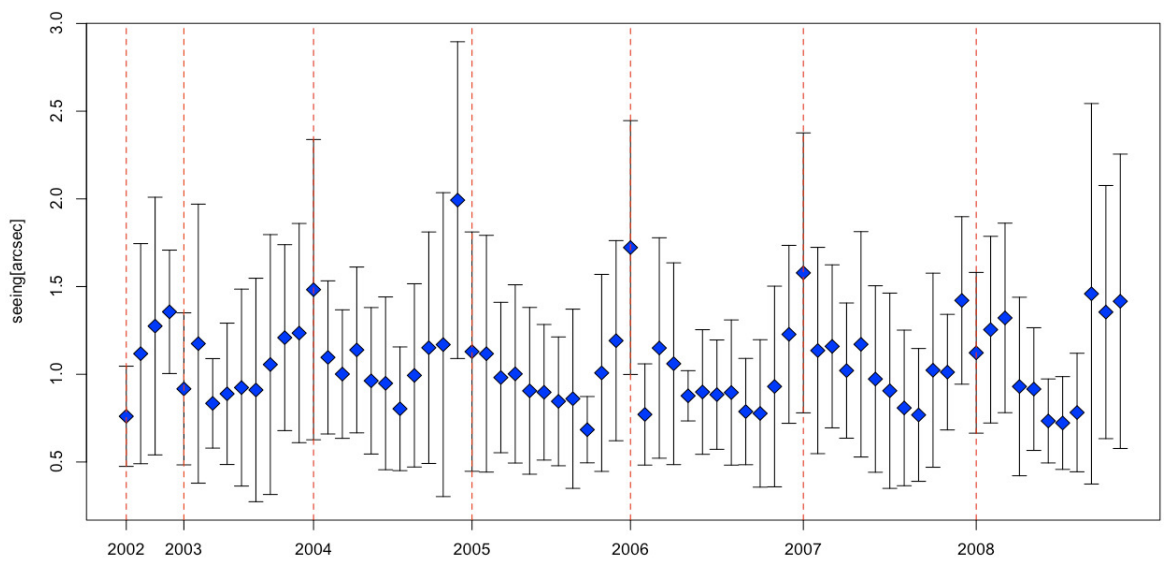


Figure B.4: Monthly seeing distribution retrieved from the Rododimm data from September 2002 to December 2008 showing the standard deviation in vertical bars.

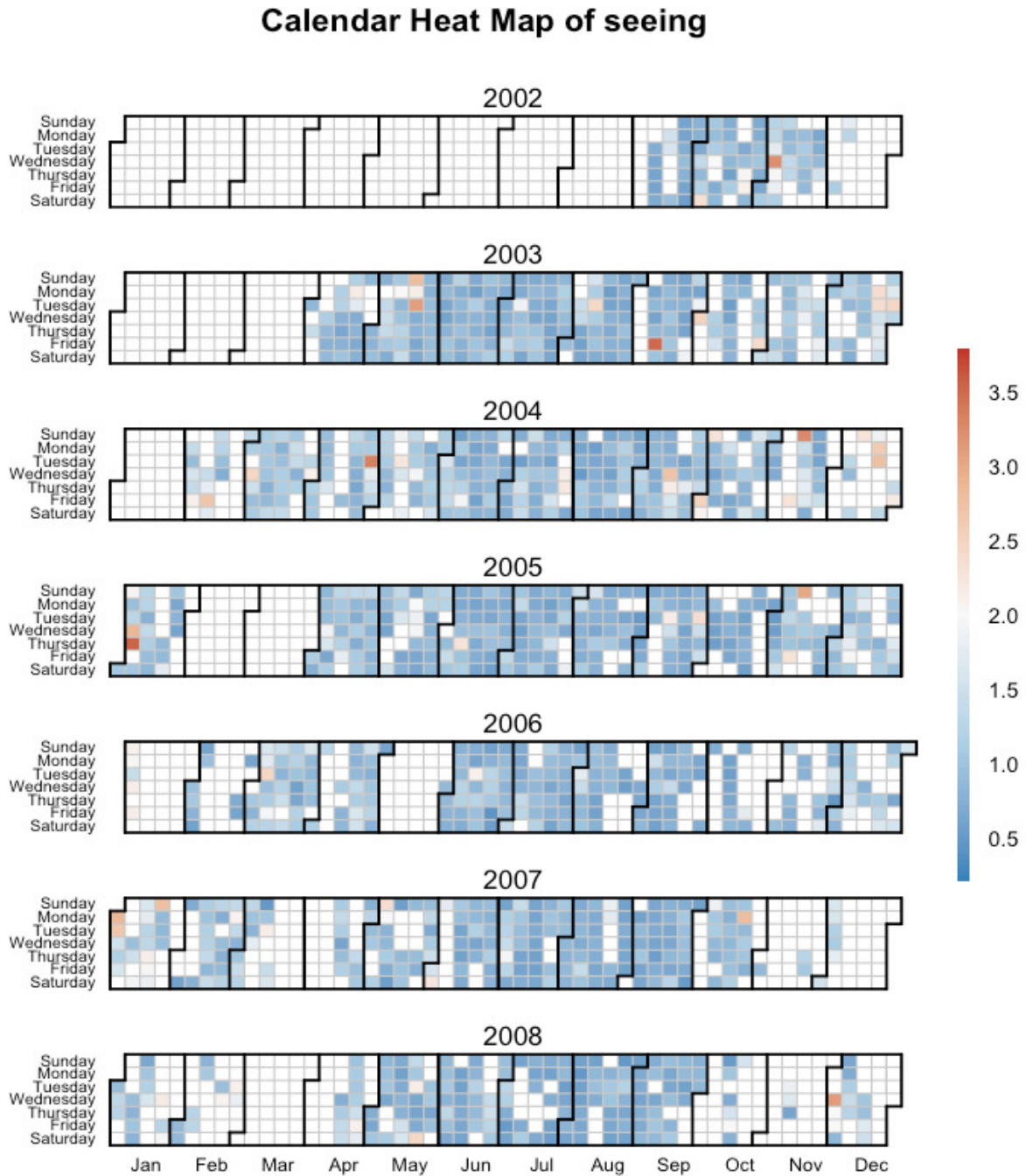


Figure B.5: Calendar of the mean seeing calculated per very day since 2002 to 2008. The year 2002 starts to get data on September. The white cells indicate not data available and it has to be noted that the year 2002 starts on September and March 2008 the robodimm was stopped by technical problems.

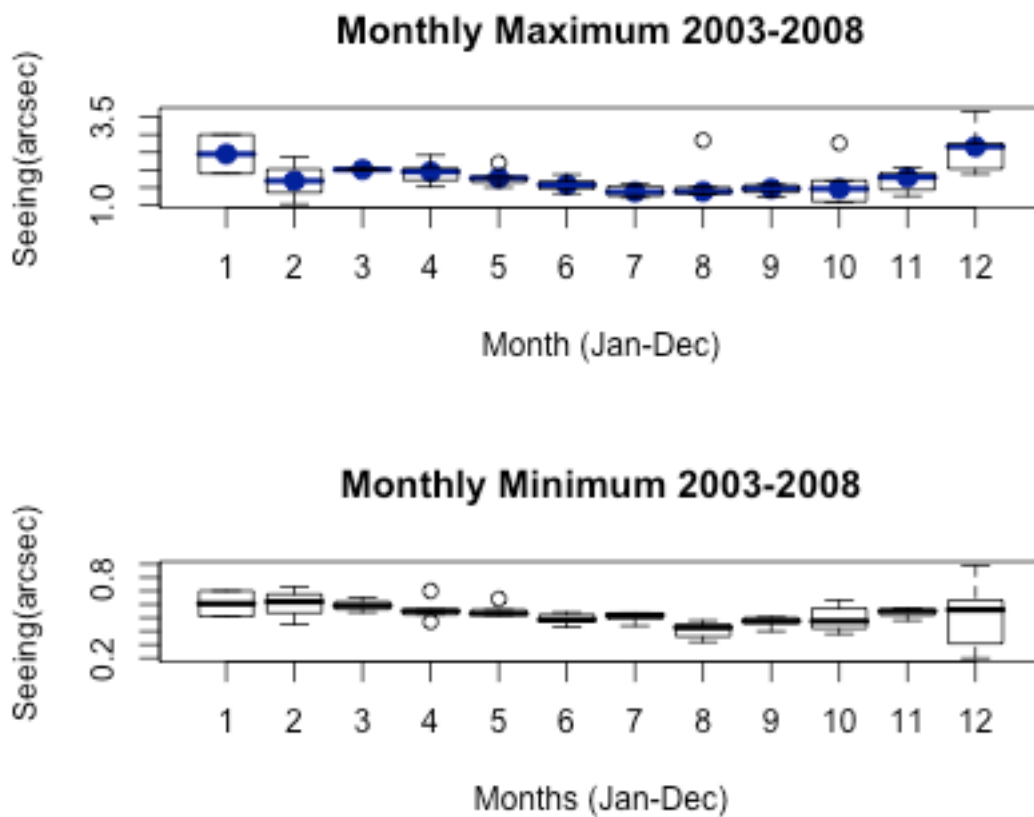


Figure B.6: Boxplot statistics for the maximum and minimum seeing calculated from 2003 to 2008. The x-axis represents the months (1 to 12 means January to December)

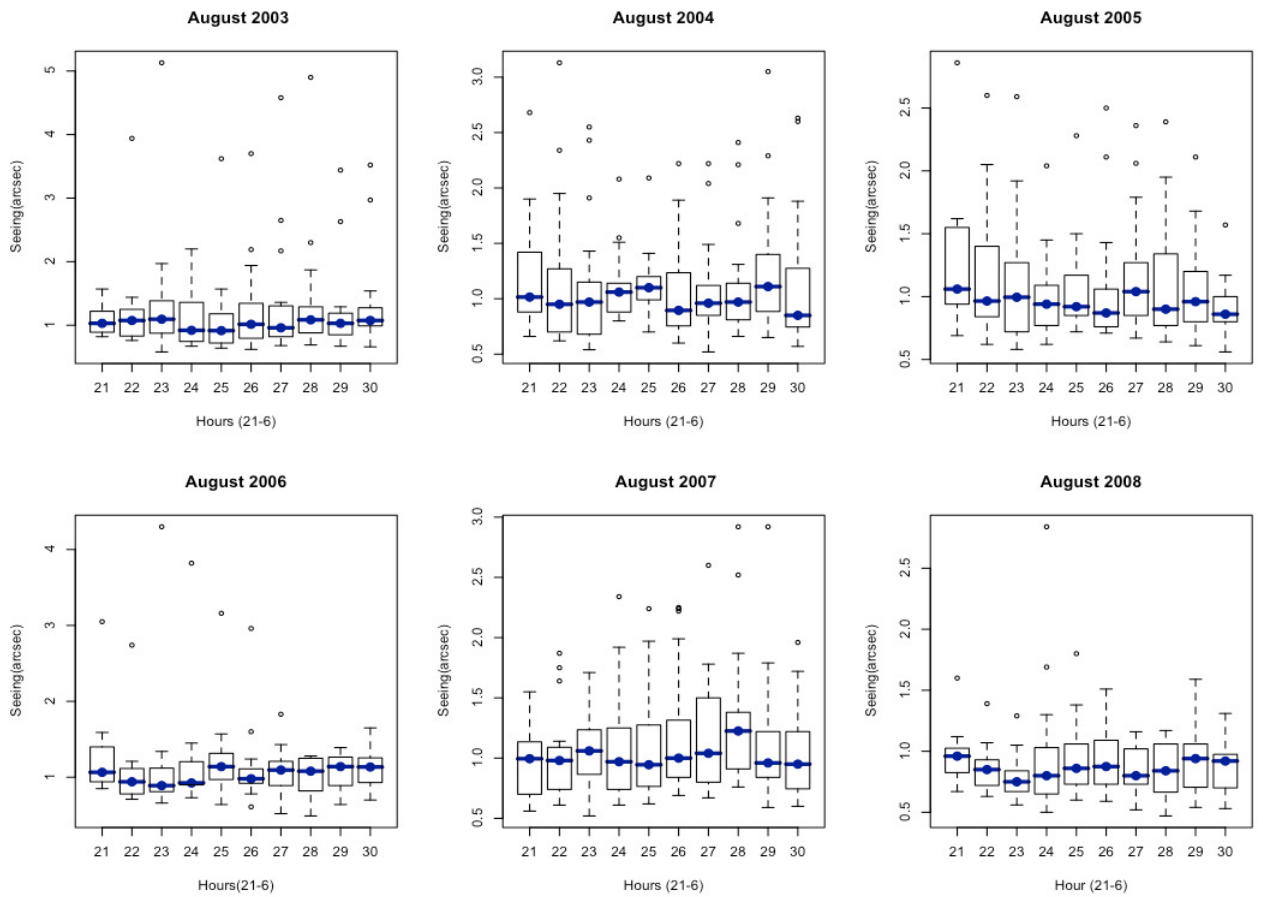


Figure B.7: Daily variation of the maximum seeing calculated for every hour during August for the years from 2002 to 2008

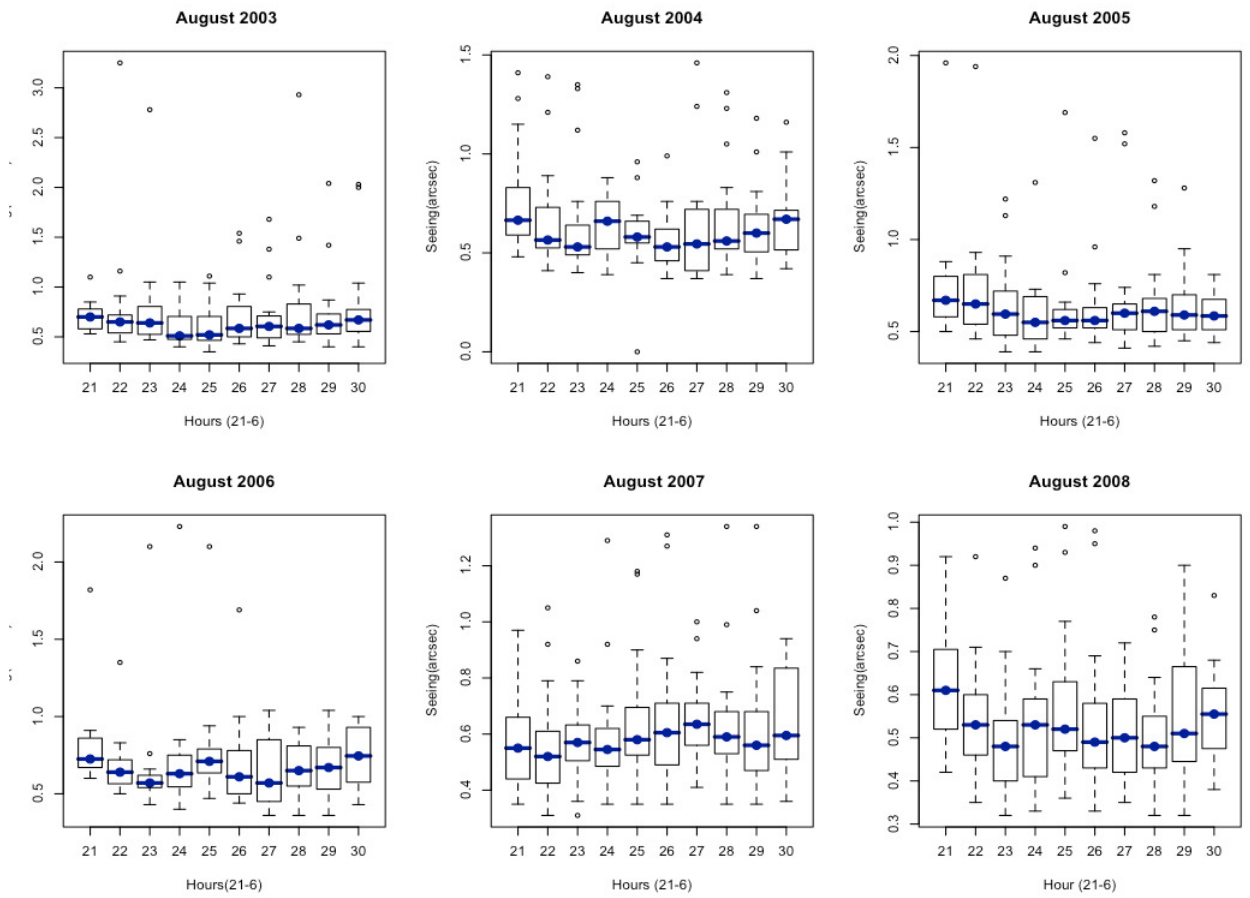


Figure B.8: Daily variation of the minimum seeing calculated for every hour during August for the years from 2002 to 2008

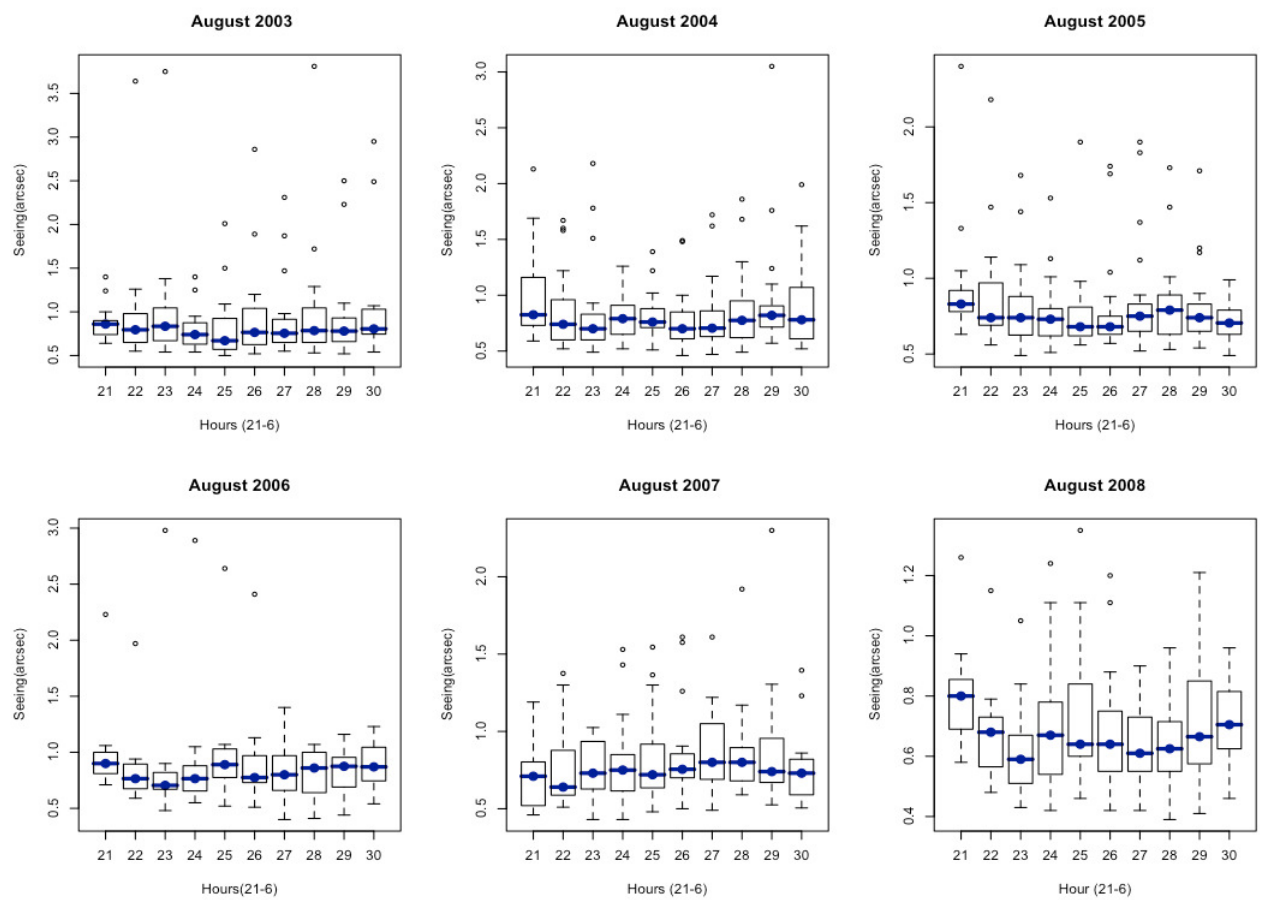


Figure B.9: Daily variation of the median seeing calculated for every hour during August for the years from 2002 to 2008

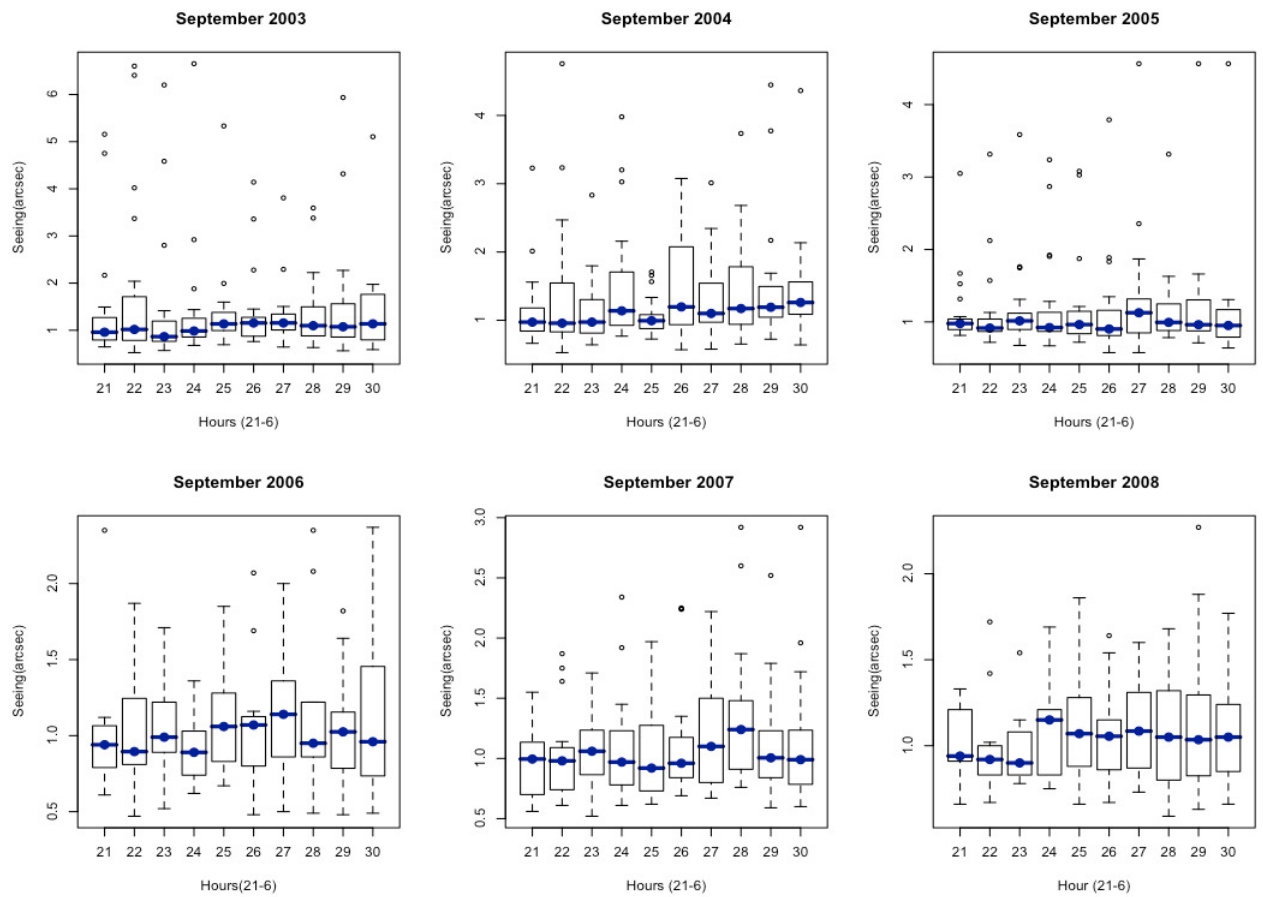


Figure B.10: Daily variation of the maximum seeing calculated for every hour during September for the years from 2002 to 2008

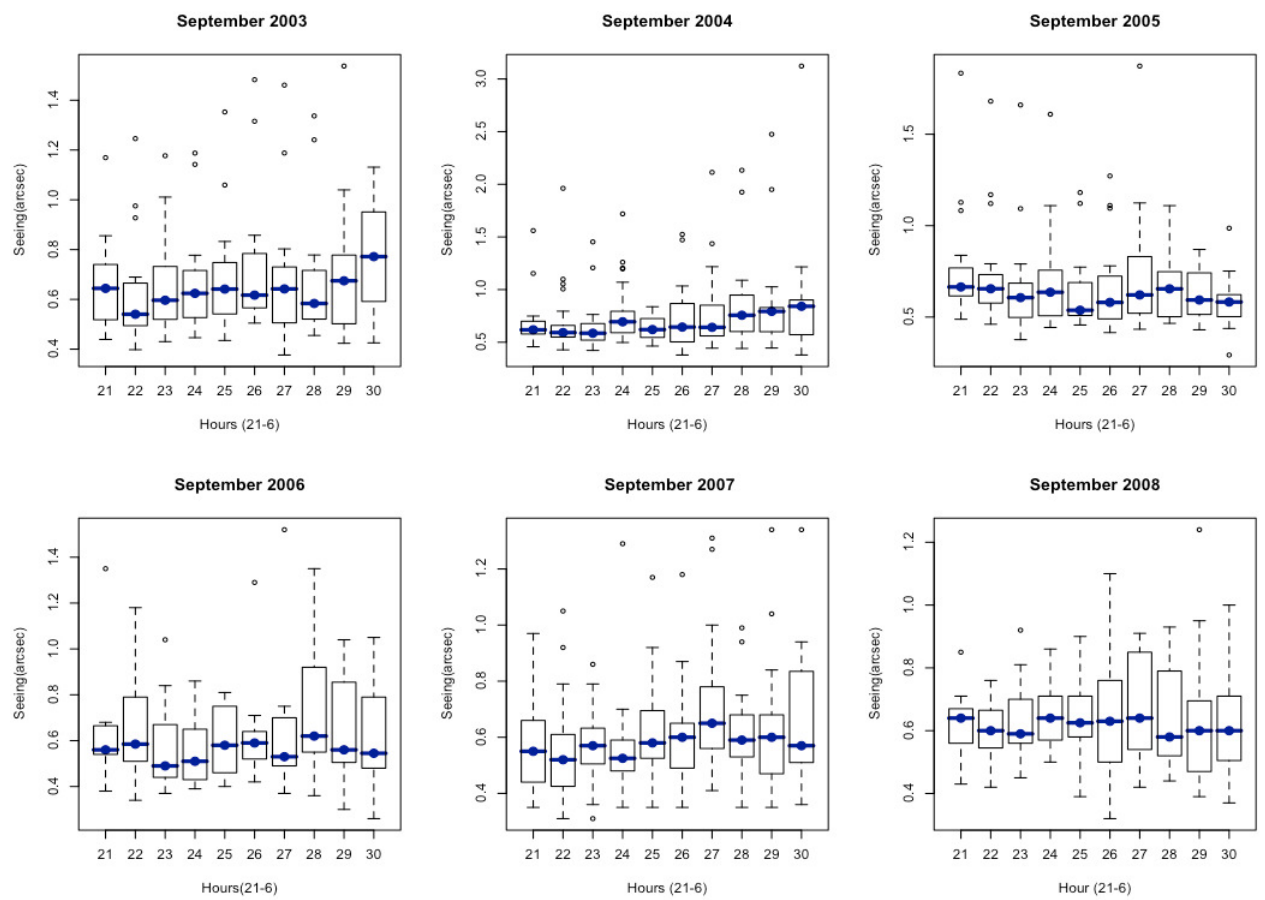


Figure B.11: Daily variation of the minimum seeing calculated for every hour during September for the years from 2002 to 2008

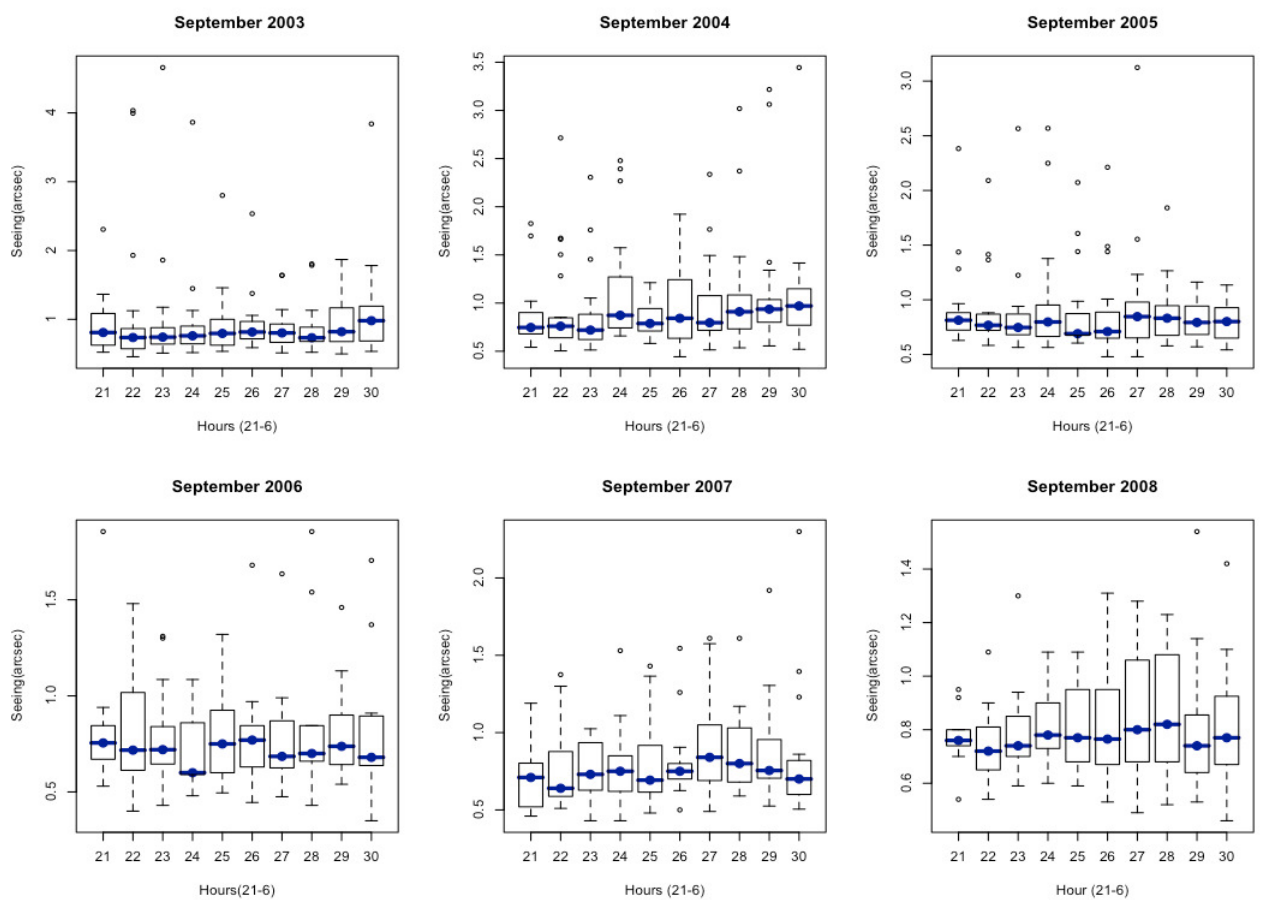


Figure B.12: Daily variation of the median seeing calculated for every hour during September for the years from 2002 to 2008

# Appendix C

## Raw Files

### C.1 Meteorological Raw.

Example of how looks like the raw file from the meteorological database: webpage [<http://weather.wyo.edu/upperair/sounding.html>] before to start to process the columns used for the analysis.

## C.2 MASS-DIMM and Robodimm.

The raw files from the MASS-DIMM and Robodimm instruments stores many instruments parameters which are not going to be used in the analysis of the seeing, astroclimate or refractive index  $C_n^2$ . The MASS channel has to filtered and extracted the values needed for the pos-ptocessing analysis. The way to filter and to extract the values of the  $C_n^2$ , isoplanatic angle, free seeing and coherence time is using AWK scripts. The filtering scripts have been distributed by Andrei Tokovinin and are adapted to the MASS@ING, the following script is applied to any MASS file. The flux in the aperture D is an important to monitor and it the base for the filtering of the data. It is considered a good values for flux in D (fluxd) when it is larger than 100. The figure C.3 shows the script.

To have a view of the raw saved data from the MASS channel, the figure ?? gives a portion of a file before going through a filtering process. The table C.5 summarise those parameters of free seeing,  $C_n^2$ , isoplanatic angle and coherence time versus the time that it will be saved in another file for a post-processing analysis and plotting. The DIMM channel store many instrument parameter and the files looks like figure C.6 and the robodimm measurements are stored with the parameters that we can see in the figure C.7

**60018 Guimar-Tenerife Observations at 00Z 12 Jun 2010**

PRES	HGHT	TEMP	DWPT	RELH	MIXR	DRCT	SKNT	THTA	THTE	THTV
hPa	m	C	C	%	g/kg	deg	knot	K	K	K
1008.0	105	17.4	12.5	73	9.11	250	2	289.9	315.8	291.5
1006.0	122	18.8	12.8	68	9.31	285	2	291.4	318.1	293.1
1000.0	173	18.6	12.6	68	9.24	30	3	291.8	318.2	293.4
925.0	834	12.6	10.7	88	8.80	35	8	292.2	317.5	293.7
913.0	943	11.6	10.2	92	8.66	20	10	292.2	317.1	293.7
893.0	1129	9.8	9.5	98	8.41	17	12	292.2	316.5	293.7
875.0	1298	9.0	8.0	93	7.73	15	14	293.1	315.5	294.5
850.0	1539	7.8	5.8	87	6.85	350	16	294.3	314.3	295.5
845.0	1588	7.4	5.7	89	6.82	345	17	294.4	314.4	295.6
828.0	1755	6.0	5.2	94	6.73	345	15	294.7	314.4	295.9
825.0	1785	5.8	5.1	95	6.72	339	14	294.7	314.4	295.9
821.0	1825	8.0	-9.0	29	2.37	332	13	297.4	304.9	297.9
812.0	1916	9.8	-10.5	23	2.13	315	10	300.3	307.1	300.7
810.0	1936	10.2	-10.8	22	2.08	312	11	300.9	307.6	301.3
809.0	1947	10.3	-11.5	20	1.97	310	11	301.1	307.4	301.5
784.0	2208	11.8	-29.2	4	0.44	314	15	305.5	307.0	305.6
781.0	2240	11.8	-29.0	4	0.45	315	16	305.8	307.4	305.9
754.0	2534	11.6	-27.4	5	0.54	303	22	308.7	310.6	308.8
739.0	2701	9.6	0.6	53	5.44	296	26	308.3	325.3	309.3
716.0	2963	8.9	-1.9	47	4.69	285	32	310.3	325.2	311.2
700.0	3150	8.4	-3.6	43	4.21	280	31	311.8	325.3	312.6
673.0	3475	7.2	-8.6	31	2.98	265	30	314.0	323.8	314.6
672.0	3487	7.2	-8.8	31	2.94	265	30	314.1	323.8	314.6
646.0	3808	5.0	-9.5	34	2.90	260	31	315.2	324.8	315.7
597.0	4449	0.7	-10.8	42	2.83	280	27	317.4	326.9	317.9
589.0	4558	0.0	-11.0	43	2.82	277	28	317.8	327.2	318.3
575.0	4751	-1.5	-16.5	31	1.84	270	30	318.2	324.5	318.5
569.0	4834	-1.1	-27.1	12	0.73	268	31	319.6	322.3	319.8
563.0	4918	-1.9	-26.3	13	0.80	265	32	319.7	322.6	319.8
535.0	5322	-5.5	-22.5	25	1.18	267	34	320.0	324.2	320.2
525.0	5470	-6.1	-41.1	4	0.20	268	35	321.0	321.8	321.1
500.0	5850	-8.5	-41.5	5	0.20	270	37	322.6	323.4	322.6
495.0	5928	-8.7	-45.7	3	0.13	270	37	323.3	323.8	323.3
463.0	6442	-11.7	-42.7	6	0.19	270	39	325.8	326.6	325.8
400.0	7540	-21.7	-32.7	36	0.61	270	42	326.7	329.0	326.8
359.0	8323	-29.5	-35.5	56	0.52	270	48	326.5	328.5	326.6
341.0	8688	-31.5	-53.5	10	0.08	270	50	328.6	328.9	328.6
319.0	9155	-35.1	-52.1	16	0.10	270	54	329.9	330.4	330.0
300.0	9580	-38.1	-57.1	12	0.06	270	57	331.6	331.8	331.6
295.0	9695	-38.9	-60.9	8	0.04	270	58	332.0	332.2	332.0
250.0	10810	-47.3	-62.3	16	0.04	270	68	335.6	335.8	335.6
248.0	10863	-47.9	-62.9	16	0.03	270	68	335.5	335.6	335.5
207.0	12037	-54.1	-69.1	14	0.02	270	72	343.5	343.6	343.5
200.0	12260	-55.3	-70.3	14	0.01	270	70	345.0	345.1	345.0
179.0	12962	-59.0	-74.0	13	0.01	275	67	350.2	350.2	350.2
175.0	13104	-59.7	-74.7	12	0.01	270	63	351.2	351.3	351.2
164.0	13511	-59.1	-75.1	11	0.01	257	62	358.8	358.8	358.8
162.0	13588	-59.3	-75.7	10	0.01	255	62	359.8	359.8	359.8
150.0	14070	-60.3	-79.3	7	0.00	265	62	366.0	366.0	366.0
144.0	14324	-59.9	-81.2	5	0.00	270	61	370.9	370.9	370.9
137.0	14633	-59.5	-83.5	3	0.00	259	54	377.0	377.0	377.0
132.0	14861	-60.4	-84.3	3	0.00	250	48	379.5	379.5	379.5
130.0	14954	-60.7	-84.6	3	0.00	245	49	380.5	380.5	380.5
117.0	15599	-63.2	-86.7	3	0.00	265	55	387.6	387.6	387.6
111.0	15921	-64.5	-87.8	3	0.00	280	41	391.1	391.1	391.1
102.0	16439	-66.4	-89.5	3	0.00	280	26	396.9	396.9	396.9
100.0	16560	-66.9	-89.9	3	0.00	265	28	398.2	398.2	398.2

Figure C.1: Meteorological parameters from the station 60018 sited in Guimar, Tenerife Island. This is 150 km away from the La Palma.

96.0	16804	-67.9	-90.6	3	0.00	255	33	400.9	400.9	400.9
94.0	16930	-68.5	-91.0	3	0.00	270	37	402.2	402.2	402.2
91.0	17124	-69.3	-91.6	3	0.00	295	31	404.4	404.4	404.4
86.7	17414	-70.5	-92.5	3	0.00	290	21	407.5	407.6	407.5
85.0	17532	-69.9	-92.2	3	0.00	305	17	411.1	411.1	411.1
84.0	17603	-69.5	-92.0	3	0.00	300	11	413.2	413.2	413.2
82.0	17747	-68.8	-91.6	2	0.00	260	3	417.6	417.6	417.6
80.7	17842	-68.3	-91.3	2	0.00	236	5	420.5	420.5	420.5
78.8	17986	-64.3	-88.3	2	0.00	200	9	431.6	431.6	431.6
78.0	18048	-64.3	-88.8	2	0.00	185	10	432.9	432.9	432.9
75.0	18288	-64.3	-90.8	2	0.00	200	17	437.8	437.8	437.8
72.0	18538	-64.3	-92.9	1	0.00	245	19	442.9	442.9	442.9
71.0	18623	-64.3	-93.6	1	0.00	260	18	444.7	444.7	444.7
70.0	18710	-64.3	-94.3	1	0.00	280	15	446.5	446.5	446.5
69.0	18799	-64.2	-94.2	1	0.00	320	15	448.5	448.5	448.5
65.0	19166	-63.9	-93.9	1	0.00	10	14	457.0	457.0	457.0
63.0	19358	-63.7	-93.7	1	0.00	85	11	461.5	461.5	461.5
61.0	19557	-63.5	-93.5	1	0.00	130	4	466.2	466.2	466.2
56.0	20091	-60.7	-91.2	1	0.00	65	11	484.0	484.0	484.0
53.0	20434	-59.0	-89.8	1	0.00	115	21	495.8	495.8	495.8
51.6	20601	-58.1	-89.1	1	0.00	101	17	501.6	501.6	501.6
50.0	20800	-59.3	-90.3	1	0.00	85	12	503.3	503.3	503.3
49.4	20876	-59.7	-90.7	1	0.00	79	12	504.1	504.1	504.1
49.0	20928	-59.6	-90.6	1	0.00	75	12	505.5	505.5	505.5
47.0	21193	-59.1	-90.3	1	0.00	90	14	512.9	512.9	512.9
46.0	21330	-58.8	-90.1	1	0.00	75	10	516.7	516.7	516.7
43.0	21759	-57.9	-89.5	1	0.00	80	19	528.9	528.9	528.9
42.0	21909	-57.6	-89.3	1	0.00	100	18	533.2	533.2	533.2
40.0	22219	-57.0	-88.8	1	0.00	75	20	542.2	542.3	542.2
39.0	22380	-56.7	-88.6	1	0.00	80	28	547.0	547.0	547.0
37.0	22715	-56.0	-88.2	1	0.00	100	19	557.0	557.0	557.0
36.0	22890	-55.6	-87.9	1	0.00	90	15	562.3	562.3	562.3
35.0	23069	-55.3	-87.7	1	0.01	70	14	567.8	567.8	567.8
34.0	23253	-54.9	-87.4	1	0.01	50	20	573.5	573.5	573.5
31.0	23841	-53.7	-86.6	1	0.01	70	34	592.0	592.1	592.0
30.0	24050	-53.3	-86.3	1	0.01	70	31	598.7	598.8	598.7
26.0	24983	-50.7	-84.7	1	0.01	95	32	631.0	631.1	631.0
23.0	25782	-48.5	-83.3	1	0.02	110	33	660.0	660.1	660.0
22.2	26013	-47.9	-82.9	1	0.02	98	28	668.5	668.7	668.6
22.0	26073	-48.0	-82.9	1	0.02	95	27	670.0	670.2	670.0
20.0	26700	-48.9	-82.9	1	0.02	110	23	685.7	686.0	685.7
19.4	26899	-49.9	-83.9	1	0.02	98	21	688.6	688.8	688.6
19.0	27037	-49.2	-83.3	1	0.02	90	19	695.0	695.2	695.0
17.3	27655	-45.9	-80.9	1	0.03	86	21	724.3	724.7	724.3
17.0						85	21			

### Station information and sounding indices

```

Station number: 60018
Observation time: 100612/0000
Station latitude: 28.47
Station longitude: -16.38
Station elevation: 105.0
Showalter index: 11.21
Lifted index: 9.12
LIPT computed using virtual temperature: 8.85
SWEAT index: 138.62
K index: 10.10
Cross totals index: 14.30
Vertical totals index: 16.30
Totals totals index: 30.60
Convective Available Potential Energy: 8.83
CAPE using virtual temperature: 13.23
Convective Inhibition: -4.53

```

Figure C.2: Extracted file from the radiosonde database with all the meteorological parameters used in the Wind speed and potential temperature analysis and the columns are the input for different  $C_n^2$  models (Hufnagel-Valley and AXP).

```

#!/bin/awk -f
## March 2004, new format
## Filters MASS file from wrong data:
## bad background (>3%), Chi2>100
## Use as: filter.awk <mass-file> > <result-file>
BEGIN{
  # flag to mark good data:
  good = 0; backd=1; fluxd=1; tgood=0;
}
{
  if(S1=="P" && substr(S4,12,10)=="Background") {backd = S8}
  if(S1=="F") {fluxd = S10; if(fluxd==0) {fluxd=1};
  if(backd/fluxd<0.03 && fluxd>200 && S11<0.01) {good = 1; print S0} else {good = 0}
  }
}
## output part
if(S1=="O") {print S0}
if(S1=="P") {print S0}
if(good = 1) {
  if(S1=="I") {print S0}
  if(S1=="A" && S5<0.2) {print S0}
  if(S1=="T" && S6<100) {print S0; tgood=1}
  if(S1=="R" && tgood==1 ) {print S0; tgood=0}
}
}
}

```

Figure C.3: AWK script used to filter the MASS raw files

```

#I  UTbeg  SI_A  e_SI_A  SI_B  e_SI_B  SI_C  e_SI_C  SI_D  e_SI_D  DSI_AB  e_DSI_AB  DSI_AC  e_DSI_AC  DSI_AD
e_DSI_AD  DSI_BC  e_DSI_BC  DSI_BD  e_DSI_BD  DSI_CD  e_DSI_CD  DESI_A  e_DESI_A  DESI_B  e_DESI_B  DESI_C  e_DESI_C
DESI_D  e_DESI_D  UTend
I 2008-07-13 22:15:26 0.0400 0.026 0.0342 0.025 0.0241 0.024 0.0153 0.024 0.0025 0.211 0.0063 0.065 0.0149 0.038 0.0032
0.075 0.0106 0.037 0.0037 0.040 0.0004 0.781 0.0007 0.193 0.0003 0.159 0.0001 0.270 2008-07-13 22:16:27
#F  UT  FLUX_A  e_FLUX_A  FLUX_B  e_FLUX_B  FLUX_C  e_FLUX_C  FLUX_D  e_FLUX_D
F 2008-07-13 22:15:56 20.56 0.003 49.41 0.003 162.3 0.002 175.7 0.002
#A  UT  fSee  e_fSee  See  e_See  fM0  e_fM0  M0  e_M0  fHeff  e_fHeff  Heff  e_Heff  Isopl  e_Isopl  M2  e_M2  Tau
e_Tau
A 2008-07-13 22:15:56 0.25 0.097 0.00 0.000 7.80e-14 0.162 1.00e-17 0.000 17821 0.072 1 0.000 2.73 0.024 1.26e-05 0.062 19.69
0.468
#T  UT  Met Nz Chi2  SeeCn z_1  Cn2_1  z_2  Cn2_2  z_3  Cn2_3  z_4  Cn2_4  z_5  Cn2_5  z_6  Cn2_6
T 2008-07-13 22:15:56 L 3 9.05 0.29 0.5 5.72e-14 10.8 2.10e-14 25.7 7.79e-15
R 2008-07-13 22:15:56 L -0.002 0.009 -0.013 0.002 0.147 -0.049 -0.027 0.149 0.041 0.053
T 2008-07-13 22:15:56 X 6 9.25 0.30 0.5 6.36e-14 1.0 2.52e-23 2.0 3.34e-22 4.0 3.49e-15 8.0 2.02e-16 16.0 2.57e-14
R 2008-07-13 22:15:56 X -0.012 0.002 -0.015 0.018 0.074 -0.088 -0.044 0.118 0.031 0.049
# 2008-07-13 22:16:29 Temperature: 15.5
M 2008-07-13 22:16:30 Normal 1.13
#I  UTbeg  SI_A  e_SI_A  SI_B  e_SI_B  SI_C  e_SI_C  SI_D  e_SI_D  DSI_AB  e_DSI_AB  DSI_AC  e_DSI_AC  DSI_AD
e_DSI_AD  DSI_BC  e_DSI_BC  DSI_BD  e_DSI_BD  DSI_CD  e_DSI_CD  DESI_A  e_DESI_A  DESI_B  e_DESI_B  DESI_C  e_DESI_C
DESI_D  e_DESI_D  UTend

```

Figure C.4: Raw file of the the MASS channel, with many parameters saved.

#A	UT		fSee	e_fSee	See	e_See	fM0	e_fM0	M0	e_M0	fHeff	e_fHeff	Heff	e_Heff	Isopl	e_Isopl	M2	e_M2	Tau	e_Tau
A	30/7/08	21:10:09	0.39	0.049	0	0	1.63E-13	0.081	17	0	8762	0.074	1	0	3.15	0.026	8.84E-06	0.086	6.56	0.08
#T	UT		Met	Nz	Chi2	SeeCo	z_1	Cn2_1	z_2	Cn2_2	z_3	Cn2_3	z_4	Cn2_4	z_5	Cn2_5	z_6	Cn2_6		
T	30/7/08	21:10:09	X	6	11.51	0.39	0.5	3.26E-22	1	1.78E-15	2	6.50E-14	4	6.22E-14	8	7.67E-24	16	1.21E-14		

Figure C.5: Extracted output file from the MASS channel with the  $C_n^2$  values per each layer and the isoplanatic angle and the coherence time (Tau)

1	2	3	4	5	6	7	8	9	10	11
25/4/08	21:01:08	0	_p/a_	1.15	10697	2.521	2.336	2.31	6423	57.7
25/4/08	21:05:51	0	_p/a_	1.14	10301	2.709	2.552	2.568	6080	57.3
25/4/08	21:11:27	0	_p/a_	1.14	8036	2.792	2.645	2.605	6777	57.4
25/4/08	21:12:35	0	_p/a_	1.14	5839	2.917	2.821	2.793	6513	57
25/4/08	21:13:41	0	_p/a_	1.14	10608	2.509	2.44	2.442	6816	54.8
25/4/08	21:14:45	0	_p/a_	1.14	9714	2.681	2.603	2.582	6643	54.6

Figure C.6: Extract of a output file from DIMM channel. The value of seeing used in the analysis of the thesis is the values in the column 7. Each column has an identification that is; **1.** UT-Date, **2.** UT-Time (from PC unless 'time 1' is set in telescope.ini), **3.** HR star number (from name field in the object list), **4.** Star name (from the comment field in the object list), **5.** Airmass, **6.** Total number of exposures (short+long), **7.** Seeing [arcsec],  $(x+y)/2$ , corrected for zenith distance and exposure time, **8.** x-seeing, corrected for zenith distance and exposure time, **9.** y-seeing, corrected for zenith distance and exposure time, **10.** Total flux (short exposure), **11.** dx, star-separation [pixels] in 'X' (focus), **12.** dy, star separation (pixels) in 'Y' (alignment).

ID	Date	time	star	am						Seeing <sub>01</sub>	Seeing <sub>02</sub>	Seeing <sub>11</sub>	Seeing <sub>12</sub>				
159496	4/10/08	07:17:04+01	SAO94027	1.1	287.391566	294.295181	67.538889	106	105	1.981918	1.925385	1.808916	1.957049	200	83	1	£
159497	12/10/08	21:37:08+01	SAO49941	1.3	1880.421233	2289.702055	73.361389	108	109	0.506299	0.564547	0.532312	0.505495	200	146	0	‡
159498	12/10/08	21:40:19+01	SAO49941	1.3	1898.8975	2111.4775	73.273611	111	110	0.415882	0.511425	0.483028	0.522631	200	200	0	‡

Figure C.7: Extract of a output file from RoboDimm channel. The Robodimm gives 4 measurements of the seeing, two longitudinal and two transversal, that the median of those give the seeing.

# Appendix D

## MASS-DIMM

### D.1 Basic Results

With the aim to provide knowledge of the atmosphere turbulence conditions above the Observatory Roque de Los Muchachos during the Laser Guide Star (LGS) nights, the ING has settled a MASS-DIMM instrument close to the WHT in the Robodimm tower.

The instrument has been well described and tested in different site evaluation campaigns in Chile (Els,G, 2008) and the ING has take the advantage to use this instrument by its easy hardware and installation requirements. The MASS-DIMM has been used since in July 2007 when it took the first atmospheric turbulence profiles. And it has been during the commissioning runs of AO observations with the Laser Guide Star (GLAS experiment). The MASS-DIMM instrument is divided into two separated parts but connected each other. The DIMM part measures the whole atmosphere integrated which gives to calculate the seeing parameter on a time scale of 1 minute. The MASS takes a vertical profile of the turbulence distribution fitting in 6 layers (0.5, 1, 2, 4, 8 and 16) and return the estimated  $C_n^2(h)$  during the data acquisition and the calculated free seeing, isoplanatic angle and coherence time. The MASS can not resolve altitudes below 0.5 km, them to determine the ground layer  $C_n^2(0)$  a combination of MASS-DIMM is necessary and it can be estimated as

$$C_n^2(0) = \mu_0 - \sum_{i=1}^6 C_n^2(h_i) \quad (\text{D.1.1})$$

where  $\mu_0 = 0.06\lambda^2 r_0^{-5/3}$  (at zenith) getting from the DIMM and the summation is from the MASS data.

## D.2 System description.

The MASS-DIMM instrument settled at Roque de Los Muchachos by the ING is based on a scope of aperture 12 (manufacture by Meade Telescope and the model RCX400) (Tokovinin, 2005), this scope has the advance of a Ritchey-Chrtien optics and an automatic focusing in the secondary mirror. The MASS-DIMM device is installed in the pigy back of the scope (see figure ??). The instrument is running using two different software packages in two different PCs; one to control the MASS channels and the another one to control the telescope and the DIMM channel. The PCs used to run the software are; a fan less PC (stelth PC) running on LINUX Operating System Red Hat, and a standard PC on Windows XP. The MASS channel and the DIMM channel are running specific software packages that are;

- TURBINA software under Linux OS to run the MASS. This software was developed by Kornilov and collaborators at Sternberg Moscow (Kronilov,2003) which was designed to drives the MASS unit and to calculate the  $C_n^2(0)$  profiles at different altitudes and other astroclimate parameters as; isolanatic angle , the calculated free atmosphere seeing and the coherence time.
- CDIMM software under Windows XP to run the DIMM and the telescope. Software developed by Christoph Birk at Las Campanas Observatory (Thomas-Osip, 2007)and it was used for the Thirty Meter Telescope (TMT) site testing campaigns. This software package drives the telescope and the CCD (SBIG-7) and makes the calculation for the measurements of the seeing.

Both computers are connected by Ethernet to the internal ING network. See the figure D.5 that shows a network diagram. The two devices are synchronized

to get measurements with a small time lag of about 20 seconds. The data from both instruments are displayed on line and saved locally in the PCs. The figure D.2 and D.2 shows the realtime GUIs for TURBINA and CDIMM packages. In the figure D.1 shows the actual configuration of the MASS-DIMM placed in the existing robodimm tower side by side with a RoboDIMM monitor.

## D.3 Observations

The current operations of the MASS-DIMM instrument are under the supervision of an operator, the WHT telescope operators are taking care of the instrument and its night performances. The telescope operates from the sunset twilight till the sunrise twilight. The numbers of observed nights are depended of the weather and sky conditions. We have been used the systems during cloudy nights and it has showed a bad results making the instrument to loose the star and it makes a discontinuity in the data acquisition with the result of bad data quality due to loosing the star and reacquire again. The observing range is above elevation 55 degrees and the numbers of star observed per night is about 4.

There is a climatologic phenomenon called *calima*<sup>1</sup>, that it affects to the sky transparency and to measurements of the MASS-DIMM. This phenomenon occurs mostly 5 times per year that could affect the astronomical observations with a reduction of the sky transparency and in a most important way during the Laser Guide Star observing mode where the dust in the air increase the laser scatter reducing the performances of the AO systems and sometimes force to stop the observations. The figure D.8 shows the laser scatter due to the calima event during an AO+LGS mode observations. Depending how strong is this dust storm the instrument MASS-DIMM stop its operations to prevent possible damage to the equipments.

### D.3.1 Basic Measurements Results.

The MASS device is working under the Turbina program control (Kornilov et al., 2003) which operates under LinuxOS. Although the functionality of this program includes not only the measurement control but also the real-time data processing spanning from scintillation indices calculation to the restoration of a current altitude turbulence prole, the repetitive on-line data reprocessing allows one to obtain more reliable and homogeneous results. The MASS measurements can be displayed in

---

<sup>1</sup>Calima is the canarian name to define the Saharas desert dust. This dust plume originated by storms located in the Sahara desert that can be elevated to a heights about 5000 meters asl and that can travel through the Atlantic Ocean moved by the tropospheric winds.

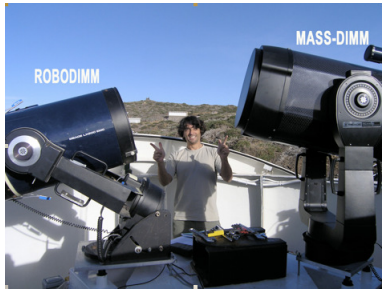


Figure D.1: View of the robodimm and MASS-DIMM



Figure D.2: MASS-DIMM instrument with the MASS device and the CCD attached.

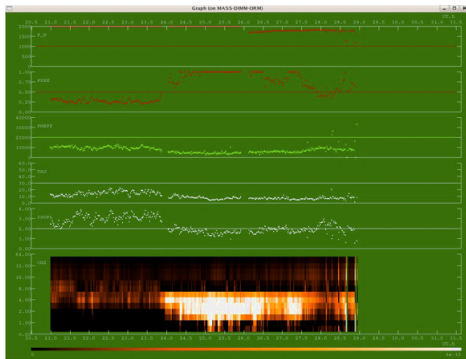


Figure D.3: Real time display for the MASS channel.

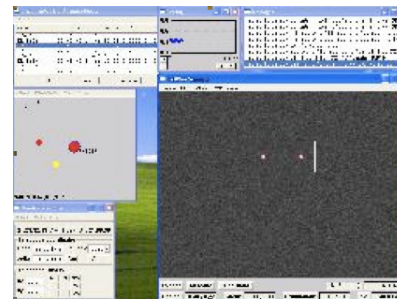


Figure D.4: Real time display of the DIMM channel.

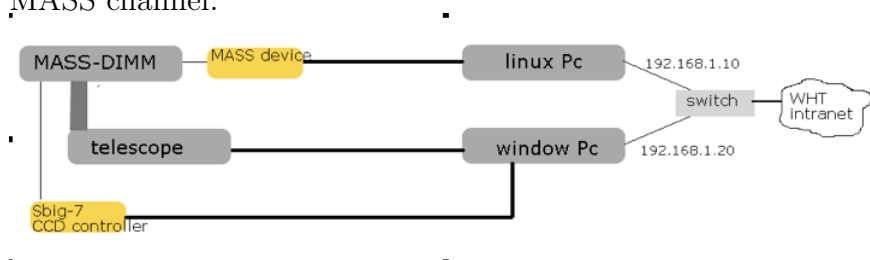


Figure D.5: Block diagram of the instruments set up.

Figure D.6: Mainly description of the MASS-DIMM systems. With the hardware and also the realtime displays are shown. Turbina realtime screenshot showing the strength of the turbulence at different altitudes, the free atmosphere seeing, the scintillation index and the isoplanatic angle images of the photocounts are sampled at 1ms during 1 minute. The real time GUI interface for the DIMM channel (CDIMM package) which measure the seeing in drift mode with an integration time of 4msec and control the telescope and the detector. The system Turbina and DIMM and synchronized during the measurements procedure. which control the telescope and the CCD.

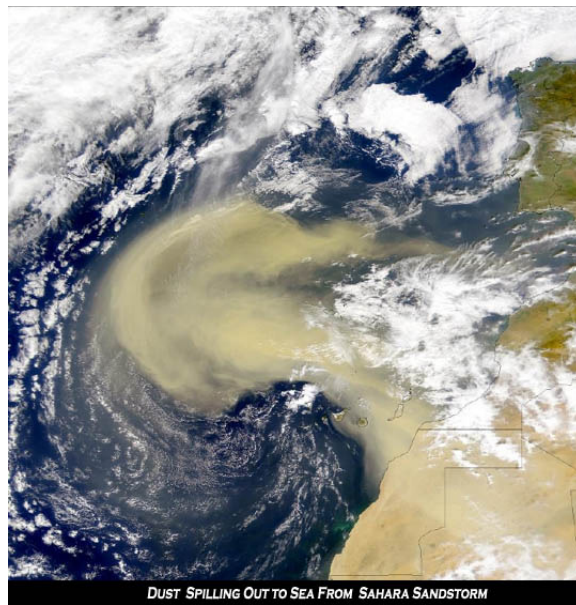


Figure D.7: Sahara dust plume. Image captured by the MODIS. Credit NASA.



Figure D.8: Laser Guide Star scatter due to an event of dust. Credit. Juan Carlos Guerra

real time by using the Turbina software package where shows the strength of the  $C_n^2$  in altitude and other astroclimate parameter as; free seeing, isoplanatic angle and coherence time in a temporal variation.

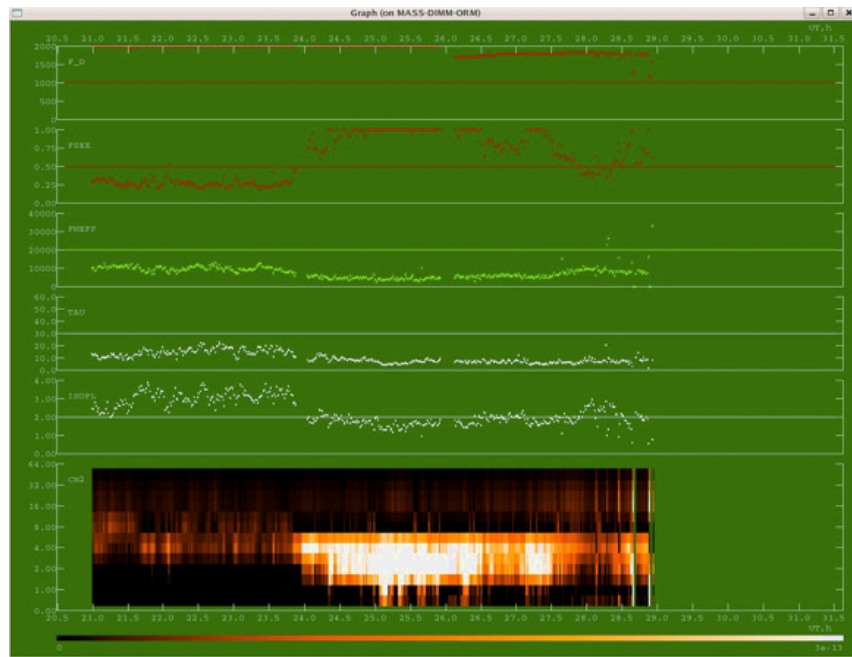


Figure D.9: Turbina screenshot during the observing night on august 24th of 2008. It is showed a strong turbulence between the 1 and 8 kilometers starting at midnight 24:00 and finishing at 3:30. The astroclimate parameters; the isoplanatic angle, the free seeing and the coherence time are also plotted. The x-axis corresponds with the time where midnight corresponds with 24 and 1 a.m. is 25. The y-axis is the altitude (Km).

### D.3.2 Comparison between two MASS-DIMM instruments.

In the process to work out with the data collected from the MASS-DIMM instrument, it is important to know how good are the data and if they can be correlated (calibrated) with a similar instrument in site. It has been a fortune that ESO has started a site testing campaigns in the Roque de los Muchachos Observatory in the 2008 as part of the E-ELT campaign. This device has been deployed by the IAC, which with its experience and knowledge running seeing monitors has contributed to calibrate and to run the instrument since 2008. This has been an opportunity to compared the two instruments in site. The IAC has placed the MASS-DIMM in Las Moradas and the ING has placed in the robodimm tower close to the WHT. The figure D.11 shows the sites for the two MASS-DIMM instruments. The two

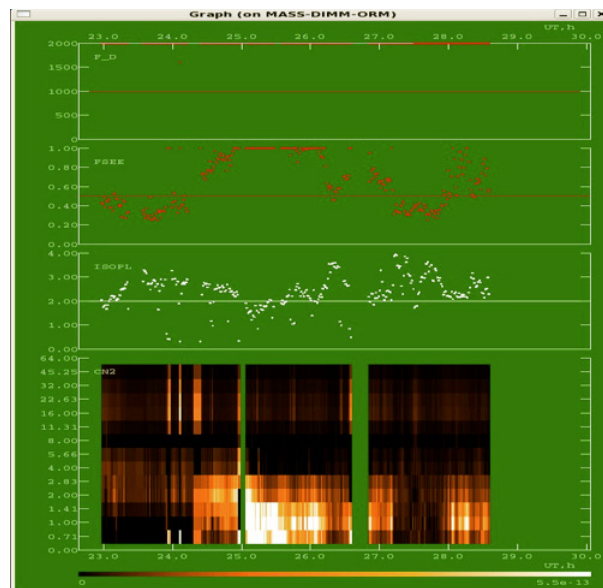


Figure D.10: Screenshot of the turbina package working during one observations night (September 4th 2009) showing a strong turbulence below 4 kilometers after the 24:00. This night shows a variability profile of the isoplanatic angle and the free seeing after the long turbulent burst of about one hour (1pm to 2 pm) after this burst the atmosphere shows a turbulent residual where it doesn't reach a dissipation of the turbulent energy and reach a more stable condition. The x-axis is the time (0 UT is 24) the y-axis is the altitude (kilometers) and the  $C_n^2$  is represented by the gradient colour bars with the minimum 0 (non-turbulent) with a  $C_n^2$  about  $10^{-21}$  to a turbulent with a  $C_n^2$  about  $10^{-14}$ .

sites are well separated and they have different local seeing influenced mainly by the orography but free atmosphere seeing and the vertical turbulence profiles can be correlated. The local seeing or the contribution of the surface it will be determined by the combination of the free seeing with the whole seeing measured by the DIMM channel.

Unfortunately the IAC data are not freely accessible and only a few nights could be correlated. The DIMM channel measurements (of the MASS-DIMM instrument at the WHT) has been correlated with the Robodimm. About the Robodimm data which it has been used in this thesis, the IAC has recently published an internal document where shows a big discrepancy between the IAC seeing monitor (which



Figure D.11: Location of the two sites for the mass-dimm instruments. The IAC sets up the unit in the DHV location [1] and the ING sets up the unit close to the WHT [2]. Robodimm tower.

it has been used to calibrate the ESO MASS-DIMM) and the Robodimm. This discrepancy is more noticed for a good seeing ( 0.6 arcsec) after the year 2003 and this behavior would produce not only a truncation of good seeing values but also a redistribution of data in the statistical function misrepresenting, therefore, the real mean and median. This comparison of the two seeing instruments; the robodimm from the ING and the dimm from the IAC has to be considered with carefully because we don't know if the DIMM from the IAC has been calibrated during the years with other similar instruments and also we don't know what it was the method for the post-processing of the data ( robodimm and dimm).

But, we can say that the MASS-DIMM device is a compact package, it has been considered that the measurements are correct they are not affected by mismatch in the hardware or software configurations. Considering this assumption the MASS-DIMM could be taken as good instrument to measure the atmosphere turbulence and the seeing. The figure D.12 shows the comparison of the two vertical profiles

taken by the MASS-DIMM instruments, the two devices show a close trend profile for the upper layers above 0.5km and a discrepancy for the lower layer.

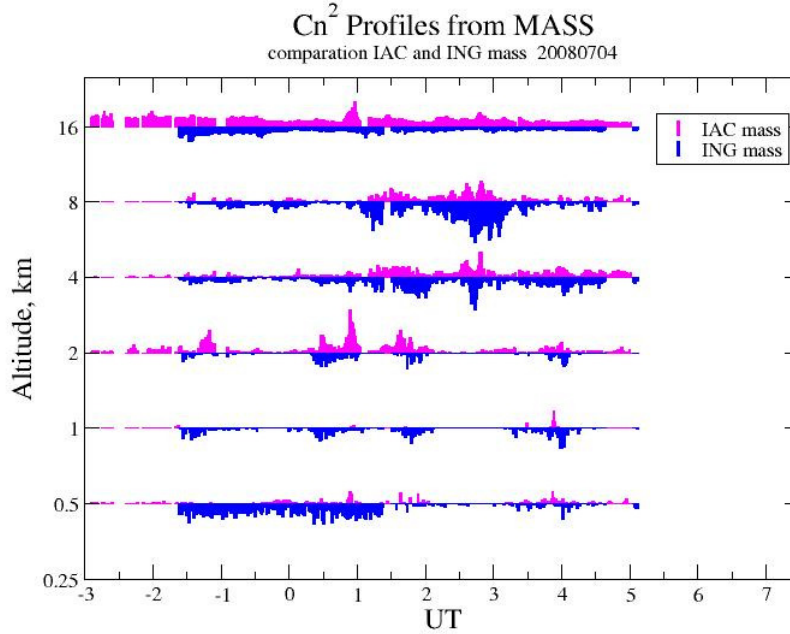


Figure D.12: Vertical profiles of the  $C_n^2$  for the two MASS-DIMM. The vertical bars at each altitude represents the magnitude of the refractive index structure constant integrated over that layer. The figure shows the discrepancy for the lower layers when it was observed Gamma Draconis with the MASS-DIMM@ING. The IAC device is located at south east from the ING. Data taken on 4<sup>th</sup> on July

In the Figure D.12 we can see that the lower layer at 0.5 km shows a different pattern between the ING and IAC MASS measurements during that night. This discrepancy in the measurements as help to identify a strange behaves of the MASS@ING observing the star Gamma Draconis showing that the layers at 0.5 and 1km with a higher  $C_n^2$  values. The Figure D.13 shows the compartion of the two  $C_n^2$  profiles for the two MASS instruments on the night 12<sup>th</sup> on June, where the effect of the lower layer is not observed.

The free seeing from the measurements of the MASS instruments are retrieved and they are shown in the figures D.14 and D.15. The free seeing is not counted in the ground layer and the orography contribution of the two sites is minimum.

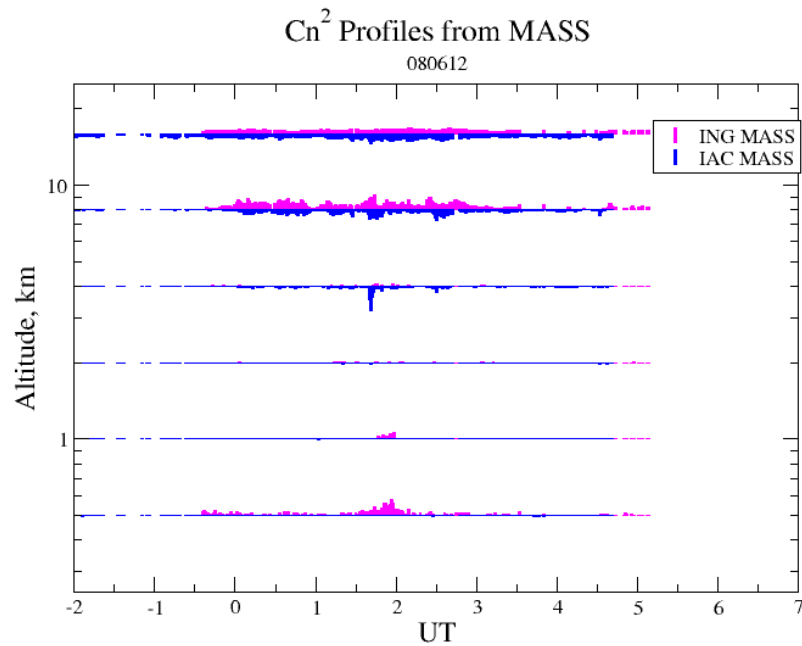


Figure D.13: Vertical profiles of the two MASS-DIMM. The vertical bars at Each altitude represents the magnitude of the refractive index structure constant Integrated over that layer. The figure shows the discrepancy in the lower layer, where the MASS@ING has detected a burst between 1:30 to 2:15 am that the MASS@IAC has not detected.

The first look of the figures D.14 and D.15 of the two measurements shows a good trend. The figure D.14 is the reduction of the free seeing for the profiles showed in the figure D.12 where there is a discrepancy of the two  $C_n^2$  profiles

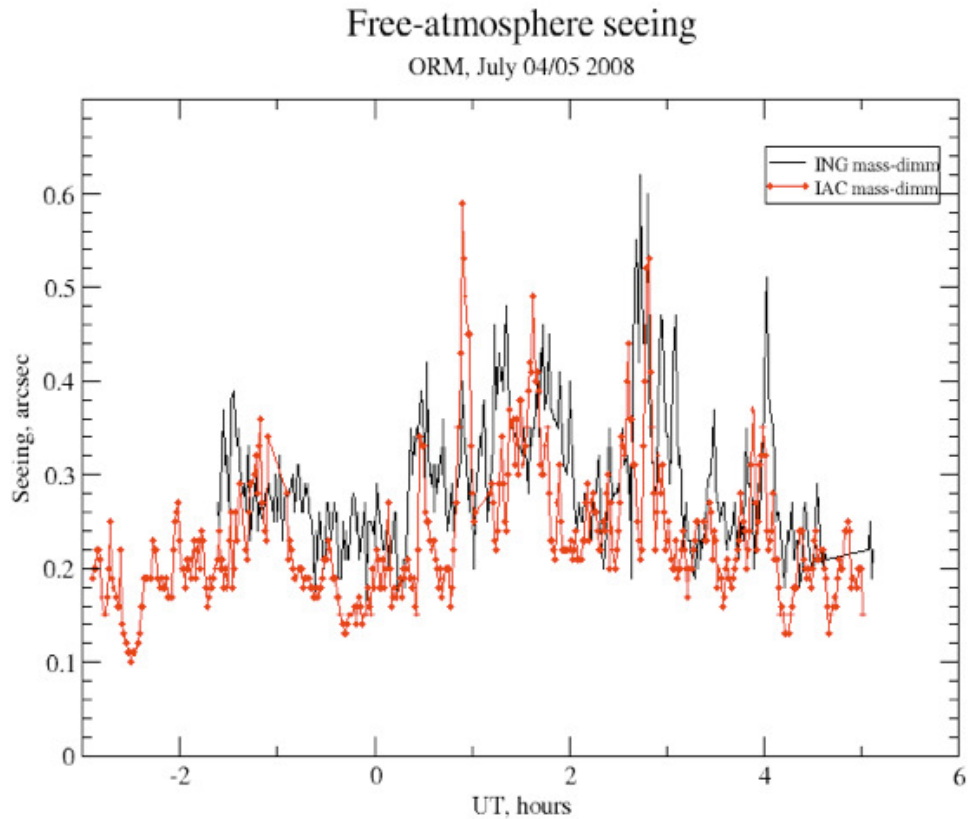


Figure D.14: Free seeing measurements for the MASS@las Moradas and the MASS@ING. There are a few differences, but in general view the two plots are quite similar. Data taken the night 4th on July 2008

But calculating the cumulative distribution of the free seeing measurements of two nights (12th on June and 4th on July) showed in the figure D.16 gives lower values of the free seeing for the MASS@IAC respect to the MASS@ING.

The discrepancy of the results of the measurement of the  $C_n^2$  can suggest that the restoration of the free seeing can give a mismatch in the results. Taking the analysis of the isoplanatic angle that is dependant of the higher layers and plotting the two measurements together as shown in figure D.17 we can see that the two graphs have a good correspondence. But calculating its Pearson correlation for the same time periods and taking that during 10 minutes the atmosphere can be considered stable, the results gives a Pearson value of 0.57 which is not too good a correlation.

The comparison results shows a discrepancy of the measurements of the two

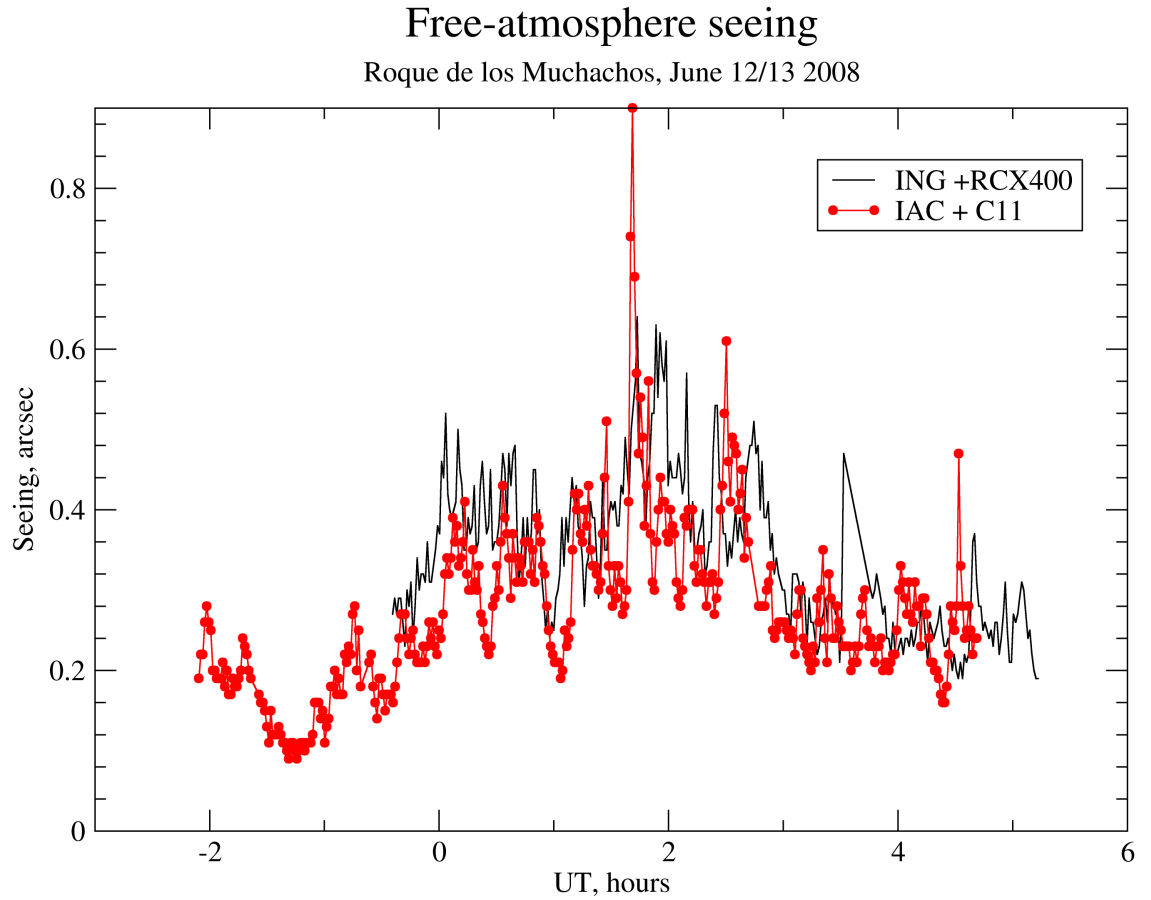


Figure D.15: Comparison plot of the free seeing measurements for the MASS@las moradas and the MASS@ING. The measurements were taken the night on the 12th on June, 2008.

MASS instruments when we suppose that there will be not any. It is true that the two MASS instruments are not set up with the same equipment (different telescopes) and the response of the photomultipliers are different, which means that the measurements of the flux in the four pupils can be different, therefore the measurements of the  $C_n^2$  are different and the instruments can over or under estimate the  $C_n^2$ .

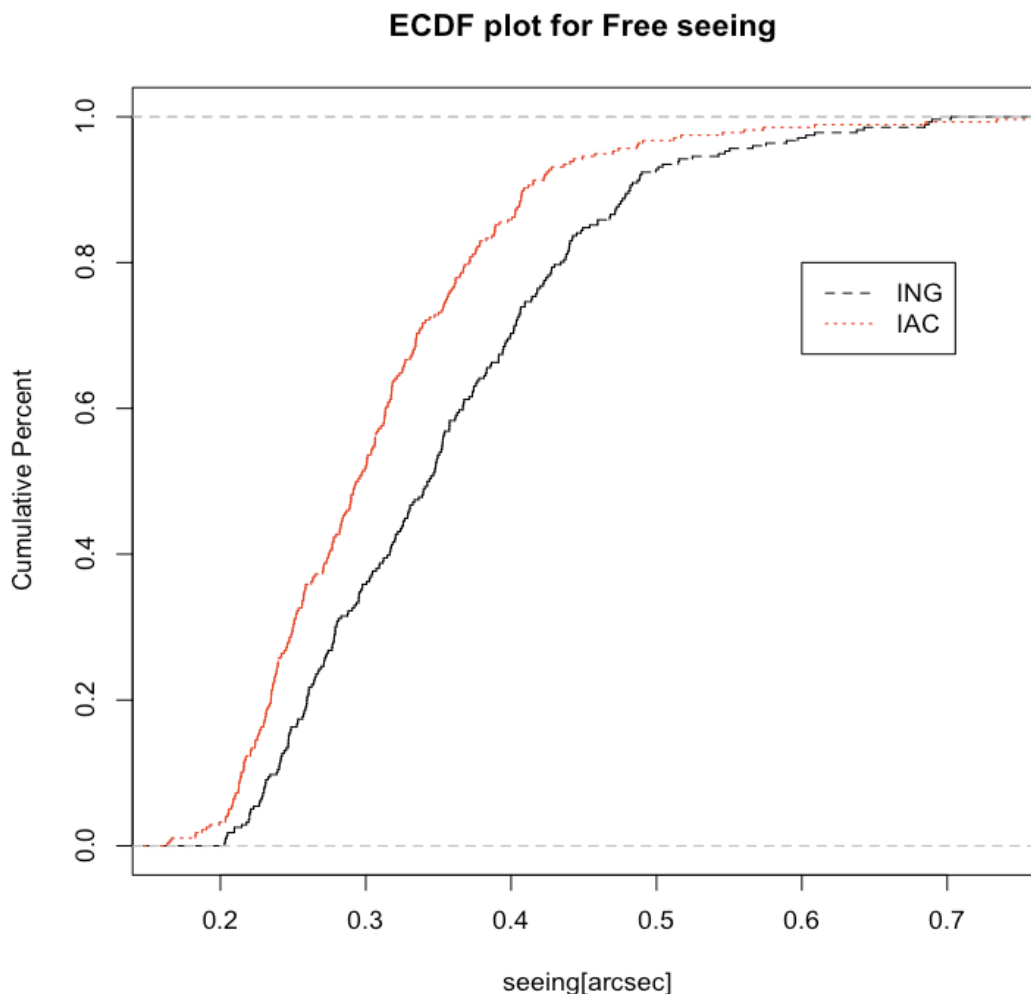


Figure D.16: Cumulative distribution of the free seeing measurements for two nights (the 12th on June and 4th on July, 2008) taken by the MASS@IAC and MASS@ING.

## D.4 MASS-DIMM. GLAS@WHT Experience.

As is well known, for the new AO techniques using LGS it is important to get knowledge of the vertical distribution of the turbulence and its strength. In the case of the AO system at the WHT, it has been upgraded with a Rayleigh LGS system (Morris, t., 2003 ). The system is specified to correct the first 15 km of atmosphere, which is the part of the atmosphere where there is concentrated about the 80% of the turbulence.

An AO+LGS running system takes too many resources; technical and human,

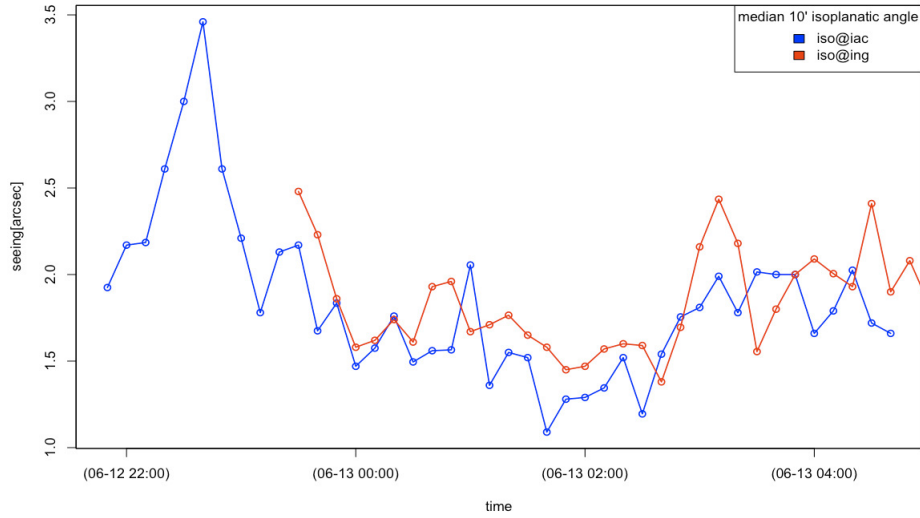


Figure D.17: The isoplanatic angle measured by the MASS@IAC and MASS@ING during one night 12th on June. The analysis in the plot shows the 10 minutes median values for the measurements.

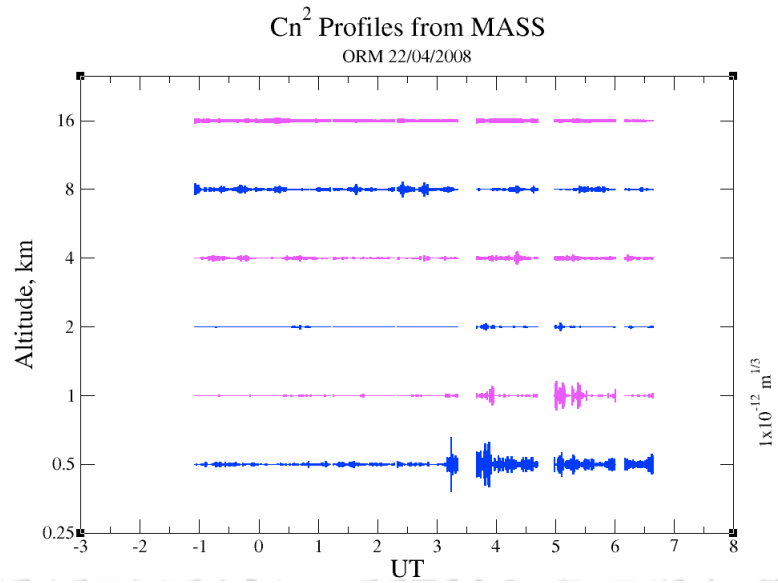
and the way to minimize or to improve its efficiency is an important issue that has to be considered and it is in this scenario where the real time  $C_n^2$  profiler such as the MASS-DIMM takes on its importance. The MASS-DIMM can help during the real time observations, evaluating the sky conditions through the knowledge of the  $C_n^2$  and total and free seeing, also the coherence time and isoplanatic angle can be measured. Or by taking a long term statistics of the sky conditions, it can help to better characterize the atmosphere and to know the best periods to run AO+LGS observations.

Taking a few runs with the LGS and the MASS-DIMM instrument working during the same nights, we see the importance that a real monitor of the atmosphere turbulence has.

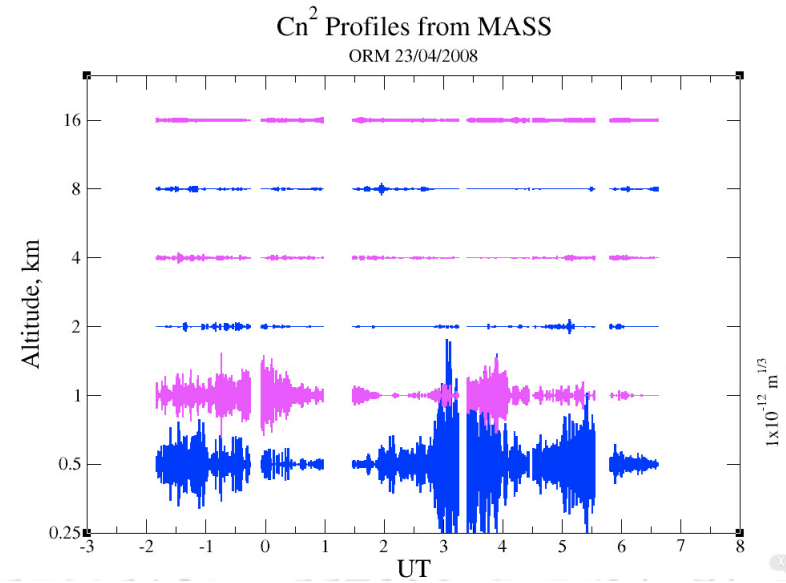
### D.4.1 Observations

During the April of 2008 it has been schedule five AO nights for the GLAS system characterization. Due to some technical problems the only nights available of MASS-DIMM data are; the 21<sup>st</sup>, 22<sup>nd</sup> and the 23<sup>rd</sup>. The 21<sup>st</sup> starts with a variable seeing

and some technical problems, those force to stop the AO observations and to switch to another non-AO instrument. Also the 23rd the AO instrument was switched to another instrument due to a poor seeing conditions. The best full night is the 22<sup>nd</sup> with a good example of turbulence changes. The figure D.18 show the temporal evolution of the  $C_n^2$  during the nights 22<sup>nd</sup>, 23<sup>rd</sup>, 24<sup>th</sup>, and 25<sup>th</sup> where two different turbulent scenarios has showed; a calm and turbulent nights. The strength of the turbulence is shown by the vertical thickness of the plot, and the height of the different layers is plotted on the y axis

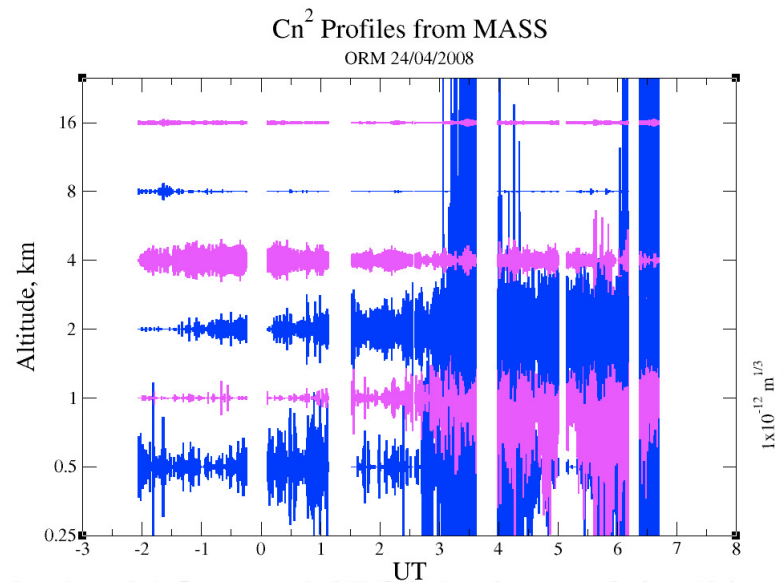


(a)  $C_n^2$  profiles for the 22nd

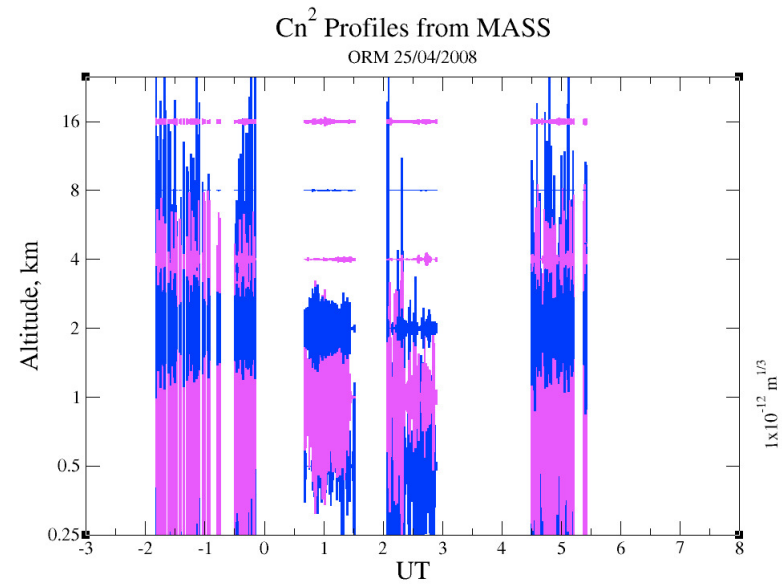


(b)  $C_n^2$  profiles for the 23rd

Figure D.18: Post-processing profile from  $C_n^2$  data. The temporal evolution of the strength of the during the four days is very well identified, passing from very stable night 22<sup>nd</sup> to a very turbulent night 24<sup>th</sup> and 25<sup>th</sup>, the 23<sup>rd</sup> is identified that the ground layer is starting to be turbulent. The vertical bars at each altitude represents the magnitude of the refractive index structure constant integrated over that layer.



(a)  $C_n^2$  profiles for the 24th



(b)  $C_n^2$  profiles for the 25th

Figure D.19: Post-processing profile from  $C_n^2$  data. The temporal evolution of the strength of the during the four days is very well identified, passing from very stable night 22<sup>nd</sup> to a very turbulent night 24<sup>th</sup> and 25<sup>th</sup>, the 23<sup>rd</sup> is identified that the ground layer is starting to be turbulent. The vertical bars at each altitude represents the magnitude of the refractive index structure constant integrated over that layer.

We can see that during those four nights the atmospheric conditions have changed and the AO performance has been influenced by that. The total seeing measured by the DIMM channel and the integrated free seeing measured by the MASS channel are shown in figure D.20 showing the temporal evolution for the mean values. The mean of the measurements is calculated for every 10 minutes of the raw data. From the figure D.20(below) it is clearly a better night conditions during the 22nd, with a total seeing below 0.8 and free seeing around 0.2 for the first half of the night. The low free atmosphere seeing suggest a very stable upper atmosphere, which can be seen in a large isoplanatic angle and coherence time. Figure D.21 shows the isoplanatic angle and the coherence time for the same run period with a 10 minutes mean. Table D.1 summarises the statistics result of the astroclimate parameters retrieved from the MASS measurements during three nights.

day	$\tau(ms)$	$\theta(arcsec)$	F. seeing(arcsec)
22-04-2008	$7.68 \pm 2.26$	$2.77 \pm 0.52$	$0.26 \pm 0.090$
23-04-2008	$8.2 \pm 2.19$	$2.41 \pm 0.46$	$0.58 \pm 0.249$
24-04-2008	$2.94 \pm 1.38$	$2.94 \pm 1.38$	$1.14 \pm 0.99$

Table D.1: Statistics summary for the free seeing, isoplanatic angle and the coherence time of the MASS measurements during the GLAS nights of 22nd, 23rd and 24th on June 2008.

It can be seen in the set of figures D.19 that the atmosphere conditions had been changing during those three days and considering the best AO performances was during the night of the 22<sup>nd</sup>. The table D.2(below) summarises the performances taking the seeing before and after the atmosphere correction by GLAS system, and including the MASS information about the contribution of the turbulence layers. The height slabs measured by the MASS channel are reduced to the boundary and free atmosphere. The boundary atmosphere merges the three height slabs which are; the 0.5, 1 and 2 km. The free atmosphere merges the layers from 2 to 16 km (4,8 and 16). The laser is focused at 15 km with the deformable mirror conjugated to the ground, the expected performance has to be good when the atmosphere turbulence is ground predominant. The Figure D.22(below) shows a corrected image of a 10th

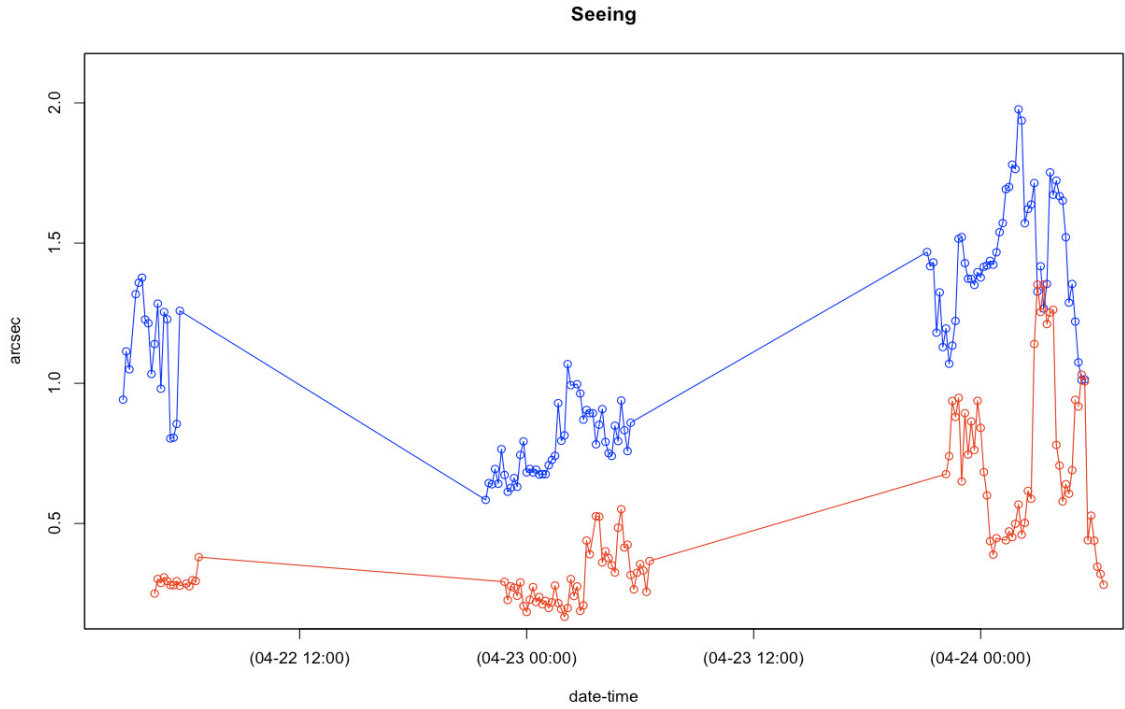


Figure D.20: Statistical 10 minutes median seeing and free seeing during the GLAS observing nights. The x-axe shows the time the data are available from 21-04-08 at 2:47:48. showing different evolution patterns Blue lines shows the total seeing measured with the DIMM channel and the red lines shows the Free seeing computed from the  $C_n^2$  profiles with the altitude from 0.5 km to 16 km.

magnitude star observing with the LGS and INGRID camera as scientific imager. The corrections were done when the total seeing was about 0.8 and a free seeing of about 0.25 and it is shown in the table D.2. The predominant turbulence is registered in the upper atmosphere.

Focusing the analysis on the night of the 22<sup>nd</sup>, which has shown a change in the atmosphere turbulence distribution in the spatial and temporal scales, the figure D.23 show the distribution of the atmosphere turbulence parameter  $C_n^2$  by its percentage of contribution to the total. The variation of the percentage of boundary and free atmosphere to the total turbulence can be also seeing in the temporal evolution of the total and free seeing. See figure D.24. The summary of the median value for the boundary and free seeing during the night of the 22<sup>nd</sup> is showed in the table D.3

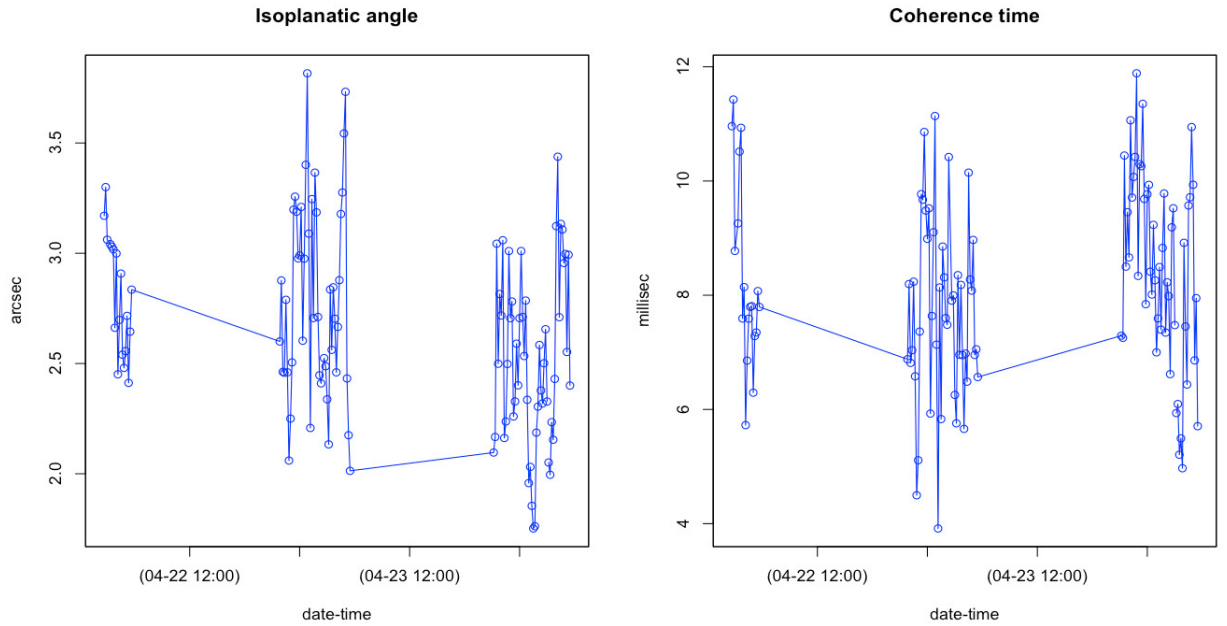


Figure D.21: Statistical of 10 minutes median values per the isoplanatic angle and coherence time ( $\tau$ ) evolution during the GLAS run.

Day	DIMM	INGRID		MASS		
		Open	Close	Layer	F.see	Isop
21	0.8-1.6	1.1	0.4	NA	NA	NA
21		0.9	0.5	NA	NA	NA
21		0.8	0.4	NA	NA	NA
22	0.85	0.7	0.18	Upper	0.25	3.2
22	0.9	0.6	0.28	Upper	0.25	3.0
22	0.8	0.4	0.34	Upper	0.20	3.0
22	1.3	0.6	0.48	Upper	0.35	3.5
22	1.3	0.7	0.7	Boundary - upper	0.4	2.0
22	1.2	0.9	0.44	Boundary	0.4	3.0
23	1.5	1.0	0.6	Boundary	NA	NA

Table D.2: Resume of the observations logs getting the seeing measured with the instrument INGRID at open and close loop.

where a 10 minutes median value are shown.

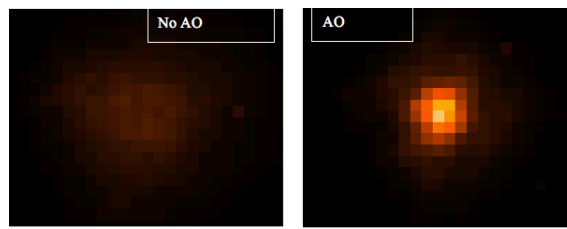


Figure D.22: Shows a 10th magnitude star observed with NAOMI+GLAS+INGRID, the seeing measured by the Robodimm was 0.8 arcsec and the corrections brings this down to 0.2 arcsec. Pixel scale: 0.04 arcsec/pixel.

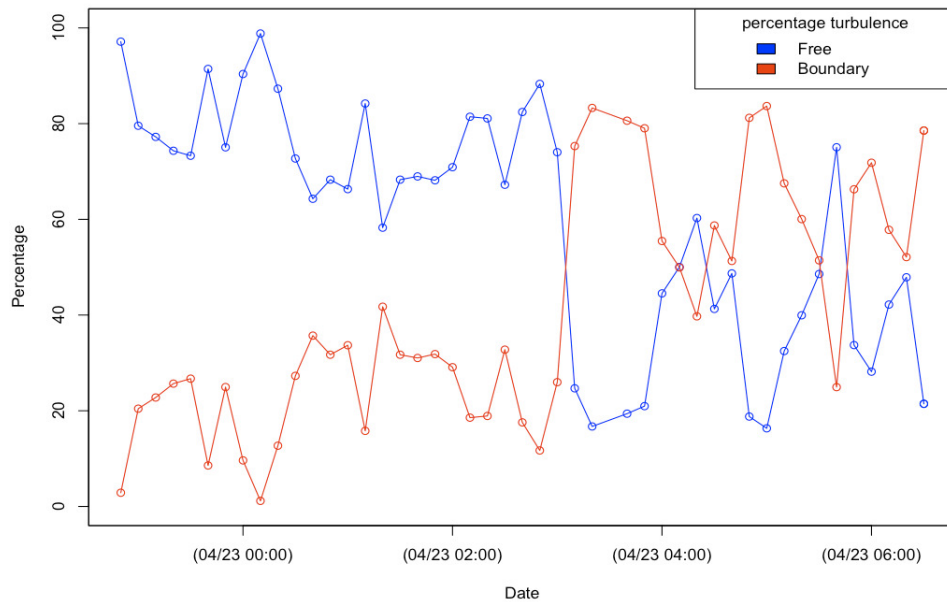


Figure D.23: Percentage of the vertical distribution of the  $C_n^2$ .

Time	Boundary	Free
22:50:00	2.87	97.13
23:00:00	20.44	79.56
23:10:00	22.77	77.23
23:20:00	25.67	74.33
23:30:00	26.71	73.29
23:40:00	8.57	91.43

Time (cont.)	Boundary (cont.)	Free (cont.)
23:50:00	24.95	75.05
00:00:00	9.63	90.37
00:10:00	1.17	98.83
00:20:00	12.70	87.30
00:30:00	27.29	72.71
00:40:00	35.70	64.30
00:50:00	31.71	68.29
01:00:00	33.69	66.31
01:10:00	15.80	84.20
01:20:00	41.74	58.26
01:30:00	31.71	68.29
01:40:00	31.03	68.97
01:50:00	31.84	68.16
02:00:00	29.10	70.90
02:10:00	18.56	81.44
02:20:00	18.91	81.09
02:30:00	32.77	67.23
02:40:00	17.57	82.43
02:50:00	11.70	88.30
03:00:00	25.97	74.03
03:10:00	75.31	24.69
03:20:00	83.28	16.72
03:40:00	80.61	19.39
03:50:00	79.03	20.97
04:00:00	55.47	44.53
04:10:00	49.95	50.05
04:20:00	39.73	60.27
04:30:00	58.72	41.28
04:40:00	51.30	48.70
04:50:00	81.21	18.79

Time (cont.)	Boundary (cont.)	Free (cont.)
05:00:00	83.67	16.33
05:10:00	67.52	32.48
05:20:00	60.05	39.95
05:30:00	51.43	48.57
05:40:00	24.94	75.06
05:50:00	66.28	33.72
06:00:00	71.83	28.17
06:10:00	57.81	42.19
06:20:00	52.11	47.89
06:30:00	78.55	21.45
06:30:00	78.55	21.45

Table D.3: Statistics of the percentage distribution of the boundary and free turbulence over the total turbulence measured by the MASS-DIMM instrument. The time series is averaged every 10 minutes.

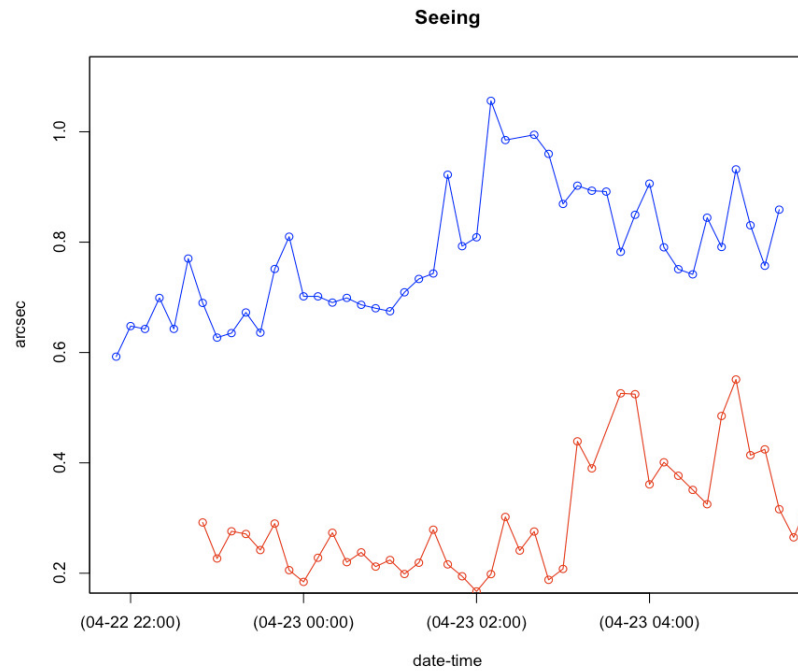


Figure D.24: Statistical variation of the free atmosphere seeing and the total seeing. Every point represents a 10 minutes median value. Blue line is the total seeing and red line is the free atmosphere seeing (from 0.5 to 16km).

The MASS-DIMM instrument as it has been described can give other interesting AO parameters that can be useful to analyse the performance of an AO system and in this case a LGS system. The isoplanatic angle and the coherence time for the night 22<sup>nd</sup> on April is shown in the figure D.25.

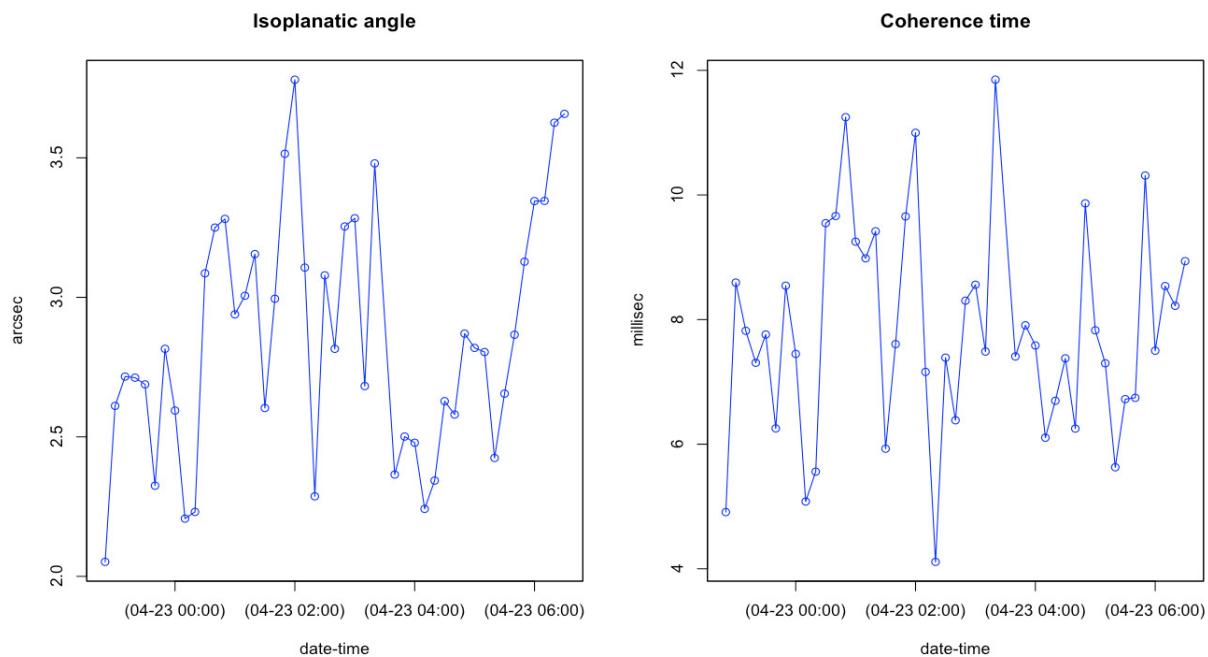


Figure D.25: Statistical values per 10 minutes median for the isoplanatic angle and time coherence parameters during the NAOMI+GLAS run (22nd on April 2008).

#### D.4.2 Conclusion of MASS-DIMM and GLAS experience

The MASS-DIMM instrument has shown its importance during the Rayleigh laser nights giving information about the sky conditions and helping to understand better how the LGS system works. The Rayleigh laser didn't give the expected power, which was low and stable between 8 to 12 watts. But considering this technical disadvantage the performances of the GLAS/NAOMI system was good giving a factor of corrections of about two from the natural seeing (open loop) to corrected seeing (closed loop) when the predominant turbulence was concentrated in the boundary layers. Having a total seeing of 1.2 and a free seeing of 0.9, the correcting system can give a corrected image with a FWHM of 0.44 in H band; this is a good performance of the system designed to correct the fast evolution of the turbulence at the ground. Also it is seen that when the upper turbulence is predominant with a total seeing of 0.6 and a free seeing of 0.25 the system can reach a PSF not much greater than the diffraction limit.

The MASS-DIMM instrument gives real time information about the atmosphere

turbulence conditions; this information can be relevant or not, but when we consider a scenario where the seeing in open loop is about 0.7 and the corrected FWHM is 0.7, which means that the system is not correcting, many questions arise and it is in this kind of scenario where the MASS-DIMM instrument can give an important clue. This was the case during the night on 22nd when the seeing started to change and there was a period where the atmosphere turbulence was distributed in the whole atmosphere, and there were not any predominant layers. It was in this scenario where GLAS/NAOMI could not get any correction at all. This is the kind of knowledge and experiences where the MASS-DIMM instrument can help to understand the LGS performances and it can help in the optimization of AO systems.

# Appendix E

## ZERNIKES POLYNOMIALS AND KARHUENEN-LOEVE FUNCTIONS. WAVEFRONT DEFORMATIONS

### E.1 ZERNIKES POLYNOMIALS.

Considering that the telescopes and most of the optical systems have a circular pupil, and it is, this geometry the interest to describe the wavefront on a circular pupil. The Zernikes polynomial are a group of orthogonal functions applied on a circular pupil with a radius one. These polynomials were introduced by F. Zernikes in 1934 and they are commonly used in the description of the wavefront aberrations where the low orders are like to the classical aberrations. Following the normalization of the polynomials done by Noll 1976, the Zernikes polynomials in polar coordinates  $(\rho, \theta)$  can be described as;

$$\begin{aligned}Z_{j, even} &= \sqrt{n+1}R_n^m(\rho)\sqrt{2}\cos(m\theta), \quad m \neq 0 \\Z_{j, odd} &= \sqrt{n+1}R_n^m(\rho)\sqrt{2}\sin(m\theta), \quad m \neq 0 \\Z_j &= \sqrt{n+1}R_n^0(\rho), \quad m = 0\end{aligned}$$

The radial part is described as;

$$R_n^m(\rho) = \sum_{s=0}^{(n-m)/2} \frac{(-1)^s (n-s)!}{s! [(n+m)/2 - s]! [(n-m)/2 - s]!} \cdot \rho^{m-2s} \quad (E.1.1)$$

The radial component goes from 0 to 1. The values of the parameters n and m are integers and to be fulfill the  $mn$  and  $m - |m| = \text{even}$ . The j index is the order of the modes and its a function of n and m. The modes with j even corresponds with symmetric modes and for j odd the modes are antisymmetrics. The first Zernikes modes are showed in the table E.1 and its graphical representation is showed in the figure E.2.

		Frequency (m)				
		0	1	2	3	4
Radial order (n)	0	$Z_1=1$ Piston				
	1		$Z_2 = 2\rho \cos \theta$ $Z_3 = 2\rho \sin \theta$ Tip-Tilt			
	2	$Z_4 = 3^{1/2}(2\rho^2 - 1)$ Defocus		$Z_5 = 6^{1/2}\rho^2 \sin 2\theta$ $Z_6 = 6^{1/2}\rho^2 \cos 2\theta$ Astigmatism		
	3		$Z_7 = 8^{1/2}(3\rho^3 - 2\rho) \sin \theta$ $Z_8 = 8^{1/2}(3\rho^3 - 2\rho) \cos \theta$ Coma		$Z_9 = 8^{1/2}3\rho^3 \sin 3\theta$ $Z_{10} = 8^{1/2}3\rho^3 \cos 3\theta$ Coma curvature 0	
	4	$Z_{11} = 5^{1/2}(6\rho^4 - 6\rho^2 + 1)$ Spheric		$Z_{12} = 10^{1/2}(4\rho^4 - 3\rho^2) \cos 2\theta$ $Z_{13} = 10^{1/2}(4\rho^4 - 3\rho^2) \sin 2\theta$ Astigmatism 5 order		$Z_{14} = 10^{1/2}\rho^4 \cos 4\theta$ $Z_{15} = 10^{1/2}\rho^4 \sin 4\theta$

Figure E.1: Summary of the first 15th Zernikes polynomious in polar coordinates. The radial component  $\rho$  varies between 0 and 1.

The wavefront on a circular pupil of radius R can be described in the Zernikes polynomials as;

$$\phi(\rho, \theta) = \sum_{i=2}^{\infty} a_i Z_i(\rho, \theta) \quad (E.1.2)$$

where the first coefficient (piston) can be considered zero because doesnt affect to the image formation. The residual error after a correction of j polynomials can be represented as the residual variance of the wavefront on the pupil. This variance in the atmosphere studies was defined by Noll (1976) and its described as;

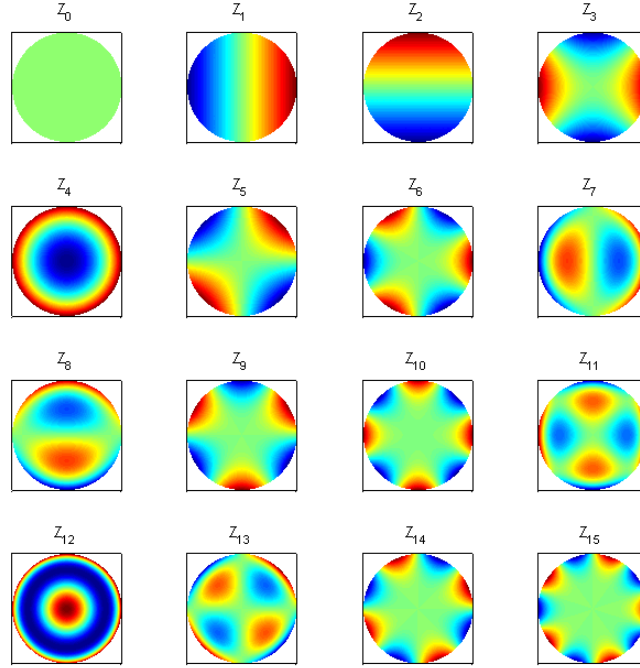


Figure E.2: Spatial representation of the Zernikes polynomial.

$$\Delta_j = \langle \phi^2(\vec{r}) \rangle = \sum_{i=j}^{\infty} \text{coef}(j) \left( \frac{D}{r_0} \right)^{5/3} \quad (\text{E.1.3})$$

where  $\text{coef}(j)$  is the coefficient for  $j$  corrected polynomials,  $D$  is the telescope diameter and  $r_0$  is the Fried parameter. The table E.1 shows the values predicted by Noll for the variance as function of the correction.

If we normalize the factor  $(D/r_0) = 1$  and studding the variance of  $j$ -esimo mode, that  $\sigma_j^2 - \sigma_{j-1}^2$ , the first 10 modes corrected the residual errors is 0.04, thats mean, that the 96% of the total wavefront aberrations is concentrated in the first 10 modes. This can be summarize in the table refvarianceKL

## E.2 Karhunen-Love fuctions.

For the atmospheric turbulence the Zernike polynomials are not the most optimal base, because it was seen that the covariance matrix is not diagonal. This means that

Index of the last corrected mode	Residual variance $\Delta_j rad^2$
1	$1.0299(D/r_0)^{5/3}$
2	$0.582(D/r_0)^{5/3}$
3	$0.134(D/r_0)^{5/3}$
4	$0.111(D/r_0)^{5/3}$
5	$0.088(D/r_0)^{5/3}$
6	$0.0648(D/r_0)^{5/3}$
7	$0.0587(D/r_0)^{5/3}$
8	$0.0525(D/r_0)^{5/3}$
9	$0.0463(D/r_0)^{5/3}$
10	$0.0401(D/r_0)^{5/3}$

Table E.1: Residual variance of a wavefront after the corrections of the  $j$  first Zernikes polynomials for the atmosphere case.

j	1	2	3	4	5	6	7	8	9	10
	0.44	0.02	0.02	0.02	0.02	0.006	0.006	0.006	0.006	

Table E.2: Variance of the  $\sigma_j^2 - \sigma_{j-1}^2$  for the modes  $j$ -esimo. The fist mode piston is not considered.

the Zernike coefficients are statistically dependent and therefore are not orthogonal polynomials. K-L functions are a basis of polynomials with diagonal covariance matrix, whose calculation for the atmospheric turbulence was developed by Fried (Fried, 1978).

In a manner similar to how the Zernike polynomials are defined, The K-L bi-dimensional functions are defined as the product of a radial component and a polar function;

$$K_i(\rho, \theta) = S_p^q(\rho)\Theta^q(\theta) \quad (\text{E.2.4})$$

where the polar functions are similar to those in Zernikes polynomials. The index  $p$  is the radial and  $q$  represents the frequencies. This type of functions represent many advantages for the Kolmogorov turbulence representation, in fact, this

function can represents the turbulence and it is statistically independent.

The radial components can be expressed as; (Dai, 1994)

$$\int_0^1 Y_q(\rho, \rho') S_p^q d\rho = \langle \alpha_i^2 \rangle S_p^q(\rho') \quad (\text{E.2.5})$$

where  $\langle \alpha_i^2 \rangle$  is the normalized variance of the K-L coefficients,  $Y_q(\rho, \rho')$  is the q-esima kernel function for the normalized wave function. A solution of the equation E.2.4 was done by Dai using a least square fitting;

$$S_p^q \rho = \rho^q \sum_{s=0}^{\infty} g_s \rho^{2s} \quad (\text{E.2.6})$$

where  $g_s$  are g-esimo coefficients. This equation can be represented as;

$$S_p^q = \left\{ \begin{array}{ll} \rho^q \sum_{s=0}^M (-1)^{s+p+1} g_s \rho^{2s} & q \neq 0 \\ \sum_{s=0}^M (-1)^{s+p} g_s \rho^{2s} & q = 0 \end{array} \right\} \quad (\text{E.2.7})$$

Using this expression the coefficient are always positive.

A result of the K-L polynomial adjusted using the Singular Value Decomposition (SVD) for the first 21 modes of the K-L is showed in the table E.3 (Dai,1995)

The K-L functions gives a better information of the wavefront for number of modes and also gives a better minimizations of the wavefront aberrations than the Zernikes polynomials. Figure E.3 shows the Zernikes polynomial, K-L functions and a zonal corrections for a wavefront, given a better results for the K-L functions.

## E.3 THE MODAL AND ZONAL RECONSTRUCTORS.

There are two methods used by the wavefront sensor to reconstruct the wavefront: MODAL and ZONAL reconstructors.

### E.3.1 Zonal reconstructor.

The wavefront phase is represented by its value in an independent matrix of sub-apertures or zones distributed in the telescope aperture which coincide with the

i	p	q	g0	g1	g2	g3	g4	g5	g6	g7
2,3	1	1	1.55446	0.24434	0.04385					
4	1	0	2.15576	6.45447	4.12302	1.36543	0.21918	0.03205		
5,6	1	2	3.22726	2.74883	1.02448	0.1758	0.02689			
7,8	1	3	6.05553	8.18948	4.59945	1.32543	0.21393			
9,10	2	1	6.52874	19.11418	17.92194	8.66138	2.32351	0.35262		
11,12	1	4	10.72881	9.05265	14.21464	5.77876	1.36987	0.12793		
13	2	0	3.1888	32.76501	85.09094	97.4123	62.7581	24.97385	6.18314	0.71581
14,15	2	2	16.38248	5	6.72672	73.05406	50.1898	20.788	5.28535	0.62336
16,17	1	5	18.30503	39.48987	36.31838	18.55142	5.49183	0.71997		
18,19	2	3	36.40221	1	141.52391	215.99768	173.6211	76.34609	14.95592	
20,21	3	1	14.09872	111.14654	291.50516	375.1872	274.52527	113.87555	21.43536	

Table E.3: K-L coefficients for the first 21 first radial modes.

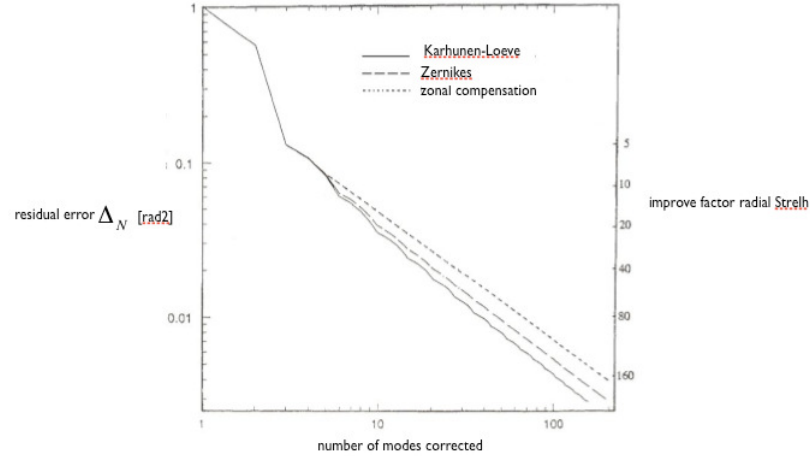


Figure E.3: Relationship of the normalized residual error ( $D = r_0$ ) for the Zernikes polynomial and K-L functions. Credit. (Dai, 1996)

actuators position in the deformable mirror. Most of the systems working with this technique work in the telescope pupil plane. If the wavefront arriving to the telescope is divided in  $N$ -sub-apertures distributed in the telescope aperture and the phase of each sub-aperture is expressed with a number, the total wavefront is characterized by the  $N$ -sub-apertures. In fact, the wavefront is better characterized with a large number of  $N$ . But  $N$  is a finite number and each subaperture has to be characterized by the piston to compensate the phase and the tip-tilt of the wavefront, then it is needed three actuators for each zone or sub-aperture of the deformable mirror. The matrix which relate the measurements of the wavefront sensor ( $S$ ) and the distorted phase ( $\phi$ ) is represented as;

$$S = A \cdot \phi \quad (\text{E.3.8})$$

where  $A$  is the Interaction matrix.

### E.3.2 Modal reconstructor.

The wavefront is expressed with the polynomial terms  $F_i(r)$ , which are orthogonal and normalized to the circular pupil.

$$\int d^2r W(r) F_i(r) F_j(r) = \delta_{ij} \quad (\text{E.3.9})$$

where  $\delta_{ij}$  is the Kronecker delta and  $W(r)$  is the weight function for the pupil defined as;

$$W(r) = \begin{cases} \frac{1}{\pi(1-r)^2} & |r| < 1 \\ 0 & |r| > 1 \end{cases} \quad (\text{E.3.10})$$

The reconstructor method retrieve a coefficient vector  $\phi = \phi_i$  so that the phase of the wavefront can be reconstructed at any point of the pupil as;

$$\phi(r) = \sum_{i=1}^N a_i F_i(r) \quad (\text{E.3.11})$$

where  $N$  is the number of modes used in the polynomial base. There are two polynomials bases to characterize the turbulence of the atmosphere, on hand the Zernikes polynomials (Noll, 1976) which represents very well the turbulence on a circular aperture and the Karhunen-Loeve in an annular aperture (Wang and Markey, 1978) which is the case of a telescope aperture with the secondary mirror obscuration.

Combining the equation E.3.9 (orthogonality of the function  $F_i(r)$ ) and the equation E.3.11 the coefficients  $a_i$  can be calculated as;

$$a_i = \int d^2r W(r) \phi(r) F_i(r) \quad (\text{E.3.12})$$

The variance of the phase of the waqvefront on the telescope aperture can be retrieved as;

$$\sigma_\phi^2 + \int d^2r W(r) \langle \phi(r)^2 \rangle = \sum_{ij} \langle a_i a_j \rangle \int d^2r W(r) F_i(r) F_j(r) = \sum_i \langle a_i \rangle^2 \quad (\text{E.3.13})$$

where  $\langle a_i a_j \rangle$  are the elements of the covariance modal matrix  $V \cong \langle a_i a_j \rangle$ , whose diagonal coefficients are the modes variance and describes its contribution to the atmosphere turbulence. Considering the piston mode ( $i=1$ ) which is a contant amount  $\langle a a^t \rangle$  is infinite and as only is interested the deviation respect to the median, this term can be exclude of the serie of reconstructed modes, then  $i=2,3,4,..$

# Bibliography

- [Abahamid et al, 2004] Abahamid, A. et al., "Seeing, outer scale of optical turbulence and coherence outer scale at different astronomical sites using instruments on meteorological balloons". *Astronomy and Astrophysics*, 422, pp.1123-1127, 2004.
- [Adelaman,1977] Adelman, N.T. "Spherical Mirror with Piezoelectrically Controlled Curvature". *Appl. Opt.* 16, pp3075, 1977.
- [Allen et al, 1987] Allen, J. G., Vankevics, A., Wormell, D., and Schmutz, L., "Digital wavefront sensor for adaptive imaging in astronomy", *Nature* 328,(6127), pp.229-231,1987.
- [Andrew et al, 2005] Andrews, L.C. and Phillips, R.L., *Laser Beam propagation through Random Media* (2nd Edition), SPIE Optical Engineering Press, 2005.
- [Angel, 1994] Angel, J.R., *Nature* 368, 203, 1994.
- [Ayra, 2001] Ayra, S. P., *Introduction to Micrometeorology*. Kluwer Academic Press, 307 pp., 2001.
- [Azouit and Vernin 1980] Azouit M. and Vernin J., *J. Atmos. Sci.* 37, 1550,1980.
- [Babcock, 1953] Babcock, H, W., "The Possibility of Compensating Astronomical Seeing". *PASP*, 65, October 1953.
- [Babcock, 1958] Babcock, H, W., "Deformable Optical Elements With Feedback". *JOSA*, Vol. 48, Issue 7, pp. 500-500, 1958.
- [Beckers et al. 1993] Beckers, J.M. *Annual Rev. Ast. Astroph.* 31, 13, 1993.

- [Beland, 1993] Beland, R. "Atmospheric Propagation of Radiation", Vol2, SPIE Optical and Engineering Press, 1993
- [Beyrich, 1997] Beyrich, F., "Mixing Height Estimation from SODAR Data - a Critical Discussion". Atmos. Environ., 31, pp. 3941-3953, 1997.
- [Bonaccini et al. 1991] Bonaccini, D. et al. "Adaptive Optics wavefront corrector using addressable liquid crystals retarders II". SPIE Proceeding 1543, pp133-143, 1991.
- [Borgnino, 1990] Borgnino, J. Applied. Optics., 29, pp1863. 1990.
- [Born and Wolf, 1993] Born, M. and Wolf E. , Principle of Optics. Pergamon Press. Oxford, 1993.
- [Boyer et al., 1990] Boyer, C., Michau V., Rousset G., "Adaptive optics: interaction matrix measurements and real-time control algorithms for the Come-on project", SPIE Proceeding 1237, pp. 406-421, 1990.
- [Boyer et al., 1991] Boyer, C. and Gaffard, J. "Adaptive optics, transfer loops modeling". SPIE Proceeding 1542, pp46-61, 1991.
- [Buffton et al, 1972] Buffton, J.I, Minott, P.O. J.Opt.Soc.Am.62,1068, 1972.
- [Butterley et al, 2006] Butterley et al . "Determination of the profile of atmospheric optical turbulence strength from SLODAR data". Mon. Not. R. Astron. Soc. 369, pp.835-845, 2006
- [Businger, et al. 2002] Businger, S. R. et al. "Starcasting". Bull. Amer. Meteor. Soc., 83. 858-871, 2002.
- [Businger et al, 2003] Businger, S., Cherubini, T., et al., "Supporting the Missions of Mauna Kea Observatories with GroundWinds Incoherent UV LIDAR Measurements", SPIE Proceedings Vol. 4839, pp. 858-868, 2003.
- [Carrasco et al, 2003] Carrasco, E. et al . "High altitude wind velocity at San Pedro Martir and Manua Kea". RevMexAA, 19, pp.103-106, 2003.

- [Chapman et al ,1997] Chapman, D. and Browning, K. A., "Radar observations of wind-shear splitting within evolving atmospheric Kelvin-Helmholtz billows." Quart. J. Roy. Meteor. Soc., 123, pp1433-1439, 1997
- [Chauvin et al, 2004] Chauvin, G. et al. "A Giant Planet candidate near a young brown dwarf, Direct VLT/NACO observations using IR wavefront sensing". A.A. 425, pp.29-32, 2004.
- [Cherubini et al, 2008] Cherubini,T. "Modeling optical turbulence and seeing over Mauna Kea". J. Appl. Meteor. Climatol., 47, pp.1140-1155, 2008.
- [Cho and Petersen, 1989] Cho,K.H. and Petersen, D.P. "Optimal observations apertures for a turbulence distorted wave-front". J.Opt.Soc.Am. 6, pp.1767-1775, 1989.
- [Chueca et al, 2004] Chueca, S. et al. "Statistical and analysis of high-altitude wind above the Canary Islands Observatory", Mon.Not. Astron. soc., 349,pp.627-631, 2004.
- [Chun et al, 2009] Chun, M, et al, "Mauna Kea Ground-Layer Characterization Campaign", Monthly Notices of the Royal Astronomical Society, 394, pp. 1121-1130. 2009.
- [Clafkin and Bereket, 1986] Clafkin, E.S. and Bereket, N. "Configuring an electrostatic membrane mirror by least-square fitting with analytical derived influence function". J.Opt. Soc.Am, 3, pp.1883-1839, 1986.
- [Clampin et al. 1991] Clampin, M. et al. "The John Hopskin adaptive optics coronagraph". SPIE Proceeding 1542, pp165-174, 1991.
- [Cleveland, 1979] Cleveland, W.S. "Robust Locally Weighted Regression and Smoothing Scatterplots," Journal of the American Statistical Association, Vol. 74, pp.829-836, 1979.
- [Clifford et al,1978] Clifford, S.F. et al. "The Classical Theory of Wave Propagation in a Turbulent Medium: Chapter 2 of Laser Beam Propagation in the Atmosphere." J.W. Strohbehn ed., Springer-Verlag. Berlin, 1978

- [Coles et al, 2001] Coles, D. et al. "An Introduction to Statistical Modelling of Extreme Values". London: Springer, 2001.
- [Coulman et al, 1986] Coulman, C. E. ,et al., "The Observation, Calculations and Possible Forecasting of Astronomical Seeing", PASP, 98, pp. 376-387, 1986.
- [Coulman, 1995] Coulman, C.E, et al., "Optical seeing-mechanism of formation of thin turbulent laminae in the atmosphere". Atmos. Ocean., 34, pp. 5461-5474, 1995.
- [Davis et al, 2000] Davis, R. et al. "The ALFA laser Guide Star: Operations and Results". Experimental Astronomy. 2000.
- [Dewan et al, 1993] Dewan, E. M. Good, R. E., Beland, B. and Brown, J. " A Model for  $C_n^2$  (Optical Turbulence) Profiles using Radiosonde Data." Phillips Laboratory Technical Report, PL-TR-93-2043., ADA 279399, 1993.
- [Dewan et al, 1994] Dewan, E. M., "The saturated-cascade model for atmospheric gravity wave spectra, and the wavelengthperiod (W-P) relations". Geophys. Res. Lett., 21, pp. 817-820, 1994.
- [Dunn, 1987] Dunn R.B., LEST Proceeding workshop on adaptive optics in solar observations (F. Merkle, O. Engvold y R. Falomo eds.) LEST Tech. Rep. 28, pp. 87, 1987.
- [Dunn, 1989] Dunn R.B., Bulletin. Am. Astron. Soc. 21, pp. 847, 1989.
- [Dunn, 1990] Dunn R.B. SPIE Proceeding, 1271, pp.216, 1990.
- [Durance and Clampin, 1989] Durance, S. and Clampin, M. SPIE Proceeding 1114, pp97, 1989.
- [Edgar et al, 2008] Edgar, R.G. et al. "Beyond conventional G-SCIDAR, the Ground-Layer in high vertical resolution", SPIE proceeding 6272, pp. 56-59, 2006.
- [Egner et al, 2007] Egner, S. E., Masciadri, E., and McKenna, D., "Generalized SCIDAR Measurements at Mount Graham", PASP 119, pp.669-686, 2007.

- [Ellerbroek, et al 1997] Ellerbroek, B.L., et al. "Including outer scale in zonal adaptive optics calculations", *Appl. Opt.*, 36, pp. 9456-9467, 1997.
- [Els et al, 2008] Els, S. et al. "The ground layer turbulence observed by MASS-DIMM during the TMT site testing and its relation to meteorological parameters". *Meeting Astronomy meets Meteorology*, pp.224-231, 2008.
- [Esposito et al, 2010] Esposito, S, et al. "Laboratory characterization and performance of the high-order adaptive optics system for the Large Binocular Telescope", *Ap. Optics* , Vol. 49, No. 31, 2010.
- [Fiorino,2005b] Fiorino, S.T. Class lecture notes, METG 611, Atmospheric and Space Environmental Effects on Electromagnetic Propagation, School of Engineering and Management, AirForce Institute of Technology, Wright-Patterson AFB OH, Spring Quarter 2005.
- [Foken, 2006] Foken, T. " 50 years of Monin-Obuckov similarity theory". *Boundary-layer Meteorology*, 119, pp.431-447, 2006.
- [Forbes, 1989] Forbes, F. "Bimorph pzt active mirror in Active telescope system". *SPIE Proceeding*, 1114, pp.146-161, 1989.
- [Forbes and Roddier, 1991] Forbes, F., Roddier, N. *SPIE Proceeding* 1542, pp.140-47, 1991.
- [Fried, 1965] Fried D.L., *J. Opt. Soc. Am.* 55, pp.1427, 1965.
- [Fried, 1967] Fried, D.L., *IEEE Proceeding*, Volume 55, pp. 57-67, 1967.
- [Fried, 1982] Fried D.L., "Anisoplanatism in adaptive optics", *J. Opt. Soc. Amer. A.*, 72, pp. 52-61, 1982.
- [Fuchs et al, 1998] Fuchs, A. et al "Focusing on a Turbulent Layer: Principle of the Generalized-SCIDAR" , *Astronomical Society of the Pacific*, 110, pp.86-91, 1998
- [Fugate et al, 1991] Fugate, R. Q., Fried, D. L., Ameer, G. A., Boeke, B . R., Browne, S. L., et al., *Nature* 353, pp. 144-146, 1991.

- [Fuensalida et al, 2004] Fuensalida, J., et al. "Cute-SCIDAR: An Automatically Controlled SCIDAR Instrument for the Jacobus Kapteyn Telescope", ING Newsl., 8, p15. 2004.
- [Fuensalida et al, 2004] Fuensalida, J., et al. "Turbulence profiles in the observatories of the Canary Islands: Preliminary statistics for Adaptive Optics". Proc. SPIE, Vol. 5382, pp.619, 2004.
- [Fugate et al. 1991] Fugate, R.Q. et al. NATURE 353, pp144, 1991.
- [Fusco et al, 2006] Fusco, T. et al. SPIE Proceeding 4007, pp.1044, 2006.
- [Gaffard and Boycr, 1989] Gaffard, J.P., Boycr, C., SPIE Proceeding, 1114, pp. 105-119, 1987
- [Gaffard and Ledanois 1991] Gaffard, J.P., Ledanois, G. "Adaptive Optics transfer function modeling". SPIE Proceeding 1542, pp.34-45, 1991.
- [Garcia-Lorenzo et al. 2005] Garcia-Lorenzo, B, et al. "Astronomical site ranking based on tropospheric wind statistics." Monthly Notices of the Royal Astronomical Society. Volume 356, Issue 3, pp. 849-858, 2005.
- [Garder et al 1990] Gardner, C. S. Welsh, B. M., Thompson, L. A. "Design and performance analysis of adaptive optical telescopes using laser guide stars", IEEE Proceeding., Vol. 78, No. 11, pp. 1721-1743, 1990.
- [Gendron, 1993] Gendron, J., "Modal control optimization in an adaptive optics system: in Active and Adaptive Optics". ICO 16 Satellite Conference. ESO Conference Proceeding 48, pp. 87-92, 1993.
- [Genzel et al, 2003] Genzel, R., et al. Ap. J 594, pp812, 2003.
- [Gibbard et al, 2005] Gibbard, I. de Pater, H. B. Hammel, "Near-infrared adaptive optics imaging of the satellites and individual rings of Uranus", Icarus 174, pp. 253, 2005.
- [Gilbert et al, 2006] Gilbert, M., et al. Phys. Rev. Lett. 96, 084501, 2006.

- [Gillelan et al, 2006] Gillelan, et al. "Analyzing seasonal to interannual extreme weather and climate variability with the extremes toolkit (extremes)", 18th Conference on climate Variability and Change, 86th AMS, P 2.15, 2006.
- [Glindemann et al, 1997] Glindemann, A., et al. "Relevant parameter for relevant Tip/Tilt systems on Large Telescopes" ,.PASP 109, pp.682-687, 1997.
- [Goad et al, 1986] Goad, L., Roddier, L., Backers, J., e Eisenhardt, P. "National Optical Astronomy Observatories (NOAO) IR adaptive optics program III: criteria for the wavefront selection". Proc. Soc. Photo-Opt. Instrum. Eng., 628, pp.305-313., 1986.
- [Good et al, 1988] Good R.E. et al. "Atmosphere Model of Optical Turbulence". SPIE Proceeding, 928, p165-186, 1988.
- [Graves et al, 1991] Graves, J.E. and Mckenna, D.L. SPIE Proceeding 1542, pp. 262, 1991.
- [Grosso and Yellin, 1977] Grosso, R.P. and Yellin, M. " The membrane mirror an adaptive optical elements". JOSA 67, issue 3, pp. 399-406, 1977.
- [Hammel, de Pater, 2004] Hammel, H.B., dePater, I. ,2004.
- [Hardy, 1977] Hardy P. et al. JOSA. 67, pp.360, 1977.
- [Hardy, 1978] Hardy, J. W. IEEE Proceeding. 66: 65 pp.1-97, 1978.
- [Hardy, 1982] Hardy, J. W. SPIE Proceeding. 332, pp. 252-259, 1982
- [Hardy et al, 1987] Hardy, P. and McGovern, A.J. SPIE Proceeding 816, pp. 180, 1987.
- [Hardy, 1998] Hardy, J. W. " Adaptive optics for astronomical telescopes", Oxford University Press, 1998.
- [Heffter, 1980] Heffter,. "Transport Layer Depth Calculations, Second Joint Conference on applications of Air pollutions Meteorology, New Orleans,1980.
- [Henault et al, 2009] Henault, F., et al. Opt. A, Pure Appl. Opt. 11 125503, 2009.

- [Herrman, 1980] Herman, N. J. "Least Square Wavefront error of minimum norm". J. Opt. Soc. Am. 70, 1, 1990.
- [Hipper et al 1999] Hipper S., et al. "The ALFA: Wavefront-sensing with Natural and LGS". Proceeding of the Canterbury Conference on Wavefront sensing and its applications. Canterbury, 1999.
- [Hogge and Butts, 1982] Hogge, C.B. and Butts, R. R. "Effects of using different wavelength in wavefront sensing and corrections". J. Opt. Soc. Am. 72, pp.60-66, 1982.
- [Hostrom, 1988] Hostrom U. "Non-dimensional wind and temperature profile in the atmosphere surface layer". Boundary-layer meteorology. 42, p55-78, 1988.
- [Hostrom, 1996] Hostrom U. "A review of some basic characteristics of the atmospheric surface layer". Boundary-layer Meteorology. 78, pp.215-246, 1996.
- [Hudgin, et al, 1977] Hudgin, R.H., "Wavefront reconstruction for compensated imaging". J Opt. Soc. am. 67, pp 374-378, 1977.
- [Hufnagel, 1974] Hufnagel, R. E. "Propagation through atmospheric turbulence", in The Infrared Handbook, Chap. 6, USGPO, Washington, D.C. 1974.
- [Hufnagel, 1978] Hufnagel, R.E. "Propagation through Atmospheric Turbulence," Chapter 6 of The Infrared Handbook, William L. Wolfe and George Zissis, Editors, 1978.
- [Hufnagel et al, 1993] Hufnagel et al. "Propagation Through Atmospheric Optical Turbulence," in The Infrared and Electro-Optical Systems Handbook, vol. 2, Chap. 2, F. G. Smith, Ed. Bellingham, WA: SPIE, 1993.
- [Ishimuru et al 1978] Ishimuru, A. et al. Wave Propagation and Scattering in Random Media, Vol 2: Multiple Scattering Turbulence, Rough surfaces and Remote Sensing. Academic Press, NY, 1978.
- [Jagourel, 1990a] Jagourel P., Madec P.Y. and Schaud M., "Adaptive optics: a bimorph mirror for wavefront correction". Proc. SPIE 1237, 394 1990a.

- [Karasawa et al, 1988] Karasawa, T., et al. "A new prediction method for tropospheric scintillation on Earth-space paths," *IEEE Trans. Antennas Propag.* 36, pp.1068-1614, 1988.
- [Kluckers et al, 1998] Kluckers, V.A., et al. "Profiling of atmospheric turbulence strength and velocity using a generalised SCIDAR technique", *Astron. Astrophys. Suppl. Ser.* 130, pp.141-155, 1998.
- [Kokorowski et al, 1979] Kokorosky, S.A. "Analysis of Adaptive optical elements from pzt bimorph". *J Opt. soc. Am.* 69, pp.180-187, 1979.
- [Kolopoulus 1980] Koliopoulos, C. L.. "Radial grating lateral shear heterodyne interferometer," *Appl. Opt.* 19, pp.1523-1528, 1980.
- [Kolmogorov, 1941] Kolmogorov, A. N. "The local structure of turbulence in incompressible viscous fluid for very large Reynolds numbers". *Proceedings of the USSR Academy of Sciences* 30, pp. 299-303. (Russian), translated into English by Kolmogorov, Andrey Nikolaevich (July 8 1991). "The local structure of turbulence in incompressible viscous fluid for very large Reynolds numbers". *Proceedings of the Royal Society of London, Series A: Mathematical and Physical Sciences* 434 (1890).
- [Kopeika et al, 1998] Kopeika, et al. "A system engineering Approach to Imaging", *SPIE Optical engineering Press*, Bellingham, WA, 1998.
- [Kornilov et al, 2002] Kornilov, V et al. "MASS: a monitor of the vertical turbulence distribution.", *SPIE Proceedings*, Volume 4839, pp. 837-845, 2003.
- [Kornilov et al, 2007] Kornilov, V. et al. . "Combined MASS-DIMM instruments for atmospheric turbulence studies", *Monthly Notices of the Royal Astronomical Society*, Volume: 382, Issue: 3, pp. 1268-1278, 2007.
- [Lascaux et al, 2009] Lascaux, F. et al., "Mesoscale optical turbulence simulations at Dome C". *MNRAS*, 398, 3, pp.1093-1104, 2009.

- [Law et al, 2006] Law N.H, et al. , "Lucky imaging: high angular resolution imaging in the visible from the ground". *Astronomy and Astrophysics*, Volume 446, Issue 2, pp.739-745, 2006.
- [Le Mingnant et al. 1999] Le Mingnant et al. ESO-OSA Topical Meeting on Astronomy with Adaptive Optics. *ESO Conference Proc.* 56, pp.287, 999.
- [Lawrence, 2003] Lawrence, J et al. "Exceptional astronomical seeing conditions above Dome C in Antarctica", *Nature, Letter to Nature*, vol431, 2004.
- [Liu et al 2008] Liu, M et al. "LGS AO science impact: present and future perspectives", *SPIE Proceeding.* , Vol. 7015, 701508, 2008.
- [Mahrt, 1999] Mahrt, L., "Stratified atmospheric boundary layer". *Bound.-Layer. Meteor.*, 90, pp. 375-396, 1999.
- [Mahrt, 2000] Mahrt, T. "Surface heterogeneity and vertical structure of the boundary layer". *Boundary Layer Journal*. Vol 96, Numbers 1-2, 2000.
- [Marais, 1991] Marais T., Michau V., Fertin G., Primot J. y Fontanella J.C., "Deconvolution from wavefront sensing on a 4 m telescope". *ESO Proceedings symposium on high resolution imaging by interferometry*. ESO, Garching bei Mnchen, Germany 39, 589, 1991.
- [Masciadri et al 1999a] Masciadri, E., et al. "3D mapping of optical turbulence using an atmospheric numerical model- I. A useful tool for the ground-based Astronomy". *AAS*, 137, p185-202, 1999.
- [Masciadri et al 1999b] Masciadri, E., et al. "3D mapping of optical turbulence using an atmospheric numerical model - II. First results at Cerro Paranal". *AAS*, 137, 203216, 1999.
- [Masciadri et al, 2006] Masciadri, E. and Egner, S. "First seasonal study of optical turbulence with an atmospheric model". *PASP*, 118, pp. 1604-1619, 2006.

- [McHugh et al, 2006] McHugh, J.P., Jumper, G. Y. Chun, M. "Balloon Thermosonde Measurements over Mauna Kea and Comparison with Seeing Measurements" ,PASP, vol.120, pp.1318-1324. 2008.
- [McInnes, 1973] McInnes, B. and Walker, M. F. "Astronomical Site Testing in the Canary Islands". PASP, Vol. 86, No. 512, p.529, 1974.
- [Merkle,1981] Merkle, F.K. "Development of an active optical mirror for astronomical applications". ESO Conference pp.41-44,1981.
- [Morris et al 2003] Morris, T., et al. "Rayleigh Laser Guide Star return to the WHT". Newsletter of the Isaac Newton Group of Telescopes, issue 7, pp. 18, 2003.
- [Myers et al 2003] Myers, R. M. et al. "The NAOMI Adaptive Optics System for the 4.2m William Herschel Telescope". SPIE Proceedings on Adaptive Optical System Technologies, 4839, pp. 647-658, 2003.
- [Morris et al 2010] Morris, T., et al. "CANARY: The NGS/LGS MOAO demonstrator for EAGLE", 1st AO4ELT conference, 08003, 2010.
- [Noll, 1975] Noll, R.J. "Zernike polynomials and atmospheric turbulence". J. Opt. Soc. Am, 66, Suppl 14-1, pp. 307-310, 1975.
- [Noll, 1975] Noll, R.J., "Zernikes polynomials and atmospheric turbulence", J.Opt. soc.Am. 66,207-211, 1976.
- [Nonin, 1971] Monin, A. S. and Yaglom, A.M. Statistical Fluid Mechanics. Mit Pr., ISBN-10:026213098X, 1971.
- [Osborn et al 2009] Osborn, J., et al. "Proceeding of Optical Turbulence Characteristics for Astronomical application", pp.371-378, 2009.
- [Parenti and Sasiela, 1994] Parenti, R. R. and Sasiela, R.J., "Laser-guide star system for astronomical application", JOSA A, Vol. 11, pp.288-309, 1994

- [Parlange, 1988] Parlange, M.B. and Brutsaerf, W. "Forest and surface shear stress under neutral conditions". *Boundary Layer Meteorology*, Vol48, pp.69-81, 1989.
- [Pike et al, 2011] Pike,H.A., Stotts,L.B.,Kolodz,D and Northcott, M. "Parameters Estimate for free Space Optical Communication". *Applications of Lasers for Sensing and Free Space Communications*, paper LWB3, 2011.
- [Poyneer et al 2004] Poyneer, L.A. and Macintosh, B. "Spatially filtered wave-front sensor for high-order adaptive optics". *J.Opt.Soc.Am.* 216, pp810-819 , 2004.
- [Racine, 1996] Racine, R., *PASP*,108, pp. 372, 1996.
- [Ragazzoni et al, 1996] Ragazzoni, R, et al. *J. Mod. Opt*, 43, pp. 289, 1996.
- [Ragazzoni et al, 2002] Ragazzoni, R, Diolaiti, E. Vernet,E. "A pyramid wavefront sensor with no dynamic modulation", *Optics Communications* 208 , pp5160, 2002.
- [Riccardi et al, 2004] Riccardi, A., et al. "The Adaptive secondary mirror for the LBT". *SPIE Proceeding*, 5490, 192, 2004
- [Richardson, 1922] Richardson, L.F. *Weather Prediction by Numerical Process*. Cambridge University Press, 1922.
- [Rigaut et al, 1997] Rigaut, R. et al. "Performance of the Canada-France-Hawaii Telescope Adaptive Optics Bonnette". *Astronomy and Astrophysics*, 1997.
- [Rigaut et al, 1998] Rigaut, F., et al. 1998, *PASP*, 110, 152, 1998.
- [Rodcap and Murphy, 1999] Roadcap, J. R. and Murphy, E. A. *Pure Appl. Geophys.*, 156, pp. 503, 1999.
- [Roddier, 1981] Roddier, R., "The effects of atmospheric turbulence in optical astronomy", *Prog. Opt.* XIX pp281-376, 1981.
- [Roddier et al, 1982] Roddier,F. Gilli,J.M and Vernin, J. *J.Opt*, 13 pp. 63, 1982.

- [Roddier et al, 1987] Roddier, F., Forbes, F., Shaklan, S., Pinches, C. See Merkle et al 1987, pp. 107-116, 1987.
- [Roddier, 1988] Roddier, F. Appl Opt. 27, 1223, 1988.
- [Roddier and Roddier, 1988] Roddier, F., Roddier, N. 1988, SPIE Proceeding., 976, 203, 1988.
- [Roddier, 1989] Roddier, N., Roddier, F. SPIE Proceeding, 1114, pp. 92-96, 1989.
- [Roddier, 1990] Roddier, F. "Atmospheric wavefront simulation using Zernike polynomials". Optical Engineering, 29, pp.1174-1180. 1990
- [Roddier, 1991] Roddier, F., Northcott, M.E., Graves, J. E.. "A simple low-order adaptive optics system for near-infrared applications". Pub. Astr. Soc. Pac., 103, pp. 131-149. 1991.
- [Roddier, 1991a] Roddier, F., Graves, J. E., McKenna, D., Northcott, SPIE Proceeding. 1, 542, pp. 248-253, 1991a
- [Roddier, 1991b] Roddier, F., Northcott, M., Graves, J. E., Proc. Astron. Soc. Pac. 103: 131-149, 1991b
- [Roddier, 1999] Roddier, F. "Adaptive Optics in Astronomy, Cambridge University Press, 1999.
- [Rogermann and Welsh, 1996] Roggemann, M. C. and Welsh, B. M. "Imaging Through Turbulence." Boca Raton: CRC Press, 1996.
- [Rousset et al, 1987] Rousset, G., et al. "Visible wavefront development. Workshop on Adaptive Optics in Solar Observations", Freiburg, Federal Republic of Germany, September 8-9, 1987.
- [Rousset et al, 1990] Rousset, G., Fontanella, JC, Kern, P., Gigan, P., Rigaut, F., "First diffraction-limited astronomical images with adaptive optics". Astron. Astrophys., 230, pp.29-32, 1990.

- [Rousset et al, 2003] Rousset, G., Lacombe, F., Puget, P., et al. Proceeding. SPIE, 4839, 140, 2003.
- [Sarazin et al, 1990] Sarazin, M. and Roddier, F., "The ESO Differential image motion monitor". Astronomy and Astrophysics (ISSN 0004-6361), vol. 227, no. 1, p. 294-300. 1990.
- [Sarazin, 1997] Sarazin M. "Automated Seeing Monitoring for Queue Scheduled Astronomical Observations" ; SPIE Proceeding, 3125, Propagation and Imaging through the Atmosphere. San Diego, pp. 29-31, 1997.
- [Sarazin and Tokovinin, 2001] Sarazin, M. and Tokovinin, A. "The Statistics of Isoplanatic Angle and Adaptive Optics Time Constant derived from DIMM Data". Venice 2001 Beyond Conventional Adaptive Optics, 2001.
- [Sarazin, 2002] Sarazin, M. and Tokovinin, A., ESO Astrophys. Symp., 58, 321, 2002.
- [Sasiela, 1994] Sasiela, R. J. Electromagnetic Wave propagation in Turbulence : Evaluation and Application of Mellin Transforms (Springer-Verlag), 1994.
- [Sasiela, 1985] Sasiela R.J. and Mooney, J.G., "An Optical Phase Reconstructor Based on Using a Multiplier-Accumulator Approach," SPIE Proceeding, 551, pp.170, 1985.
- [Sechaud et al 1991] Sechaud, M., Rousset, G., Michau, V., Fontanella, J.C., Cuby, J. G., et al. SPIE Proceeding, 1543, pp. 479-491, 1991.
- [Seibert, 2000] Seibert, P., et al., "Review and intercomparison of operational methods for the determination of the mixing height". Atmos. Environ., 34, pp.1001-1027, 2000.
- [slodar web] <http://www.cfai.dur.ac.uk/new/rd/SLODAR/SLODAR.html>.
- [Smithson, 1987] Smithson, R.C. "Adaptive Optics in Solar Observatories". LEST Technical report. 28, p193, 1987.

- [Smithson et al., 1988] Smithson, R.C. et al. "Qualitative simulation of image corrections for Astronomy with segmented active mirror.", *App. Opt.* 27, pp.1615-1620, 1988.
- [Steinhaus and Lipson 1979] Steinhaus, E. and Lipson, S.G., "Bimorph pzt flexible mirrors". *J Opt. Soc. Am.* 69, pp.478-481, 1979.
- [Stoez, 2008] Stoesz, J.A., et al. "Wide-field performance gradient at a mid-latitude site and at Dome C". *SPIE Proceeding*, 7012, 2008.
- [Stull, 1988] Stull, R.B, *An introduction to boundary layer meteorology* , Kluwer Academic Publishers, Dordrecht, 1988.
- [Tatarski, 1961] Tatarski, V. I. "Wave Propagation in a Turbulent Medium", McGraw-Hill, 1961.
- [Tatarski, 1971] Tatarski, V. I.. *The Effects of the Turbulent Atmosphere on Wave propagation*. IPST Catalog No. 5319 (National Technical Information Service, Springfield, Va., 1971.
- [Tatarski et al, 1985] Tatarski, V. et al. "Wave propagation in random media with fluctuating turbulent parameters," *J. Opt. Soc. Am.* A2, pp.2069-2076, 1985.
- [Tjernstrom et al, 1993] Tjernstrom, A .et al. "Turbulence length scale in stable stratified free shear flow analysed from slant aircraft profiles". *Journal of Applied Meteorology*, Vol.32, pp. 948-963, 1993.
- [Tokovinin, et al. 1998] Tokovinin, A. et al. "Wavefront outer scale in La Silla", *Astron. Astrophys.* 336, pp.49-52, 1998.
- [Tokovinin, 2002] Tokovinin, A., "From Differential Image Motion to Seeing", *P.A.S.P.*, Volume 114, Issue 800, pp. 1156-1166, 2002.
- [Tokovinin, et al. 2003] Tokovinin A. Baumont S, Vasquez J, "Statistics of turbulence profile at Cerro Tololo". *Monthly Notices of the Royal Astronomical Society*. Vol 340, Issue 1, pp. 5258, 2003.

- [Tokovinin and Kornilov, 2003] Tokovinin A., Kornilov V., Shatsky N., et al., MN-RAS 343, 891, 2003.
- [Tokovinin et al. 2005] Tokovinin A., Vernin J., Ziad A. and Chun M., "Optical Turbulence Profiles at Mauna Kea Measured by MASS and SCIDAR", PASP, 117, pp.395, 2005.
- [Trinquet et al, 2006] Trinquet, A, et al. "A model to forecast seeing and estimate  $C_n^2$  profiles from meteorological data", Astron. Soc. Pac. 118, pp. 756-764, 2006.
- [Trinquet et al, 2008] Trinquet, H., et al. "Nighttime optical turbulence vertical structure above Dome C in Antarctica." PASP, 120, pp.203-211,2008.
- [Turner, 1973] Turner, J.S., "Buoyancy Effects in Liquids". Cabridge University Press, 1973.
- [Tyson, 1991] Tyson, R.K., "Principle of Adaptive Optics"., Academic Press. San Diego, 1991.
- [Tyson and Frazier, 2004] Tyson, R. K. and Frazier, B. W. "Field guide to adaptive optics". SPIE Press. p. 14. ISBN 0819453196., 2004.
- [Ulrich, 1988] Ulrich, P.B. "Hufnagel-Valley profiles for specified values of the coherence length and isoplanatic angle" ,MA-TN-88-013, W. J. Schafer Associates, 1988.
- [Ulrich, 1993] Ulrich, P.B., "Aesthetic and affective responses to natural environment". In: Altman, I., Wohlwill, J.F. (Eds.), Behavior and the Natural Environment. Plenum, New York, pp. 85-125, 1993.
- [Valley, 1980] Valley,G. C. "Isoplanatic degradation of tilt correction and short-term imaging systems," Appl. Opt. 19, pp. 574-577, 1980.
- [VanZandt, et al, 1978] VanZandt. T. E. et al. "Vertical Profiles of Refractivity Turbulence Structure Constant- Comparison of Observations by the Sunset Radar with a New Theoretical Model". Radio Sci. 13, pp.819-829, 1978.

- [Varela et al 2006] Varela A., et al. "Tropospheric wind regimes and site topography effects: importance for site characterization". SPIE Proceedings 6267, pp. 62671, 2006.
- [Vernin and Azouit, 1983] Vernin J., Azouit M., J. Opt. (Paris) 14, pp. 131,1983.
- [Vernin et al, 1992] Vernin J, Munoz-Tunon.C. A.&A., 257, 811, 1992.
- [Vernin and Avila, 1998] Vernin, J. and Avila, R. "Mechanism of formation of atmospheric turbulence relevant for optical astronomy. An Interstellar Turbulence", J. Franco and A. Carraminana, eds., Cambridge University Press., 1998.
- [VonKarman, 1948] Von Karman. T. "Progress in the statistical theory of turbulence. J. Mar. Res. 7, p252264, 1948.
- [Wallance and Hobbs, 2006] Wallace, J. M. and P. V. Hobbs, :,Atmospheric Science. Vol. 92 of International Geophysics Series. Academic Press, San Diego, CA, second edition. 2006
- [Walker, 1971] Walker, M.F. PASP, 80,672, 1971.
- [Wallner, 1983] Wallner, E.P. "Optimal corrections using slopes measurements". J.Opt.Soc.Am, 73, pp.1771-1776, 1983.
- [Wang and Markey1978] Wang, J.Y. and Markey, J.K. "Modal compensation of atmospheric turbulence phase distortion". J.Opt. Soc. Am. 68, pp.78-87, 1978.
- [Warnock and VanZandt 1985] Warnock J.M. and VanZandt, T.E., NOAA, Tech. Report, ERL,AL-10, 175, 1985.
- [Weber et al,1993] Weber B. L, et al. "Quality controls for profiler measurements of winds and RASS temperatures". J Atmos Oceanic Technol 10, pp. 452-464,1993.
- [Wilson et al, 2002] Wilson, R. et al. "SLODAR: measuring optical turbulence altitude with a Shack-Hartmann wavefront sensor. Mon. Not. R. Astron. Soc. 337, pp.103-108, 2002.

- 
- [Young et al, 1998] Young, C.I. et al. "Time of arrival fluctuation of a space time Gaussian pulse in weak optical turbulence; an analytical solution". Appl. Opt.37, pp.7655-7660, 1988.
- [Ziad et al, 1999] Ziad, A, et al. "Generalized seeing monitor (GSM): a dedicated monitor for wavefront optical parameter measurements", SPIE proceeding, 3866, 152, 1999.